

Catalysis, chemistry, and automation

Addressing complexity to explore practical limits of homogeneous Mn catalysis

van Putten, R.

DOI

[10.4233/uuid:e94a4c47-b3f7-45a7-a38c-9c319c38a51f](https://doi.org/10.4233/uuid:e94a4c47-b3f7-45a7-a38c-9c319c38a51f)

Publication date

2021

Document Version

Final published version

Citation (APA)

van Putten, R. (2021). *Catalysis, chemistry, and automation: Addressing complexity to explore practical limits of homogeneous Mn catalysis*. [Dissertation (TU Delft), Delft University of Technology]. <https://doi.org/10.4233/uuid:e94a4c47-b3f7-45a7-a38c-9c319c38a51f>

Important note

To cite this publication, please use the final published version (if applicable). Please check the document version above.

Copyright

Other than for strictly personal use, it is not permitted to download, forward or distribute the text or part of it, without the consent of the author(s) and/or copyright holder(s), unless the work is under an open content license such as Creative Commons.

Takedown policy

Please contact us and provide details if you believe this document breaches copyrights. We will remove access to the work immediately and investigate your claim.

CATALYSIS

CHEMISTRY

AND

AUTOMATION

ADDRESSING COMPLEXITY
to explore

practical
LIMITS

OF HOMOGENEOUS
Mn catalysis

by

ROBERT *van*
PUTTEN



Catalysis, chemistry, and automation

Addressing complexity to explore practical limits of homogeneous Mn catalysis

Dissertation

for the purpose of obtaining the degree of doctor

at Delft University of Technology

by the authority of the Rector Magnificus, Prof.dr.ir. T.H.J.J. van der Hagen,

chair of the Board of Doctorates

to be defended publicly on

Wednesday 13 October 2021 at 17:30 o'clock

by

Robbert VAN PUTTEN

Master of Science in Chemical Engineering,

Eindhoven University of Technology, the Netherlands

Born in Zevenbergen, the Netherlands

This dissertation has been approved by the promotor.

Composition of the doctoral committee:

Rector Magnificus	Chairperson
Prof. dr. E.A. Pidko	Delft University of Technology, promotor
Prof. dr. K.F. Jensen	Massachusetts Institute of Technology, promotor

Independent members:

Prof. dr. M. Beller	Leibniz-Institut für Katalyse e.V., Germany
Prof. dr. A.G. Doyle	University of California, Los Angeles, USA
Prof. dr. F. Hollmann	Delft University of Technology
Dr. R. Eelkema	Delft University of Technology
Dr. L. Lefort	Janssen Research & Development, Belgium
Prof. dr. A. Urakawa	Delft University of Technology (reserve member)

To my parents

.....

“One, remember to look up at the stars and not down at your feet. Two, never give up work. Work gives you meaning and purpose, and life is empty without it. Three, if you are lucky enough to find love, remember it is there and don’t throw it away.”

Stephen Hawking

Robbert van Putten

Catalysis, chemistry, and automation

ISBN

978-94-6384-246-4 (paperback), 978-94-6384-245-7 (hardcover).

A catalogue record is available at the Delft University of Technology library.

Copyright

© 2021 by Robbert van Putten

About this work

The research described in this dissertation has been carried out in the laboratory of Inorganic Systems Engineering. This laboratory is part of the Chemical Engineering department of the faculty of Applied Science at Delft University of Technology, the Netherlands. The work described in chapter six has been performed in the Jensen Research Group at the Massachusetts Institute of Technology, United States of America. The research described in this dissertation was funded by the European Research Council.

**Cover design & illustrations**

Ilse Schrauwers | isontwerp.nl

Printing

Ridderprint | Alblasserdam, the Netherlands

Contents

PREFACE

Summary.....	vii
Samenvatting.....	xi
CHAPTER 1 Introduction.....	1

PART I: CHEMISTRY & CATALYSIS

CHAPTER 2 The asymmetric transfer hydrogenation of ketones with bidentate Mn ^I -N,N' catalysts.....	17
CHAPTER 3 The preparation of Mn ^I -NHC complexes and their application as transfer hydrogenation catalysts.....	47
CHAPTER 4 Mn-mediated C-C bond formation: alkoxycarbonylation of organoboranes.....	69
CHAPTER 5 Deactivation of Mn ^I -NHC transfer hydrogenation catalysts and its prevention.....	101

PART II: CHEMISTRY & AUTOMATION

CHAPTER 6 Automation-guided reaction development of high-pressure gas-liquid catalytic reactions in oscillatory microflow.....	161
CHAPTER 7 Automation and information sciences for catalysis R&D.....	189
CHAPTER 8 Outlook.....	229

APPENDIX

APPENDIX A Acknowledgements.....	239
APPENDIX B List of publications.....	245
APPENDIX C Curriculum Vitae.....	249

Summary

Catalysis is a critical enabling technology that directly contributes to higher standards of living. This is a remarkable feat for a technology that most consumers have no direct contact with and perhaps only vaguely know from their car's catalytic converter. Even many technical users regard catalysts as ideal substances that promote a target transformation without being consumed in the reaction. Reality, however, is much more complex because catalysts can also produce undesirable side-products or stop working before the target reaction is complete. This dissertation explores such complexity.

The aim of this work was to study real catalytic systems under relevant reaction conditions, and to use the obtained insight to develop improved methods of operation (*e.g.*, faster, cheaper, safer) at lower catalyst loading. This challenge was approached from two different directions, and the dissertation is therefore divided into two parts: **Part I** of this dissertation focuses on catalysis and chemistry, whereas **Part II** is most concerned with automation and the development of advanced data-rich chemical experimentation tools.

Part I describes our study of non-noble Mn complexes as catalysts for a variety of reduction chemistries. Particular attention was given to the study of deactivation phenomena to understand why some catalysts stop operating early in their lifetime. This part opens with **Chapter 2**, which details the preparation, characterisation, and application of Mn^I-*N,N'* complexes for the asymmetric transfer hydrogenation of ketones. Detailed mechanistic studies revealed that simple diamine ligands could not induce sufficient steric strain to facilitate high enantioselectivity, and that such strain could not realistically be applied without dramatic loss of catalytic activity. Ultimately, these complexes were moderately active catalysts that enabled the quantitative reduction of aryl ketones in good enantiomeric excess.

Chapter 3 builds on the findings of the preceding chapter and describes the preparation and application of bidentate Mn^I-NHC complexes as ketone transfer hydrogenation catalysts. These compounds exhibited significantly improved performance compared to their Mn^I-*N,N'* counterparts. The higher activity of these systems enabled a reduction of catalyst loading from 0.5 mol% for the Mn^I-*N,N'* catalyst to 0.0075 mol% for the Mn^I-NHC system. A further reduction of catalyst loading was prevented by extensive catalyst deactivation that was particularly sensitive to reaction temperature. This deactivation reaction was investigated in more detail in **Chapter 5**.

Chapter 4 describes a conceptually new alkoxycarbonylation reaction between Mn^I carbonyl complexes and organo(alkoxy)borate salts. This reaction was serendipitously discovered during our studies into the origin of deactivation of Mn^I -NHC catalysts. The new alkoxycarbonylation reaction led to the formation of aliphatic and aromatic ester products that contained a new sp^2 - sp^2 or sp^2 - sp^3 carbon-carbon bond. Finally, a reaction mechanism was proposed on the basis of stoichiometric reactivity studies, *in situ* spectroscopy, and quantum chemical calculations. We found that the reaction between Mn-bound carbonyl ligands and hard alkoxide bases was very favourable and might directly contribute to the deactivation of Mn^I catalysts under basic conditions.

Chapter 5 is a detailed study into the deactivation behaviour of the Mn^I -NHC transfer hydrogenation catalyst described in **Chapter 3**. This process was studied with a variety of techniques that include kinetic measurements, modelling efforts, stoichiometric reactivity studies, and several modes of spectroscopy. These studies indicated that the deactivation reaction produces large, antiferromagnetically coupled, paramagnetic Mn-oxo clusters that are at least partially oxidised to Mn^{II} . Dedicated EXAFS experiments are expected to provide structural insight into these clusters once synchrotron beamtime becomes available. Addition of triethylborane to the reaction mixture significantly improved catalyst lifetime and regularly enabled turnover numbers as high as 30.000 at 50 ppm Mn. Stoichiometric reactivity studies finally revealed that the resulting organo(alkoxy)borate salt anions were significantly less reactive towards Mn^I complexes compared to ‘unprotected’ alkoxides, and might thus prevent the formation of unstable intermediates that lead to deactivation. **Chapter 5** marks the end of **Part I** of this dissertation.

Part II focuses on the development and application of automation and data-rich experimentation methods for catalysis R&D. These tools were used to study and optimise the performance of a variety of chemistries, and are expected to provide the dense data that are required for contemporary data-driven analysis tools.

Chapter 6 describes the development and application of automated microfluidic screening and optimisation tools that enable high-pressure gas-liquid catalytic chemistry. MIT’s existing oscillatory flow platform was modified to support the desired reaction conditions and enable continuous operation at 70 °C and 40 bar. The platform’s capabilities were demonstrated with a challenging Ru-catalysed asymmetric hydrogenation of a highly base-labile β -aminoketone substrate. Favourable reaction conditions were identified and the reaction was rapidly scaled-up to multigram quantities. This automation-guided reaction development approach ultimately enabled the discovery and scale-up of a challenging chiral reduction in less than a week of total experimental time.

Chapter 7 finally describes our ongoing efforts in automation and data-rich chemical experimentation, as well as their anticipated impact on homogeneous catalysis R&D. A sampling system was developed that enabled the automated acquisition of high-quality kinetic data. This autosampler was incorporated into a powerful and flexible reaction analysis platform that produced simultaneous kinetic measurements and several representative modes of *operando* spectroscopy. A data management and analytics tool was developed to reproducibly store, visualise, and gain insight from the produced data. Finally, a novel integral experimental and computational work flow was proposed that aims to provide the data required for modern data-driven methods and unlock the power of machine learning in catalysis R&D.

Chapter 8 is the last chapter of **Part II** and provides a brief perspective on future developments in the field. First, an outlook is provided on the development of high-turnover, non-noble metal catalysts, and their practical application. This is followed by a discussion of recent trends in automation and modern data-science tools, as well as their projected impact on catalyst development in the near future. The chapter closes with a very short outlook on the changing culture of academia.

Samenvatting

Katalyse is een zeer veelzijdige en waardevolle technologie welke direct bijdraagt aan het verhogen van de mondiale levensstandaard. Katalyse heeft daarmee een grote impact op ons dagelijks leven. Het is daarom opmerkelijk dat de meeste consumenten geen direct contact met katalysatoren hebben, en waarschijnlijk slechts vaag bekend zijn met de driewegkatalysator in hun auto. Dit beeld is hetzelfde voor chemici en andere gebruikers van katalysatoren. Velen houden vast aan wat ze op de middelbare school geleerd hebben: een katalysator is een ideale stof die de gewenste reactie versnelt, maar zelf niet in de reactie verbruikt wordt. De realiteit is echter niet zo simpel. Het is bijvoorbeeld mogelijk dat de katalysator ongewenste zijproducten maakt, of dat deze wél verbruikt wordt in de reactie en daarmee activiteit verliest. Dit proefschrift gaat over dergelijke complexiteit.

Het doel van dit onderzoek was het bestuderen van realistische katalysatoren (in tegenstelling tot modelsystemen die gemakkelijker te bestuderen zijn), en om de opgedane kennis te gebruiken om betere (bijvoorbeeld efficiëntere, goedkopere, of veiligere) katalysatoren te ontwerpen die in lage concentraties gebruikt kunnen worden. Deze onderzoeksvraag is vanaf twee richtingen benaderd, en het proefschrift is daarom opgedeeld in twee delen: **Deel I** beschrijft onze ontwikkeling van katalysatoren vanuit een chemische invalshoek, terwijl **Deel II** een meer technologische aanpak heeft en leunt op automatisering en geavanceerde experimentele technieken.

Deel I beschrijft de ontwikkeling van nieuwe mangaancomplexen en hun katalytische toepassing in verschillende reductiereacties. Hierbij is vooral aandacht gegeven aan het bestuderen van deactiveringsreacties om te gaan begrijpen waarom sommige katalysatoren hun activiteit relatief snel verliezen. **Hoofdstuk 2** is het eerste hoofdstuk van dit deel en gaat over de bereiding, karakterisatie, en katalytische toepassing van nieuwe $Mn^{I-N,N'}$ complexen voor de asymmetrische transfer hydrogenatie van ketonen. Gedetailleerde mechanistische studies lieten zien dat simpele, op diamines gebaseerde liganden onvoldoende sterische druk uitoefenden om hoge enantioselectiviteit te behalen. Zulke druk kon praktisch gezien ook niet gerealiseerd worden zonder een significant verlies van katalytische activiteit. Uiteindelijk waren deze mangaancomplexen matig actieve katalysatoren en faciliteerden ze de volledige reductie van aromatische ketonen in goede optische zuiverheid.

Hoofdstuk 3 beschrijft de synthese, karakterisatie, en katalytische toepassing van nieuwe Mn^I -NHC complexen voor de transfer hydrogenatie van ketonen. Dit hoofdstuk borduurt voort op het vorige hoofdstuk, en de resulterende katalysatoren waren significant beter dan die beschreven in **Hoofdstuk 2**. De hogere intrinsieke activiteit van de Mn^I -NHC katalysatoren maakte het mogelijk om de katalysatorconcentratie te verlagen van 0.5 mol% van de Mn^I - N,N' complexen tot 0.0075 mol% van het Mn^I -NHC systeem. Een verdere verlaging werd verhinderd door deactivatie van de katalysator. Dit fenomeen was vooral gevoelig voor de reactietemperatuur en werd verder bestudeerd in **Hoofdstuk 5**.

Hoofdstuk 4 gaat over de vondst van een nieuwe alkoxy-carbonylering tussen Mn^I carbonylcomplexen en organo(alkoxy)boraatzouten. Deze reactie werd per toeval ontdekt gedurende ons onderzoek naar deactivatiereacties van Mn^I -NHC katalysatoren. De nieuwe alkoxy-carbonylering leidde tot de vorming van alifatische en aromatische esters met een nieuwe sp^2 - sp^2 of sp^2 - sp^3 koolstof-koolstofbinding. Het reactiemechanisme werd onderzocht met stoichiometrische reactiviteitsstudies, *in situ* spectroscopie, en kwantumchemische berekeningen. Hieruit werd geconcludeerd dat de reactie van een mangaan-gebonden carbonyl ligand en een 'hard' alkoxyde zeer gemakkelijk verloopt. Het is daarom goed mogelijk dat deze reactie direct bijdraagt aan de deactivatie van Mn^I katalysatoren in basische media.

Hoofdstuk 5 beschrijft een gedetailleerde studie naar het deactivatiegedrag van de Mn^I -NHC katalysator uit **Hoofdstuk 3**. Het deactivatieproces werd bestudeerd met verschillende technieken, waaronder het meten van reactiekinetiek, modelleerstudies, stoichiometrische reactiviteitsstudies, en verschillende soorten spectroscopie. Deze metingen gaven aan dat de deactivatiereactie resulteert in de vorming van relatief grote, antiferromagnetisch gekoppelde, paramagnetische Mn -oxo clusters, welke op z'n minst gedeeltelijk geoxideerd zijn tot Mn^{II} . De precieze structuur van deze clusters is momenteel nog onduidelijk, maar we verwachten dat toekomstige EXAFS-metingen hier duidelijkheid in zullen verschaffen. De toevoeging van kleine hoeveelheden triethylboor aan het reactiemengsel leidde tot een significante verlenging van de katalysatorlevensduur en maakte het mogelijk om omzettinggetallen te behalen van meer dan 30.000 met 50 ppm Mn . Stoichiometrische reactiviteitsstudies lieten tot slot zien dat de resulterende anionische organo(alkoxy)boraatzouten significant minder reactief waren jegens Mn^I complexen wanneer vergeleken met 'onbeschermde' alkoxydes. Dergelijk afschermen van reactiviteit voorkomt daarom mogelijk de vorming van instabiele intermediairen welke leiden tot deactivatie. **Hoofdstuk 5** is het laatste hoofdstuk van **Deel I** van dit proefschrift.

Deel II van dit proefschrift gaat over de toepassing van automatisering en de ontwikkeling van geavanceerde experimentele technieken. Deze apparaten werden vervolgens gebruikt om verschillende reacties te bestuderen en optimaliseren. Het is de verwachting dat dergelijke technologieën de waardevolle data zullen produceren die benodigd zijn voor moderne analysetechnieken zoals *machine learning* en andere vormen van kunstmatige intelligentie.

Hoofdstuk 6 beschrijft de ontwikkeling en toepassing van geautomatiseerde microfluidische screening- en optimalisatie-apparatuur voor katalytische gas-vloeistofreacties onder hoge druk. MIT's bestaande *oscillatory flow platform* werd aangepast om de gewenste reactieomstandigheden mogelijk te maken en reacties tot maximaal 70 °C en 40 bar uit te kunnen voeren. De mogelijkheden van het platform werden vervolgens gedemonstreerd met een uitdagende ruthenium-gekatalyseerde asymmetrische hydrogenatie van een β -aminoketon. Gunstige reactieomstandigheden werden snel geïdentificeerd met het systeem en de reactie werd opgeschaald tot meerdere grammen. Deze geautomatiseerde aanpak leidde uiteindelijk tot de ontdekking en opschaling van een uitdagende chirale reactie in minder dan een week experimentele tijd.

Hoofdstuk 7 beschrijft ons werk op het gebied van automatisering en de ontwikkeling van geavanceerde experimentele technieken. Dit begon met het ontwerp en de constructie van een innovatief geautomatiseerd bemonsteringssysteem dat het mogelijk maakte om kinetische informatie te verkrijgen van hoge kwaliteit. Dit systeem werd vervolgens geïntegreerd in een krachtig analyseplatform dat tegelijkertijd bemonstert en meerdere *operando* spectroscopietechnieken toepast, en daarmee uniek inzicht produceert. Een datamanagementsysteem werd ontwikkeld om de geproduceerde data op een reproduceerbare manier op te slaan, te visualiseren, en inzicht te verkrijgen. Het hoofdstuk eindigt met een voorstel voor een nieuwe en innovatieve manier van werken wat de krachten van experimenten en simulaties integreert. We verwachten dat dit systeem unieke en waardevolle data zal produceren welke geschikt zijn voor populaire analysetechnieken zoals *machine learning*, en dat dit de kracht van kunstmatige intelligentie zal ontketen voor de ontwikkeling van katalysatoren.

Hoofdstuk 8 geeft tot slot een kort commentaar betreffende verdere ontwikkelingen in het veld van dit proefschrift. Dit hoofdstuk begint met een perspectief op de toepassing en ontwikkeling van op onedele metalen gebaseerde katalysatoren. Dit wordt gevolgd door een korte beschrijving van recente trends binnen het veld van automatisering en nieuwe data-gedreven technieken, alsmede de verwachte impact hiervan op de ontwikkeling van katalysatoren in de nabije toekomst. Het hoofdstuk sluit af met een kort perspectief op de veranderende cultuur binnen de academische wereld.



Chapter

1



Introduction



“Have no fear of perfection—you’ll never reach it.”

Salvador Dalí

1.1 Introduction

Catalysis has become a mission critical technology for modern society and global trade. An estimated 85% to 90% of production processes in the chemical industry are operated in the presence of a catalyst, and more than half of the world's population is directly supported by Haber-Bosch's nitrogen fixation process.¹⁻² This production of ammonia accounts for approximately 1% of global energy consumption and produces 1.4% of global carbon dioxide emissions.³ (Which exceeds the emissions of a typical European country.) Operation at such scale means that even incremental efficiency gains can have a pronounced impact.

The significant impact and potential of catalytic technologies has not gone unnoticed. Approximately 13% of Nobel prizes in chemistry have been awarded for inventions or scientific discoveries that relate to catalytic or enzymatic transformations.⁴ (That were shared by 17% of laureates awarded the prize.) These breakthroughs also matter in industry; market analysts estimate that the global catalyst business was worth upwards of 20 billion USD in 2020.⁵⁻⁹ This market is expected to grow substantially in the near future with diversification of energy supplies and the potential pivot to a green hydrogen economy.¹⁰⁻¹² It is therefore reasonable to conclude that catalysis is one of the most important and promising enabling technologies today. This is a remarkable feat for a technology that most consumers have no direct contact with and only vaguely know from the automotive catalytic converter that is mounted underneath their car. Many users regard catalysts as ideal substances that promote a target transformation without being consumed in the reaction. Reality, however, is far more complex because catalysts can also produce undesirable side-products or stop working before the reaction is complete. This dissertation explores such complexity.

1.2 Development of catalytic technologies

Catalysts are generally subdivided into two classes that have distinct characteristics (**Table 1.1**). Heterogeneous catalysts are most often applied under harsh reaction conditions in large-scale (petro)chemical processes. These catalytic systems are referred to as being 'heterogeneous' because the catalyst and reaction mixture are present in different phases, which greatly simplifies continuous operation at high material throughput. Such metal catalysts are conventionally supported on ceramic carriers and extruded into particles that optimise productivity, pressure drop, mechanical stability, and mass and heat transfer. Heterogeneous catalysts often are relatively robust and can be operated for extended amounts of time.

Table 1.1. Generalised overview of different catalytic technologies, their properties, and their application.

	Heterogeneous	Homogeneous
	Solid and supported catalysts	Transition metal complexes Enzymes
Activity	Low	Moderate to high
Selectivity	Low	High
Stability	High	Low
Conditions	Harsh	Mild
Scale	Large	Small
Recycling	Easy	Difficult
Relative cost	Low	High
Application	Commodities	Fine and specialty chemicals

Homogeneous catalysts are used in the same phase as the reaction mixture, which is usually a solution that contains a dissolved catalyst. This class of catalysts is diverse and encompasses, *e.g.*, strong (Lewis and Brønsted) acids or bases, enzymes, and transition metal complexes. The chemical scope of these catalysts ranges from relatively straightforward base-catalysed elimination reactions to highly complex and specific transformations that are catalysed by enzymes and molecular catalysts. Enzymes are particularly elegant catalysts that enable highly complex conversions with excellent activity, selectivity, and specificity. Because homogeneous catalysts are dissolved in the reaction mixture, post-reaction recovery of the catalyst is very difficult, and these compounds are therefore usually used only once. (Note that there are exceptions, of which industrial ‘oxo-synthesis’ (hydroformylation) is perhaps the most notable example.)

This dissertation focuses on the development of well-defined transition metal catalysts. These catalytic systems are most commonly applied in the fine-chemical, pharmaceutical, and agrochemical industries where their relatively high cost can be offset by the high added value of the target transformation. Catalytic reactions are usually performed in batch in multi-purpose facilities, which makes consumption of the (single-use) catalytic system a major driver of operational cost that determines a process’s viability. The availability of more active, selective, and stable catalysts would thus likely drive further adoption of advanced chemical solutions in the chemical industry. Prominent examples of such chemistries include cross-coupling reactions, olefin metathesis reactions, carbonylations, and asymmetric hydrogenations (**Figure 1.1**). These reactions are particularly useful because their chemistry cannot reasonably be performed by other, non-catalytic, means. This fundamental and practical importance was recognised by the Nobel committee, who awarded the 2001, 2005, and 2010 Nobel prizes in chemistry for the discovery of three of these transformations.

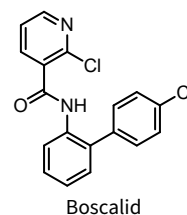
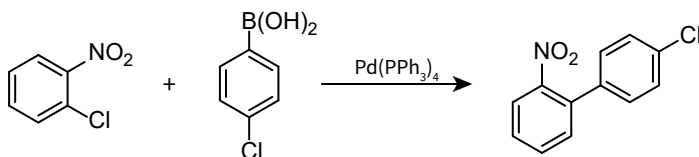
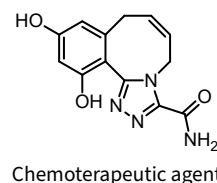
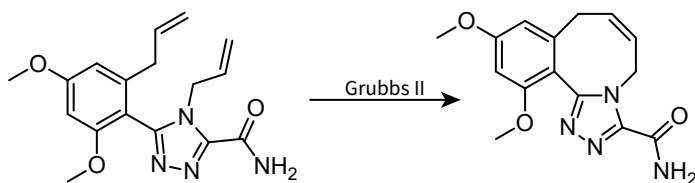
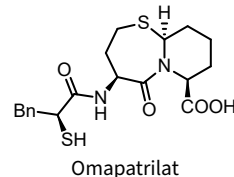
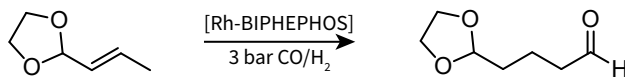
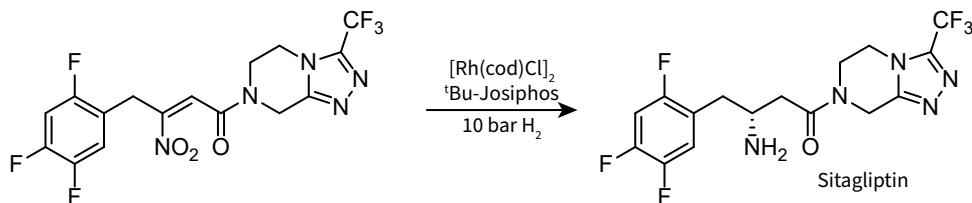
a) Pd-catalysed Suzuki coupling**b) Ru-catalysed olefin metathesis****c) Rh-catalysed hydroformylation****d) Rh-catalysed asymmetric hydrogenation**

Figure 1.1. Selected examples of industrially-applied processes with homogeneous catalysts. **a)** Pd-catalysed Suzuki coupling towards fungicide Boscalid by BASF.¹³ **b)** Ru-catalysed olefin metathesis towards a chemotherapeutic agent by Synta Pharmaceuticals.¹⁴ **c)** Rh-catalysed hydroformylation toward Omapatrilat by Chirotech Technology.¹⁵ **d)** Rh-catalysed asymmetric hydrogenation toward Sitagliptin by Merck & Co.¹⁶

Introduction of a catalytic step can bring tremendous ecological and economical benefits that become particularly clear when cumulative savings over the product's lifetime are considered. Although production volumes in the fine-chemical industry are relatively small compared to those of the (petrochemical) bulk industry, its production of waste per kg of the finished product is considerably higher (this ratio is conventionally referred to as a process's E-factor).^{1,17} For example, Merck & Co.'s introduction of asymmetric catalysis to the production of Sitagliptin (**Figure 1.1d**) led to a reduction of 200 kg waste per kg product and the elimination of an entire aqueous waste stream.^{16,18} The company expects that this next-generation catalytic route will save 150 kilotonnes of waste over the product's lifetime—savings that would have been difficult to realise with other methods. This demonstrates that homogeneous catalysis can play an important role in industry, provided that suitably active, selective, and stable catalysts are available at scale.

1.3 High-turnover catalytic systems

Development of catalytic routes is often challenging and time-consuming. Most real-world catalytic systems are complex multicomponent mixtures that contain metal centres, ligands, promoters, additives, substrates, and products, all under specific reaction conditions, while being dissolved in a solvent. This means that a supposedly well-defined homogeneous *catalyst* is actually part of a much more complex *catalytic system*. Because of this, commercial off-the-shelf (pre)catalysts cannot realistically meet all possible requirements that could exist for diverse use cases, which usually necessitates some degree of in-house development. Sometimes specific adaptations have to be made to address particular needs, such as, *e.g.*, limitations on use of intellectual property. Other requirements and trends are more general. For example, in recent years there has been a significant push to substitute noble metals for non-noble alternatives such as Fe and Mn. This campaign is driven by two main factors that are discussed below.

First, most non-noble metals are more abundant in the Earth's crust, which potentially leads to cheaper and more sustainable catalysts because they don't rely on scarce, precious metals. Here it is noted that non-noble metal catalysts are not *by definition* cheaper to use than their noble metal analogues, because the required organic ligands often add significantly to the cost of the catalytic solution. Non-noble metal catalysts also often require higher loadings to offset their lower intrinsic activity, which could make the overall catalytic system more expensive.

The second reason to develop non-noble metal catalysts considers the needs of some specific users. Many products of homogeneously catalysed reactions are intended for human consumption, which means that residual metal levels are important. Most metals are strongly genotoxic, and allowable levels are therefore strictly regulated.^{19–22} (Some metal complexes are used as chemotherapeutic agents because of their pronounced toxicity.^{23–25}) Non-noble metals—specifically Fe and Mn—are considerably less harmful, and their allowable levels in the final product often exceed those of noble metals. (Although neither iron or manganese is fully benign, and their excessive consumption should nevertheless be limited.²⁶) Use of high-performance non-noble metal catalysts could thus lead to a situation where (quantitative) post-reaction removal of trace metal impurities is no longer strictly required and significant economic and ecological savings could be realised.

(Note that the removal of trace metal impurities is a standard practise in industry that can, *e.g.*, be achieved with (selective) adsorption on a porous material.²⁷ Spent adsorbents are then processed and valuable platinum group metals are recovered and recycled.^{28–29} Introduction of high-performance non-noble metal catalysis would eliminate this process step and prevent the formation of waste.)

Final development and tailoring of a catalytic system is typically performed by a specialised in-house team or dedicated contract research organisation by means of high-throughput experimentation (HTE) or data-rich experimental techniques such as *in situ* spectroscopy and/or detailed kinetic measurements. This phase requires the holistic optimisation of a catalytic solution such that it becomes practically and economically viable, which means that many parameters need to be considered simultaneously. Often specific targets are set for the yield, selectivity, catalyst consumption, and cost to realise the target transformation.

The useful lifetime of a catalytic system is a particularly important parameter that is characterised by the turnover number (TON). (Where lifetime effectively is the inverse of catalyst consumption.) Realistic catalytic systems differ from ideal catalysts in the sense that they often have a limited lifespan and can deactivate. Such catalyst deactivation suppresses the maximum TON that can be achieved with a certain amount of the catalyst, which in turn drives cost. In fact, deactivation often is so problematic that multiple industrial accounts cite high catalyst loading as one of the largest hurdles towards commercial implementation of homogeneous catalysts.^{17,30-31} It is for this reason that this dissertation is focused on exploring practical means to reduce the required loading of non-noble metal catalysts. This was in part achieved by understanding catalyst deactivation in more detail, but also by the development of advanced screening and optimisation tools that make it possible to study such behaviour under realistic process conditions.

Before the scope of this dissertation is described in more detail, it is important to provide a conceptual overview of how catalyst lifetime may be optimised. Generally one of two approaches is used to achieve operation with less catalyst. One can: *i*) develop an intrinsically more active and robust catalyst, or *ii*) push an existing system by changing reaction conditions and using additives to make it perform better. These methods come with specific advantages and disadvantages and have both been employed in this work. Development of intrinsically more active and robust catalysts *in principle* is the most attractive strategy because it offers near-perfect, tailor-made catalytic systems for individual applications. However, it is also one of the slowest and most expensive options as it requires fundamental insight into the reaction and its critical intermediates.³⁰ These investigations generally don't scale well, and are therefore most suitable when only a small pool of catalytic systems is considered and specific target improvements are required.

The second method is more attractive from a practical point of view, particularly if time-to-market is a concern. Catalytic systems are highly sensitive to reaction conditions and the presence of additives or promoters. Catalyst lifetime may thus be optimised by selection of favourable conditions that balance activity, selectivity, and, importantly, stability. This means that catalyst consumption can

often be decreased by finding conditions that minimise catalyst deactivation. (A more thorough introduction and overview of catalyst deactivation phenomena is provided in **Chapter 5**.) Finding such conditions, however, is not trivial. Contemporary fundamental understanding is insufficiently developed to (*a priori*) predict optimal conditions. High-throughput screening was therefore developed as a more pragmatic and brute-force approach to quickly provide answers to specific questions. (HTE is introduced in more detail in **Chapter 6**.)

Finally, the effect of reaction temperature deserves further mentioning because it affects multiple aspects simultaneously. Occasionally a simple increase of reaction temperature (or time) is sufficient to achieve the required productivity. Often, however, this approach is not feasible and higher reaction temperature leads to lower product yield, selectivity, and/or catalyst lifetime. This is particularly problematic for sensitive catalysts and for chiral reactions—precisely those applications where homogeneous catalysis can make a difference. For example, enantioselective transformations are very sensitive to temperature because they rely on minor activation energy differences to favour the formation of one specific enantiomer. Operation at higher temperature requires intrinsically better catalysts to maintain identical enantioselectivity (*i.e.*, a catalyst with higher enantioselectivity $\Delta\Delta G^\ddagger$, **Figure 1.2**). Operation at elevated temperature may thus lead to reduced enantioselectivity and thereby defeat the original purpose of the catalytic reaction.

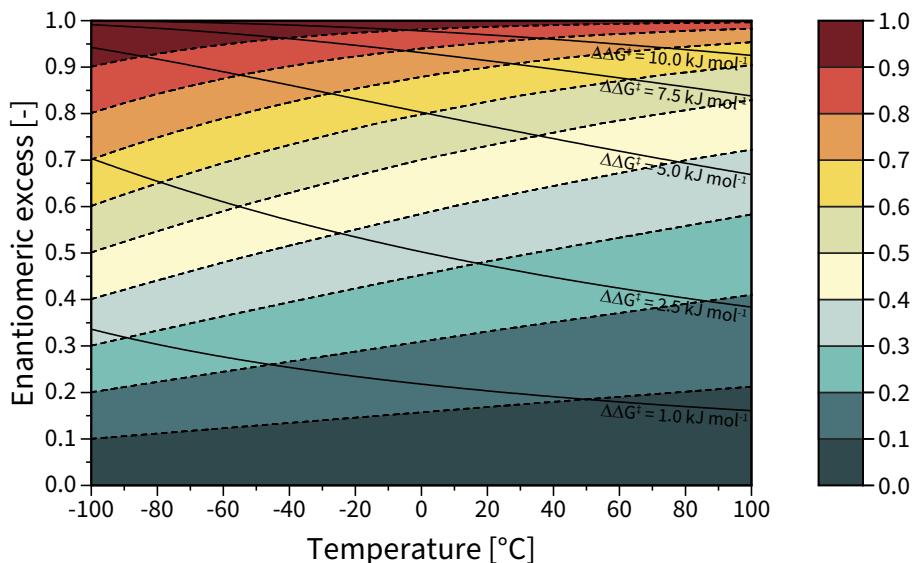


Figure 1.2. Calculated product enantiomeric excess for an irreversible first order chiral reaction as a function of temperature and $\Delta\Delta G^\ddagger$. The required $\Delta\Delta G^\ddagger$ to achieve a target product enantiomeric excess increases with reaction temperature.

The development of high-performance and/or high-turnover catalyst clearly is no easy task. Different phenomena are often correlated and observed only from their complex interaction where ‘everything depends on everything’. This, however, is no reason to become pessimistic, and the many successful applications of homogeneous catalysis serve as a humbling reminder of what is possible with the right mindset, energy, and resources. Chemical space is vast and relatively unexplored, and undoubtedly many catalytic systems remain to be discovered. This dissertation aims to contribute to this exciting field of research and hopefully leads to further adoption of homogeneous catalysis for synthetic purposes.

1.4 Scope of this dissertation

The aim of this work was to study non-noble metal catalysts for a variety of reduction chemistries and to develop methods that enable better (*e.g.*, faster, cheaper, safer) operation of these systems at lower catalyst loading. Particular attention was given to the study of deactivation phenomena to understand why some catalysts stop operating relatively early in their lifetime. The dissertation is divided into two parts, where **Part I** focuses on catalysis and chemistry, and **Part II** is most concerned with automation and the development of data-rich chemical experimentation methods.

Chapters 2–5 describe our efforts to study the chemistry of Mn^I complexes as catalysts for the transfer hydrogenation of ketones and as carbonyl donors for the alkoxycarbonylation of organoboranes. Transfer hydrogenations and carbonylations are particularly relevant for the fine-chemical and pharmaceutical industries and are considered to be relevant examples. The second part of the dissertation (**Chapter 6** and **Chapter 7**) is focused on the development and application of automation and data-rich experimentation methods in catalysis R&D. These tools were used extensively to optimise and improve the performance of catalytic systems, and their development was an important part of this work.

Chapter 2 describes the development of Mn^I-N,N' catalysts for the asymmetric transfer hydrogenation of aryl ketones. A ligand screening revealed that bidentate diamine DACH ligands provided the best balance between activity and enantioselectivity. The corresponding precatalyst was isolated and its reactivity was studied in detail with combined kinetic studies, measurement of kinetic isotope effects, stoichiometric reactivity studies, and DFT calculations. These studies indicated that the simple diamine ligands did not induce sufficient steric strain to facilitate high enantioselectivity, and that such strain could not realistically be applied without dramatic loss of catalytic activity. Ultimately the Mn^I-N,N' catalysts enabled the quantitative reduction of aryl ketones in good enantiomeric excess.

Chapter 3 builds on the findings of the preceding chapter and describes the preparation and application of bidentate Mn^I -NHC complexes as ketone transfer hydrogenation catalysts. These compounds exhibited significantly improved performance compared to the Mn^I - N,N' systems and could be used to reduce a wide scope of ketones under mild conditions. The higher activity of these systems enabled a reduction of catalyst loading from 0.5 mol% for the Mn^I - N,N' catalyst to 0.0075 mol% for the Mn^I -NHC system. A further reduction of catalyst loading was prevented by extensive catalyst deactivation that was particularly sensitive to reaction temperature. This deactivation reaction was investigated in more detail in **Chapter 5**.

Chapter 4 describes a conceptually new alkoxyacylation reaction between Mn^I carbonyl complexes and organo(alkoxy)borate salts. This reaction was serendipitously discovered during our studies into the origin of deactivation of Mn^I -NHC catalysts. The new alkoxyacylation reaction led to the formation of aliphatic and aromatic ester products that contained a new sp^2 - sp^2 or sp^2 - sp^3 carbon-carbon bond. Several new Mn^I compounds were synthesised and characterised to help understand the new chemistry. A reaction mechanism was proposed on the basis of stoichiometric reactivity studies, *in situ* spectroscopy, and quantum chemical calculations. We found that the reaction between Mn-bound carbonyl ligands and hard alkoxides was very favourable and might directly contribute to the deactivation of Mn^I catalysts under basic conditions.

Chapter 5 is a detailed study into the deactivation behaviour of the Mn^I -NHC transfer hydrogenation catalyst described in **Chapter 3**. This process was studied with a variety of techniques that include kinetic experiments, modelling efforts, stoichiometric reactivity studies, and several modes of spectroscopy. Our results indicated that the deactivation reaction produces large, antiferromagnetically coupled, paramagnetic Mn-oxo clusters that are at least partially oxidised to Mn^{II} . Attempts to isolate or prepare these clusters have thus far been unsuccessful and their exact structure is not yet clear. Dedicated EXAFS experiments are expected to provide more insight into these clusters once synchrotron beamtime becomes available. Addition of triethylborane to the reaction mixture significantly improved catalyst lifetime and regularly enabled turnover numbers as high as 30.000 at 50 ppm Mn. Stoichiometric reactivity studies finally revealed that the resulting organo(alkoxy)borate anions were significantly less reactive towards Mn^I complexes compared to 'unprotected' alkoxides, and might thus prevent the formation of unstable intermediates that lead to deactivation. **Chapter 5** marks the end of **Part I** of this dissertation.

Chapter 6 shows the development and application of automated microfluidic screening and optimisation tools that enable high-pressure gas-liquid catalytic chemistry. MIT's existing oscillatory flow platform was modified to support the desired reaction conditions and enable continuous operation at 70 °C and 40 bar. The platform's capabilities were demonstrated with a challenging Ru-catalysed asymmetric hydrogenation of a highly base-labile β -aminoketone. Favourable reaction conditions were identified that led to high yield and enantiopurity. The reaction was finally scaled-up to multigram quantities in a batch autoclave system. The automation-guided reaction development approach ultimately enabled the discovery and scale-up of a challenging chiral reduction in less than a week of total experimental time.

Chapter 7 describes our ongoing efforts in automation and data-rich chemical experimentation, as well as their anticipated impact on homogeneous catalysis R&D. A sampling system was developed that enabled the automated acquisition of high-quality kinetic data. This autosampler was incorporated into a powerful and flexible reaction analysis platform that produced simultaneous kinetic measurements and several representative modes of *operando* spectroscopy. A data management and analytics tool was developed to reproducibly store, visualise, and gain insight from the produced data. Finally, a novel integral experimental and computational work flow was proposed that aims to provide the data required for modern data-driven methods and unlock the power of machine learning in catalysis R&D.

Chapter 8 is the last chapter of **Part II** and provides a brief perspective on future developments in the field. First, an outlook is provided on the development of high-turnover, non-noble metal catalysts, and their practical application. This is followed by a discussion of recent trends in automation and modern data-science tools, as well as their projected impact on catalyst development in the near future. The chapter closes with a very short outlook on the changing culture of academia.

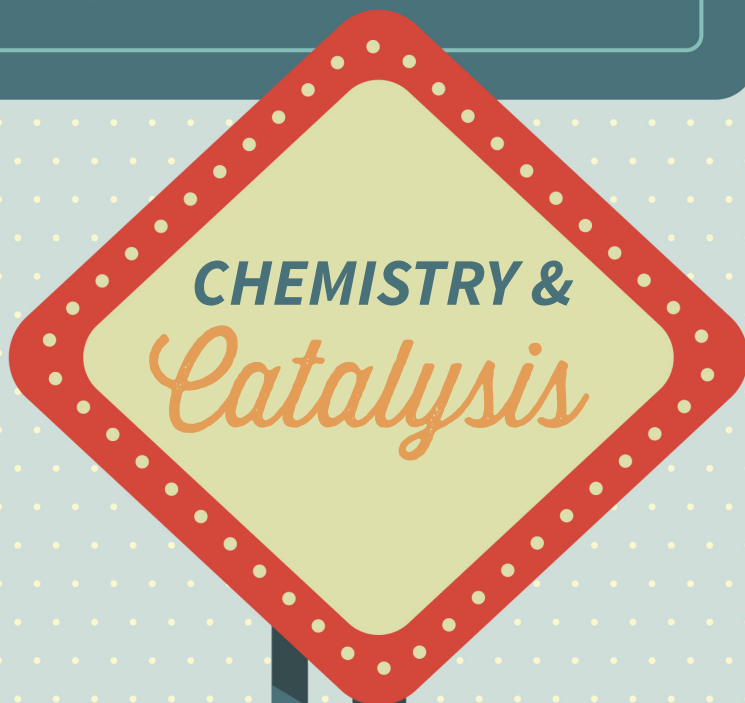
1.5 References

1. Chorkendorff, I.; Niemantsverdriet, J.W., *Concepts of Modern Catalysis and Kinetics*, Wiley-VCH Verlag GmbH & Co. kGaA, Weinheim, Germany, **2003**, 1–21;
2. Erisman, J.W.; Sutton, M.A.; Galloway, J.; Klimont, Z.; Winiwarter, W., *How a century of ammonia synthesis changed the world*, *Nature Geoscience* **2008**, 1 (10), 636–639;
3. Capdevila-Cortada, M., *Electrifying the Haber–Bosch*, *Nature Catalysis* **2019**, 2 (12), 1055–1055;
4. Thayer, A.M., *Nobel Prizes Recognized Notable Developments In Catalysis*, *C&EN* **2013**, 91 (36);
5. Grand View Research, *Catalyst Market Size, Share & Trends Analysis Report By Raw Material (Chemical Compounds, Zeolites, Metals), By Product (Heterogeneous, Homogeneous), By Application, By Region, And Segment Forecasts, 2020 - 2027*, **2020**;
6. Allied Market Research, *Catalyst market by Type (Zeolites, Chemical Compounds), Application (Petroleum Refining, Chemical Synthesis, Polymer Catalysis and Environmental) - Global Opportunity Analysis and Industry Forecast, 2014 - 2022*, **2016**;
7. IMARC group, *Industrial Catalyst Market: Global Industry Trends, Share, Size, Growth, Opportunity and Forecast 2021-2026*, **2020**;
8. Verified Market Research, *Global Industrial Catalyst Market Size By Material, By Type, By Application, By Geographic Scope And Forecast*, **2020**;
9. Hexa Research, *Catalyst Market Analysis, Market Size, Application Analysis, Regional Outlook, Competitive Strategies And Forecasts, 2014 To 2020*, **2015**;
10. Chen, Z.; Dodelet, J.P.; Zhang, J., *Non-Noble Metal Fuel Cell Catalysts*, Wiley-VCH Verlag GmbH & Co. kGaA, Weinheim, Germany, **2014**;
11. Friend, C.M.; Xu, B., *Heterogeneous Catalysis: A Central Science for a Sustainable Future*, *Accounts of Chemical Research* **2017**, 50 (3), 517–521;
12. Perathoner, S.; Gross, S.; Hensen, E.J.M.; Wessel, H.; Chraye, H.; Centi, G., *Looking at the Future of Chemical Production through the European Roadmap on Science and Technology of Catalysis the EU Effort for a Long-term Vision*, *ChemCatChem* **2017**, 9 (6), 904–909;
13. Torborg, C.; Beller, M., *Recent Applications of Palladium-Catalyzed Coupling Reactions in the Pharmaceutical, Agrochemical, and Fine Chemical Industries*, *Advanced Synthesis & Catalysis* **2009**, 351 (18), 3027–3043;
14. Hughes, D.; Wheeler, P.; Ene, D., *Olefin Metathesis in Drug Discovery and Development—Examples from Recent Patent Literature*, *Organic Process Research & Development* **2017**, 21 (12), 1938–1962;
15. Franke, R.; Selent, D.; Börner, A., *Applied Hydroformylation*, *Chemical Reviews* **2012**, 112 (11), 5675–5732;
16. Shultz, C.S.; Krska, S.W., *Unlocking the Potential of Asymmetric Hydrogenation at Merck*, *Accounts of Chemical Research* **2007**, 40 (12), 1320–1326;
17. Behr, A.; Neubert, P., *Applied Homogeneous Catalysis*, Wiley-VCH Verlag GmbH & Co. kGaA, Weinheim, Germany, **2012**;
18. Hansen, K.B.; Hsiao, Y.; Xu, F.; Rivera, N.; Clausen, A.; Kubryk, M.; Krska, S.; Rosner, T.; Simmons, B.; Balsells, J.; Ikemoto, N.; Sun, Y.; Spindler, F.; Malan, C.; Grabowski, E.J.J.; Armstrong, J.D., *Highly Efficient Asymmetric Synthesis of Sitagliptin*, *Journal of the American Chemical Society* **2009**, 131 (25), 8798–8804;

19. Valyaev, D.A.; Lavigne, G.; Lugan, N., *Manganese organometallic compounds in homogeneous catalysis: Past, present, and prospects*, *Coordination Chemistry Reviews* **2016**, 308, 191–235;
20. Bullock, R.M., *Abundant Metals Give Precious Hydrogenation Performance*, *Science* **2013**, 342 (6162), 1054;
21. European Medicines Agency, *ICH guideline Q3D (R1) on elemental impurities*, **2019**;
22. U.S. Department of Health and Human Services; Food and Drug Administration, *Q3D(R1) Elemental Impurities*, **2020**;
23. Bonetti, A.; Leone, R.; Muggia, F.; Howell, S.B., *Platinum and Other Heavy Metal Compounds in Cancer Chemotherapy*, 1st ed., Humana Press, **2009**;
24. Antonarakis, E.S.; Emadi, A., *Ruthenium-based chemotherapeutics: are they ready for prime time?*, *Cancer Chemotherapy Pharmacology* **2010**, 66 (1), 1–9;
25. Lin, K.; Zhao, Z.Z.; Bo, H.B.; Hao, X.J.; Wang, J.Q., *Applications of Ruthenium Complex in Tumor Diagnosis and Therapy*, *Frontiers in Pharmacology* **2018**, 9, 1323–1323;
26. Kumar, P.; Clark, M., *Kumar & Clark's Clinical Medicine*, 7th ed., Elsevier, **2009**;
27. Bien, J.T.; Lane, G.C.; Oberholzer, M.R., *Organometallics in Process Chemistry*, Springer, Berlin & Heidelberg, Germany, **2004**, 263–283;
28. Hagelüken, C., *Recycling the Platinum Group Metals: A European Perspective*, *Platinum Metals Review* **2012**, 56, 29–35;
29. Johnson Matthey, *Pgm refining*, <https://matthey.com/en/products-and-services/precious-metal-products/pgm-refining> (accessed 24 October 2020);
30. Hübner, S.; de Vries, J.G.; Farina, V., *Why Does Industry Not Use Immobilized Transition Metal Complexes as Catalysts?*, *Advanced Synthesis & Catalysis* **2016**, 358 (1), 3–25;
31. Blaser, H.U., *The Chiral Switch of (S)-Metolachlor: A Personal Account of an Industrial Odyssey in Asymmetric Catalysis*, *Advanced Synthesis & Catalysis* **2002**, 344 (1), 17–31.



Part I





Chapter



The asymmetric transfer hydrogenation of ketones

with bidentate Mn^I-N,N' catalysts

.....

“The unattainable is invariably attractive.”

Jenny Holzer

Abstract

Mn^I carbonyl complexes bearing chiral diamine ligands are effective catalysts for the asymmetric transfer hydrogenation of ketones. Mn(CO)₅Br reacts with chiral multidentate ligands to form Mn^I complexes. These compounds could be transformed into catalytically active species upon addition of potassium *tert*-butoxide in 2-propanol. Our screening revealed that the combination of Mn(CO)₅Br and *N,N'*-dimethyl-1,2-diaminocyclohexane provided the best balance between catalytic activity and enantioselectivity. We therefore isolated the corresponding precatalysts and used them to study the catalytic reaction.

The reaction mechanism of the Mn^I-catalysed asymmetric transfer hydrogenation was investigated with the well-defined systems. Activation of the stereoisomerically distinct precatalysts led to a shared intermediate and corresponding identical catalytic activity. A reaction mechanism was proposed that was based on kinetic studies, measurement of kinetic isotope effects, stoichiometric reactivity studies, and DFT calculations. Our studies indicated that simple diamine ligands could not induce sufficient steric strain to facilitate high enantioselectivity. Introduction of additional steric limitations resulted in improved selectivity at the cost of significantly reduced catalytic activity. Ultimately, the Mn^I-*N,N'* complexes under study enabled the quantitative reduction of aryl ketones to their corresponding chiral alcohols in good enantiomeric excess.

.....

This chapter has been published as:

R. van Putten, G.A. Filonenko, A. Gonzalez-de-Castro, C. Liu, M. Weber, C. Müller,
L. Lefort, E.A. Pidko, *Organometallics* **2019**, 38, 3187–3196

2.1 Introduction

Homogeneous hydrogenation catalysis with earth-abundant 3d transition metals such as Fe, Co, and Mn has received significant attention from the catalytic community in recent years.¹⁻² This move is important because these materials—particularly Fe and Mn—are generally considered to be relatively benign and sustainable alternatives to processes involving noble metals. These increased R&D efforts have led to the rapid development of first-row transition metal catalysts that are now applicable to a broad scope of transformations that involve hydrogen-transfer steps such as hydrogenations, dehydrogenations, and dehydrogenative couplings.³⁻⁷ Although Ru and Ir still remain the metals of choice for these reactions⁸⁻⁹, there have been several cases where early transition metal catalysts matched or even surpassed the noble metal's performance.¹⁰⁻¹³

There have also been reports of first-row transition metal complexes that showed chemically divergent reactivity compared to their noble metal congeners.^{3,5,14-15} A distinct feature of some manganese hydrogenation catalysts is that they do not require the application of strong donor ligands to become catalytically active (*e.g.*, organophosphines).¹⁶⁻¹⁷ For these complexes the introduction of simple bidentate or tridentate nitrogen-donor ligands was sufficient to promote the hydrogenation of carbon dioxide to formates or formamides¹⁸, and the transfer hydrogenation of ketones, imines, and aldimines.¹⁹⁻²⁵

When we started our investigations the groups of Kirchner²⁶, Clarke²⁷, Beller²⁸⁻²⁹, and Morris³⁰ had reported several Mn^I precatalysts as catalysts for the asymmetric (transfer) hydrogenation of ketones (**Figure 2.1**). The catalytic performance of these systems was high, and they enabled the efficient production of enantiopure alcohols in good yields. These systems required relatively complex air-free chemistry to prepare the chiral organophosphine ligands.

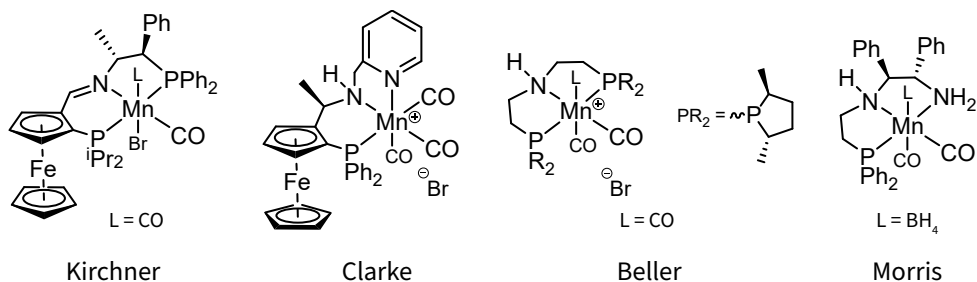


Figure 2.1. Well-defined chiral Mn^I precatalysts for the asymmetric (transfer) hydrogenation of ketones available in the open literature.

We hypothesised that the combination of Mn^I with simple chiral diamine ligands could also result in active systems. These compounds would be more attractive from a practical point of view, and would thus be better aligned with industrial requirements.^{9,31} We therefore prepared a series of Mn^I - N,N' complexes and evaluated their performance as catalysts for the asymmetric transfer hydrogenation of ketones. (The catalytic activity of a number of *in situ* generated Mn^I - N,N' systems was disclosed by Sortais and co-workers while our work was in progress.³²)

2.2 Ligand screening and system identification

We started our studies with a screening of commercial chiral diamines and aminophosphines to evaluate their potential as ligands for the Mn^I -catalysed asymmetric transfer hydrogenation of ketones. Acetophenone was selected as a representative model substrate. The Mn complexes were generated *in situ* by stirring $Mn(CO)_5Br$ with one equivalent of the chiral ligand in toluene for 15 minutes. The solution that contained the Mn/L-combination was then telescoped into a mixture of the substrate and KO^tBu in 2-propanol. An Mn loading of 1 mol% with respect to the substrate was used, and the base activator was present at 10 mol%. The reaction mixtures were heated to 60 °C for 1.5 h. This relatively short reaction time was used for the screening experiments to prevent the mixtures from reaching full conversion. (Which would have led to a loss of information on relative catalytic performance.) Mixtures were quenched with a dilute solution of acetic acid in 2-propanol and were analysed with chiral GC. The results from the ligand screening are summarised in **Figure 2.2**.

The highest catalytic activity was observed with bidentate aminophosphine ligands **L6**, **L9**, and **L10**. We speculate that this was caused by the relatively strong phosphine donor group of these compounds, which led to additional electron density on the Mn^I centre and presumably increased Mn-H hydricity. Enantioselectivity was low for the few highly active systems and product enantiomeric excess did not exceed 20%. A good enantiomeric excess of 76% was achieved with tosyl-protected DPEN (*diphenylethyleneamine*) ligand **L8**, but at much lower conversion compared to the unprotected analogue **L7**. Use of the Salen-derived tetradentate ligand **L11** did not result in a good performance. The combination of $Mn(CO)_5Br$ with DACH ligands (*1,2-diaminocyclohexane*) led to the best balance of catalytic activity and stereoselectivity. Dialkylated-DACH ligands **L2** and **L4** exhibited modest catalytic activity with alcohol yields of 46% and 63%, and achieved 62% and 69% enantiomeric excess, respectively. The catalytic system derived from non-alkylated analogue **L1** was significantly less active and selective. BOC-protected DACH **L3** and fully-alkylated DACH **L5** did not exhibit the desired reactivity under the selected reaction conditions.

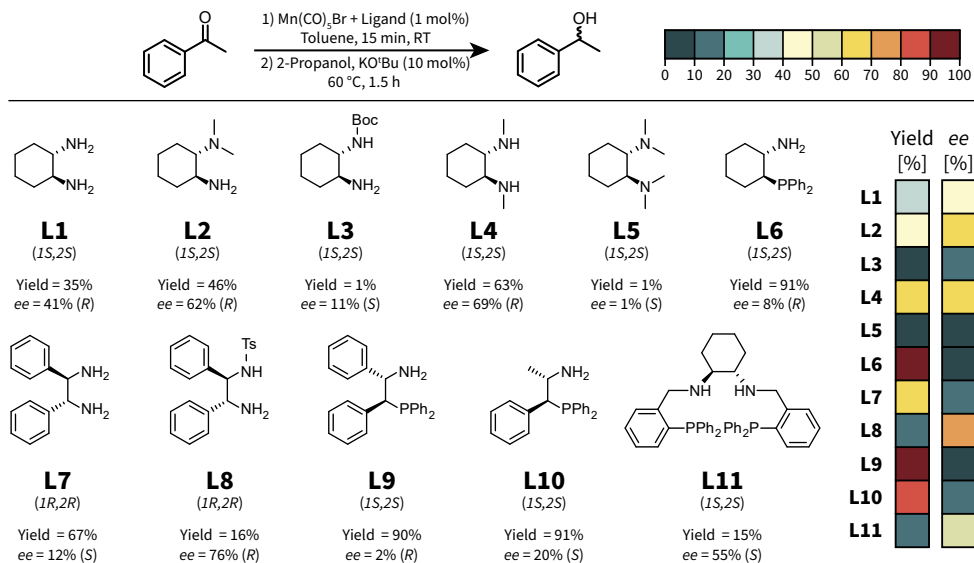


Figure 2.2. Ligand screening for the Mn-catalysed asymmetric transfer hydrogenation of acetophenone. Conditions: 0.5 mmol acetophenone, 1.0 mol% $\text{Mn}(\text{CO})_5\text{Br}$, 1.0 mol% ligand, 10 mol% KO^tBu , 2.5 ml 2-propanol + 0.5 ml toluene, 60 °C, 1.5 h. Yields were determined by GC-FID using *n*-dodecane as an internal standard.

2.3 Precatalyst isolation and characterisation

After the identification of **L4** (*N,N'*-dimethyl-1,2-diaminocyclohexane) as the best performing ligand in the screening, we sought to isolate the precatalyst that formed upon complexation of **L4** to $\text{Mn}(\text{CO})_5\text{Br}$ (**Figure 2.3**). The corresponding complex **1** was obtained after refluxing the mixture in *n*-hexane for several hours. Recrystallisation of the crude material from dichloromethane/*n*-hexane/diethyl ether at -20 °C provided analytically pure **1** in 34% yield.

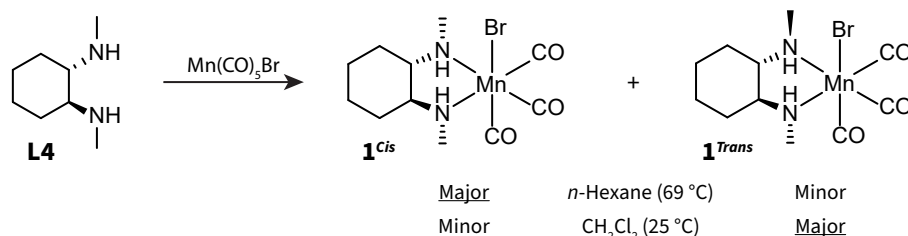


Figure 2.3. Preparation of well-defined Mn -*N,N'* precatalysts **1^{cis}** and **1^{trans}**. The mixture of *cis* and *trans* isomers is referred to as **1**.

The methyl groups of ligand **1** lost chemical equivalence upon complexation and appeared in the ^1H NMR spectrum of **1**^{*cis*} as two sharp doublets at $\delta = 2.85$ ppm and $\delta = 2.66$ ppm (**Figure 2.4a**). This dissimilarity presumably originated from the specific chair conformation of the cyclohexane ring, which was locked upon chelation to the Mn centre. The different steric environments of the axially- and equatorially-bound nitrogen atoms (*i.e.*, that were located in varied proximity to the ring-bound C-H atoms) led to the presence of two distinct signals in the ^1H NMR spectrum. The N-H resonances in **1**^{*cis*} were present as two broad singlets at $\delta = 4.19$ ppm and $\delta = 3.07$ ppm. These different chemical shifts provided another indication of the chemical inequivalence of the two amino groups.

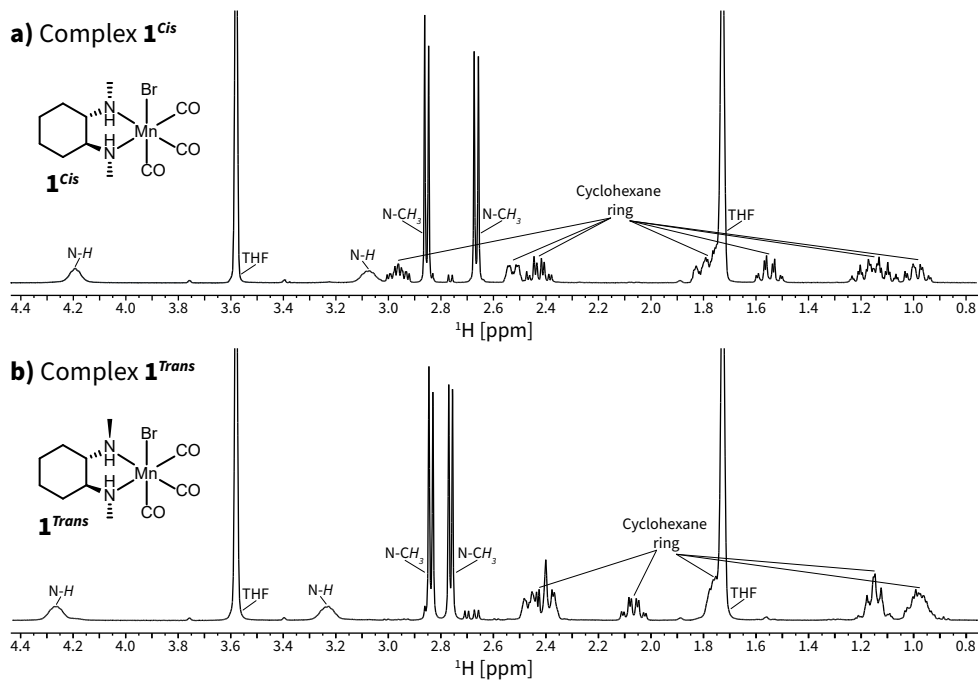


Figure 2.4. ^1H NMR spectra of Mn^I-N,N' complexes in THF-*d*₈ (400 MHz). **a)** **1**^{*cis*}. **b)** **1**^{*trans*}.

The conditions used for the preparation of **1** also produced a minor product (<20%) that had a distinct ^1H NMR spectrum from **1**^{*cis*} (**Figure 2.4b**). The resonances originating from the nitrogen-bound methyl groups appeared as two doublets at different chemical shifts of $\delta = 2.84$ ppm and $\delta = 2.76$ ppm. This compound was identified as the *trans* isomer of **1**. Complex **1**^{*trans*} could be separated from **1**^{*cis*} by slow vapour diffusion crystallisation from the original mother liquor.

The ratio of formation of $\mathbf{1}^{cis}/\mathbf{1}^{trans}$ was found to strongly depend on the utilised reaction conditions. A nearly inverse isomeric ratio was obtained when the reaction was performed at room temperature in dichloromethane. Isomers $\mathbf{1}^{cis}$ and $\mathbf{1}^{trans}$ did not interconvert upon extended heating at 70 °C in THF- d_8 or C_6D_6 . This indicated that their formation and relative abundance is a kinetic ratio that is governed by synthetic conditions, rather than by chemical exchange phenomena. Ligand substitution was not observed when $\mathbf{1}^{cis}$ or $\mathbf{1}^{trans}$ were refluxed in benzene in the presence of two equivalents of triphenylphosphine. Furthermore, addition of a two-fold excess of **L4** during complexation did not result in the formation of the cationic $[Mn(L)_2(CO)_2]^+$ species that are customarily observed when stronger phosphine donor ligands are used.^{27,28,33} These observations provided additional evidence for the thermal and chemical stability of complex **1**.

Single-crystal X-ray diffraction studies of the isolated materials confirmed their identities as isomers of neutral Mn^I diamine complex **1** (Figure 2.5). In the solid-state structure of $\mathbf{1}^{cis}$ the methyl groups were oriented in *cis* fashion: both methyl groups faced away from the bromide ligand. Complex $\mathbf{1}^{trans}$ was structurally similar to $\mathbf{1}^{cis}$ and featured the methyl and hydrogen groups bound *trans* to each other. In this complex the methyl groups were situated on opposite sides of the horizontal plane of Figure 2.5.

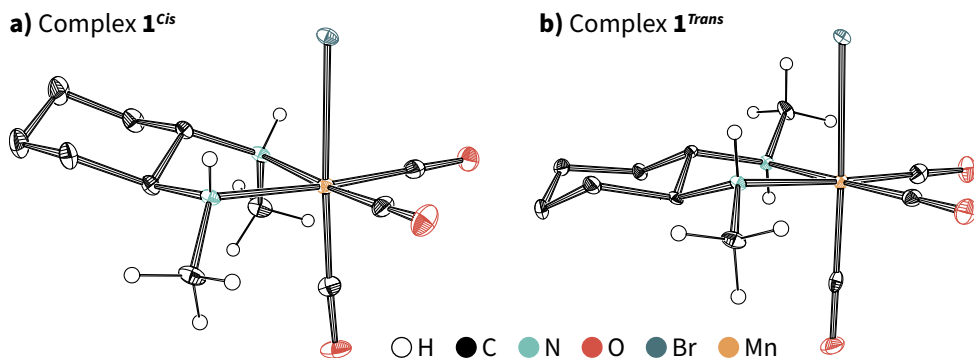


Figure 2.5. ORTEP diagrams of $\mathbf{1}^{cis}$ (a) and $\mathbf{1}^{trans}$ (b). Thermal ellipsoids were drawn at 30% probability. Co-crystallised solvent and hydrogen atoms (except those bound to nitrogen or its methyls) have been omitted for clarity. Key: H (white), C (black), N (turquoise), O (red), Br (green), Mn (orange).

The isolated complexes of **1** were used as precatalysts for the asymmetric transfer hydrogenation of acetophenone (Table 2.1). We found that the catalytic performance of $\mathbf{1}^{cis}$ and $\mathbf{1}^{trans}$ was practically identical; both led to the formation of (*R*)-1-phenylethanol in approximately 40% yield and 74% enantiomeric excess. The activity of the isolated complexes was slightly higher compared to that of the *in situ* generated system. Activation of the Mn^I precatalysts with $NaHBET_3$ —an established

method to enable base-free operation^{30,34}—led to identical product *ee* at marginally lower productivity. Both isomers of **1** consistently produced a comparable product composition. This provided a strong indication that either precatalyst activation or the utilised reaction conditions transformed the distinct isomers into a shared intermediate. This phenomenon was investigated computationally and experimentally, and the results of these studies are described in the following sections.

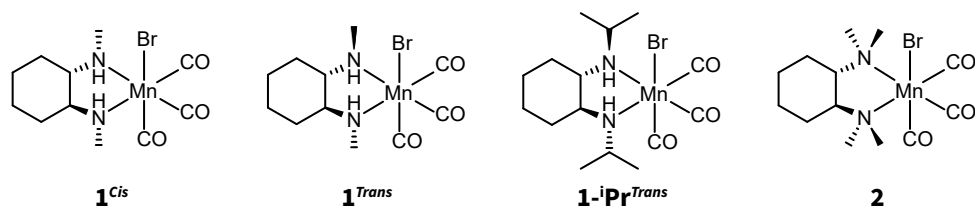


Figure 2.6. Overview of well-defined Mn-*N,N'* precatalysts used in this work.

Table 2.1. Results of catalytic activity tests with Mn-*N,N'* precatalysts.^{a)}

Entry	Complex	Conversion [%] ^{b)}	Alcohol yield [%] ^{b)}	<i>ee</i> [%]	TON [-]
1	1^{Cis}	39	39	74	39
2	1^{Trans}	40	40	74	40
3 ^{c)}	1	29	29	75	29
4 ^{d)}	1^{Cis}	27	27	72	27
5 ^{d)}	1^{Trans}	29	29	75	29
6	1-^{iPr}Trans	1	1	71	1
7	2	0	-	-	-

a) Conditions: 0.5 mmol acetophenone, 1.0 mol% precatalyst, 5.0 mol% KO^tBu, 3.0 ml 2-propanol, 60 °C, 1 h. **b)** Yield were determined by GC-FID using *n*-dodecane as an internal standard. **c)** *In situ* generated catalyst. **d)** 1.0 mmol acetophenone. Precatalyst activated with 1 eq. NaHBET₃. No KO^tBu in reaction.

We finally investigated the impact of varied *N*-substitution on catalytic performance. Two additional complexes were prepared for this purpose: sterically demanding complex **1-^{iPr}Trans**, and fully methylated analogue **2** (**Figure 2.6**). Transfer hydrogenation of acetophenone with **1-^{iPr}Trans** resulted in (*R*)-1-phenylethanol with a similar *ee* of 71%, while catalytic productivity was dramatically reduced to only one turnover. Fully methylated complex **2** did not show any catalytic activity. This result highlighted the critical importance of accessible *N-H* protons for the catalytic reaction.

2.4 DFT Calculations

Density functional theory (DFT) calculations were performed to rationalise the observed trends in catalysis with complexes **1^{Cis}** and **1^{Trans}**. The reaction mechanism was investigated at the PBE0-D3(BJ)-SMD(iPrOH)/Def2-QZVPP level of theory using the Gaussian 09 D.01 program.³⁵ Van der Waals interactions were described by the dispersion-corrected DFT-D3 (BJ) method.³⁶ The SMD solvation model for 2-propanol was employed during geometry optimisations.³⁷ The proposed reaction mechanism is summarised in **Figure 2.7**. ΔG and ΔG^\ddagger represent the standard computed reaction and activation Gibbs free energies for the elementary reaction steps in kJ mol^{-1} .

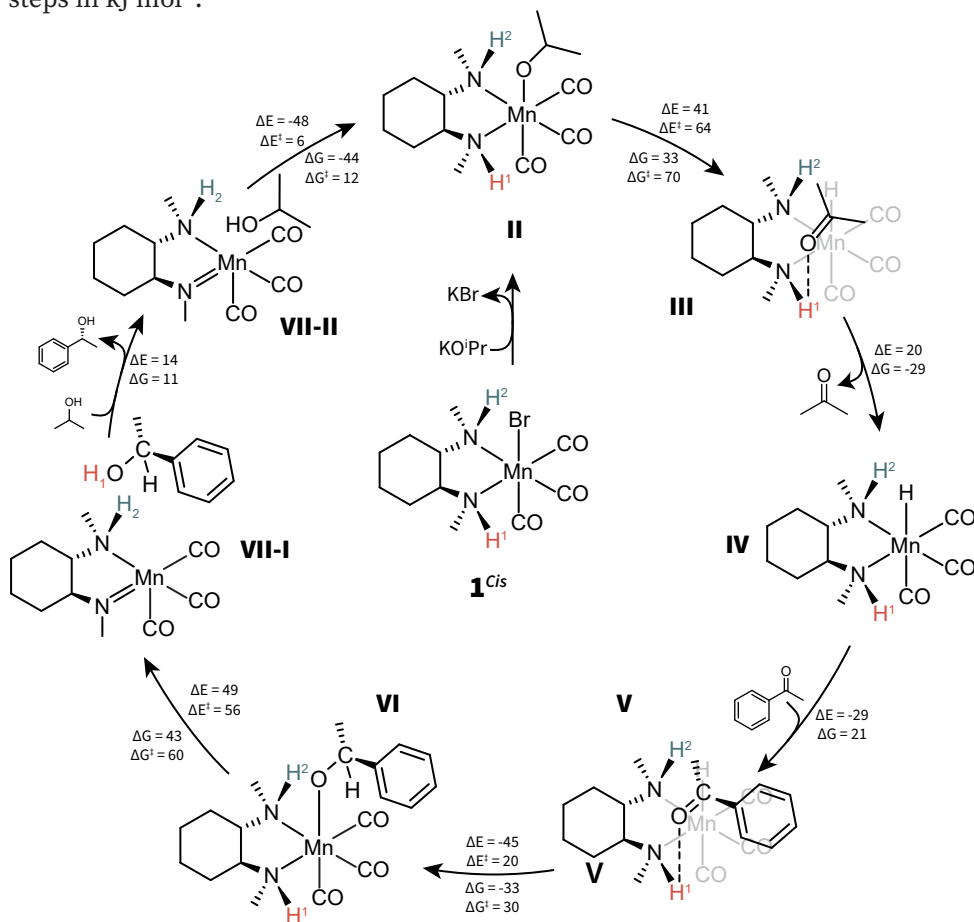


Figure 2.7. Proposed catalytic cycle for the asymmetric transfer hydrogenation of acetophenone with **1^{Cis}**. ΔG and ΔG^\ddagger represent the reaction and activation Gibbs free energy changes in kJ mol^{-1} at 333 K, respectively. The cycle that leads to the major (*R*)-1-phenylethanol product is shown.

The catalytic cycle starts with the activation of precatalyst **1^{Cis}** with KOⁱPr, which is formed *in situ* from KOⁱBu and ⁱPrOH. This reaction produces Mn-isopropoxide complex **II** and KBr. Mn-isopropoxide **II** is a resting state in the catalytic cycle. β -Hydride elimination of the isopropoxide ligand to Mn-hydride complex **III** proceeds with the highest activation Gibbs free energy in the catalytic cycle of 70 kJ mol⁻¹. Acetone is formed in this reaction, which is removed from the complex in a slightly exergonic step that produces ‘free’ Mn-hydride **IV**. The ketone substrate (acetophenone in our calculations) next coordinates to **IV** *via* N-H-assisted hydrogen bonding to form **V**. This N-H-assisted pre-coordination was found to be important for the catalyst’s stereoselectivity.

(Note that the reaction of **1^{Cis}** with KOⁱBu is also feasible and produces the corresponding Mn-butoxide complex (not pictured). This complex is an off-cycle species that cannot participate in the catalytic reaction because of its inability to undergo β -hydride elimination. The metathesis reaction of **II-OⁱBu** and KOⁱPr produces **II** and KOⁱBu, and allows the Mn complex to re-enter the catalytic cycle.)

Hydride transfer from the manganese centre to the substrate’s acyl carbon is the enantiodetermining step, and is moderately endergonic ($\Delta G_{(R)}^\ddagger = 30$ kJ mol⁻¹, $\Delta G_{(S)}^\ddagger = 39$ kJ mol⁻¹). The resulting Mn-alkoxide complex **VI** is another stable species in the catalytic cycle that is similar to **II**. Liberation of the 1-phenylethanol product is an activated process and proceeds with a barrier of 60 kJ mol⁻¹. This product elimination from **VI** deprotonates one amino ligand of the Mn complex and produces Mn-amido **VII-I**.

The deprotonated complex is highly reactive towards (secondary) alcohols (transformation **VII-II** to **II**). The reaction with 2-propanol proceeds with a low barrier of only 12 kJ mol⁻¹ and regenerates Mn-isopropoxide **II**. The reaction of **VII-II** with 1-phenylethanol also occurs and ultimately leads to an erosion of the product’s optical purity. This phenomenon was investigated in more detail and is discussed in **Chapter 2.8**.

Complex **1^{Cis}** has two accessible and reactive N-H moieties (labelled H¹ and H² in **Figure 2.7**), whereas *trans*-ligated complex **1^{Trans}** features only one: H¹. The steric environments of the N-H groups in complex **1^{Cis}** are different because of the close proximity of up or down oriented carbon/hydrogen atoms in the cyclohexane ring (**Figure 2.8**). This difference potentially impacts stereoselectivity because it could lead to preferential pre-coordination of the *Re* or *Si* face of acetophenone to the catalyst. The enantiodetermining step was therefore studied in more detail with further DFT calculations. Activation energies were computed for all coordination modes, which included the four combinations for **1^{Cis}**, and two combinations for **1^{Trans}**. The results of these calculations are summarised in **Table 2.2**.

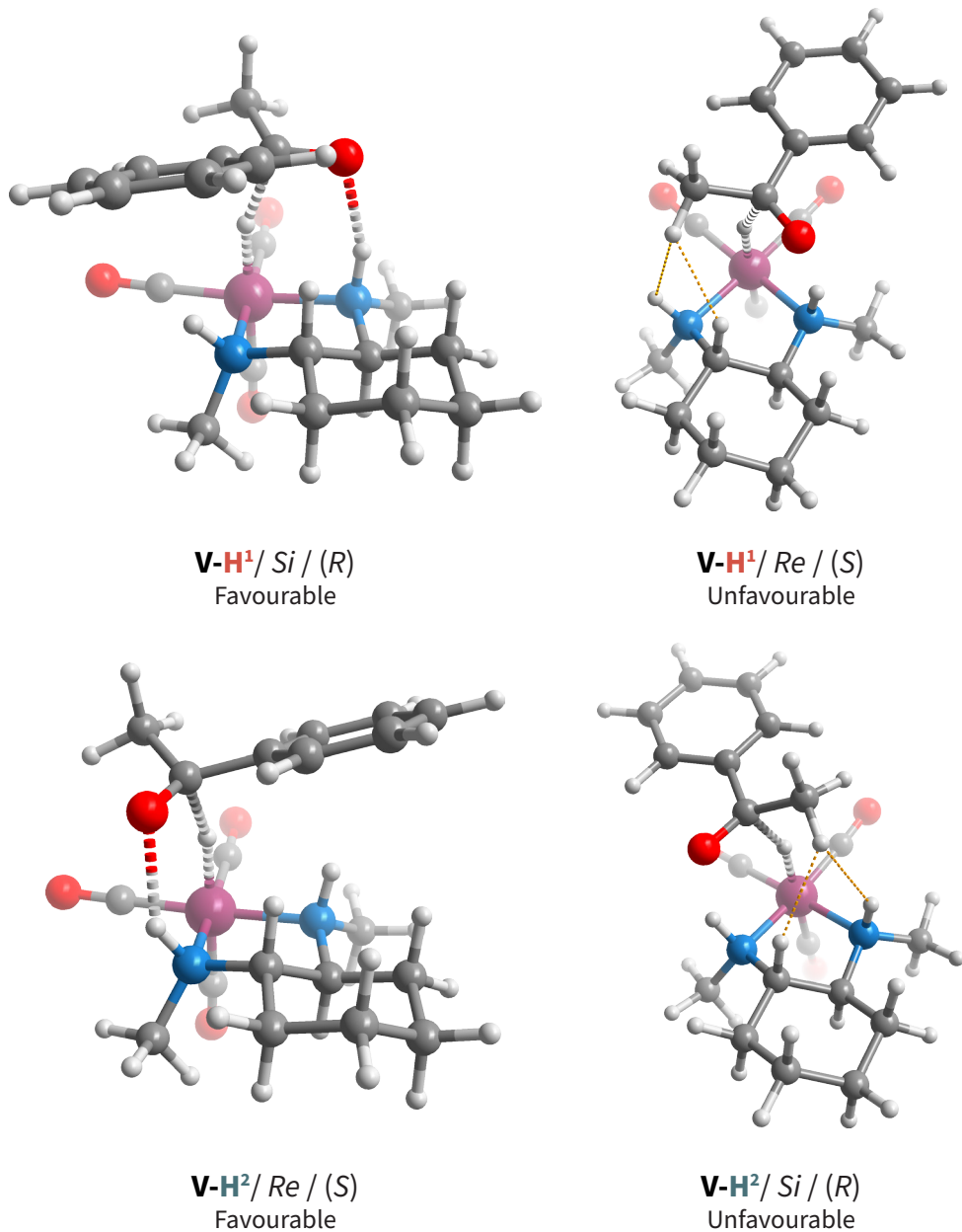


Figure 2.8. Calculated transition states for the pre-coordination of acetophenone to **1^{cis}**. Yellow dashed lines highlight steric interactions that lead to an unfavourable high-energy transition state. The calculated energies for pre-coordination of acetophenone to different amino protons in **1^{cis}** and **1^{trans}** are summarised in **Table 2.2**.

Table 2.2. Computed energies for the coordination of acetophenone to **1^{Cis}** or **1^{Trans}** in kJ mol⁻¹.

Product	1^{Cis}				1^{Trans}	
	Reaction site H ¹		Reaction site H ²		Reaction site H ¹	
	ΔE^\ddagger	ΔG^\ddagger	ΔE^\ddagger	ΔG^\ddagger	ΔE^\ddagger	ΔG^\ddagger
(<i>R</i>)-1-phenylethanol	20	30	31	44	20	33
(<i>S</i>)-1-phenylethanol	26	40	22	39	25	40

Our calculations suggested that the interaction between acetophenone's *Si* face and proton **1^{Cis}**-H¹ resulted in the preferred reaction path and produced (*R*)-1-phenylethanol. Interaction of the *Re* face with proton **1^{Cis}**-H² was also relatively favourable and led to the (*S*)-alcohol. Enantioselective induction was predominantly achieved by steric repulsion between the substrate's methyl group and the nearby protons of the ligand's amino group and cyclohexane ring. These unfavourable steric interactions are indicated with dashed yellow lines in **Figure 2.8**.

The computed Gibbs free energy difference for the competing enantiodetermining steps of Mn-hydride transfer to acetophenone (*i.e.*, $\Delta\Delta G^\ddagger$) was 9 kJ mol⁻¹ for complex **1^{Cis}**, and 7 kJ mol⁻¹ for **1^{Trans}**. The calculations correctly predicted the preferential formation of the (*R*) enantiomer. The computed $\Delta\Delta G^\ddagger$ of 7–9 kJ mol⁻¹ is in good agreement with the experimentally observed *ee* of approximately 75%.

2.5 Stoichiometric reactivity studies

The stoichiometric reactivity of complex **1** was studied with ¹H NMR spectroscopy. These experimental results were in line with those obtained from our DFT calculations, and are summarised in **Figure 2.9**. The reaction of **1^{Cis}** or **1** with 1.1 equivalents KO^tBu (*i.e.*, in the absence of 2-propanol) led to the formation of octahedral Mn^I-alkoxide complex **II-O^tBu**. This was evidenced by the significant change of the ¹H NMR spectrum. The protons of the *tert*-butoxy ligand were shifted downfield to $\delta = 1.20$ ppm (compared to $\delta = 1.15$ ppm for *tert*-butanol), and the amino protons appeared at $\delta = 3.61$ ppm and $\delta = 3.13$ ppm. The FTIR spectrum of the new complex was very similar to that of **1**, and contained three sharp $\nu(\text{CO})$ bands at 2004, 1897, and 1869 cm⁻¹. This suggests that the *fac* orientation of the carbonyl ligands in **1** is retained in the octahedral Mn^I-butoxide complex.

Addition of 2-propanol to a solution of **II-O^tBu** in THF-*d*₆ led to Mn-isopropoxide **II**. Upon mixing the solution rapidly changed colour from red to yellow, and a new resonance appeared in the ¹H NMR spectrum at $\delta = 4.07$ ppm. This peak was assigned to the CH(CH₃)₂ proton of the Mn-isopropoxide moiety, which appeared slightly downfield of free KOⁱPr ($\delta = 4.02$ ppm). 2D NOESY spectroscopy suggested

that the isopropoxide ligand in **II** was dynamic and rapidly exchanged with free isopropanol in solution. (The diagonal peak for free 2-propanol could not be observed, which suggests an exchange on the NMR-timescale.)

Treatment of **1^{Cis}** or **1^{Trans}** with ⁱPrOH/KO^tBu or KO^tBu led to *cis* Mn-alkoxide complexes **II** and **II-O^tBu**, which provided evidence for the isomerisation of complex **1^{Trans}** to the *cis* form upon activation. Our DFT calculations suggested that this transformation can proceed *via* Mn-amido species **VII**, where intermediate **VII** adopts a trigonal pyramidal geometry around the reactive nitrogen centre (**Figure 2.7**). *Syn* addition of an alcohol across the Mn-amido bond produces the experimentally observed *cis* complex. Thus, complex **VII** probably is the shared intermediate that leads to the identical catalytic performance of **1^{Cis}** and **1^{Trans}**.

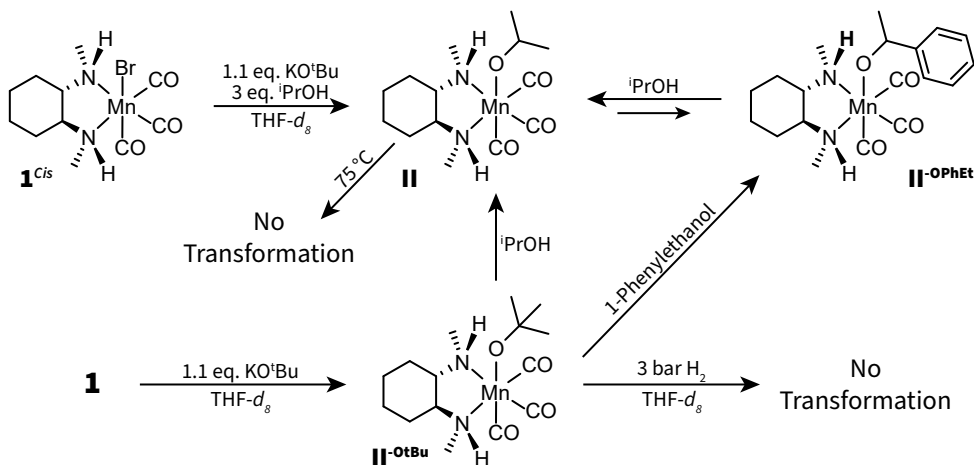


Figure 2.9. Stoichiometric reactivity of complexes **1^{Cis}** and **1**.

Mn-isopropoxide complex **II** was relatively stable and did not produce observable dehydrogenation products (*e.g.*, acetone), even in the presence of only minor quantities of ⁱPrOH or at 75 °C. Exposure of **II-O^tBu** to 3 bar H₂ did not yield the anticipated Mn-hydride species. This behaviour is different from aminopincer Mn-PNP or Mn-NHC complexes^{26,38}, which promote secondary alcohol dehydrogenation and typically form Mn-hydrides that are detectable with ¹H NMR spectroscopy.³⁹

Addition of acetophenone to a solution of **II** and 2-propanol in THF-*d*₈ led to its reduction to the corresponding alcohol. The product was bound to the Mn-centre and was identified with ¹H NMR as the corresponding alkoxide **II-OPhEt** (**Figure 2.9**). This complex could also be obtained from the reaction of **1^{Cis}** or **II-O^tBu** with 1-phenylethanol in the presence of base. Addition of approximately 3 equivalents 2-propanol to a solution of **II-OPhEt** and 1.1 equivalents of KO^tBu in THF-*d*₈ gave

a mixture of Mn-alkoxides **II** and **II-OPhEt**. We therefore concluded that both alkoxides could be formed under catalytic conditions and that product and/or alcohol inhibition could not be ruled out.

2.6 Analysis of reaction kinetics

Our stoichiometric reactivity studies indicated that complex **II** and its related alkoxides were relatively stable and thus might inhibit catalytic turnover. We therefore analysed the reaction kinetics of the asymmetric transfer hydrogenation reaction with precatalyst **1^{cis}**. We first performed several experiments under standardised conditions to validate our method and to demonstrate the reproducibility of these kinetic experiments (**Figure 2.10** and **Table 2.3**).

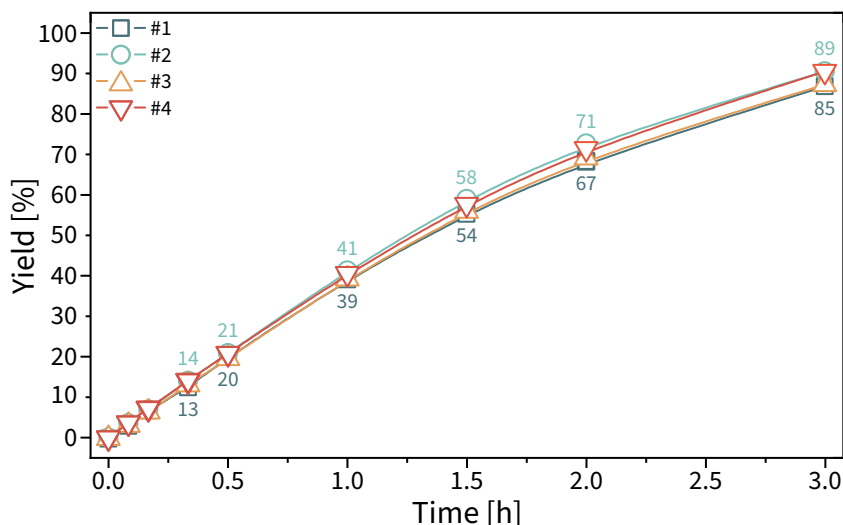


Figure 2.10. Time versus conversion for reproducibility study. Accompanying statistics are provided below. Conditions: 0.5 mmol acetophenone, 0.5 mol% **1^{cis}**, 1.0 mol% KO^tBu, 3.8 ml 2-propanol, 60 °C. Yields were determined by GC-FID using *n*-dodecane as an internal standard.

Table 2.3. Initial reaction rates for reproducibility study and derived statistics. TOF⁰ was determined from the slope of a linear fit of the initial phase of the reaction (first five points, 31 minutes, $R^2 \geq 0.998$ for all fits).

Entry	TOF ⁰ [h ⁻¹]	$\overline{\text{TOF}}^0$ [h ⁻¹]	$\sigma(\overline{\text{TOF}}^0)$ [h ⁻¹]	$\sigma^2(\overline{\text{TOF}}^0)$ [h ⁻²]	$\overline{\text{TOF}}^0 \pm \sigma$ [h ⁻¹]
1	77.4				75.5–79.3
2	81.0				79.1–82.9
3	76.8	79.0	1.913	3.660	74.9–78.7
4	80.8				78.9–82.7

After we had established that our method was sound, we moved to the kinetic study (summarised in **Figure 2.11**). Under the standardised conditions, the reaction proceeded with an initial turnover frequency (TOF⁰) of $79.0 \pm 1.9 \text{ h}^{-1}$ and produced (*R*)-1-phenylethanol in 73% enantiomeric excess. The initial reaction rate increased with increased catalyst loading and was consistent with a catalyst reaction order of 1.0 (**Figure 2.11b**). Identical results were obtained when 2 or 10 equivalents of the alkoxide base were used relative to **1^{Cts}**. Further reduction of base concentration led to diminished catalytic performance. These findings indicated that base solely acted as the precatalyst activator and did not play a large role in the catalytic cycle.

A reaction order of zero was found for the substrate (**Figure 2.11c-d**). We propose that the observed (pseudo) zeroth reaction order is caused by the specific conditions of the transfer hydrogenation reaction and the nature of the catalytic cycle. Our DFT calculations and stoichiometric reactivity studies have previously demonstrated that the reaction between activated complex **VII** and free 2-propanol is highly favourable and results in stable Mn-isopropoxide complex **II**.

The β -H elimination step that follows converts **II** to Mn-hydride **III** and acetone. This step was identified as the rate-determining step (RDS) in the computed catalytic cycle (**Figure 2.7**). The subsequent steps in the catalytic cycle (in which the hydride is transferred to the substrate and the product is decoordinated) all have low barriers. This means that acetophenone only interacts with the Mn complex *after* the rate-determining reaction step. Because our specific reaction conditions ensured that 2-propanol was always in at least 80-fold excess compared to the substrate (up to 400-fold), it is possible that acetophenone was effectively 'drowned out' of the reaction rate equation. This situation resembles that of conventional saturation kinetics.⁴⁰

A positive fractional reaction order of approximately 0.6 was found for 2-propanol (**Figure 2.11e-f**). Our measurements were complicated by the fact that isopropanol fulfils a dual role in transfer hydrogenation reactions as both a reactant and the solvent. Experimental variation of the isopropanol concentration required the addition of a secondary—assumed to be inert—co-solvent. Experiments were performed using toluene or THF as the co-solvent to verify the validity of this assumption. These tests gave very similar values for the reaction order of 2-propanol: 0.57 in toluene and 0.59 in THF. We therefore concluded that our assumption probably was reasonable and that our approach did not significantly alter critical solvent-solute interactions or the reaction mixture's properties.

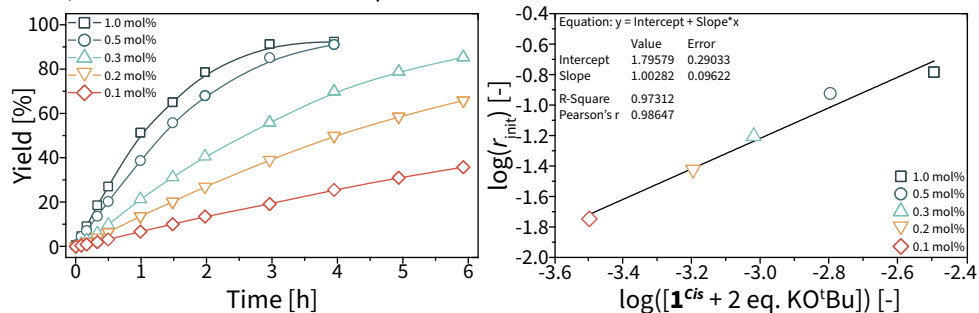
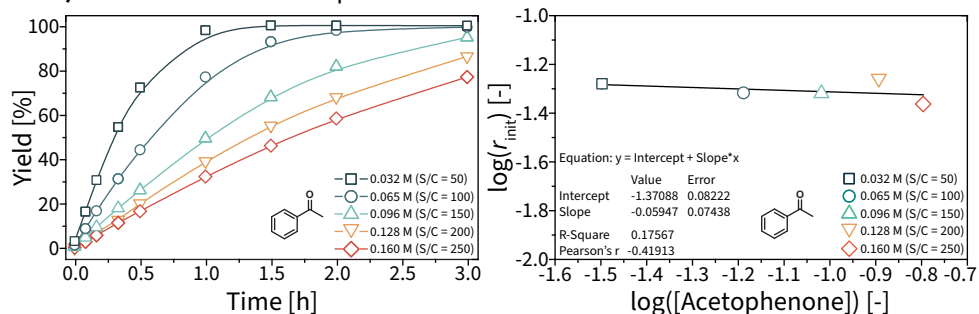
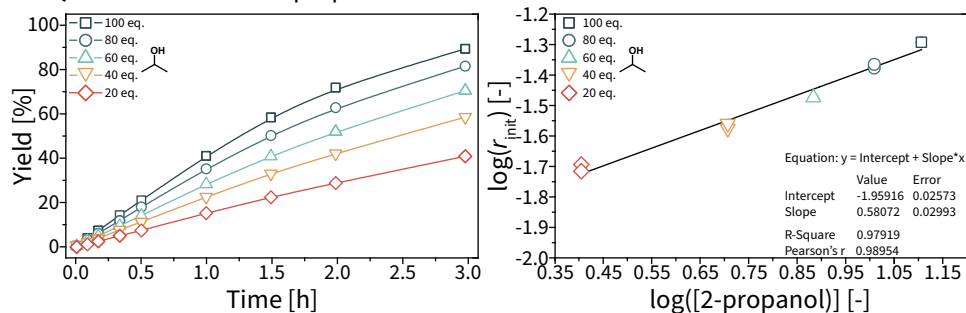
a & b) Reaction order in 1^{cis} + 2 eq. KO^tBu**c & d)** Reaction order in acetophenone**e & f)** Reaction order in 2-propanol

Figure 2.11. Kinetic analysis of 1^{cis} -catalysed asymmetric transfer hydrogenation of acetophenone. **a-b)** Reaction order 1^{cis} + 2 eq. KO^tBu. **c-d)** Reaction order acetophenone. **e-f)** Reaction order 2-propanol. Conditions unless stated otherwise: 0.5 mmol acetophenone (0.128 M), 0.5 mol% 1^{cis} , 1.0 mol% KO^tBu, 3.82 ml ⁱPrOH (diluted with toluene for **e** and **f**), 60 °C. Yields were determined by GC-FID using *n*-dodecane as an internal standard.

A more thorough analysis was required to rationalise the observed reaction order of ~0.6. We next derived a full kinetic rate equation following the work of Heeres and co-workers on the Ru-catalysed asymmetric transfer hydrogenation of ketones.⁴¹ Their rate equation (**Equation 2.1**) corrected for the effects caused by the equilibrium reaction (terms in the nominator), as well as the effects originating from catalyst inhibition by the different components (terms in the denominator).

The parameters A through D describe the individual components (acetophenone (A), *i*PrOH (B), 1-phenylethanol (C), and acetone (D)), while parameters k , m , n , and p describe the reaction orders for inhibition caused by the respective component.

$$-\frac{dC_A}{dt} = -r_A = \frac{k_1^+ C_A C_B - k_1^- C_C C_D}{1 + k_2 C_A^k + k_3 C_B^m + k_4 C_C^n + k_5 C_D^p} \quad (2.1)$$

The kinetic rate expression in **Equation 2.1** was unnecessarily complicated for our application and could be simplified to **Equation 2.2** by assuming that the reaction's products (*i.e.*, C and D) and the reverse reaction have negligible influence at the beginning of the reaction. This is a reasonable simplification because our kinetic experiments evaluated the reaction rates during the initial phase of the reaction.

$$-\frac{dC_A}{dt} = -r_A = \frac{k_1^+ C_A C_B}{1 + k_2 C_A^k + k_3 C_B^m} \quad (2.2)$$

The observed facile formation of Mn-alkoxide **II** also provided a rationalisation for the fractional reaction order of the hydrogen donor and solvent. If one assumes that inhibition by 2-propanol (B) is much more important than substrate (A) inhibition (*i.e.*, $k_3 C_B^m \gg 1 + k_2 C_A^k$) and C_A is effectively constant, then **Equation 2.2** reduces further to **Equation 2.3**.

$$-\frac{dC_A}{dt} = -r_A = \frac{k_1^+ C_A C_B}{k_3 C_B^m} = K_{obs} C_B^{1-m}; \text{ with } K_{obs} = \frac{k_1^+ C_A}{k_3} \quad (2.3)$$

The extent of catalyst inhibition by 2-propanol is expressed by the parameter m , and directly impacts the observed reaction order. Thus, the combination of the desired transfer hydrogenation reaction and the inhibition reaction leads to the observed positive fractional reaction order of ~ 0.6 in isopropanol.

2.7 Activation energies and kinetic isotope effects

The mechanistic study was concluded with additional experiments that were aimed at understanding the nature of the rate-determining step. We found that the transfer hydrogenation of acetophenone with **1^{cis}** proceeded with an apparent (non-asymmetric) activation energy of 87 kJ mol⁻¹ (**Figure 2.12a**). Further analysis of the individual reaction rates enabled us to determine the apparent activation energies for the formation of individual (R) and (S) enantiomers, which was particularly useful for benchmarking of computational models.

The reaction that leads to (*R*)-1-phenylethanol exhibited an apparent barrier of 85 kJ mol⁻¹, while the pathway to (*S*)-1-phenylethanol proceeded with a slightly higher barrier of 93 kJ mol⁻¹. The observed $\Delta\Delta E_{\text{A}}^{\text{App}}$ of 8 kJ mol⁻¹ corresponded reasonably well with the computationally predicted value $\Delta\Delta E^{\ddagger}$ of 11 kJ mol⁻¹ (**Table 2.2**). The experimental and computational barriers for the RDS showed some absolute divergence that was not further investigated. (This divergence could have originated from, *e.g.*, the selection of the basis set, specific solvent correction models, or even the calculation of an improper reaction mechanism. The attempted convergence of experimental and computational results, however, arguably is not very useful, and was therefore not prioritised.)

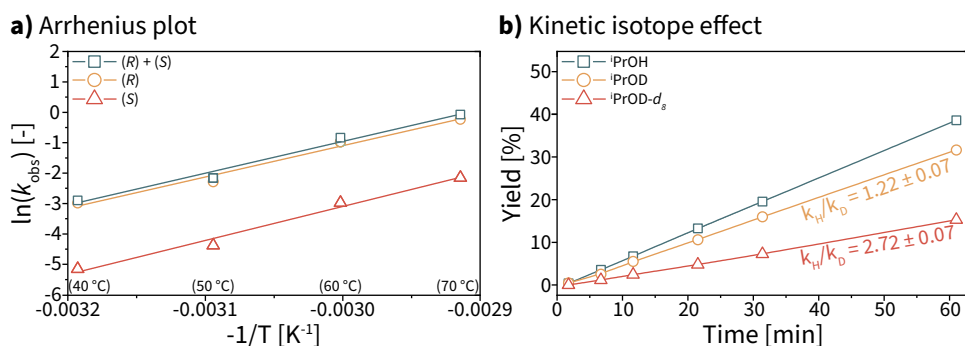


Figure 2.12. **a)** Arrhenius plot for acetophenone reduction with **1^{Cs}**. **b)** Kinetic isotope effect studies for asymmetric transfer hydrogenation with **1^{Cs}**. Conditions: 0.5 mmol acetophenone (0.128 M), 0.5 mol% **1^{Cs}**, 1.0 mol% KO^tBu, 3.82 ml isopropanol, 40–70 °C. Yields were determined by GC-FID using *n*-dodecane as an internal standard.

Kinetic isotope effects were measured with deuterium-labelled isotopologues of 2-propanol (**Figure 2.12b**). Experiments performed in fully-deuterated ¹PrOD-*d*₈ revealed a strong primary kinetic isotope effect of 2.72 ± 0.07. The reaction in partially-deuterated ¹PrOD led to a secondary KIE 1.22 ± 0.07. These results suggest that the carbon-bound hydride atom of the hydrogen donor is involved in the rate-determining step. Proton transfer is less important than hydride transfer, but still has a measurable impact on the reaction rate. The experimentally observed KIEs are consistent with the proposed mechanism and our DFT calculations, which indicate that hydride transfer from 2-propanol is the most energetically demanding reaction step (*i.e.*, β-hydride elimination from the coordinated isopropoxide ligand to Mn hydride **III**).

2.8 Erosion of enantiomeric excess

The reversible nature of alcohol-based transfer hydrogenation reactions can result in a loss of product enantiomeric excess over time.⁴² This is known as *ee*-erosion, and is caused by the (preferential) dehydrogenation of the enantio-enriched product. Two strategies have been developed that counter this loss of selectivity. In the first method the alcoholic hydrogen donor is substituted for an azeotropic mixture of formic acid and triethylamine.^{31,43} Dehydrogenation of this mixture liberates the required hydrogen *in situ*, as well as gaseous CO₂ that leaves the reaction mixture and thereby prevents the reverse reaction. However, reduction of ketones with 3*d* base metals and formic acid has not yet been reported, and our attempts with **1**^{Cr} and [HCOOH][NEt₃] were unsuccessful. The second strategy requires the reaction to be performed under dilute conditions to kinetically favour dehydrogenation of the hydrogen donor relative to the product.⁴² This option is less attractive than the formic acid/triethylamine mixture because it reduces the process's productivity (*i.e.*, yield per unit volume) and requires significantly more solvent.

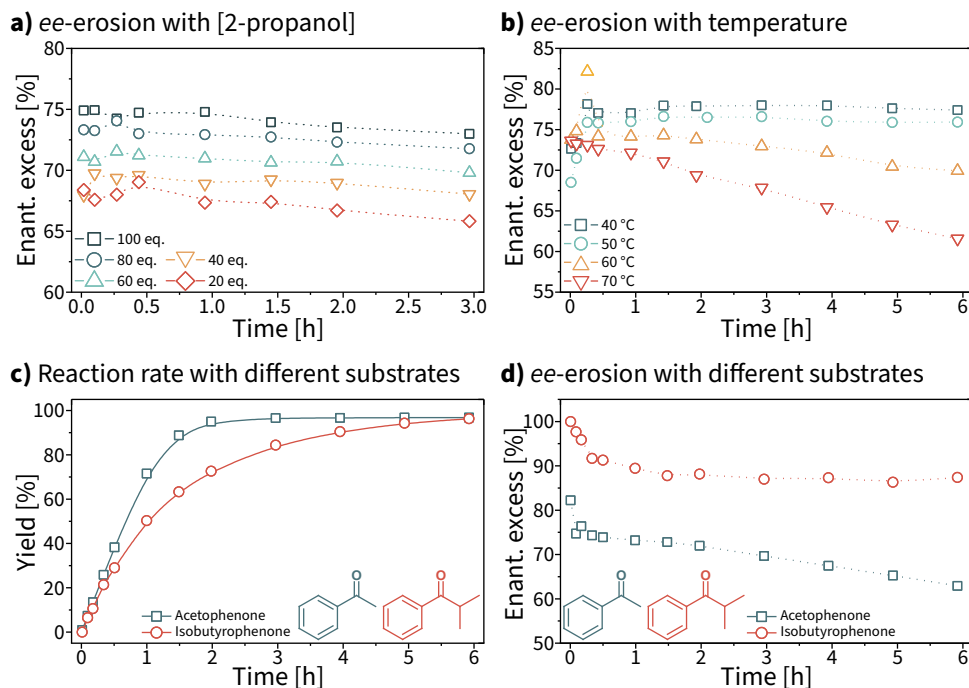


Figure 2.13. **a)** Erosion of *ee* as function of ⁱPrOH concentration. **b)** Erosion of *ee* as function of reaction temperature. **c)** Reaction rate of acetophenone and isobutyrophenone ATH with **1**^{Cr}. **d)** Erosion of *ee* for acetophenone and isobutyrophenone reduction. Conditions unless stated otherwise: 0.5 mmol acetophenone (0.128 M), 0.5 mol% **1**^{Cr}, 1.0 mol% KO^tBu, (1.0 mol% **1**^{Cr} and 2.0 mol% KO^tBu for **c** and **d**), 3.82 ml ⁱPrOH (diluted with toluene for **a** and **b**), 40–70 °C. Yields were determined by GC-FID using *n*-dodecane as an internal standard.

Analysis of the obtained kinetic data revealed that product *ee* was somewhat sensitive to the concentration of the hydrogen donor relative to the substrate, whereas the rate of erosion was not (**Figure 2.13a**). A five-fold increase of the isopropanol concentration (from 20 to 100 equivalents relative to the substrate) resulted in a 7 percentage point increase of the product's enantiomeric excess. Reaction temperature also influenced the rate of *ee*-erosion, which was most pronounced at elevated reaction temperature (**Figure 2.13b**).

We hypothesised that the use of a more sterically demanding ketone substrate could suppress the rate of the reverse reaction and thus reduce the rate of *ee*-erosion. The reaction under identical conditions using isobutyrophenone as the substrate (**Figure 2.13c-d**) indeed produced (*R*)-2-methyl-1-phenylpropanol with an improved *ee* of 87%, while erosion of enantiopurity was considerably slower. The rate of the forward reaction was also lower and occurred at approximately 85% of the initial rate found for acetophenone. Ultimately a quantitative alcohol yield was obtained with 1 mol% **1**^{*Cis*} after 6 h at 60 °C.

2.9 Conclusion

In conclusion, we have synthesised and characterised a series of simple chiral manganese diamine complexes and have evaluated their catalytic performance for the asymmetric transfer hydrogenation of aryl ketones. Complexes **1**^{*Cis*} and **1**^{*Trans*} are moderately stereoselective transfer hydrogenation catalysts that enable the synthesis of enantio-enriched secondary alcohols in good to quantitative yields. We conducted a detailed theoretical and experimental mechanistic investigation, as well as an extensive study of the reaction kinetics of the Mn-catalysed asymmetric transfer hydrogenation reaction. These studies revealed that the introduction of simple diamine ligands did not induce sufficient steric strain to facilitate high enantioselectivity, and that such strain could not practically be applied without significant loss of catalytic activity. We have demonstrated that different stereoisomeric precatalysts converged to a shared intermediate upon activation, which rationalised their identical catalytic performance.

We identified several potentially important performance parameters during our studies. Promising catalytic activity was observed in our initial ligand screening for strong donor bidentate aminophosphine ligands. These systems were dismissed at the time because of their low stereoselectivity for the target reaction. We later hypothesised that the introduction a strongly-donating bidentate ligand based on an *N*-heterocyclic carbene (NHC) could provide a viable design strategy for Mn^I carbonyl reduction catalysts, but without the challenges that are typically associated with the preparation and handling of air and/or moisture sensitive

organophosphines. The next chapter describes the preparation of such a prototype complex and its activity for the non-asymmetric transfer hydrogenation of ketones.

2.10 Experimental section

General considerations

All manipulations were, unless stated otherwise, performed under an inert atmosphere in an Ar-filled Inert glove box or using standard Schlenk techniques. Anhydrous solvents were dispensed from an Inert PureSolv solvent purification system or were dried using 3 or 4 Å molecular sieves. Solvents were degassed before use. Chemicals were purchased from Sigma-Aldrich, Strem, abcr, or TCI, and were dried and/or degassed before use. Air and/or moisture sensitive materials were stored in the glove box. Deuterated solvents were purchased from Eurisotop, dried using molecular sieves, degassed, and stored in the glove box.

NMR spectra were recorded on an Agilent 400-MR DD2 400 MHz spectrometer equipped with a 5 mm ONE NMR probe. ^1H and ^{13}C chemical shifts were referenced to residual solvent peaks (^1H : 5.32 ppm CD_2Cl_2 , 7.16 ppm C_6D_6 , 3.58 ppm $\text{THF-}d_8$. ^{13}C : 53.84 ppm CD_2Cl_2 , 128.06 ppm C_6D_6 , 67.21 ppm $\text{THF-}d_8$). Proton and carbon assignments were made on basis of combined gCOSY and gHSQC spectra. FTIR (ATR) was measured on a Bruker Alpha II spectrometer inside the glove box. Elemental analyses were performed in duplo by Mikroanalytisches Laboratorium Kolbe (Oberhausen, Germany).

Synthetic procedures

Full characterisation for the compounds below is available in the electronic supporting information of the published work: *Organometallics* **2019**, 38, 3187–3196, DOI: 10.1021/acs.organomet.9b00457.

CAUTION: Manganese carbonyl complexes release poisonous and flammable carbon monoxide gas upon complexation!

1^{cis} – *cis*-Mn(*N,N'*-dimethyl-1,2-cyclohexanediamine)(CO)₃Br

Inside the glove box, Mn(CO)₅Br (275 mg, 1.0 mmol) and (*S,S*)-(+)-*N,N'*-dimethyl-1,2-cyclohexanediamine (142 mg, 1.0 mmol) were added as solids to a Schlenk tube that contained 10 ml *n*-hexane and a PTFE-coated magnetic stirring bar. The mixture was taken out of the glove box and was heated overnight (~15 h) at 70 °C. Over the course of the reaction a bright yellow powder formed in the pale yellow solution.

Afterwards the solids were collected by filtration, washed with *n*-hexane (2 x 10 ml), and were dried *in vacuo*. The crude product contained a minor amount of **1^{Trans}** that was removed by crystallisation. The material was dissolved in 2 ml dichloromethane and 2 ml *n*-hexane, and 2 ml diethyl ether was added to induce the precipitation of a small amount of solids. The mixture was filtered and was transferred to a freezer at -20 °C. The supernatant was removed after one hour and the crystals were dried *in vacuo*. Analytically pure **1^{Cis}** was obtained as a yellow crystalline solid. Yield: 124 mg (34%).

¹H NMR (400 MHz, CD₂Cl₂): δ 3.21 (br s, NH, 1H), 2.91 (overlap of d, *J* = 5.5 Hz, NCH₃ (3H) and C¹H (1H)), 2.73 (d, *J* = 5.4 Hz, NCH₃, 3H), 2.63 (br s, NH, 1H), 2.55 (m, C²H₂, 1H), 2.38 (m, C¹H, 1H), 1.93–1.70 (m, overlap of C²H₂ (1H) and C³H₂ (2H)), 1.53 (m, C²H₂, 1H), 1.34–0.75 (m, overlap of C²H₂ (1H) and C³H₂ (2H)).

¹³C NMR (101 MHz, CD₂Cl₂): all resonances are singlets: δ 63.6, 61.1, 40.6, 38.6, 31.7, 29.6, 24.7, 24.5.

FTIR (ATR): 2017, 1900, 1885 cm⁻¹.

EA: found (calc. MnC₁₁H₁₈N₂BrO₃): C: 36.30 (36.59), H: 4.92 (5.02), N: 7.81 (7.76).

1^{Trans} – *trans*-Mn(*N,N'*-dimethyl-1,2-cyclohexanediamine)(CO)₃Br

Inside the glove box, Mn(CO)₅Br (550 mg, 2.0 mmol) and (*S,S*)-(+)-*N,N'*-dimethyl-1,2-cyclohexanediamine (320 mg, 2.25 mmol) were added as solids to a Schlenk tube that contained 20 ml dichloromethane and a PTFE-coated magnetic stirring bar. The mixture was stirred at room temperature inside the glove box (~18 h) and released gas over the course of the reaction.

Afterwards the solvent was removed *in vacuo*, the solid residue was washed with 10 ml *n*-pentane, and was dried *in vacuo*. The crude product contained **1^{Trans}** and **1^{Cis}** (~3:1) and was purified by an additional precipitation. The crude material was redissolved in 2 ml dichloromethane, and **1^{Trans}** was precipitated by addition of 10 ml *n*-pentane. The solid material was filtered off, washed with *n*-pentane, and dried *in vacuo* to give analytically pure **1^{Trans}** as a yellow solid. Yield: 310 mg (43%).

¹H NMR (400 MHz, CD₂Cl₂): δ 3.00–2.78 (m, overlap of NH (2H) and NCH₃ (6H)), 2.45 (m, overlap of C²H₂ (2H) and C¹H (1H)), 2.10 (m, C¹H, 1H), 1.80 (m, C³H₂, 2H), 1.14 (m, C³H₂, 2H), 0.97 (m, C²H₂, 2H).

¹³C NMR (101 MHz, CD₂Cl₂): all resonances are singlets: δ 68.6, 63.8, 40.6, 37.7, 31.0, 30.5, 24.6, 24.5.

FTIR (ATR): 2017, 1895, 1880 cm⁻¹.

1-ⁱPr^{Trans} – *trans*-Mn(*N,N'*-diⁱPr-1,2-cyclohexanediamine)(CO)₃Br

Diamine ligand **L4-ⁱPr** (*S,S*)-*N,N'*-diisopropyl-1,2-cyclohexanediamine was prepared following a modified literature procedure and was purified by distillation.⁴⁴

Inside the glove box, Mn(CO)₅Br (851 mg, 3.1 mmol) and (*S,S*)-*N,N'*-diisopropyl-1,2-cyclohexanediamine (675 mg, 3.4 mmol) were added to a Schlenk tube that contained 15 ml benzene and a PTFE-coated magnetic stirring bar. The mixture was taken out of the glove box and was heated overnight (~12 h) at 70 °C. Over the course of the reaction the solution became turbid and a yellow microcrystalline powder appeared after several minutes.

Afterwards the solids were collected by filtration, washed with 1 ml benzene and 10 ml *n*-pentane, and were dried *in vacuo*. This produced analytically pure **1-ⁱPr^{Trans}** as a yellow solid. Yield: 230 mg (18%).

¹H NMR (400 MHz, CD₂Cl₂): δ 3.69 (br s, CH(CH₃)₂, 1H), 3.49 (m, overlap of CH(CH₃)₂ (1H) and NH (1H)), 3.13 (br q, *J* = 10.5 Hz, C¹H, 1H), 2.58 (br d, NH, 1H), 2.43 (br d, *J* = 10.8 Hz, C²H₂, 1H), 2.33 (br d, *J* = 10.8 Hz, C²H₂, 1H), 2.17 (br q, *J* = 10.3 Hz, C¹H, 1H), 1.80 (br m, C³H₂, 2H), 1.46 (br s, CH(CH₃)₂, 6H), 1.38–0.82 (m, overlap of CH(CH₃)₂ (6H), C²H₂ (2H), and C³H₂ (2H)).

¹³C NMR (101 MHz, CD₂Cl₂): all resonances are singlets: δ 64.7, 59.8, 50.6, 50.4, 32.8, 25.5, 24.9, 23.3, 21.9, 20.7.

EA: found (calc. MnC₁₅H₂₆N₂BrO₃): C: 43.32 (43.18), H: 6.15 (6.28), N: 6.77 (6.71).

2 – Mn(*N,N'*-tetramethyl-1,2-cyclohexanediamine)(CO)₃Br

Diamine ligand **L5** (*S,S*)-*N,N'*-tetramethyl-1,2-cyclohexanediamine was prepared following a modified literature procedure and was purified by distillation.⁴⁵

Inside the glove box, Mn(CO)₅Br (413 mg, 1.5 mmol) and (*S,S*)-*N,N'*-tetramethyl-1,2-cyclohexanediamine (272 mg, 1.6 mmol) were added to a Schlenk tube that contained 15 ml benzene and a PTFE-coated magnetic stirring bar. The mixture was taken out of the glove box and was heated for 3 hours at 70 °C. Over the course of the reaction the solution became turbid and a yellow microcrystalline powder appeared.

Afterwards the solids were collected by filtration, washed with *n*-pentane (3 x 20 ml), and dried *in vacuo*. This produced analytically pure **2** as a yellow solid. Yield: 465 mg (80%). Complex **2** slowly decomposed in solution upon exposure to light.

^1H NMR (400 MHz, CD_2Cl_2): δ 3.04 (s, NCH_3 , 3H), 3.03 (s, NCH_3 , 3H), 2.86 (s, NCH_3 , 3H), 2.78 (s, NCH_3 , 3H), 2.72 (m, C^1H , 1H), 2.61 (m, C^1H , 1H), 2.03 (m, C^2H_2 , 2H), 1.78 (m, C^2H_2 , 2H), 1.27 (m, C^3H_2 , 2H), 1.04 (m, C^3H_2 , 2H).

^{13}C NMR (101 MHz, CD_2Cl_2): all resonances are singlets: δ 69.1, 66.6, 55.7, 50.9, 49.7, 49.5, 24.8, 24.3, 23.8, 22.7.

Catalytic (kinetic) experiments

Inside the Ar-filled glove box, a 4 ml glass vial was loaded (in order) with a PTFE-coated magnetic stirring bar, *n*-dodecane, solvent and/or 2-propanol, precatalyst, and base (both as stock solutions). The vial was capped, placed inside a preheated metal heating block, stirred at 500 rpm, and was heated for 30 minutes. Substrate was added to the mixture after preheating and the experiment was started. A 50 μl aliquot was removed from the reaction mixture at the appropriate time, and was immediately quenched by its addition to 100 μl of a 2 wt% solution of acetic acid in 2-propanol. The mixture was diluted with 1.0 ml 2-propanol and was analysed as described.

Typical loadings: 25.0 μl *n*-dodecane, 3.02 ml 2-propanol (Σ 3.82 ml), 0.90 mg **1^{cs}** in 400 μl 2-propanol (2.5 μmol , 0.5 mol%), 0.56 mg KO^tBu in 400 μl 2-propanol (5.0 μmol , 1.0 mol%), and 58.4 μl acetophenone (0.5 mmol, initial concentration 0.128 M).

Analytical details

Measurements were performed on an Agilent 6890 gas chromatograph equipped with an FID detector and an Agilent CP-Chirasil-Dex CB column (25 m, 0.25 mmID, 0.25 μm film thickness). Method details: 120 $^\circ\text{C}$ (hold 1 min), ramp to 180 $^\circ\text{C}$ at 20 $^\circ\text{C min}^{-1}$ (hold 2 min). Isobutyrophenone: isothermal operation at 120 $^\circ\text{C}$ for 30 min. Products and their absolute configuration were identified using the retention times from analytically pure reference samples. Mass balances were calculated using *n*-dodecane as an internal standard and were verified to be within 90%–110% for all experiments.

Computational details

DFT calculations were performed by dr. C. Liu using the Gaussian 09 D.01 program.³⁵ The hybrid PBE0 exchange-correlation functional⁴⁶ and def2TZVP basis set^{47–48} were used for geometry optimisations. Van der Waals interactions were described by the dispersion-corrected DFT-D3 (BJ) method.³⁶ The SMD solvation model³⁷ was used during geometry optimisations with the standard parameters for 2-propanol, as implemented in Gaussian 09 D.01.

Vibrational analysis was performed at the same level to identify the nature of the stationary points. All positive frequencies were found for local minima. A single imaginary frequency was found for transition states, which corresponded to the expected reaction coordinate. The connectivity between transition states and the corresponding minima was confirmed by the intrinsic reaction coordinate approach.

More accurate electronic energies were obtained from single point calculations on the optimised structures at the PBE0-D3(BJ)-SMD(iPrOH)/Def2-QZVPP level of theory. Reaction (ΔE) and activation (ΔE^\ddagger) energies reported in this work were corrected for zero-point energy from the normal-mode frequency analysis. Reaction Gibbs free energies (ΔG) and activation Gibbs free energies (ΔG^\ddagger) were computed using the results of the normal-mode analysis with the ideal gas approximation at a pressure of 1 atm and a temperature of 333.15 K (60 °C).

Crystallographic details

X-ray diffraction studies were performed by M. Weber and prof. dr. C. Müller (Freie Universität Berlin). Crystallographic details are available in the electronic supporting information of the published work: *Organometallics* **2019**, 38, 3187–3196, DOI: 10.1021/acs.organomet.9b00457. CCDC entries 1903883 (**1^{cis}**), 1903884 (**1^{Trans}**), and 1903885 (**1-^{iPr}Trans**) contain the supplementary data for this work.

2.11 References

1. Bullock, R.M., *Abundant Metals Give Precious Hydrogenation Performance*, *Science* **2013**, 342 (6162), 1054;
2. Valyaev, D.A.; Lavigne, G.; Lugan, N., *Manganese organometallic compounds in homogeneous catalysis: Past, present, and prospects*, *Coordination Chemistry Reviews* **2016**, 308, 191–235;
3. Filonenko, G.A.; van Putten, R.; Hensen, E.J.M.; Pidko, E.A., *Catalytic (de)hydrogenation promoted by non-precious metals – Co, Fe and Mn: recent advances in an emerging field*, *Chemical Society Reviews* **2018**, 47 (4), 1459–1483;
4. Reed-Berendt, B.G.; Polidano, K.; Morrill, L.C., *Recent advances in homogeneous borrowing hydrogen catalysis using earth-abundant first row transition metals*, *Organic & Biomolecular Chemistry* **2019**, 17 (7), 1595–1607;
5. Garbe, M.; Junge, K.; Beller, M., *Homogeneous Catalysis by Manganese-Based Pincer Complexes*, *European Journal of Organic Chemistry* **2017**, 2017 (30), 4344–4362;
6. Kallmeier, F.; Kempe, R., *Manganese Complexes for (De)Hydrogenation Catalysis: A Comparison to Cobalt and Iron Catalysts*, *Angewandte Chemie International Edition* **2018**, 57 (1), 46–60;
7. Gorgas, N.; Kirchner, K., *Isoelectronic Manganese and Iron Hydrogenation/Dehydrogenation Catalysts: Similarities and Divergences*, *Accounts of Chemical Research* **2018**, 51 (6), 1558–1569;
8. Pritchard, J.; Filonenko, G.A.; van Putten, R.; Hensen, E.J.M.; Pidko, E.A., *Heterogeneous and homogeneous catalysis for the hydrogenation of carboxylic acid derivatives: history, advances and future directions*, *Chemical Society Reviews* **2015**, 44 (11), 3808–3833;
9. Magano, J.; Dunetz, J.R., *Large-Scale Carbonyl Reductions in the Pharmaceutical Industry*, *Organic Process Research & Development* **2012**, 16 (6), 1156–1184;
10. Zuo, W.; Lough, A.J.; Li, Y.F.; Morris, R.H., *Amine(imine)diphosphine Iron Catalysts for Asymmetric Transfer Hydrogenation of Ketones and Imines*, *Science* **2013**, 342 (6162), 1080;
11. Bielinski, E.A.; Förster, M.; Zhang, Y.; Bernskoetter, W.H.; Hazari, N.; Holthausen, M.C., *Base-Free Methanol Dehydrogenation Using a Pincer-Supported Iron Compound and Lewis Acid Co-catalyst*, *ACS Catalysis* **2015**, 5 (4), 2404–2415;
12. Bielinski, E.A.; Lagaditis, P.O.; Zhang, Y.; Mercado, B.Q.; Würtele, C.; Bernskoetter, W.H.; Hazari, N.; Schneider, S., *Lewis Acid-Assisted Formic Acid Dehydrogenation Using a Pincer-Supported Iron Catalyst*, *Journal of the American Chemical Society* **2014**, 136 (29), 10234–10237;
13. Fu, S.; Shao, Z.; Wang, Y.; Liu, Q., *Manganese-Catalyzed Upgrading of Ethanol into 1-Butanol*, *Journal of the American Chemical Society* **2017**, 139 (34), 11941–11948;
14. Maji, B.; Barman, M.K., *Recent Developments of Manganese Complexes for Catalytic Hydrogenation and Dehydrogenation Reactions*, *Synthesis* **2017**, 49 (15), 3377–3393;
15. Buhaibeh, R.; Filippov, O.A.; Bruneau-Voisine, A.; Willot, J.; Duhayon, C.; Valyaev, D.A.; Lugan, N.; Canac, Y.; Sortais, J.B., *Phosphine-NHC Manganese Hydrogenation Catalyst Exhibiting a Non-Classical Metal-Ligand Cooperative H₂ Activation Mode*, *Angewandte Chemie International Edition* **2019**, 58 (20), 6727–6731;
16. Misal Castro, L.C.; Li, H.; Sortais, J.B.; Darcel, C., *When iron met phosphines: a happy marriage for reduction catalysis*, *Green Chemistry* **2015**, 17 (4), 2283–2303;
17. Kallmeier, F.; Irrgang, T.; Dietel, T.; Kempe, R., *Highly Active and Selective Manganese C=O Bond*

- Hydrogenation Catalysts: The Importance of the Multidentate Ligand, the Ancillary Ligands, and the Oxidation State*, *Angewandte Chemie International Edition* **2016**, 55 (39), 11806–11809;
18. Dubey, A.; Nencini, L.; Fayzullin, R.R.; Nervi, C.; Khusnutdinova, J.R., *Bio-Inspired Mn(I) Complexes for the Hydrogenation of CO₂ to Formate and Formamide*, *ACS Catalysis* **2017**, 7 (6), 3864–3868;
 19. Perez, M.; Elangovan, S.; Spannenberg, A.; Junge, K.; Beller, M., *Molecularly Defined Manganese Pincer Complexes for Selective Transfer Hydrogenation of Ketones*, *ChemSusChem* **2017**, 10 (1), 83–86;
 20. Bruneau-Voisine, A.; Wang, D.; Dorcet, V.; Roisnel, T.; Darcel, C.; Sortais, J.B., *Transfer Hydrogenation of Carbonyl Derivatives Catalyzed by an Inexpensive Phosphine-Free Manganese Precatalyst*, *Organic Letters* **2017**, 19 (13), 3656–3659;
 21. Martínez-Ferraté, O.; Werlé, C.; Franciò, G.; Leitner, W., *Aminotriazole Mn(I) Complexes as Effective Catalysts for Transfer Hydrogenation of Ketones*, *ChemCatChem* **2018**, 10 (20), 4514–4518;
 22. Shvydkiy, N.V.; Vyhivskiy, O.; Nelyubina, Y.V.; Perekalin, D.S., *Design of Manganese Phenol Pi-complexes as Shvo-type Catalysts for Transfer Hydrogenation of Ketones*, *ChemCatChem* **2019**, 11 (6), 1602–1605;
 23. Ganguli, K.; Shee, S.; Panja, D.; Kundu, S., *Cooperative Mn(I)-complex catalyzed transfer hydrogenation of ketones and imines*, *Dalton Transactions* **2019**, 48 (21), 7358–7366;
 24. Dubey, A.; Rahaman, S.M.W.; Fayzullin, R.R.; Khusnutdinova, J.R., *Transfer Hydrogenation of Carbonyl Groups, Imines and N-Heterocycles Catalyzed by Simple, Bipyridine-Based Mn^I Complexes*, *ChemCatChem* **2019**, 11 (16), 3844–3852;
 25. Wei, D.; Bruneau-Voisine, A.; Dubois, M.; Bastin, S.; Sortais, J.B., *Manganese-Catalyzed Transfer Hydrogenation of Aldimines*, *ChemCatChem* **2019**, 11 (21), 5256–5259;
 26. Zirakzadeh, A.; de Aguiar, S.R.M.M.; Stöger, B.; Widhalm, M.; Kirchner, K., *Enantioselective Transfer Hydrogenation of Ketones Catalyzed by a Manganese Complex Containing an Unsymmetrical Chiral PNP' Tridentate Ligand*, *ChemCatChem* **2017**, 9, 1744–1748;
 27. Widegren, M.B.; Harkness, G.J.; Slawin, A.M.Z.; Cordes, D.B.; Clarke, M.L., *A Highly Active Manganese Catalyst for Enantioselective Ketone and Ester Hydrogenation*, *Angewandte Chemie International Edition* **2017**, 56, 5825–5828;
 28. Garbe, M.; Junge, K.; Walker, S.; Wei, Z.; Jiao, H.; Spannenberg, A.; Bachmann, S.; Scalone, M.; Beller, M., *Manganese(I)-Catalyzed Enantioselective Hydrogenation of Ketones Using a Defined Chiral PNP Pincer Ligand*, *Angewandte Chemie International Edition* **2017**, 56 (37), 11237–11241;
 29. Schneekönig, J.; Junge, K.; Beller, M., *Manganese Catalyzed Asymmetric Transfer Hydrogenation of Ketones Using Chiral Oxamide Ligands*, *Synlett* **2019**, 30 (04), 503–507;
 30. Demmans, K.Z.; Olson, M.E.; Morris, R.H., *Asymmetric Transfer Hydrogenation of Ketones with Well-Defined Manganese(I) PNN and PNNP Complexes*, *Organometallics* **2018**, 37 (24), 4608–4618;
 31. Wang, D.; Astruc, D., *The Golden Age of Transfer Hydrogenation*, *Chemical Reviews* **2015**, 115 (13), 6621–6686;
 32. Wang, D.; Bruneau-Voisine, A.; Sortais, J.B., *Practical (asymmetric) transfer hydrogenation of ketones catalyzed by manganese with (chiral) diamines ligands*, *Catalysis Communications* **2018**, 105, 31–36;
 33. van Putten, R.; Uslamin, E.A.; Garbe, M.; Liu, C.; Gonzalez-de-Castro, A.; Lutz, M.; Junge, K.; Hensen, E.J.M.; Beller, M.; Lefort, L.; Pidko, E.A., *Non-Pincer-Type Manganese Complexes as Efficient Catalysts for the Hydrogenation of Esters*, *Angewandte Chemie International Edition* **2017**, 56 (26), 7531–7534;

34. Langer, R.; Diskin-Posner, Y.; Leitus, G.; Shimon, L.J.W.; Ben-David, Y.; Milstein, D., *Low-Pressure Hydrogenation of Carbon Dioxide Catalyzed by an Iron Pincer Complex Exhibiting Noble Metal Activity*, *Angewandte Chemie International Edition* **2011**, 50 (42), 9948–9952;
35. Frisch, M.; Trucks, G.; Schlegel, H.; Scuseria, G.; Robb, M.; Cheeseman, J.; Scalmani, G.; Barone, V.; Mennucci, B.; Petersson, G., *Gaussian 09 Revision D. 01*, **2009**, Gaussian Inc. Wallingford CT;
36. Grimme, S.; Ehrlich, S.; Goerigk, L., *Effect of the damping function in dispersion corrected density functional theory*, *Journal of Computational Chemistry* **2011**, 32 (7), 1456–1465;
37. Marenich, A.V.; Cramer, C.J.; Truhlar, D.G., *Universal Solvation Model Based on Solute Electron Density and on a Continuum Model of the Solvent Defined by the Bulk Dielectric Constant and Atomic Surface Tensions*, *The Journal of Physical Chemistry B* **2009**, 113 (18), 6378–6396;
38. van Putten, R.; Benschop, J.; de Munck, V.; Weber, M.; Mueller, C.; Filonenko, G.A.; Pidko, E.A., *Efficient and practical transfer hydrogenation of ketones catalyzed by a simple bidentate Mn-NHC complex*, *ChemCatChem* **2019**, 11 (21), 5232–5235;
39. Nguyen, D.H.; Trivelli, X.; Capet, F.; Paul, J.F.; Dumeignil, F.; Gauvin, R.M., *Manganese Pincer Complexes for the Base-Free, Acceptorless Dehydrogenative Coupling of Alcohols to Esters: Development, Scope, and Understanding*, *ACS Catalysis* **2017**, 7 (3), 2022–2032;
40. Swiegers, G.F., *Mechanical Catalysis: Methods of Enzymatic, Homogeneous, and Heterogeneous Catalysis*, Wiley-VCH Verlag GmbH & Co. kGaA, Weinheim, Germany, **2008**;
41. Wisman, R.V.; de Vries, J.G.; Deelman, B.J.; Heeres, H.J., *Kinetic Studies on the Asymmetric Transfer Hydrogenation of Acetophenone Using a Homogeneous Ruthenium Catalyst with a Chiral Amino-Alcohol Ligand*, *Organic Process Research & Development* **2006**, 10 (3), 423–429;
42. Hashiguchi, S.; Fujii, A.; Takehara, J.; Ikariya, T.; Noyori, R., *Asymmetric Transfer Hydrogenation of Aromatic Ketones Catalyzed by Chiral Ruthenium(II) Complexes*, *Journal of the American Chemical Society* **1995**, 117 (28), 7562–7563;
43. Fujii, A.; Hashiguchi, S.; Uematsu, N.; Ikariya, T.; Noyori, R., *Ruthenium(II)-Catalyzed Asymmetric Transfer Hydrogenation of Ketones Using a Formic Acid–Triethylamine Mixture*, *Journal of the American Chemical Society* **1996**, 118 (10), 2521–2522;
44. Chunhong, Z.; Liu, F.; Gou, S., *Application of chiral N,N'-dialkyl-1,2-cyclohexanediamine derivatives in asymmetric copper(II)-catalyzed Henry reactions*, *Tetrahedron: Asymmetry* **2014**, 25 (3), 278–283;
45. Gu, X.; Tang, Y.; Zhang, X.; Luo, Z.; Lu, H., *Organocatalytic Knoevenagel condensation by chiral C₂-symmetric tertiary diamines*, *New Journal of Chemistry* **2016**, 40 (8), 6580–6583;
46. Adamo, C.; Barone, V., *Toward reliable density functional methods without adjustable parameters: The PBE0 model*, *The Journal of Chemical Physics* **1999**, 110 (13), 6158–6170;
47. Weigend, F.; Ahlrichs, R., *Balanced basis sets of split valence, triple zeta valence and quadruple zeta valence quality for H to Rn: Design and assessment of accuracy*, *Physical Chemistry Chemical Physics* **2005**, 7 (18), 3297–3305;
48. Weigend, F., *Accurate Coulomb-fitting basis sets for H to R_n*, *Physical Chemistry Chemical Physics* **2006**, 8 (9), 1057–1065.



Chapter



The preparation of Mn^I-NHC complexes

and their application as transfer
hydrogenation catalysts

.....

“One never notices what has been done; one can only see what remains to be done.”

Marie Curie

Abstract

The reaction of $\text{Mn}(\text{CO})_5\text{Br}$ with bidentate amino-NHC ligands results in Mn^{I} -NHC complexes. These complexes were synthesised from the free carbene ligand that was prepared *in situ* by deprotonation of the corresponding imidazolium salt. The new systems are potent precatalysts for the base-promoted transfer hydrogenation of ketones and reduce a wide scope of substrates under mild conditions. The most active complex showed exceptional activity and stability, and was useful at catalyst concentrations as low as 75 ppm relative to the substrate.

Catalyst deactivation became important at these low metal concentrations and prevented a further reduction of the catalyst loading. The deactivation rate depended strongly on the temperature: a 10 °C reduction of the reaction temperature ultimately afforded a more than five-fold increase of the catalyst turnover number. These results emphasised that catalytic performance is often governed by a complex interplay of competing phenomena that depend both on catalyst structure and the reaction conditions.

This chapter has been published as:

R. van Putten, J. Benschop, V.J. de Munck, M. Weber, C. Müller, G.A. Filonenko, E.A. Pidko, *ChemCatChem* **2019**, *11*, 5232–5235

3.1 Introduction

The Mn^I-N,N' complexes described in the previous chapter are moderately active catalysts for the asymmetric transfer hydrogenation of aryl ketones. These reactions were typically performed at elevated temperature in the presence of 0.5–1.0 mol% of the precatalyst. These loadings correspond to a substrate-to-catalyst ratio in the range of hundreds. While such performance is encouraging for first-generation catalysts, several challenges remain to be addressed before these systems can be practically utilised in (industrial) organic synthesis.

The required metal loadings for 3d transition metals remain up to four orders of magnitude higher than those of noble metals; usually at several thousand ppm relative to the substrate (0.1 mol% = 1000 ppm).^{1–4} Although catalyst consumption usually is not a large concern for academic researchers, it can present a critical hurdle for industrial and commercial applications. Excessive catalyst consumption is especially problematic if the catalyst requires air-sensitive phosphine ligands, because these are challenging (and thus expensive) to produce at scale. This makes the development of simpler and more scalable alternatives highly desirable.

N-Heterocyclic carbenes (NHCs) *in principle* meet the main requirements for such alternative ligands: their steric and electronic properties are highly tuneable, their synthesis is well-established and scalable, and can conveniently be performed in air.^{5–9} Furthermore, the introduction of NHCs to noble metal complexes has resulted in highly active and (enantio)selective catalysts for a wide variety of chemistries.^{10–14} The coordination of NHCs to Mn^I has also recently been reported.^{15–16} The resulting coordination compounds were shown to be catalytically active for ketone hydrogenation¹⁷, ketone hydrosilylation¹⁸, and electrocatalytic reduction of CO_2 to CO ¹⁹ (**Figure 3.1**).

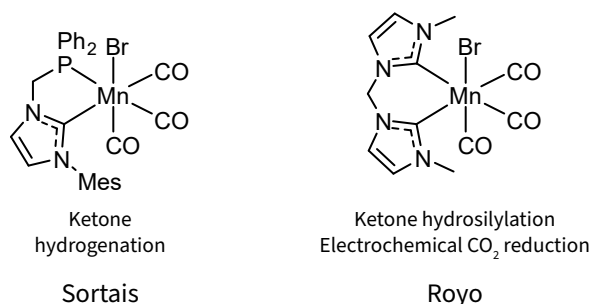


Figure 3.1. Well-defined Mn^I -NHC complexes and their reported catalytic application.

These literature reports, as well as the findings described in the previous chapter, led us to consider Mn^I-NHC complexes as potentially active and stable ketone transfer hydrogenation catalysts. More specifically, we hypothesised that the combination of a strongly electron donating NHC group and an amine would produce a potent but relatively small bidentate ligand. Based on the previous experience with NHC ligands and their complexes with transition metals in our group¹³⁻¹⁴, as well as the considerations above, we decided to synthesise and test two prototype Mn^I-NHC complexes, and to evaluate their activity as catalysts for carbonyl reductions.

3.2 Synthesis and characterisation of Mn^I-NHCs

We started our programme with the preparation of the required ligands **L1** and **L2** (Figure 3.2). Mesityl imidazole was prepared according to a modified literature procedure²⁰ and was purified by sublimation. The pure imidazole was then alkylated with the corresponding 2-bromoethylamine hydrobromide salt to give the desired imidazolium bromide product. We found that the direct use of these salts during the complexation with Mn resulted in inseparable mixtures. This was addressed by the neutralisation of hydrogen bromide with sodium carbonate and the subsequent ion metathesis to the hexafluorophosphate analogues of **L1** and **L2**. Use of these materials enabled the preparation of analytically pure **1** and **2**.

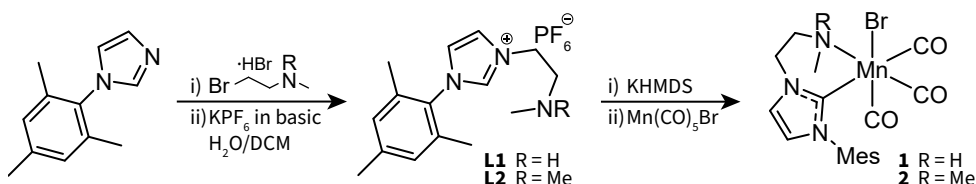


Figure 3.2. Synthetic route towards Mn^I-NHC complexes **1** and **2**.

Mn^I-NHC complexes **1** and **2** were obtained from the reaction of the *in situ* generated free carbene with Mn(CO)₅Br in THF. The imidazolium salt was deprotonated with KHMDs and the mixture was allowed to react for approximately 10 minutes at room temperature. Afterwards KPF₆ was removed by filtration, and Mn(CO)₅Br was added to the solution that contained the pre-formed free carbene. The evolution of gaseous CO was observed upon addition of the Mn precursor, and the reaction mixture was heated overnight at 60 °C to drive the reaction to completion. The analytically pure complexes were obtained in 67% (**1**) and 88% (**2**) yield by slow vapour diffusion crystallisation of the crude materials from dichloromethane/*n*-pentane. The newly-synthesised Mn^I-NHC complexes were characterised with ¹H and ¹³C NMR, FTIR, elemental analysis, and single-crystal X-ray diffraction studies.

The ^1H NMR spectrum of **1** featured four individual resonances for the inequivalent geminal protons of the ethylene linker fragment (**Figure 3.3**). This pattern is similar to that described in the previous chapter for the structurally-related Mn^{I} - N,N' compounds, and is presumably caused by the locked configuration of the coordination complex.

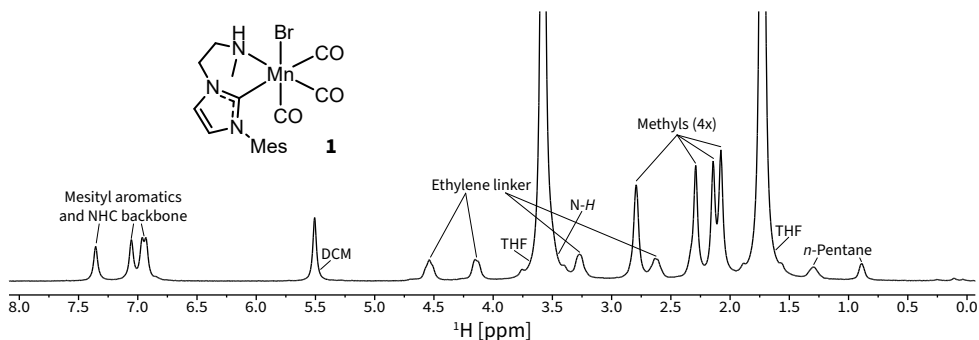


Figure 3.3. ^1H NMR spectrum of **1** in $\text{THF-}d_8$ (400 MHz).

Both complexes featured three sharp $\nu(\text{C}=\text{O})$ bands in their FTIR spectrum at 2004, 1919, and 1892 cm^{-1} (**1**), and 2007, 1922, and 1881 cm^{-1} (**2**). These spectra were indicative of a neutral octahedral Mn^{I} *cis*-tricarbonyl bromide complex. The geometry of **1** and **2** was confirmed with X-ray diffraction studies, which revealed Mn-NHC bond lengths of 2.053 Å in **1**, and 2.055 Å in **2** (**Figure 3.4**).

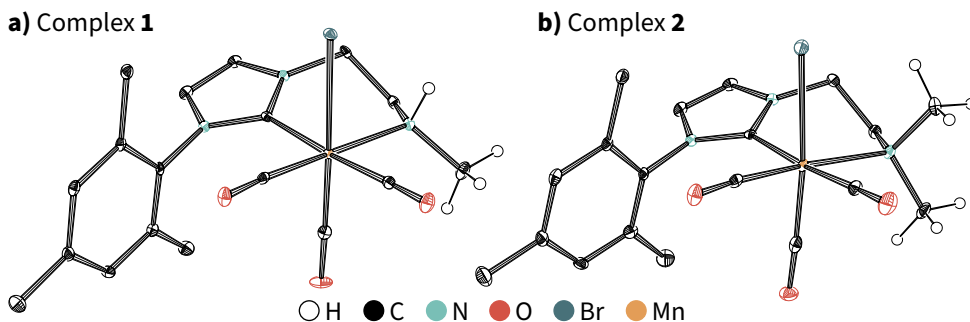


Figure 3.4. ORTEP diagrams of **1** (a) and **2** (b). Thermal ellipsoids were drawn at 30% probability. Co-crystallised solvent and hydrogen atoms (except those bound to nitrogen or to its methyl) have been omitted for clarity. Key: H (white), C (black), N (turquoise), O (red), Br (green), Mn (orange).

3.3 Catalytic performance of Mn^I-NHC complexes

Initial transfer hydrogenation catalytic activity tests were performed in 2-propanol at 50 °C with acetophenone as a model substrate. A precatalyst loading of 0.5 mol% was used relative to the substrate with 2 equivalents (*i.e.*, 1.0 mol%) potassium *tert*-butoxide as the precatalyst activator. The results of these experiments are summarised in **Table 3.1**.

Table 3.1. Results of catalytic activity tests with Mn^I-NHC precatalysts **1** and **2**.^{a)}

Entry	Complex ([mol% / ppm])	Temperature [°C]	Alcohol yield [%] ^{b)}	TON [-]
1	1 (0.5 / 5000)	50	92	184
2	2 (0.5 / 5000)	50	1	2
3	1 (0.5 / 5000)	80	93	186
4	1 (0.1 / 1000)	80	94	940
5	1 (0.05 / 500)	80	94	1880
6	1 (0.02 / 200)	80	85	4250
7	1 (0.01 / 100)	80	47	4700
8 ^{c)}	1 (0.05 / 500)	40	0	-
9 ^{c)}	1 (0.05 / 500)	80	14	280

a) Conditions: 1.0 mmol acetophenone, 0.01–0.5 mol% precatalyst, 2 eq. KO^tBu to Mn, 2.5 ml 2-propanol, 50–80 °C, 1 h. **b)** Yields were determined by GC-FID using *n*-dodecane as an internal standard. **c)** No KO^tBu, 3 h.

Activation of precatalyst **1** resulted in a highly active catalytic system for the transfer hydrogenation of ketones. This new system significantly outperformed the bidentate Mn^I-*N,N'* precatalysts described in the previous chapter. Dimethylated complex **2** was practically inactive under identical experimental conditions. This result is in line with literature data and the purported Noyori-Ikariya reaction mechanism that is generally thought to govern this type of chemistry. We therefore focused our research and analysis on Mn^I-NHC complex **1**.

Increased reaction temperature enabled a tenfold reduction of the catalyst loading to 0.05 mol% (500 ppm) and resulted in quantitative alcohol yields within 1 hour (**Table 3.1**). A further reduction of the catalyst concentration led to incomplete reaction progress despite impressive turnover numbers of over 4000. These results suggested that **1** remained catalytically active and stable over a large range of turnovers and potentially allowed for further optimisation.

Additional control experiments were carried out to establish the catalytic nature of **1** and to exclude potential background reactions²¹ (Table 3.1, not all negative results are shown). The reactions without precatalyst did not lead to any observable conversion of the substrate. The reaction without the alkoxide base at 80 °C consistently led to the production of 1-phenylethanol, albeit in significantly lower amounts than when the precatalyst was present. This reactivity was not observed at 40 °C, which suggests that it could, for example, have been caused by thermal dissociation of the ligand. The phenomenon was not investigated further because the catalytic effect of **1** on the reduction of acetophenone was clear.

3.4 Condition optimisation: screening

We performed a series of screening experiments to gain insight into critical reaction parameters such as the amount of base and the ideal solvent and/or hydrogen donor. We found that the addition of one equivalent of KO^tBu did not quantitatively activate the precatalyst (Figure 3.5). The reaction in the presence of a small excess of base gave optimal results. Further addition of base did not improve the catalytic performance, and potentially even had a slightly detrimental effect (that was not further investigated).

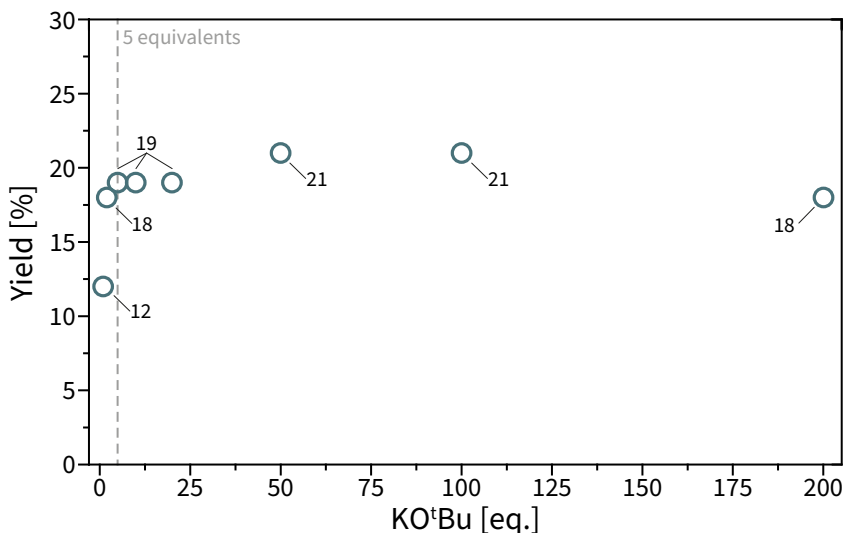


Figure 3.5. Effect of base loading on the transfer hydrogenation reaction with **1**. Stated equivalents of KO^tBu are relative to **1**. Conditions: 0.5 mmol acetophenone, 0.05 mol% **1**, 1–200 eq. KO^tBu, 3.82 ml 2-propanol, 40 °C, 3 h. Yields were determined by GC-FID using *n*-dodecane as an internal standard.

The composition of the solvent mixture had a large effect on catalytic performance (**Figure 3.6**). Reactions were performed with a mixture of 2-propanol in the respective co-solvent. The highest yields of 1-phenylethanol were obtained when solvents could also function as a hydrogen donor (e.g., 2-butanol and 2-propanol). The reaction in DMF (*dimethylformamide*) also gave a high alcohol yield. Ethers and aromatics solvents performed relatively well, while strongly coordinating solvents such as methanol and ethanol led to almost entirely diminished performance. This is probably because these solvents reacted with catalytic intermediates and inhibited them.

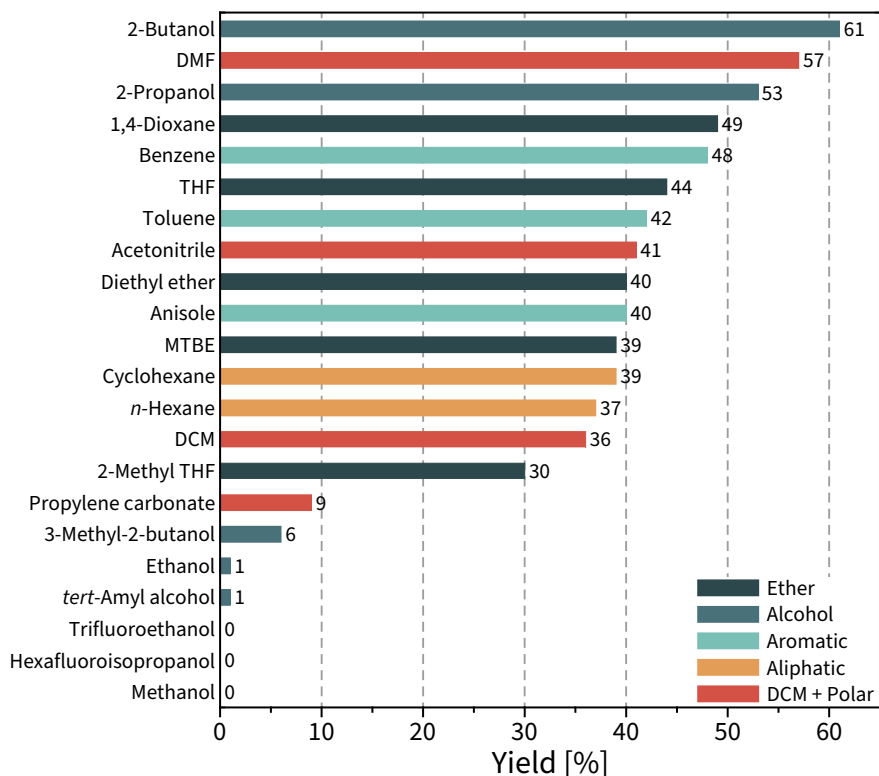


Figure 3.6. Solvent effects on the transfer hydrogenation reaction with **1**. Conditions: 0.5 mmol acetophenone, 0.05 mol% **1**, 1.0 mol% KO^tBu, 10 eq. 2-propanol to substrate, 3.5 ml solvent, 40 °C, 2 h. Yields were determined by GC-FID using *n*-dodecane as an internal standard.

We next evaluated the compatibility of precatalyst **1** with several hydrogen donor molecules (**Table 3.2**). These experiments included three secondary alcohols, the well-established azeotropic mixture of formic acid and triethylamine^{1,22}, and potassium formate²³⁻²⁴. Experiments were performed with 10 equivalents of the hydrogen donor in THF.

Table 3.2. Hydrogen donor screening for ketone transfer hydrogenation with **1**.^{a)}

Entry	Hydrogen donor	Alcohol yield [%] ^{b)}	TON [-]
1	2-Propanol	33	660
2	2-Butanol	30	600
3	3-Methyl-2-butanol	33	660
4	[HCOOH][NEt ₃]	0	-
5	KCOOH	0	-

a) Conditions: 0.5 mmol acetophenone, 0.05 mol% **1**, 1.0 mol% KO^tBu, 5.0 mmol hydrogen donor in 3.82 ml liquid (balance THF), 40 °C, 6 h. **b)** Yields were determined by GC-FID using *n*-dodecane as an internal standard.

The evaluated secondary alcohol donors showed similar reactivity and provided virtually identical alcohol yields. Reaction with the [HCOOH][NEt₃] azeotrope or potassium formate as the alternative hydrogen donor did not lead to any observable reaction progress. This is unfortunate because it would have allowed the reactions to be performed at higher substrate concentrations. (It could also have prevented the erosion of product *ee* if a chiral Mn^I-NHC would have been used.)

The results from our screening experiments thus indicated that the original system was already close to optimal and that use of alternative solvents or hydrogen donors did not significantly improve its performance. Subsequent experiments were therefore performed in neat 2-propanol with a fixed base loading of 1 mol% relative to the substrate.

3.5 Condition optimisation: continuous variables

We continued our optimisation campaign and focused on the role of reaction temperature and catalyst concentration. Kinetic experiments were performed at catalyst loadings between 25 ppm and 100 ppm at 70 °C and 80 °C. The results of these experiments are summarised in **Figure 3.7** (experiments at 75 and 100 ppm Mn provided quantitative alcohol yields and their traces are not shown).

Increased reaction temperature led to pronounced catalyst deactivation that became particularly noticeable at metal loadings below 75 ppm. At 70 °C with 50 ppm Mn (0.005 mol%), complex **1** reacted with a high initial turnover frequency (TOF⁰) of 11.800 h⁻¹ and completed 11.100 turnovers in 6 h (56% yield). The reaction at 60 °C was slower (TOF⁰ = 6100 h⁻¹), but surpassed the integral TON of the reaction at 70 °C after approximately 2.5 h (crossover at ~9600 TON). This reaction had achieved 15.100 turnovers after 6 hours of reaction time and was 76% complete.

A further reduction of catalyst concentration to 25 ppm expedited the deactivation reaction, and TON crossover took place after only 20 minutes (~1800 TON). The deactivation process was significantly more pronounced at 70 °C and reaction progress halted at only 8% completion. In contrast, the reaction at 60 °C resulted in a very high TON of 17.300 after 6 hours, and, importantly, at that time did not yet show signs of imminent reaction termination.

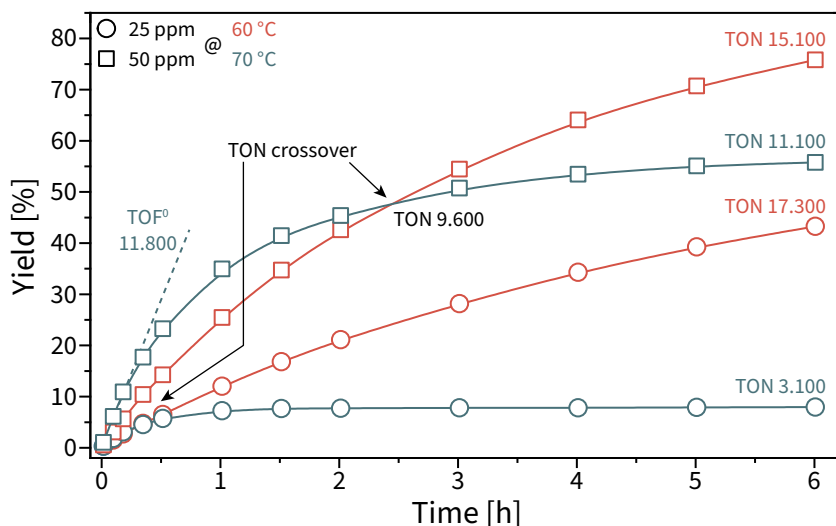


Figure 3.7. Kinetic traces of acetophenone transfer hydrogenation with **1** under deactivating conditions. Conditions: 0.5 mmol acetophenone, 25–50 ppm **1**, 1.0 mol% KO^tBu, 3.82 ml 2-propanol, 60–70 °C. Yields were determined by GC-FID using *n*-dodecane as an internal standard.

These observations indicate that catalyst deactivation is probably independent of total catalytic turnover and must therefore be caused by phenomena not directly related to the main catalytic conversion path (*e.g.*, by thermal degradation of the catalytically active Mn^I complexes). Additional investigations into the nature of catalyst deactivation are described in **Chapter 5** of this dissertation.

3.6 Substrate scope

The optimised catalytic system was used to study its substrate scope. We investigated the effects of different functional groups with varied steric and electronic properties (**Figure 3.8**). Reactions were performed at 40 °C with 500 ppm Mn (0.05 mol%). These conditions were selected to minimise potentially detrimental effects caused by irreversible catalyst deactivation. We estimated that these conditions provided a reasonable balance between reaction rate, catalyst consumption, and the temperature-dependent rate of deactivation.

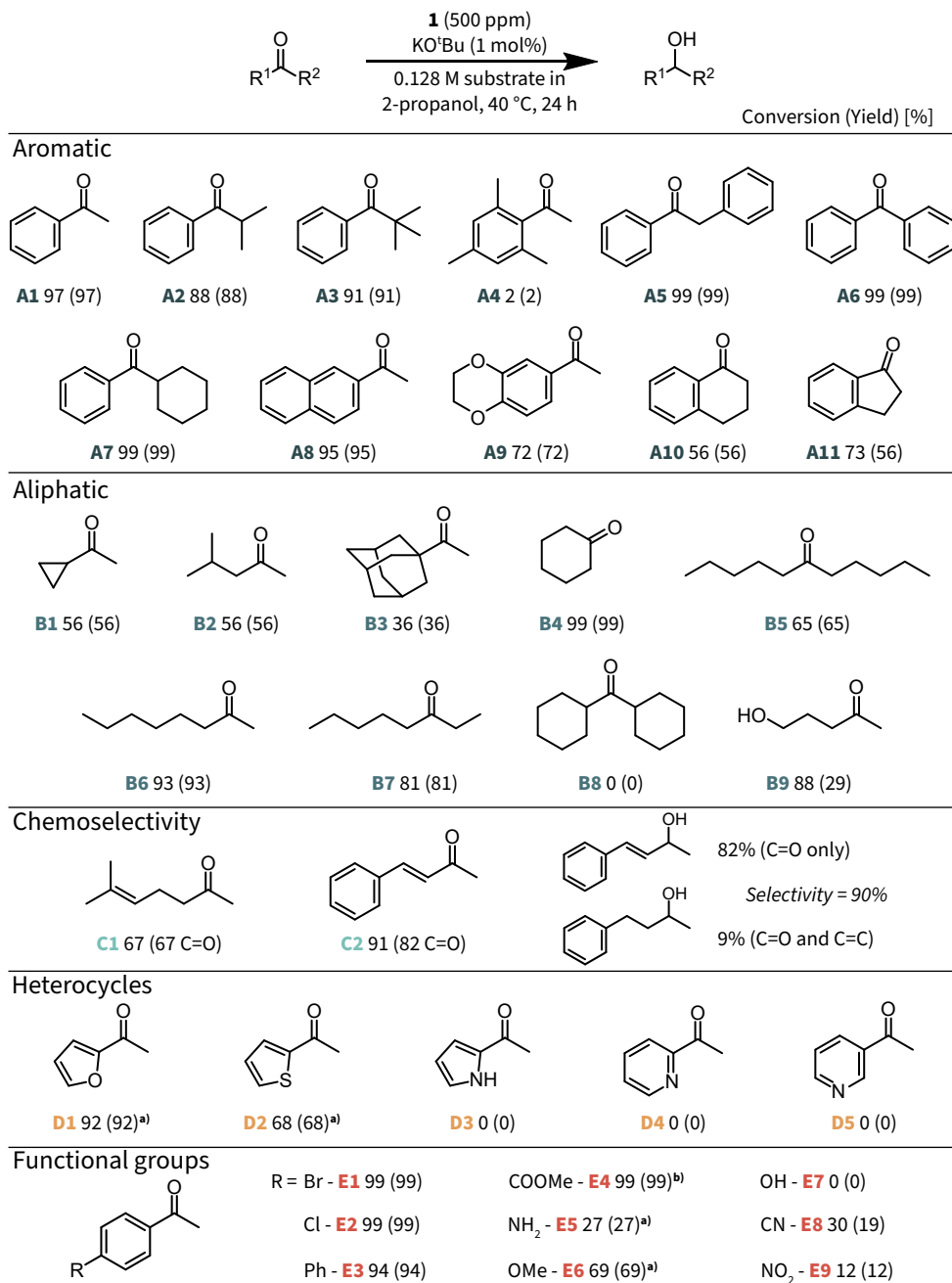


Figure 3.8. Substrate scope for **1**. Conditions: 0.5 mmol substrate, 0.05 mol% **1** (500 ppm), 1.0 mol% KO^tBu, 3.82 ml 2-propanol, 40 °C, 24 h. Yields were determined by GC-FID using *n*-dodecane as an internal standard. **a)** The corresponding dehydrated product (*i.e.*, its vinyl) was observed with GC-MS. **b)** The corresponding isopropyl esters was observed with GC-MS.

Reduction of aromatic ketones **A1** to **A9** led to the corresponding alcohols in good to quantitative yields, except for sterically demanding 2,4,6-trimethylacetophenone **A4**. The alcohols from ketones **A10** and **A11** were obtained in a fair yield of 56%. Aliphatic ketones were generally more difficult to reduce. Bulky 1-adamantyl methyl ketone **B3** was only partially reduced under the selected conditions. The long-chain aliphatic alcohols from substrates **B5–B7** were obtained in good to excellent yields, with the yield depending on the exact location of the functional group. Dicyclohexyl methyl ketone **B8** was not reduced, while the reaction with **B9** was not selective and resulted in extensive (cyclic) side-product formation. Thus, the accessibility of the carbonyl moiety in the substrate was identified as one of the key factors that govern catalysis with **1**.

Chemoselectivity for carbonyl *versus* alkene reduction was evaluated with aliphatic and aromatic examples **C1** and **C2**. 6-Methyl-5-hepten-2-one **C1** was selectively reduced to the corresponding unsaturated alcohol in 67% yield. Benzylideneacetone **C2**—a notoriously difficult substrate to reduce selectively—was predominantly reduced to the unsaturated alcohol (82% yield). The fully saturated product was obtained in 9% yield. Thus, the catalyst's C=O/C=C selectivity for the aromatic substrate was about 90%.

GC-MS indicated that the reduction of heterocyclic compounds **D1** and **D2** was followed by quantitative dehydration to 2-vinylfuran (92% yield) and 2-vinylthiophene (68%). The observed (E1cB) elimination reaction presumably is a consequence of the basic conditions in the reaction mixture. Introduction of a nitrogen atom to the heterocyclic ring led to complete loss of activity (**D3–D5**).

Functional group tolerance was studied with a series of *para*-substituted acetophenones (**E1** to **E9**). Incorporation of halides or a phenyl moiety had no significant effect on the catalyst's performance (**E1** to **E3**). Catalyst **1** selectively reduced the ketone functionality of substrate **E4** and left the ester group intact. (The basic conditions catalysed the transesterification reaction with isopropanol, and the corresponding isopropyl ester was therefore obtained.) 4-Acetylaniline **E5** and 4-acetylanisole **E6** were reduced to the corresponding vinylic products (similar to **D1** and **D2**). Catalytic performance was severely lower for substrates that contained a hydroxyl (**E7**), cyano (**E8**), or nitro group (**E9**).

In conclusion, our results showed that complex **1** is a potent catalyst for transfer hydrogenation of a broad scope of substrates. The attempted reduction of strongly donating (amine) substrates led to a complete loss of catalytic activity. (This result was not surprising because amines are known to react with Mn^I to form coordination complexes. This was described in more detail in **Chapter 2**.)

3.7 Preliminary mechanistic investigations

The precatalyst activation process was finally studied in more detail with a series of stoichiometric reactivity experiments. The addition of 2 equivalents of 2-propanol and potassium *tert*-butoxide to a solution of complex **1** in benzene-*d*₆ led to significant changes of the ¹H NMR spectrum (**Figure 3.9**).

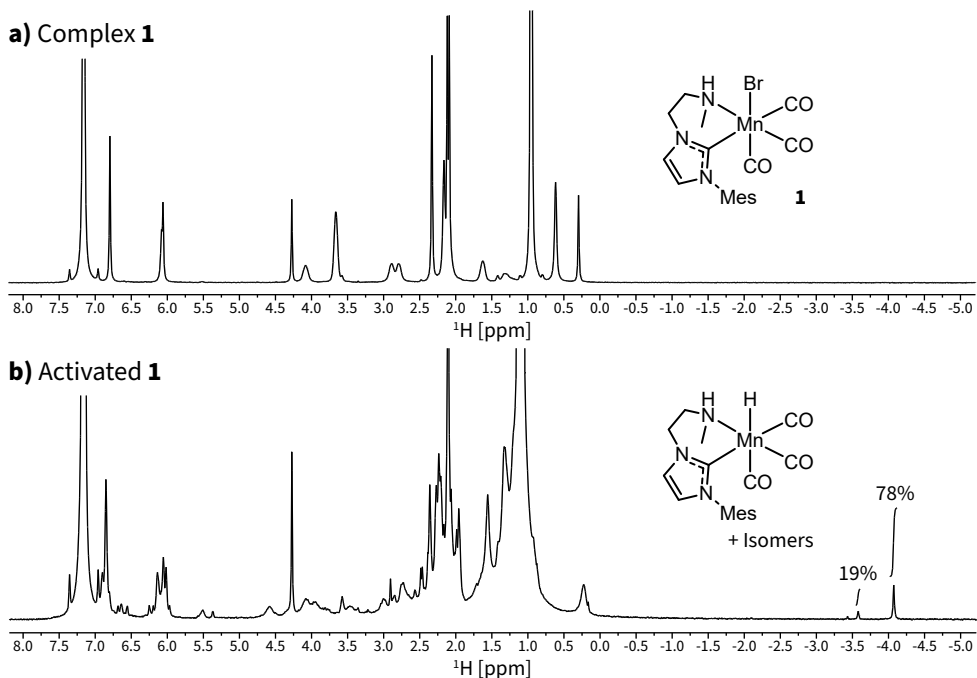


Figure 3.9. ¹H NMR spectrum of precatalyst **1** (a) and activated **1** (b) in C₆D₆ (400 MHz).

Three new peaks were observed in the hydride region of the ¹H NMR spectrum. (The third could only be detected after apodisation of the signal. This peak did not significantly exceed the noise.) We attribute these peaks to the expected Mn^I-NHC hydride isomers formed upon dehydrogenation of 2-propanol. (This process has been described in detail in the previous chapter for related Mn^I-*N,N'* complexes. A more detailed mechanistic study on catalysis with **1** is described in **Chapter 5**.)

The identical reaction with **2** resulted in trace amounts of Mn-hydrides (approximately 2% by NMR), which suggests that the loss of the reactive *N-H* functionality in **2** prevented metal-ligand cooperativity and, consequently, the formation of the reactive hydride species from 2-propanol. These findings, combined with the catalytic inactivity of **2**, indicate that catalysis with Mn^I-NHC complexes probably proceeds *via* the established bifunctional protonation/deprotonation Noyori-Ikariya mechanism.³⁻⁴

Addition of KO^tBu in 2-propanol to either of the Mn complexes caused significant broadening of the ¹H NMR spectrum (**Figure 3.9**). This could indicate the presence of paramagnetic species, which could have been formed after disproportionation or decomposition of the Mn^I complex. Such redox chemistry is poorly understood and was part of the mechanistic investigations described in **Chapter 5**.

3.8 Conclusion

We have prepared the new Mn^I-NHC complexes **1** and **2**, and have investigated their catalytic activity for the transfer hydrogenation of ketones with 2-propanol. Catalysis with **1** proceeded with a very high maximum turnover number of at least 17,000. This complex was useful at catalyst loadings as low as 75 ppm relative to the substrate. These loadings approach those of the more conventionally utilised Ru and Ir catalysts and provide a clear demonstration of the great potential of 3d transition metal complexes for sustainable catalysis.

Significant (irreversible) catalyst deactivation was observed, which inhibited further reduction of the metal loading. The rate of deactivation was particularly sensitive to the reaction temperature; a reduction of only 10 °C resulted in an over five-fold increase of the catalyst's lifetime. We hypothesised that thorough understanding of the reaction mechanism and the origin of the deactivation process could bring further improvements to the system's performance, and have therefore studied them in detail. The results of these investigations are described in **Chapter 5**.

3.9 Experimental section

General considerations

All manipulations were, unless stated otherwise, performed under an inert atmosphere in an Ar-filled Inert glove box or using standard Schlenk techniques. Anhydrous solvents were dispensed from an Inert PureSolv solvent purification system or were dried using 3 or 4 Å molecular sieves. Solvents were degassed before use. Chemicals were purchased from Sigma-Aldrich, Strem, abcr, or TCI, and were dried and/or degassed before use. Air and/or moisture sensitive materials were stored in the glove box. Deuterated solvents were purchased from Eurisotop, dried using molecular sieves, degassed, and stored in the glove box.

NMR spectra were recorded on an Agilent 400-MR DD2 400 MHz spectrometer equipped with a 5 mm ONE NMR probe. ¹H and ¹³C chemical shifts were referenced to residual solvent peaks (¹H: 5.32 ppm CD₂Cl₂, 7.16 ppm C₆D₆, 3.58 ppm THF-*d*₈).

^{13}C : 53.84 ppm CD_2Cl_2 , 128.06 ppm C_6D_6 , 67.21 ppm $\text{THF-}d_8$). Proton and carbon assignments were made on basis of combined gCOSY and gHSQC spectra. FTIR (ATR) was measured on a Bruker Alpha II spectrometer inside the glove box. Elemental analyses were performed in duplo by Mikroanalytisches Laboratorium Kolbe (Oberhausen, Germany).

Synthetic procedures

Full characterisation for the compounds below is available in the electronic supporting information of the published work: *ChemCatChem* **2019**, *11*, 5232–5235, DOI: 10.1002/cctc.201900882.

CAUTION: Manganese carbonyl complexes release poisonous and flammable carbon monoxide gas upon complexation!

L1 – [1-Mesityl-3-(2-(methylamino)ethyl)-1*H*-imidazolium][PF₆]

Mesityl imidazole (4.0 g, 21.5 mmol) was added to a suspension of *N*-methyl-2-bromoethylamine hydrobromide (5.08 g, 21.5 mmol) in 25 ml acetonitrile. The mixture was refluxed in air for 30 hours.

Afterwards the solvent was removed on the rotary evaporator. The oily residue was dissolved in 75 ml water, neutralised with saturated aqueous sodium carbonate until pH 9, and was extracted with ethyl acetate (2 x 100 ml) to remove unreacted organic materials. At this point the imidazolium salt remained in the aqueous phase.

The solution in water was vigorously stirred with KPF₆ (6.0 g, ~1.5 equivalents) to form a turbid suspension that was extracted with dichloromethane (3 x 100 ml). The organic phase was dried with sodium carbonate and was evaporated to dryness to give **L1** as a viscous oil. The oil was triturated with diethyl ether. This provided **L1** as a solid that was crushed and thoroughly dried. Analytically pure **L1** was obtained as an off-white hygroscopic powder that was stored inside the glove box. Yield: 6.02 g (72%).

^1H NMR (400 MHz, CD_2Cl_2): δ 8.60 (s, imidazole C²H, 1H), 7.64 (s, imidazole C³⁻⁴H, 1H), 7.22 (s, imidazole C³⁻⁴H, 1H), 7.08 (s, mesityl C³H, 2H), 4.47–4.15 (m, CH₂, 2H), 3.23–2.89 (m, CH₂, 2H), 2.42 (s, NCH₃, 3H), 2.37 (s, mesityl C⁴CH₃, 3H), 2.05 (s, mesityl C²CH₃, 6H).

L2 – [1-Mesityl-3-(2-(dimethylamino)ethyl)-1*H*-imidazolium][PF₆]

Compound **L2** was prepared by an analogous procedure to **L1** with *N,N*-dimethyl-2-bromoethylamine hydrobromide.

¹H NMR (400 MHz, CDCl₃): δ 8.47 (s, imidazole C²H, 1H), 7.69 (t, *J* = 1.8 Hz, imidazole C³⁻⁴H, 1H), 7.12 (t, *J* = 1.8 Hz, imidazole C³⁻⁴H, 1H), 7.00 (s, mesityl C³H, 2H), 4.41–4.32 (m, CH₂, 2H), 2.70 (m, CH₂, 2H), 2.33 (s, mesityl C⁴CH₃, 3H), 2.24 (s, NCH₃, 6H), 2.01 (s, mesityl C²CH₃, 6H).

1 – Mn(1-mesityl-3-(2-(methylamino)ethyl)-imidazolylidene)(CO)₃Br

Inside the glove box, **L1** (390 mg, 1.0 mmol) was dissolved in 5 ml THF. To it was added a solution of KHMDS (200 mg, 1.0 mmol) in 0.5 ml THF and the mixture was stirred at room temperature for approximately 10 minutes. Within minutes the mixture turned turbid. The solids were removed by filtration, and Mn(CO)₅Br (275 mg, 1.0 mmol) was added as a solid. The mixture immediately evolved CO and was heated to 60 °C overnight.

Afterwards the solvent was removed *in vacuo* to give crude **1** as an oil. The oil was washed with *n*-pentane, dissolved in minimum dichloromethane, and filtered through a plug of Celite to remove KPF₆. *n*-Pentane was added to the solution and the mixture was set to crystallise against *n*-pentane by slow vapour diffusion. Analytically pure **1** was obtained as orange crystals. Yield: 309 mg (67%).

¹H NMR (400 MHz, CD₂Cl₂): δ 7.18 (d, *J* = 1.7 Hz, imidazole C³⁻⁴H, 1H), 7.01 (s, mesityl C³H, 1H), 6.97 (s, mesityl C³H, 1H), 6.93 (d, *J* = 1.7 Hz, imidazole C³⁻⁴H, 1H), 4.63–4.49 (m, CH₂, 1H), 4.07 (m, CH₂, 1H), 3.29 (m, CH₂, 1H), 3.11 (br s, NH, 1H), 2.88 (d, *J* = 6.2 Hz, NCH₃, 3H), 2.73 (m, CH₂, 1H), 2.33 (s, mesityl CH₃, 3H), 2.14 (s, mesityl CH₃, 3H), 2.08 (s, mesityl CH₃, 3H).

¹³C NMR (101 MHz, CD₂Cl₂): all resonances are singlets: δ 225.4, 220.4, 216.8, 191.5, 139.8, 138.0, 136.9, 135.9, 129.6, 129.1, 123.9, 123.4, 54.3, 48.7, 47.3, 21.2, 18.9, 17.8.

FTIR (ATR): 2004, 1919, 1892 cm⁻¹.

EA: found (calc. MnC₁₈H₂₁N₃BrO₃): C: 46.62 (46.77), H: 4.71 (4.58), N: 8.92 (9.09).

2 – Mn(1-Mes-3-(2-(dimethylamino)ethyl)-imidazolylidene)(CO)₃Br

Complex **2** was prepared by an analogous procedure to **1** with ligand **L2**. Analytically pure **2** was obtained as orange crystals. Yield: 420 mg (88%).

¹H NMR (400 MHz, CD₂Cl₂): δ 7.20 (d, *J* = 1.7 Hz, imidazole C³⁻⁴H, 1H), 6.99 (s, mesityl C³H, 1H), 6.96 (s, mesityl C³H, 1H), 6.94 (d, *J* = 1.7 Hz, imidazole C³⁻⁴H, 1H), 4.48 (dd, *J* = 14.6, 8.7 Hz, CH₂, 1H), 4.04 (dd, *J* = 14.3, 6.4 Hz, CH₂, 1H), 3.02 (dd, *J* = 12.8, 6.5 Hz, CH₂, 1H), 2.87 (s, NCH₃, 3H), 2.82 (s, NCH₃, 3H), 2.54 (dd, *J* = 12.8, 9.0 Hz, CH₂, 1H), 2.32 (s, mesityl CH₃, 3H), 2.21 (s, mesityl CH₃, 3H), 2.07 (s, mesityl CH₃, 3H).

¹³C NMR (101 MHz, CD₂Cl₂): all resonances are singlets: δ 224.3, 222.1, 217.6, 192.2, 139.8, 138.0, 136.9, 136.0, 129.6, 129.0, 123.7, 123.6, 63.5, 57.6, 55.5, 46.8, 21.2, 19.1, 17.9.

FTIR (ATR): 2007, 1922, 1881 cm⁻¹.

Catalytic (kinetic) experiments

Inside the Ar-filled glove box, a 4 ml glass vial was loaded (in order) with a PTFE-coated magnetic stirring bar, *n*-dodecane, solvent and/or 2-propanol, precatalyst, base (both as stock solutions), and substrate. The vial was capped, placed inside a preheated oil bath, stirred at 500 rpm, and was heated for the desired reaction time. Negligible heating time was assumed because of the small diameter vials inside the large heat basin and the relatively long reaction times.

Kinetic experiments were performed inside the glove box. For these experiments the substrate was withheld from the main solution, and was added after the main solution was preheated for 30 minutes inside a metal heating block. A 50 μl aliquot was removed from the reaction mixtures at the appropriate time.

Samples were immediately quenched by their addition to 100 μl of a 2 wt% solution of acetic acid in 2-propanol. The mixture was diluted with 1.0 ml 2-propanol and was analysed as described.

Typical loadings: 25.0 μl *n*-dodecane, 3.82 ml 2-propanol, 0.114 mg **1** (0.25 μmol, 0.05 mol%, 500 ppm), 0.56 mg KO^tBu (5.0 μmol, 1.0 mol%), and 58.4 μl acetophenone (0.5 mmol, initial concentration 0.128 M).

Substrate scope

Inside the Ar-filled glove box, a 4 ml glass vial was loaded with the appropriate amount of substrate. To this was added a PTFE-coated magnetic stirring bar and 3.8 ml of a stock solution containing 0.114 mg **1** (0.25 μmol , 0.05 mol%, 500 ppm), 0.56 mg KO^tBu (5.0 μmol , 1.0 mol%), and 25.0 μl *n*-dodecane in 2-propanol. The contents were mixed and an 100 μl aliquot was removed for pre-reaction GC analysis.

The vial was taken out of the glove box and was heated in a preheated oil bath on a magnetic stirring plate. The vials were stirred at 400 rpm and heated to 40 °C for 24 h. Negligible heating time was assumed because of the small diameter vials inside the large heat basin and the relatively long reaction time.

Afterwards the vial was removed from the oil bath and the reaction was immediately quenched by the addition of 1 ml 2 wt% acetic acid in 2-propanol. The reaction mixture was sampled, diluted with 2-propanol, and analysed as described.

Analytical details

Initial experiments and reaction condition optimisations: measurements were performed on an Agilent 6890 gas chromatograph equipped with an FID detector and an Agilent CP-Chirasil-Dex CB column (25 m, 0.25 mmID, 0.25 μm film thickness). Method details: 120 °C (hold 1.0 min), ramp to 180 °C at 20 °C min⁻¹ (hold 2.0 min). Products were identified using the retention times from analytically pure reference samples. Mass balances were calculated using *n*-dodecane as an internal standard and were verified to be within 90%–110% for all experiments.

Substrate scope: measurements were performed on an Agilent 7890B gas chromatograph equipped with FID and MS detectors and an Agilent HP-5 column (30 m, 0.25 mmID, 0.25 μm film thickness). Method details: 60 °C (hold 2.0 min), ramp to 300 °C at 20 °C min⁻¹ (hold at 180 °C for 5.0 min). Cyclopropyl methyl ketone and 4-methyl-2-pentanone: 40 °C, ramp to 300 °C at 20 °C min⁻¹ (hold at 300 °C for 5.0 min). Products were identified by comparison of observed mass spectra and spectra of the authentic reference samples available in the NIST 17 library. Mass balances were calculated using *n*-dodecane as an internal standard and were, unless stated otherwise, verified to be within 90%–110% for all experiments.

Crystallographic details

X-ray diffraction studies were performed by M. Weber and prof. dr. C. Müller (Freie Universität Berlin). Crystallographic details are available in the electronic supporting information of the published work: *ChemCatChem* **2019**, *11*, 5232–5235, DOI: 10.1002/cctc.201900882. CCDC entries 1906472 (**1**) and 1906473 (**2**) contain the supplementary data for this work.

3.10 References

1. Wang, D.; Astruc, D., *The Golden Age of Transfer Hydrogenation*, *Chemical Reviews* **2015**, 115 (13), 6621–6686;
2. Filonenko, G.A.; van Putten, R.; Hensen, E.J.M.; Pidko, E.A., *Catalytic (de)hydrogenation promoted by non-precious metals – Co, Fe and Mn: recent advances in an emerging field*, *Chemical Society Reviews* **2018**, 47 (4), 1459–1483;
3. Noyori, R.; Kitamura, M.; Ohkuma, T., *Toward efficient asymmetric hydrogenation: Architectural and functional engineering of chiral molecular catalysts*, *Proceedings of the National Academy of Sciences of the United States of America* **2004**, 101 (15), 5356;
4. Dub, P.A.; Gordon, J.C., *The role of the metal-bound N–H functionality in Noyori-type molecular catalysts*, *Nature Reviews Chemistry* **2018**, 2 (12), 396–408;
5. Hopkinson, M.N.; Richter, C.; Schedler, M.; Glorius, F., *An overview of N-heterocyclic carbenes*, *Nature* **2014**, 510 (7506), 485–496;
6. Nelson, D.J.; Nolan, S.P., *Quantifying and understanding the electronic properties of N-heterocyclic carbenes*, *Chemical Society Reviews* **2013**, 42 (16), 6723–6753;
7. Andrew, R.E.; González-Sebastián, L.; Chaplin, A.B., *NHC-based pincer ligands: carbenes with a bite*, *Dalton Transactions* **2016**, 45 (4), 1299–1305;
8. Huynh, H.V., *Electronic Properties of N-Heterocyclic Carbenes and Their Experimental Determination*, *Chemical Reviews* **2018**, 118 (19), 9457–9492;
9. Peris, E., *Smart N-Heterocyclic Carbene Ligands in Catalysis*, *Chemical Reviews* **2018**, 118 (19), 9988–10031;
10. Sluijter, S.N.; Korstanje, T.J.; van der Vlugt, J.I.; Elsevier, C.J., *Mechanistic insights into catalytic carboxylic ester hydrogenation with cooperative Ru(II)-bis{1,2,3-triazolylidene}pyridine pincer complexes*, *Journal of Organometallic Chemistry* **2017**, 845, 30–37;
11. Wylie, W.N.O.; Morris, R.H., *Ester Hydrogenation Catalyzed by a Ruthenium(II) Complex Bearing an N-Heterocyclic Carbene Tethered with an “NH₂” Group and a DFT Study of the Proposed Bifunctional Mechanism*, *ACS Catalysis* **2013**, 3 (1), 32–40;
12. Zhao, D.; Beiring, B.; Glorius, F., *Ruthenium–NHC-Catalyzed Asymmetric Hydrogenation of Flavones and Chromones: General Access to Enantiomerically Enriched Flavanones, Flavanols, Chromanones, and Chromanols*, *Angewandte Chemie International Edition* **2013**, 52 (32), 8454–8458;
13. Filonenko, G.A.; Cosimi, E.; Lefort, L.; Conley, M.P.; Copéret, C.; Lutz, M.; Hensen, E.J.M.; Pidko, E.A., *Lutidine-Derived Ru–CNC Hydrogenation Pincer Catalysts with Versatile Coordination Properties*, *ACS Catalysis* **2014**, 4 (8), 2667–2671;
14. Filonenko, G.A.; Aguila, M.J.B.; Schulpen, E.N.; van Putten, R.; Wiecko, J.; Müller, C.; Lefort, L.; Hensen, E.J.M.; Pidko, E.A., *Bis-N-heterocyclic Carbene Aminopincer Ligands Enable High Activity in Ru-Catalyzed Ester Hydrogenation*, *Journal of the American Chemical Society* **2015**, 137 (24), 7620–7623;
15. Ruiz, J.; Perandones, B.F.; García, G.; Mosquera, M.E.G., *Synthesis of N-Heterocyclic Carbene Complexes of Manganese(I) by Coupling Isocyanide Ligands with Propargylamines and Propargylic Alcohols*, *Organometallics* **2007**, 26 (23), 5687–5695;
16. Ruiz, J.; Berros, Á.; Perandones, B.F.; Vivanco, M., *NHC–manganese(I) complexes as carbene transfer agents*, *Dalton Transactions* **2009**, 35, 6999–7007;

17. Buhaibeh, R.; Filippov, O.A.; Bruneau-Voisine, A.; Willot, J.; Duhayon, C.; Valyaev, D.A.; Lugan, N.; Canac, Y.; Sortais, J.B., *Phosphine-NHC Manganese Hydrogenation Catalyst Exhibiting a Non-Classical Metal-Ligand Cooperative H₂ Activation Mode*, *Angewandte Chemie International Edition* **2019**, *58* (20), 6727–6731;
18. Pinto, M.; Friães, S.; Franco, F.; Lloret-Fillol, J.; Royo, B., *Manganese N-Heterocyclic Carbene Complexes for Catalytic Reduction of Ketones with Silanes*, *ChemCatChem* **2018**, *10* (13), 2734–2740;
19. Franco, F.; Pinto, M.F.; Royo, B.; Lloret-Fillol, J., *A Highly Active N-Heterocyclic Carbene Manganese(I) Complex for Selective Electrocatalytic CO₂ Reduction to CO*, *Angewandte Chemie International Edition* **2018**, *57* (17), 4603–4606;
20. Occhipinti, G.; Bjørsvik, H.R.; Törnroos, K.W.; Fürstner, A.; Jensen, V.R., *The First Imidazolium-Substituted Metal Alkylidene*, *Organometallics* **2007**, *26* (18), 4383–4385;
21. Berkessel, A.; Schubert, T.J.S.; Müller, T.N., *Hydrogenation without a Transition-Metal Catalyst: On the Mechanism of the Base-Catalyzed Hydrogenation of Ketones*, *Journal of the American Chemical Society* **2002**, *124* (29), 8693–8698;
22. Fujii, A.; Hashiguchi, S.; Uematsu, N.; Ikariya, T.; Noyori, R., *Ruthenium(II)-Catalyzed Asymmetric Transfer Hydrogenation of Ketones Using a Formic Acid-Triethylamine Mixture*, *Journal of the American Chemical Society* **1996**, *118* (10), 2521–2522;
23. Demmans, K.Z.; Ko, O.W.K.; Morris, R.H., *Aqueous biphasic iron-catalyzed asymmetric transfer hydrogenation of aromatic ketones*, *RSC Advances* **2016**, *6* (91), 88580–88587;
24. Wu, X.; Li, X.; Hems, W.; King, F.; Xiao, J., *Accelerated asymmetric transfer hydrogenation of aromatic ketones in water*, *Organic & Biomolecular Chemistry* **2004**, *2* (13), 1818–1821.



Chapter



Mn-mediated C-C bond formation:

alkoxycarbonylation of organoboranes

.....

“The task is not so much to see what no one has yet seen, but to think what nobody has yet thought, about that which everybody sees.”

Erwin Schrödinger

(Contested. Potentially attributable to Arthur Schopenhauer.)

Abstract

Alkoxycarbonylations are important and versatile reactions that result in the formation of a new sp^2 - sp^2 or sp^2 - sp^3 carbon-carbon bond and the introduction of a carbonyl group to an organic substrate. In this chapter we describe a new and halide-free alkoxycarbonylation reaction that does not require the application of an external carbon monoxide atmosphere. Instead, manganese carbonyl complexes and organo(alkoxy) borate salts react to form ester products that contain the target C-C bond.

The required organo(alkoxy)borate salts were conveniently generated from the stoichiometric reaction of an organoborane and an alkoxide salt, and could be telescoped and used without further purification. The new alkoxycarbonylation enabled the formation of aromatic and aliphatic esters and gave complete control over the ester's alkoxy substitution. This included methyl and ethyl esters, but also *tert*-butyl and phenyl esters that are typically more difficult to prepare. A plausible reaction mechanism was proposed on the basis of combined stoichiometric reactivity studies, *in situ* spectroscopy, and quantum chemical calculations. The described reactivity of alkoxides with Mn^I carbonyl complexes may—besides its future synthetic potential—constitute a plausible deactivation pathway in reduction catalysis with Mn^I.

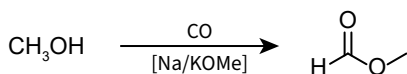
This chapter has been published as:

R. van Putten, G.A. Filonenko, A.M. Krieger, M. Lutz, E.A. Pidko,
Organometallics **2021**, *40*, 674–681

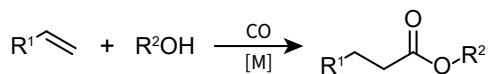
4.1 Introduction

The alkoxy carbonylation is an important and diverse synthetic method that enables the preparation of esters and other carbonyl compounds.¹ It finds widespread industrial application in the synthesis of methyl formate, where methanol, carbon monoxide, and a methoxide salt are reacted at elevated temperature and pressure (**Figure 4.1a**).^{2–3} The scope of alkoxy carbonylations has expanded considerably over the years. These reactions vary by the substrate type, the metal catalyst, and/or the source of carbon monoxide. Selected examples are presented in **Figure 4.1b–c**.

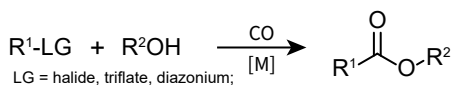
a) Industrial methyl formate synthesis



b) Reppe carbonylation (*hydroesterification*)



c) Alkoxy carbonylation of aryls/alkyls



d) Alkoxy carbonylation of organoboranes

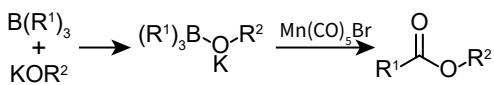


Figure 4.1. Selection of alkoxy carbonylation reactions available in the open literature. **a)** Industrial carbonylation of methanol to methyl formate. **b)** Reppe carbonylation (also called *hydroesterification*) of olefins. **c)** Alkoxy carbonylation of aryls and alkyls. These reactions require the presence of a leaving group on the substrate. **d)** Alkoxy carbonylation of organoboranes, as described in this chapter.

Alkoxy carbonylation reactions were first developed by BASF in the 1930s.⁴ This transformation—now known as the Reppe carbonylation—involves the reaction of alkenes or alkynes with CO and a nucleophile (water, alcohols, or acids) to produce carboxylic acids, esters, and anhydrides, respectively (**Figure 4.1b**).^{5–6} The original Reppe reaction was catalysed by the highly toxic and volatile $\text{Ni}(\text{CO})_4$. This undesirable nickel compound has since been replaced with less acutely dangerous alternatives. Currently it is possible to perform the alkoxy carbonylation reaction with a wide range of transition metal catalysts (Mn, Fe, Co, Ni, Mo, Ru, Rh, Pd, Ir, Pt).^{1,4,6–7} The substrate scope of these alkoxy carbonylations has also expanded considerably since its initial discovery in the 20th century. For example, it is now commonplace to perform the reaction with aryl and alkyl halides^{8–11}, alternative leaving groups^{12–15}, epoxides¹⁶, allyl phosphates and acetates¹⁷, or amines¹⁸ (**Figure 4.1c**).

Further improvements to the method have come in the form of metal-free reactions^{13,19} and reactions that do not require an external CO atmosphere. The latter is essential because it can be difficult or simply undesirable to work with

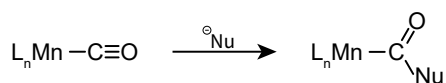
gaseous carbon monoxide. In these situations it can be more attractive to generate the required CO *in situ*, from, *e.g.*, metal carbonyl complexes under thermal or irradiative conditions^{20–24}, formates or formic acid^{25–27}, or from carbon dioxide.^{28–29} These technological advances have greatly improved the utility of carbonylation chemistries and have driven its practical adoption in organic synthesis.

This chapter describes our discovery of the alkoxyacylation of organoboranes in the presence of Mn^I carbonyl compounds (**Figure 4.1d**). The new reactivity was found during our study of Mn^I hydrogenation catalysts in the presence of inorganic bases. We found that the reaction of organoboranes and alkoxides produces an organo(alkoxy)borate anion that is reactive towards Mn^I carbonyl complexes. The reaction of such an activated borate and Mn(CO)₅Br produced an ester that contained a new *sp*²-*sp*² or *sp*²-*sp*³ carbon-carbon bond. The reaction mechanism of this new chemistry was investigated with combined experimental reactivity tests, *in situ* spectroscopy, and quantum chemical calculations.

4.2 Reaction discovery

Our study of the carbonylation activity of Mn(CO)₅Br was preceded by DFT calculations from our group. These calculations suggested that nucleophiles (*e.g.*, hydrides and alkoxides) could react with Mn^I-bound carbonyl ligands and that this interaction would produce Mn-formyl and/or Mn-acyl complexes (**Figure 4.2a**). This finding was then supported by a literature study, which indicated that such reactivity had indeed been observed before.^{30–35}

a) Nucleophilic attack on Mn^I carbonyl complexes



b) Alkoxyacylation with Mn(CO)₅Br

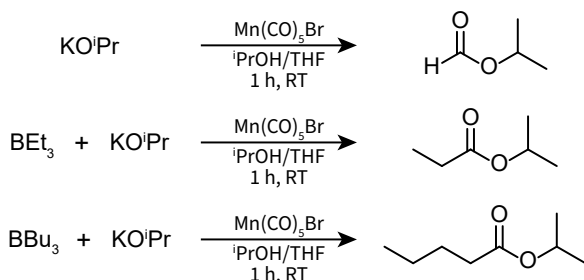
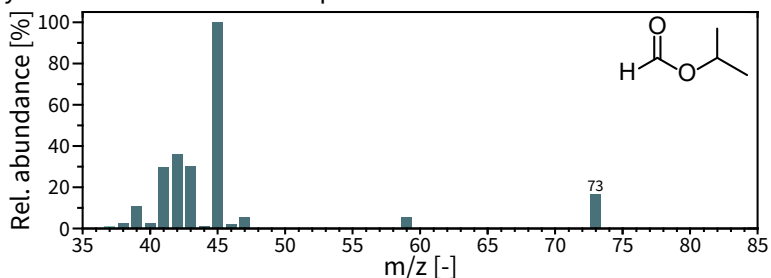


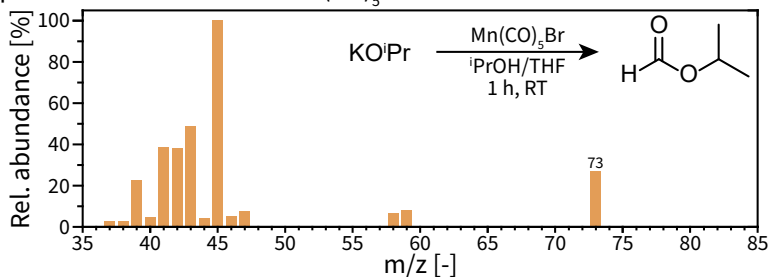
Figure 4.2. a) Nucleophilic attack on Mn^I carbonyls, leading to Mn-formyl and Mn-acyl complexes. b) New reactions described in this chapter that produced isopropyl formate and aliphatic isopropyl esters.

Experiments were performed to substantiate the computational results. $\text{Mn}(\text{CO})_5\text{Br}$ was added to a 2-propanol/THF solution that contained five equivalents of KO^iPr . This resulted in a fast reaction that was accompanied by a colour change from yellow to golden orange, effervescence of carbon monoxide, and the formation of a fine, white precipitate. The crude reaction mixture was analysed with ^1H NMR spectroscopy and GC-MS. Isopropyl formate was detected with both analytical methods (**Figure 4.2b**). Its formyl group was observed as a sharp singlet in the ^1H NMR spectrum with a characteristic chemical shift of $\delta = 7.96$ ppm ($\text{THF-}d_6$). The GC-MS chromatogram featured a peak that had an identical retention time and mass spectrum compared to that of a reference sample of isopropyl formate (**Figure 4.3a–b**). An experiment with isotopically labelled $\text{KO}^i\text{Pr-}d_7$ in $^i\text{PrOD-}d_8$ confirmed that the formyl hydrogen atom of the isopropyl formate product originated from 2-propanol, and not, *e.g.*, from THF (**Figure 4.3c** and **Table 4.1**).

a) Isopropyl formate reference EI-MS spectrum



b) EI-MS spectrum after reaction of $\text{Mn}(\text{CO})_5\text{Br}$ and KO^iPr



c) EI-MS spectrum after reaction of $\text{Mn}(\text{CO})_5\text{Br}$ and $\text{KO}^i\text{Pr-}d_7$

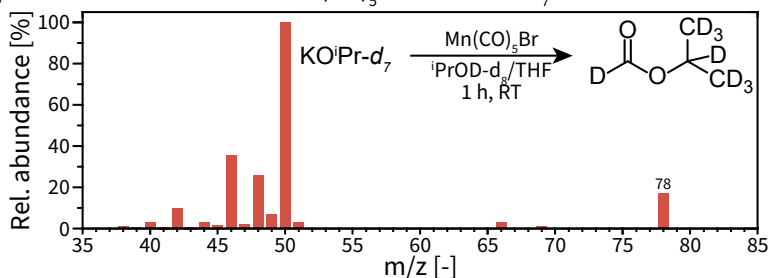


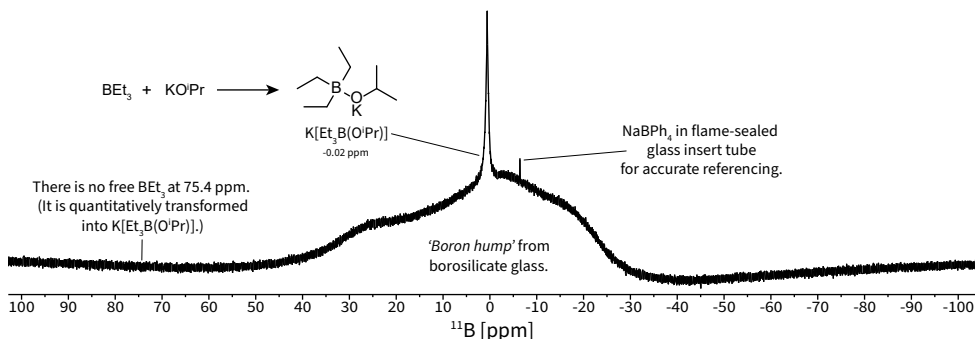
Figure 4.3. EI-MS spectra of isopropyl formate reference (**a**), after reaction of KO^iPr with $\text{Mn}(\text{CO})_5\text{Br}$ (**b**), and after reaction with $\text{KO}^i\text{Pr-}d_7$ with $\text{Mn}(\text{CO})_5\text{Br}$.

Table 4.1. Expected mass fragments for isotopologues of isopropyl formate.

Expected fragment of isotopologue (lost fragment)			
$[C_3H_7O]^+$ (-CHO)	59.1	66.1	
$[C_3H_7O]^+$ (-CDO)			66.1
$[C_3H_5O_2]^+$ (-CH ₃)	73.1		
$[C_3H_5O_2]^+$ / $[C_3D_5O_2]^+$ (-CD ₃)		77.1	78.1
$[C_3H_7]^+$ / $[C_3D_7]^+$ (-CD/DO ₂)	43.1	50.1	50.1

The new alkoxyacylation chemistry was serendipitously discovered after the implementation of a small procedural change. The solution of KO^iPr in iPrOH had thus far been obtained from the reaction of metallic potassium and isopropanol. This procedure worked well and provided clean KO^iPr , but required the undesirable handling of elemental potassium. When the solution was more conveniently prepared from $KHBET_3$ and 2-propanol, the anticipated isopropyl formate product could no longer be observed. Instead, a new product formed, which was identified as isopropyl propionate (**Figure 4.2b**). A separate experiment where tributylborane was added to the solution of KO^iPr led to the detection of isopropyl pentanoate. This confirmed that the alkyl chain of the newly formed ester had been transferred from the trialkylborane.

The ester was formed to a substantially lesser extent if triethylborane and the isopropoxide base were not pre-contacted before their reaction with the Mn complex. This suggested the involvement of the triethyl(isopropoxy)borate anion instead of free BEt_3 . We found that these anions were formed instantaneously from the stoichiometric room temperature reaction of the organoborane and the alkoxide salt (**Figure 4.4**). This reaction led to a large shift in the ^{11}B NMR spectrum: the $K[Et_3B(O^iPr)]$ adduct was observed at -0.02 ppm, whereas unassociated BEt_3 appeared at 75.4 ppm.

**Figure 4.4.** Formation of potassium triethyl(isopropoxy)borate and its corresponding ^{11}B NMR spectrum (128 MHz, $THF-d_6$).

4.3 Preparation of organometallic intermediates

We wanted to understand this new chemistry and first attempted to prepare the major organometallic products formed from the reaction of $\text{Mn}(\text{CO})_5\text{Br}$ and the alkoxide base. These experiments revealed that the outcome of the reaction strongly depended on the exact stoichiometry of the reagents (**Figure 4.5**).

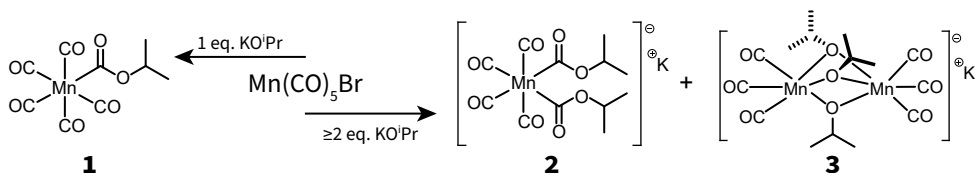


Figure 4.5. Preparation of Mn carbonyl complexes **1**, **2**, and **3**.

The equimolar (room temperature) reaction of $\text{Mn}(\text{CO})_5\text{Br}$ and KO^iPr in THF fully consumed the starting materials and predominantly formed Mn-acyl complex **1**, as well as $\text{Mn}_2(\text{CO})_{10}$, CO, and KBr (**Figure 4.5**). Compound **1** and $\text{Mn}_2(\text{CO})_{10}$ had very similar chemical properties; both were reactive and volatile solids with a practically identical solubility profile. We found that complex **1** was stable in solution for at least several days, but decomposed under high-vacuum or during column chromatography. This instability prevented us from obtaining an analytically pure (*i.e.*, $\text{Mn}_2(\text{CO})_{10}$ -free) sample of Mn-acyl **1**.

Compound **1** was instead characterised spectroscopically with ^1H NMR and solution FTIR (**Figure 4.6a**). ^1H NMR and FTIR indicated that **1** was a manganese alkoxy carbonyl complex that had a characteristic septet in the ^1H NMR spectrum at $\delta = 5.06$ ppm and a relatively intense $\nu(\text{C}=\text{O})$ band at 1642 cm^{-1} in the infrared spectrum. These values cohered well with the spectroscopic signatures for similar Mn-acyl complexes.^{36–38} Compound **1** possessed an additional CO ligand compared to the starting material, which presumably originated from carbon monoxide that was released into the reaction vessel during the reaction.

The reaction of $\text{Mn}(\text{CO})_5\text{Br}$ with two or more equivalents of KO^iPr resulted in a mixture of potassium salts of Mn-dialkoxycarbonyl **2** and alkoxide-bridging Mn- μ_2 -isopropoxo-dimer **3** (**Figure 4.5**). Compounds **2** and **3** were characterised with $^1\text{H}/^{13}\text{C}$ NMR, FTIR, ESI-MS, and elemental analysis. We found that complex **2** was unstable in solution and fully decomposed over the course of several days. Such degradation has been observed before for similar manganese and rhenium complexes^{33,39}, and is presumably induced by both heat and light. Attempted crystallisation at $-80\text{ }^\circ\text{C}$ in the dark did not appreciably stop the decomposition of Mn-diacyl **2**. Complex **3** was fully stable and crystals suitable for single-crystal X-ray diffraction analysis were obtained by slow vapour diffusion crystallisation.

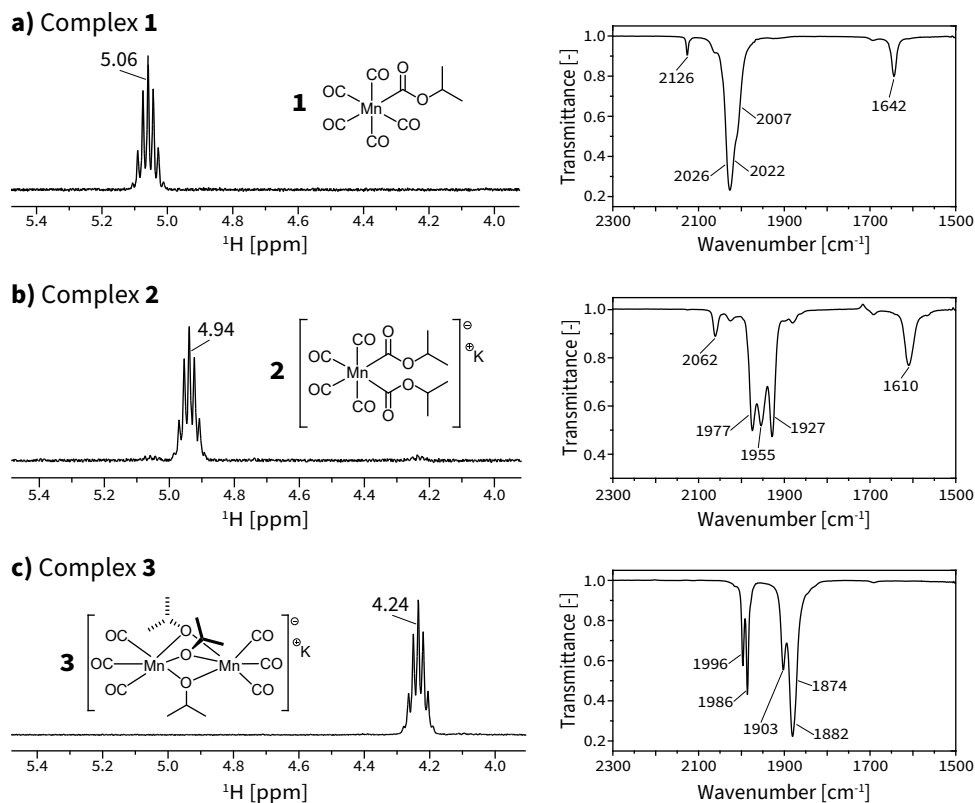


Figure 4.6. Representative ^1H NMR 'fingerprint' region and solution FTIR spectra for complexes **1-3**.

Complex **2** featured one $\text{CH}(\text{CH}_3)_2$ septet in the ^1H NMR spectrum at 4.94 ppm (**Figure 4.6b**), which suggested that the two isopropoxycarbonyl groups in **2** were chemically equivalent. This was further supported by a single $\text{C}=\text{O}$ stretching band in the FTIR spectrum at 1610 cm^{-1} . The FTIR spectrum of **2** additionally contained a medium intensity band at 2062 cm^{-1} , and three strong bands at 1977 , 1955 , and 1927 cm^{-1} .³³

The isopropoxy moieties in **3** also were equivalent in solution and were observed with ^1H NMR as one (septet) resonance at $\delta = 4.24\text{ ppm}$ (**Figure 4.6c**). The FTIR spectrum of **3** featured five sharp and intense peaks at 1996 , 1986 , 1903 , 1882 , and 1874 cm^{-1} . Single-crystal X-ray structure determination revealed that in the solid state **3** existed as a three-dimensional coordination network (**Figure 4.7**). The Mn and K atoms were six-coordinated in this particular arrangement. Two isopropoxy fragments acted as bridging ligands, while the third ligand between the symmetry-related Mn^{I} tricarbonyl centres was provided by KO^iPr .

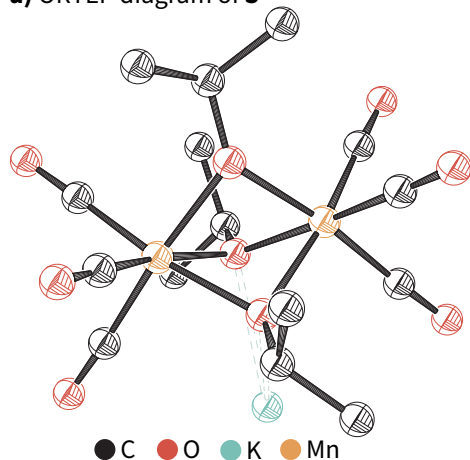
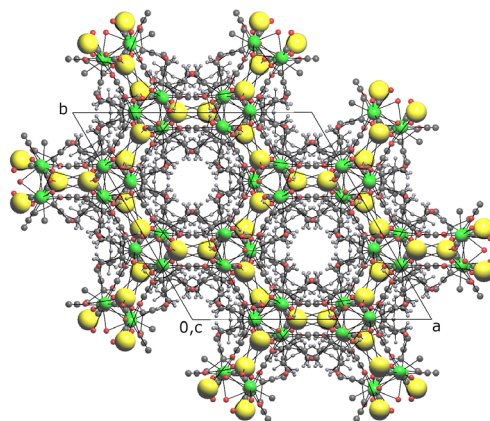
a) ORTEP diagram of **3****b) Rendering of 3D coordination network**

Figure 4.7. **a)** Simplified ORTEP diagram of **3**. Hydrogen atoms were omitted for clarity. Key: C (black), O (red), K (turquoise), Mn (orange). **b)** Rendering of the 3D coordination network of structure **3** in the solid state. Key: C (grey), O (red), K (yellow), Mn (green).

4.4 Stoichiometric reactivity studies

The new complexes provided context for further spectroscopic and reactivity studies. We investigated the stoichiometric reactivity of the materials to better understand the new alkoxy carbonylation chemistry (**Figure 4.8**). Complexes **1**, **2**, and **3** were each contacted with approximately one equivalent of BEt_3 , KO^iPr , and KHBet_3 , and the resulting $^1\text{H}/^{11}\text{B}$ NMR and FTIR spectra were recorded.

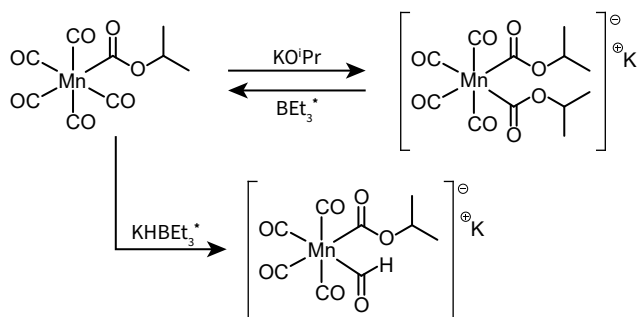


Figure 4.8. Summary of reactivity of complexes **1** and **2** towards BEt_3 , KO^iPr , and KHBet_3 . Non-reactive mixtures are not shown. Complex **3** was inert under all conditions. Reactions labelled with an asterisk decomposed to $\text{KMn}(\text{CO})_5$.

Addition of triethylborane to a solution of **1** or **3** in THF did not lead to an observable reaction; the spectra remained unchanged after the addition of the borane. Manganese diacyl **2** transformed into monoacyl **1** upon treatment with BEt_3 and ultimately decomposed to $\text{KMn}(\text{CO})_5$ (**Figure 4.8**). Such decomposition is similar to that reported by Gladysz and co-workers for the decomposition of $\text{Li}[\text{Mn}(\text{acyl})(\text{formyl})(\text{CO})_4]$ with BEt_3 , although we did not observe organic products with GC-MS after decomposition to the manganate salt (*i.e.*, Mn^{I}).³⁵

The reaction of **1** with potassium isopropoxide resulted in a mixture of dialkoxycarbonyl **2** and Mn-isopropoxo-dimer **3** (**Figure 4.8**). We therefore propose that compound **2** originated from the sequential addition of KO^iPr to $\text{Mn}(\text{CO})_5\text{Br}$ and then to **1**. Treatment of **2** with KO^iPr led to **3**. The Mn-isopropoxo-dimer itself was inert towards the alkoxide base and no obvious reaction took place.

The complexes were finally brought into contact with one equivalent of KBET_3 to test if they could sustain the formation of Mn-formyls. Addition of the hydride reagent to **1** indeed led to a new anionic $\text{Mn}(\text{acyl})(\text{formyl})$ complex (**Figure 4.8**). This new compound was unstable and decomposed over the course of approximately a day.³⁵ Compounds **2** and **3** were unreactive towards the hydride reagent. This suggested that the remaining three or four carbonyl ligands of these complexes were significantly less susceptible to nucleophilic attack.

In summary, Mn^{I} carbonyl complexes generally sustained two sequential nucleophilic attacks on their CO ligands. These reactions led to the formation of anionic acyl or formyl complexes. The Mn^{I} centres with two anionic ligands were unstable and underwent thermal or light-induced decomposition to the potassium pentacarbonylmanganate salt. This decomposition process was accelerated by the addition of trialkylboranes, although the underlying reaction mechanism is not completely understood.³⁵

4.5 Mechanistic investigations

We deduced that the isopropyl propionate ester was probably formed *via* one of two pathways (**Figure 4.9**). Despite the apparent similarity of these two mechanisms, they differ in the order in which the reaction steps take place. In route 1, the alkoxide fragment is transferred to the Mn centre, which leads to an Mn-isopropoxycarbonyl complex similar to Mn-acyl **1** or **2**. Isopropyl propionate is formed after alkyl transfer from BEt_3 to the Mn complex. In route 2 this sequence is reversed: the reaction starts with the alkylation of the CO ligand, which results in a propionyl Mn carbonyl complex. The alkylation step is followed by a nucleophilic attack of the alkoxide on the acyl carbon that results in liberation of the ester.

We speculate that the first mechanism is unlikely because the reaction of compounds **1** and **2** with BEt_3 did not produce any detectable organic products. However, at this moment we do not have definitive evidence against this pathway. (It is for example possible that the reaction proceeds *via* an unstable intermediate that could not be observed.) The pathway described by route 2 has both literature precedent and experimental support.

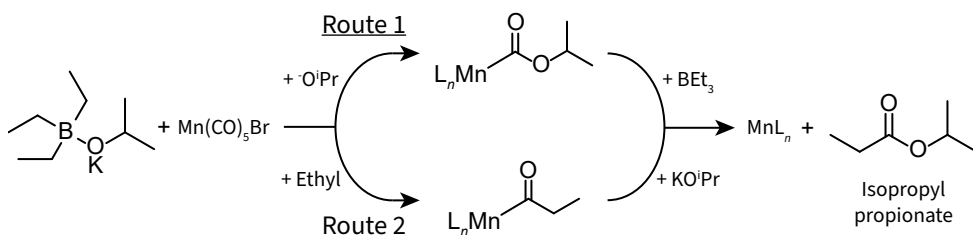


Figure 4.9. Proposed order of events that lead to isopropyl propionate. Route 1: reaction of L_nMn with KO^iPr and subsequent alkyl transfer. Route 2: reaction of L_nMn with BEt_3 and subsequent nucleophilic alkoxide attack.

Miguel and co-workers have previously investigated the intramolecular carboboration reaction of Mn^{I} carbonyl complexes (**Figure 4.10**).⁴⁰ This reaction led to the intramolecular transfer of an alkyl group from a trialkylborane to a nearby Mn^{I} carbonyl ligand. The authors concluded that the alkyl migration was induced by the coordination of triethylborane to an Mn-alkoxide and carbonyl. This complexation produced a tetrasubstituted borate anion that was identified as the critical reactive intermediate. The borate anion was highly reactive and closely resembles the organo(alkoxy)borate substrate that is described in this work. In their case the alkoxide was part of a bidentate O,N ligand, while in this work it is an independent component of the reaction mixture.

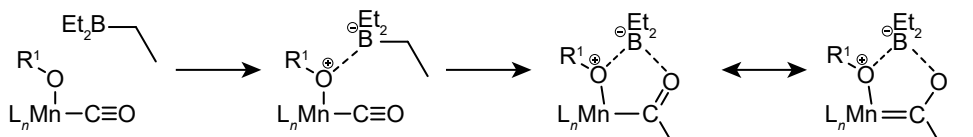


Figure 4.10. Intramolecular carboboration reaction of an Mn-alkoxycarbonyl, as reported by Álvarez *et al.*⁴⁰ This reaction produces boroxycarbenes.

These considerations enabled us to propose a reaction mechanism for the Mn-mediated alkoxy carbonylation of organoboranes. Its feasibility was supported by DFT calculations at the PBE0-D3(BJ)-SMD(THF)/6-311+g(d,p) level of theory (**Figure 4.11**).

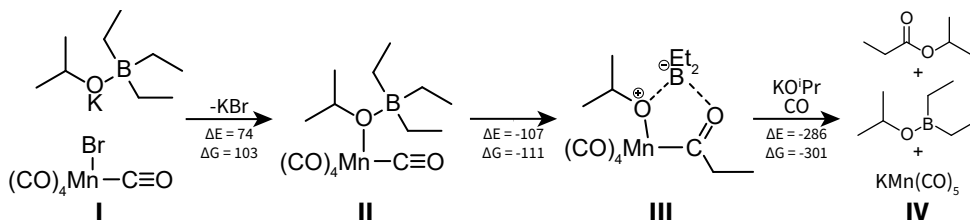


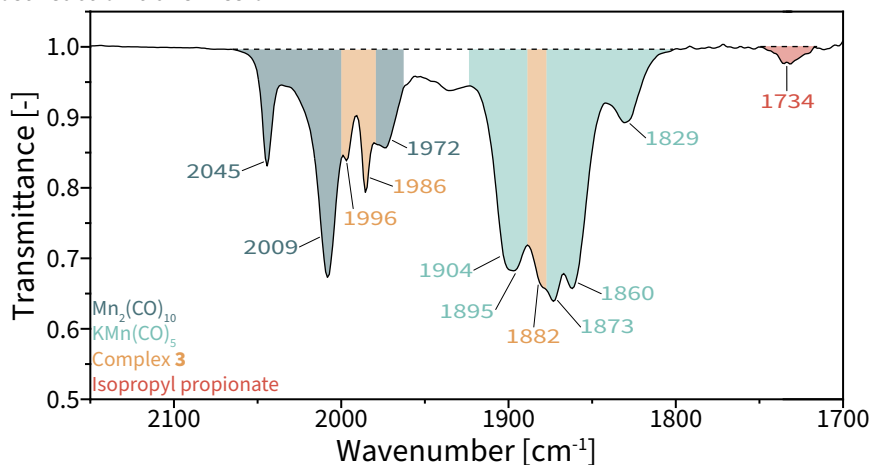
Figure 4.11. Proposed reaction mechanism for the Mn-mediated alkoxyacylation of organoboranes. DFT calculations were performed at the PBE0-D3(BJ)-SMD(THF)/6-311+g(d,p) level of theory at 298.15 K in THF. ΔE and ΔG represent the reaction energy and Gibbs free energy changes in kJ mol^{-1} .

The reaction starts with the association of $\text{Mn}(\text{CO})_5\text{Br}$ and potassium triethyl(isopropoxy)borate (species I). This produces Mn-alkoxy adduct II and KBr in a mildly endergonic reaction (103 kJ mol^{-1}). The intramolecular reaction then takes place, in which an alkyl group is transferred from BEt_3 to the nearby Mn-carbonyl to form III ($\Delta G = -111 \text{ kJ mol}^{-1}$). The target isopropyl propionate ester is liberated from III after a nucleophilic alkoxy attack on the acyl carbon, and the Mn^{+1} centre is reduced to Mn^1 . We propose that the coordinatively-unsaturated Mn centre (*i.e.*, $\text{KMn}(\text{CO})_4$) then rapidly abstracts CO from the reaction mixture and releases diethyl(isopropoxy)borane. The overall reaction is strongly exergonic: the total Gibbs free energy change amounts to -309 kJ mol^{-1} .

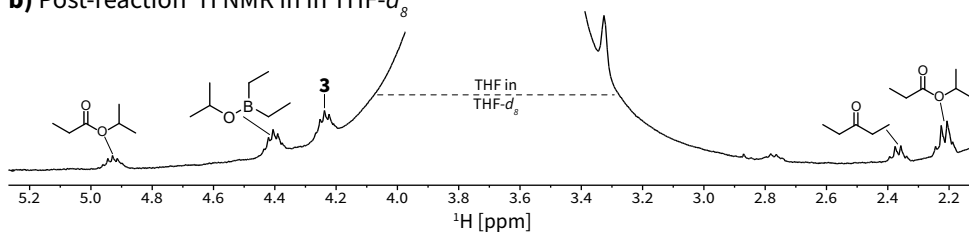
The proposed reaction mechanism rationalises why ester formation was hampered when the organoborane and alkoxy were not pre-contacted before their reaction with the manganese complex. We found that the organoborane's alkyl group and the accepting carbonyl ligand had to be in close proximity for the alkyl transfer to succeed. Such pre-activation was achieved with the sequential formation of $\text{K}[\text{Et}_3\text{B}(\text{O}^i\text{Pr})]$, followed by its reaction with $\text{Mn}(\text{CO})_5\text{Br}$ (species II in **Figure 4.11**). Without this pre-coordination the free alkoxy probably reacted with the metal centre before the required spatial configuration could be achieved. (The independent reactivity of $\text{Mn}(\text{CO})_5\text{Br}$ towards alkoxydes was described in **Chapter 4.3** of this dissertation. These reactions led to the formation of Mn-acyl species that were unreactive towards organoboranes and did not produce the isopropyl propionate ester.)

Our mechanistic proposal was supported by additional spectroscopic evidence, obtained approximately one hour after the reaction was started. Post-reaction mixtures were analysed with FTIR and NMR spectroscopy (**Figure 4.12**). Infrared spectroscopy revealed the presence of $\text{KMn}(\text{CO})_5$, as well as $\text{Mn}_2(\text{CO})_{10}$, Mn-isopropoxy-dimer **3**, and isopropyl propionate (**Figure 4.12a**). These products were also detected with ^1H NMR. ^{11}B NMR further clearly indicated the presence of the anticipated diethyl(isopropoxy)borane product at $\delta = 53.2 \text{ ppm}$. 3-Pentanone was detected as a side-product in ^1H NMR and with GC-MS.

a) Post-reaction transmission FTIR in THF



b) Post-reaction ^1H NMR in in THF- d_8



c) Post-reaction ^{11}B NMR in in THF- d_8

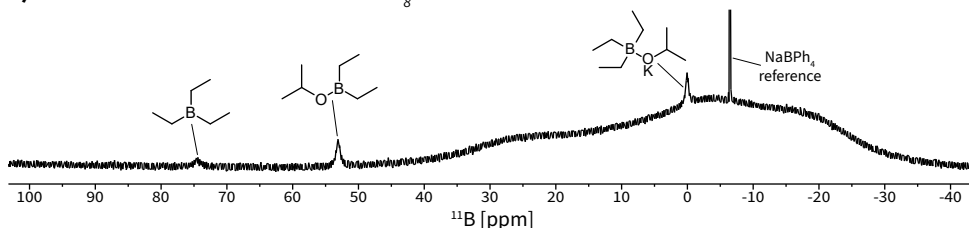


Figure 4.12. Spectroscopic support for the proposed reaction mechanism. Conditions: $\text{Mn}(\text{CO})_5\text{Br}$ + 1 eq. $\text{K}[\text{Et}_3\text{B}(\text{O}^i\text{Pr})]$ + 1 eq. KO^iPr in THF. Spectra were recorded after ~ 1 h at room temperature. **a)** Solution FTIR transmission spectrum after reaction in THF (~ 0.5 mg Mn ml^{-1}). **b)** ^1H NMR spectrum after reaction in THF- d_8 (400 MHz). **c)** ^{11}B NMR spectrum after reaction in THF- d_8 (128 MHz).

The feasibility of the proposed product liberation step was investigated with a dedicated experiment. The reaction of an independently prepared sample of propionyl manganese pentacarbonyl with potassium isopropoxide indeed produced the expected isopropyl propionate ester and the $\text{KMn}(\text{CO})_5$ salt (**Figure 4.13**).³¹ The FTIR spectrum also revealed the presence of another (unidentified) manganese carbonyl complex that had an IR spectrum similar to that of Mn-diacyl complex **2**. We therefore speculate that the unidentified species was the corresponding anionic $\text{K}[\text{Mn}(\text{-propionyl})(\text{isopropoxycarbonyl})(\text{CO})_4]$ complex.

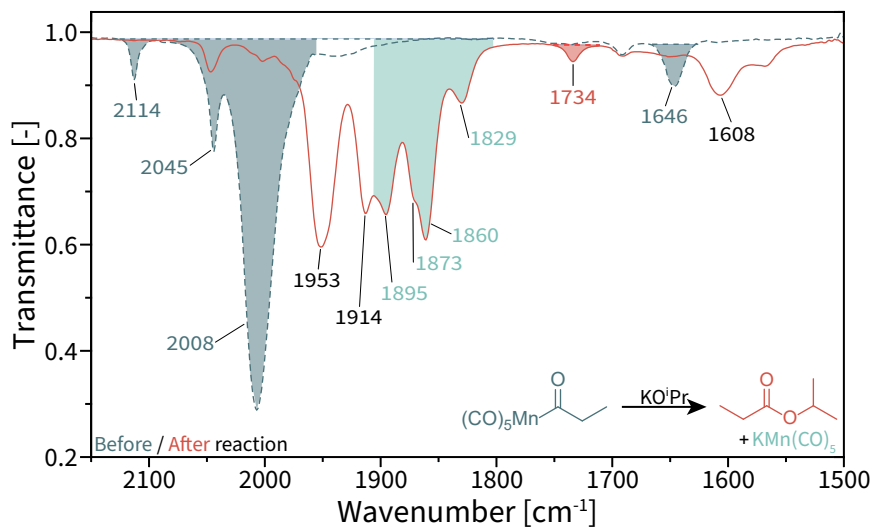


Figure 4.13. FTIR spectrum of independently prepared propionyl manganese pentacarbonyl before (dashed green line) and after reaction with KO^tPr (solid red line).

4.6 Reaction optimisation and scope

Under standardised conditions the alkoxy carbonylation reaction produced isopropyl propionate in only 4% yield. 3-Pentanoate was detected in 6% yield. These yields were low, and we therefore sought to improve the performance of the new chemistry. We screened a number of parameters that potentially impacted the reaction outcome (**Table 4.2**). Addition of a second equivalent of KO^tPr—as suggested by the proposed mechanism—resulted in a significantly improved ester yield of 38%. Further addition of base did not increase the yield but instead produced Mn-isopropoxo-dimer **3**. The reaction did not perform significantly better under a CO atmosphere. This is probably because the Mn centre not only lost CO in the reaction, but also got reduced to the -1 oxidation state. Alternative addition sequences, solvents, or reaction temperature did not lead to improved ester yields. Our control experiments did not produce the ester or ketone product, which suggests that the reaction indeed is driven by the unique combination of reagents and conditions that are described in this chapter.

We finally explored the scope of the novel alkoxy carbonylation reaction and performed a series of experiments that varied the transition metal carbonyl, boron substrate, and nucleophile salt (**Figure 4.14**). The reactions were classified by their ability to form the anticipated ester product.

Table 4.2. Summarised results of reaction optimisation experiments.^{a)}

Entry	Conditions	Ester yield [%] ^{b)}	Ketone yield [%] ^{b)}
1	Reference	4	6
2	+ 1 eq. KO ⁱ Pr ^{c)}	38	13
3	+ 4 eq. KO ⁱ Pr ^{c)}	1	0
4	5 eq. Mn(CO) ₅ Br ^{d)}	7	6
5	CO atmosphere (3 bar)	17	7
6	+ 1 eq. KO ⁱ Pr, dropwise ^{c,e)}	16	7
7	+ 1 eq. KO ⁱ Pr, BEt ₃ later ^{c,f)}	4	8
8	+ 1 eq. KO ⁱ Pr, at -84 °C ^{b,g)}	3	3
9	+ 1 eq. KO ⁱ Pr, in Et ₂ O ^{b)}	8	6
10	+ 1 eq. KO ⁱ Pr, in benzene ^{b)}	7	7
11	+ 1 eq. KO ⁱ Pr, in 2-propanol ^{b)}	10	5
12	+ 1 eq. KO ⁱ Pr, in DMSO ^{b)}	8	1
13	No Mn(CO) ₅ Br	0	0
14	No BEt ₃	0	0
15	No KO ⁱ Pr	0	0
16	No Mn, + 1 eq. KO ⁱ Pr, CO atmosphere ^{c,e)}	0	0

a) Reference conditions: 0.1 mmol pre-contacted K[Et₃B(OⁱPr)], 0.1 mmol Mn(CO)₅Br, 40 μl *n*-dodecane, Σ 2.0 ml THF, 16 h, room temperature. **b)** Yields were determined by GC-FID using *n*-dodecane as an internal standard. **c)** *i.e.*, 0.1 mmol K[Et₃B(OⁱPr)] + *x* eq. KOⁱPr. **d)** 0.5 mmol Mn(CO)₅Br. **e)** Added over ~1 min. **f)** BEt₃ added after 5 min. **g)** Reaction was performed at -84 °C (LN₂+EtOAc) for 3 h and was slowly warmed to room temperature.

Mn₂(CO)₁₀ and Co₂(CO)₈ were capable of the alkoxycarbonylation reaction of organoboranes, but performed significantly worse than Mn(CO)₅Br and gave isopropyl propionate in 4% and 16% yield, respectively. Mn piano stool complexes Mn(cp)(CO)₃ and Mn(Me-cp)(CO)₃ were inactive under these conditions, as were all other transition metal carbonyl complexes that were included in our study. KMn(CO)₅ (which was identified as a product of the reaction) did not support the formation of organic products.

The reaction with alternative boron substrates was successful for BBU₃ and BPh₃ and produced the anticipated aliphatic and aromatic isopropyl esters. Substitution of BEt₃ for the much more reactive AlEt₃ resulted in a 21% yield of isopropyl propionate (compared to 38% with BEt₃ under identical conditions). The use of boric esters and borates did not lead to ester formation. We speculate that these substrates were not sufficiently activated and could therefore not transfer one of their substituents to the Mn^I carbonyl.

Transition metal carbonyls					Substrates		Nucleophiles		
Group 6		Group 7			Group 8/9				
No Cr(CO) ₆	Yes Mn(CO) ₅ Br (38%)	Yes Mn ₃ (CO) ₁₀ (4%)	No KMn(CO) ₅	No Fe(CO) ₅	Yes BEt ₃ (38%)	Yes AlEt ₃ (21%)	Yes KOMe (14%)	Yes LiO ^t Bu (2%)	Yes KOPh (3%)
No Mo(CO) ₆	No Mn(cp)(CO) ₃	No Mn(Me-cp)(CO) ₃	No Ru ₃ (CO) ₁₂	No Ru ₃ (CO) ₁₂	Yes BBu ₃ (15%)	No B(OEt) ₃	Yes KOEt (22%)	Yes NaO ^t Bu (4%)	No NaSEt
No W(CO) ₆	No Re(CO) ₅ Cl	No Re ₂ (CO) ₁₀	Yes Co ₂ (CO) ₈ (16%)		Yes BPh ₃ (11%)	No NaBPh ₄	Yes KO ⁱ Pr (38%)	Yes KO ^t Bu (37%)	No KHMDS

Figure 4.14. Reaction scope exploration: effects of the transition metal carbonyl, boron substrate, and nucleophile salt. Mixtures were categorised by their capacity to form the anticipated ester product (GC-yields in parentheses). Conditions: 0.1 mmol pre-contacted (BEt₃/substrate + KOⁱPr/nucleophile), 0.1 mmol KOⁱPr/nucleophile, 0.1 mmol Mn(CO)₅Br/TM carbonyl, 40 μl *n*-dodecane, Σ 2.0 ml THF, 16 h, room temperature. Only one parameter was changed per experiment. Yields were determined by GC-FID using *n*-dodecane as an internal standard.

Alkoxy carbonylation with alternative alkoxide salts afforded the corresponding esters. This procedure worked for a variety of substitutions, including methyl, ethyl, *tert*-butyl, and phenyl esters. Although the yields of the presented alkoxy carbonylation cannot currently compete with more conventional synthetic strategies for the preparation of esters, it could still be a viable way to make challenging esters or organoboranes. Use of lithium and sodium *tert*-butoxide did result in ester formation, but gave a lower yield than when the potassium salt was used. The reaction with sodium thiolates (*i.e.*, sulphur analogues of alkoxides) or KHMDS did not produce the corresponding thioester or amide.

4.7 Conclusion

We have developed a new alkoxy carbonylation reaction that is based on the reactivity of Mn carbonyl complexes with organo(alkoxy)borate salts. These salts were conveniently generated from the stoichiometric reaction of organoboranes and alkoxides, and did not need to be purified or isolated before use. The described procedure enabled the formation of a variety of aliphatic and aromatic esters of diverse substitution, including phenyl and *tert*-butyl esters.

A series of new Mn^I complexes were synthesised and characterised, and their reactivity was studied. A reaction mechanism was proposed on the basis of stoichiometric reactivity studies, *in situ* spectroscopy, and DFT calculations. The new reaction probably proceeded *via* a two-step mechanism in which the alkyl or aryl group was first transferred to the nearby Mn-carbonyl. The organic product was then liberated after a nucleophilic alkoxide attack on the Mn-acyl carbon.

4.8 Experimental section

General considerations

All manipulations were, unless stated otherwise, performed under an inert atmosphere in an Ar-filled Inert glove box or using standard Schlenk techniques. Manipulations involving Mn complexes were performed in the dark or in amber glass to prevent exposure to light. Anhydrous solvents were dispensed from an Inert PureSolv solvent purification system or were dried using 3 or 4 Å molecular sieves. Solvents were degassed before use. Chemicals were purchased from Sigma-Aldrich, Strem, or TCI, and were dried and/or degassed before use. Air and/or moisture sensitive materials were stored in the glove box. Deuterated solvents were purchased from Eurisotop, dried using molecular sieves, degassed, and stored in the glove box.

NMR spectra were recorded on an Agilent 400-MR DD2 400 MHz spectrometer equipped with a 5 mm ONE NMR probe. ^1H and ^{13}C chemical shifts were referenced to residual solvent peaks (^1H : 3.58 ppm THF- d_8 , ^{13}C : 67.21 ppm THF- d_8). ^{11}B NMR spectra were referenced to a solution of NaBPh_4 in THF- d_8 (-6.42 ppm) inside a flame-sealed glass insert (see below). ^{55}Mn NMR was referenced *via* the IUPAC absolute chemical shift ($\Xi = 24.789218$). When ^1H NMR spectra could not be referenced to the residual solvent peak (*i.e.*, when protium-THF was present and/or measurements were performed with a PRESAT pulse sequence), spectra were referenced to the centre triplet resonance of NaBPh_4 in THF- d_8 inside the glass insert tube (6.84 ppm, itself referenced against THF- d_8 at 3.58 ppm). FTIR was measured in transmission mode on a Bruker Alpha II spectrometer with KBr or CaF_2 windows and 250 or 500 μm PTFE spacers (16 scans, 2 cm^{-1} resolution, approximately 0.5 mg Mn ml^{-1}). Peak locations were determined from second derivative maxima of measured spectra. ESI-MS was measured using a Thermo Scientific LTQ XL mass spectrometer (spray voltage 4.49 kV, capillary voltage 4.98 V, capillary temperature 275 °C). Elemental analyses were performed in duplo by Mikroanalytisches Laboratorium Kolbe (Oberhausen, Germany).

Internal referencing of ^{11}B NMR spectra with NaBPh_4

We found that external referencing or absolute referencing of ^{11}B NMR spectra was not sufficiently reliable for our application and resulted in ± 3 ppm deviations. Spectra were instead referenced to an 11.0 mg ml^{-1} solution of NaBPh_4 in THF- d_8 . This solution was located inside a 3.0 mm OD flame-sealed glass tube (Bruker® SampleJet) or in a flame-sealed capillary that was made from the tip of a glass Pasteur pipette. The glass insert tube was then placed inside the NMR tube together with the analyte solution. This method allowed consistent internal referencing without contacting the two solutions.

The solution of NaBPh₄ was itself referenced against the accepted standard of 15 wt% BF₃·OEt₂ in CDCl₃, which resulted in a chemical shift of $\delta = -6.42$ ppm for NaBPh₄. Note that this method *in principle* also could have been used with BF₃·OEt₂ directly. However, we decided against this because of its potential for releasing HF inside a glass tube, as well as the pronounced toxicity of BF₃ compared to NaBPh₄.

Synthetic procedures

Full characterisation for the compounds below is available in the electronic supporting information of the published work: *Organometallics* **2021**, *40*, 674–681, DOI: 10.1021/acs.organomet.0c00781.

CAUTION: Metal carbonyl complexes release poisonous and flammable carbon monoxide gas upon complexation!

Potassium isopropoxide

Inside the glove box, potassium metal (1.45 g, 37.1 mmol) was added to a Schlenk tube that contained a PTFE-coated magnetic stirring bar. The flask was capped with a rubber septum and was taken out of the glove box. While stirring 40 ml 2-propanol (31.4 g, 523.1 mmol) was slowly added under Ar flow. (**CAUTION: violent exothermic reaction that produces flammable hydrogen gas**).

The mixture was stirred for approximately one hour at room temperature until all potassium had reacted. Once the reaction was complete, excess 2-propanol was removed *in vacuo* and the mixture was heated to 70 °C to produce a lump of sticky, white solids. The lump was broken up inside the glove box and the flask was stirred and heated to 70 °C under vacuum ($\sim 5.0 \times 10^{-2}$ mbar) to purify the material by sublimation. The solids were broken up and sublimed until the title compound was obtained as a free-flowing white powder. Yield: 3.49 g.

¹H NMR (400 MHz, THF-*d*₈): δ 4.02 (sept, $J = 5.3$ Hz, CH(CH₃)₂, 1H), 1.01 (d, $J = 5.7$ Hz, CH(CH₃)₂, 6H).

¹H NMR (400 MHz, DMSO-*d*₆): δ 3.86 (sept, $J = 5.9$ Hz, CH(CH₃)₂, 1H), 0.91 (d, $J = 6.0$ Hz, CH(CH₃)₂, 6H).

Diethyl(isopropoxy)borane

Diethyl(isopropoxy)borane was prepared according to a literature procedure.⁴¹ The material was used as is and was used as a reference compound only.

¹H NMR (400 MHz, THF-*d*₈): δ 4.42 (sept, *J* = 6.0 Hz, CH(CH₃)₂, 1H), 1.18 (d, *J* = 6.1 Hz, CH(CH₃)₂, 6H), 0.97–0.80 (m, 10H, B(CH₂CH₃)₂, overlap with BEt₃).

¹¹B NMR (128 MHz, THF-*d*₈): δ 53.1 (s, br).

Potassium triethyl(isopropoxy)borate

Two methods were employed to produce THF solutions of K[Et₃B(OⁱPr)]: the reaction of KHBET₃ with excess 2-propanol (**Method A**), and the reaction of BEt₃ with KOⁱPr in THF (**Method B**).

¹H NMR (400 MHz, THF-*d*₈): δ = 3.76 (sept, CH(CH₃)₂, 1H, overlap with solvent), 0.98 (d, *J* = 6.0 Hz, CH(CH₃)₂, 6H), 0.71 (t, *J* = 7.6 Hz, B(CH₂CH₃)₃, 9H), -0.01 (q, *J* = 7.5 Hz, B(CH₂CH₃)₃, 6H).

¹¹B NMR (128 MHz, THF-*d*₈): δ -0.02 (s, br).

Method A – KHBET₃ + 2-propanol

Inside the glove box, 15 μl of a 1.0M solution of KHBET₃ (15 μmol) in THF was added to an NMR tube that contained 100 μl 2-propanol (1.3 mmol) in 400 μl THF-*d*₈ (**CAUTION: violent reaction that produces flammable hydrogen gas**). The mixture was shaken several times to release most of the H₂ gas. The solution of K[Et₃B(OⁱPr)] was used in follow-up studies without further purification.

Method B – BEt₃ + KOⁱPr

Inside the glove box, 2.0 ml of a 1.0 M solution of BEt₃ (2.0 mmol) in THF was added to a suspension of 196.4 mg KOⁱPr (2.0 mmol, 1 eq.) in 2.0 ml THF. The resulting 0.5 M K[Et₃B(OⁱPr)] solution was stable for extended time and was used without further purification.

Potassium pentacarbonylmanganate

$\text{KMn}(\text{CO})_5$ was prepared according to a literature procedure and was used without further purification.⁴² Inside the glove box, 195 mg $\text{Mn}_2(\text{CO})_{10}$ (0.5 mmol, 1 eq.) was dissolved in 5.0 ml THF, and the solution was transferred to a Schlenk flask outside the glove box. To the stirred solution was added dropwise 1.1 ml of an 1.0 M solution of K-Selectride® (1.1 mmol, 2.2 eq.), and the solution was stirred at room temperature for approximately one hour. Upon addition the colour of the solution changed from yellow to red, and later to green/brown.

Afterwards the solvent was removed *in vacuo*, the oily green residue was triturated and washed with 20 ml *n*-pentane, and the resulting solids were dried under vacuum. The title compound was obtained as a dark green solid. Yield: 205 mg.

FTIR: 1905, 1895, 1873, 1860, 1828 cm^{-1} .

ESI-MS: calculated: 194.989 ($[\text{MnC}_5\text{O}_5]^-$), found: 194.92.

1 – $\text{Mn}(\text{CO})_5(\text{COO}^i\text{Pr})$

The procedure below produced a mixture of **1** and $\text{Mn}_2(\text{CO})_{10}$. Despite repeated attempts, we were unable to separate the two, and isolation of compound **1** therefore is not claimed.

Inside the glove box, 274.9 mg $\text{Mn}(\text{CO})_5\text{Br}$ (1.0 mmol) was dissolved in 6.0 ml THF. To this solution was added 98.2 mg KO^iPr (1.0 mmol, 1 eq.) in 4.0 ml THF. The vessel was closed and the mixture was stirred overnight at room temperature inside the glove box. Immediately upon addition the solution changed colour from bright yellow to orange, bubbles appeared, and a fine, white precipitate slowly formed.

Afterwards the solvent was removed *in vacuo* to produce a yellow/orange solid. The material was extracted with *n*-pentane (3 x 5 ml), filtered through a 0.45 μm PTFE syringe filter, and the solvent was again removed *in vacuo*. Vacuum was applied for a relatively short amount of time to prevent decomposition of **1** as much as possible. *Ergo*, not all traces of solvent were removed.

The resulting oil was dissolved in minimum THF- d_8 and contained **1**, $\text{Mn}_2(\text{CO})_{10}$, and an intensely-coloured red (unidentified) compound that was light sensitive and transformed into **1** upon exposure to light. Characterisation and the presented reactivity study were performed once the solution had turned yellow.

^1H NMR (400 MHz, $\text{THF-}d_8$): δ 5.06 (sept, $J = 6.4$ Hz, $\text{CH}(\text{CH}_3)_2$, 1H), 1.16 (d, $J = 6.2$ Hz, $\text{CH}(\text{CH}_3)_2$, 6H).

FTIR: 2126, 2026, 2022, 2007, 1642 cm^{-1} .

2 – $\text{K}[\text{Mn}(\text{CO})_4(\text{COO}^i\text{Pr})_2]$ and **3** – $\text{Mn-}\mu_2$ -isopropoxo-dimer

The procedure below resulted in a mixture of **2** and **3** that was separated to obtain analytically pure **3**. Compound **2** was unstable and we were unable to obtain sufficient quantities of the analytically pure material. Isolation is therefore not claimed. Complex **2** was characterised spectroscopically as a mixture with **3**.

Inside the glove box, 274.9 mg $\text{Mn}(\text{CO})_5\text{Br}$ (1.0 mmol) was dissolved in 4.0 ml THF. To this solution was added 196.4 mg KO^iPr (2.0 mmol, 2.0 eq.) in 4.0 ml THF. The vessel was closed and the mixture was stirred overnight at room temperature inside the glove box. Immediately upon addition the solution changed colour from bright yellow to red, bubbles appeared, and a fine, white precipitate slowly formed.

Afterwards the suspension was filtered through Celite and the solvent was removed *in vacuo* to give an orange/golden yellow oil. The oil was triturated with ~2 ml *n*-pentane for several hours. The solids were filtered off, washed with *n*-pentane, and dried under vacuum to give 107 mg of the crude product as a pale orange powder. The crude product contained approximately 63% **2** and 37% **3** (Figure 4.15–4.16).

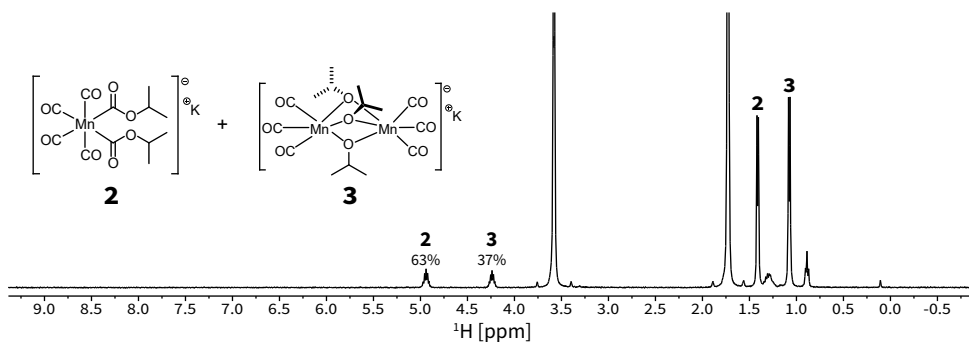


Figure 4.15. ^1H NMR spectrum of the crude mixture of **2** and **3** in $\text{THF-}d_8$ (400 MHz).

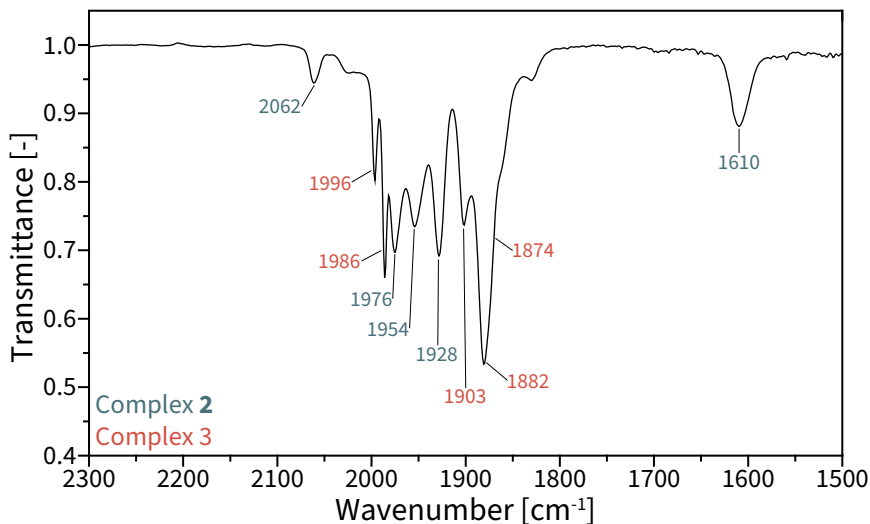


Figure 4.16. FTIR transmission spectrum of the crude mixture of **2** and **3** in THF.

3 – Mn- μ_2 -isopropoxo-dimer

The crude mixture was suspended in 4.0 ml Et₂O and was passed through a 0.45 μ m PTFE syringe filter to remove residual KBr. Compound **3** was precipitated from the solution by the addition of 30 ml *n*-pentane. Subsequent filtration, washing with *n*-pentane, and vacuum drying provided 61 mg of **3** as a yellow solid. The material was recrystallised by slow vapour diffusion of *n*-pentane into a saturated solution of **3** in Et₂O. Analytically pure **3** was obtained as a red crystalline solid.

Compound **3** could also be crystallised directly from the mixture in diethyl ether *via* an identical procedure. These conditions led to the decomposition of **2**. When performed in a regular glass vial, a dark green solution was obtained that contained KMn(CO)₅ (assigned on basis of its FTIR spectrum). When performed in amber glass vials, compound **1** was slowly (~days) and partially formed from **2**. Mn-isopropoxo-dimer **3** was inert under these conditions and could be obtained regardless of the fate of **2**.

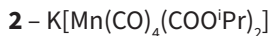
¹H NMR (400 MHz, THF-*d*₈): δ 4.23 (sept, $J = 6.1$ Hz, CH(CH₃)₂, 1H), 1.41 (d, $J = 6.0$ Hz, CH(CH₃)₂, 6H).

¹³C NMR (101 MHz, THF-*d*₈): all signals are singlets: δ 224.6, 73.2, 28.4.

FTIR: 1996, 1986, 1903, 1882, 1874 cm⁻¹.

ESI-MS: calc.: 454.995 ([Mn₂C₁₅H₂₁O₉]⁻), found: 454.76.

EA: found (calc.): C: 35.08 (36.45), H: 4.21 (4.28).



Compound **2** was removed from the mixture after the initial precipitation of **3**. The supernatant was concentrated *in vacuo*. Minimum Et₂O was added to redissolve the oil, and approximately 20 ml *n*-pentane was added to precipitate **2**. This procedure gave small amounts of nearly pure **2** that were used for spectroscopic characterisation. Solutions that contained **2** immediately started to decompose to KMn(CO)₅. This process gave observable decomposition within hours at room temperature.

¹H NMR (400 MHz, THF-*d*₈): δ 4.94 (sept, *J* = 6.3 Hz, CH(CH₃)₂, 1H), 1.08 (d, *J* = 6.2 Hz, CH(CH₃)₂, 6H).

¹³C NMR (101 MHz, THF-*d*₈): all signals are singlets: δ 239.4, 219.5, 218.8, 62.16, 22.8.

FTIR: 2062, 1977, 1955, 1950, 1927, 1610 cm⁻¹.

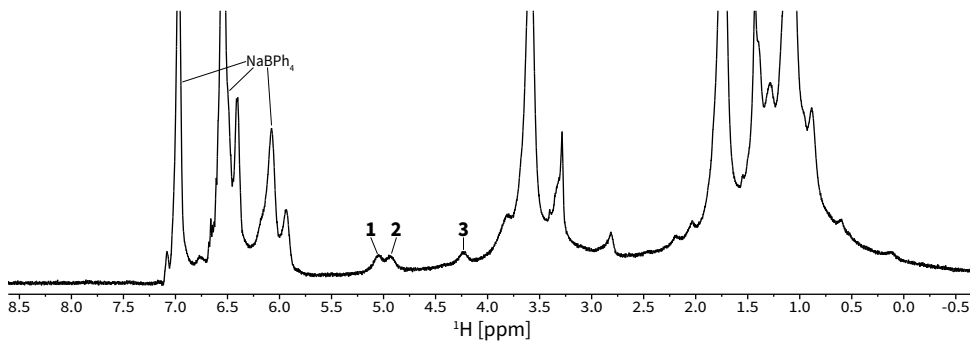
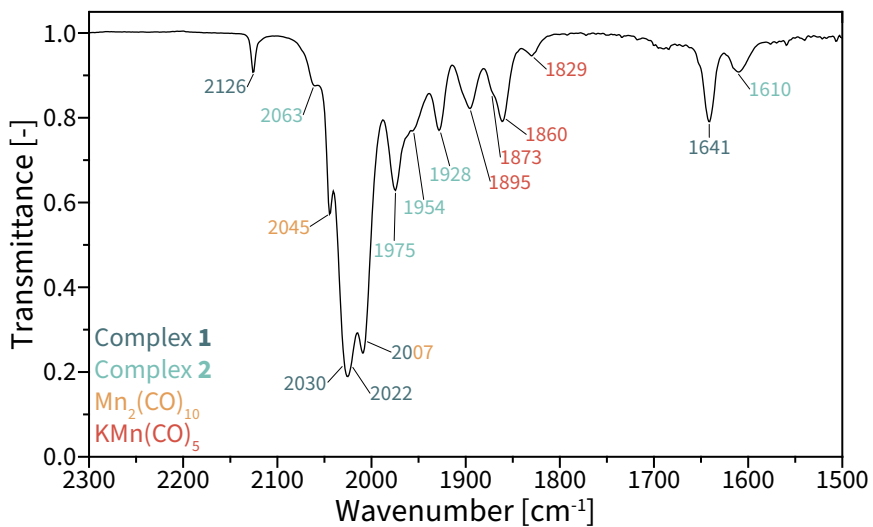
ESI-MS: calc.: 341.007 ([MnC₁₂H₁₄O₈]⁻), found: 340.76.

Reactivity study with compounds 1-3

Experiments were performed with the mixtures of **1** and Mn₂(CO)₁₀, and **2** and **3**. The analysis was repeated with pure Mn₂(CO)₁₀ and **3** to understand the reactivity of Mn-acyls **1** and **2**. Only spectra of reactive mixtures are provided in this section (see **Figure 4.8** for an overview of their reactivity).

Procedure for NMR: the material containing the Mn compound was dissolved in THF-*d*₈ and was transferred to a screw-cap or J. Young NMR tube with a glass referencing insert. To the solution was added approximately one equivalent of the required reagent (in THF or THF-*d*₈). The components were thoroughly mixed and were allowed to react for at least 30 minutes at room temperature before ¹H, ¹¹B, and ⁵⁵Mn NMR spectra were acquired.

The procedure that was used for the FTIR experiments was identical to the described NMR experiments. THF-*d*₈ was substituted for protium-THF because deuterated THF absorbs significantly in the infrared range of interest. Mixtures were diluted with THF to approximately 0.5 mg Mn ml⁻¹.

Reactivity study: 1 + KO^tPr**Figure 4.17.** ¹H NMR spectrum after reaction of **1** with KO^tPr in THF-*d*₈ (400 MHz).**Figure 4.18.** FTIR transmission spectrum after reaction of **1** with KO^tPr in THF.

Reactivity study: **1** + KBHET_3

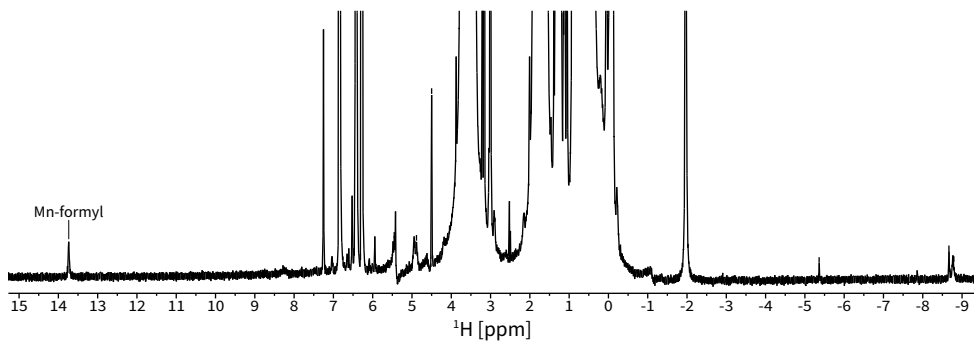


Figure 4.19. ^1H NMR spectrum after reaction of **1** with KBHET_3 in $\text{THF-}d_8$ (400 MHz).

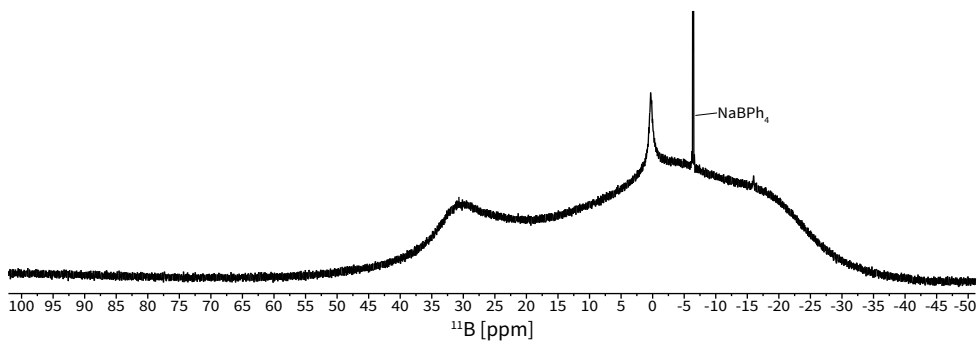


Figure 4.20. ^{11}B NMR spectrum after reaction of **1** with KBHET_3 in $\text{THF-}d_8$ (128 MHz).

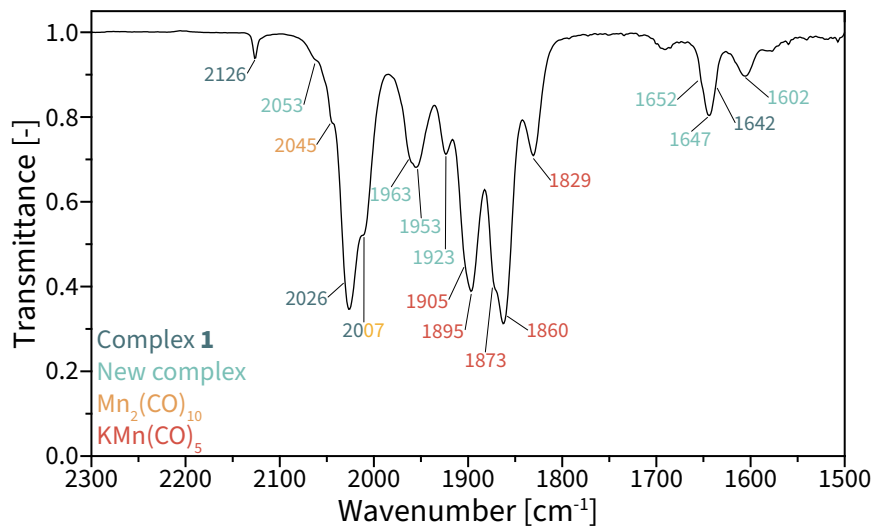


Figure 4.21. FTIR transmission spectrum after reaction of **1** with KBHET_3 in THF.

Reactivity study: **2** + BEt_3

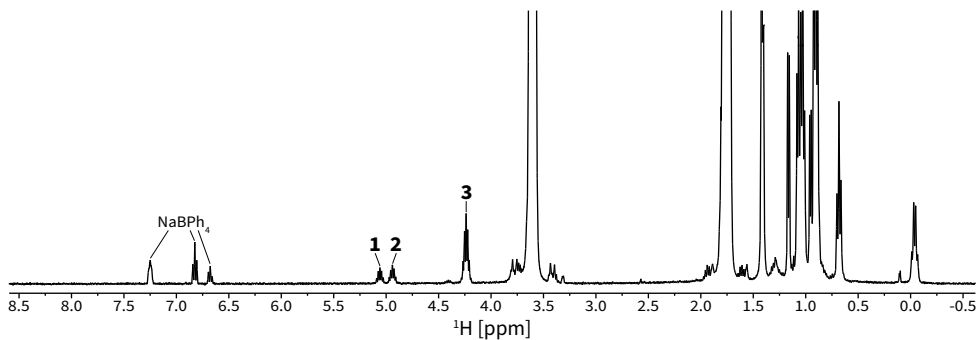


Figure 4.22. ^1H NMR spectrum after reaction of **2** with BEt_3 in $\text{THF-}d_8$ (400 MHz).

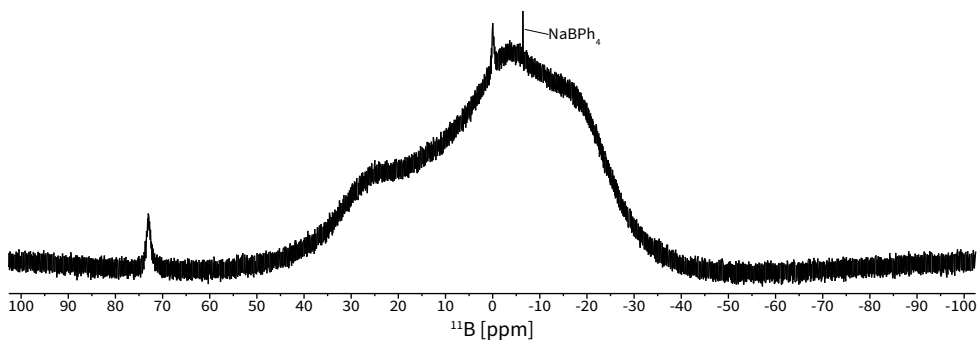


Figure 4.23. ^{11}B NMR spectrum after reaction of **2** with BEt_3 in $\text{THF-}d_8$ (128 MHz).

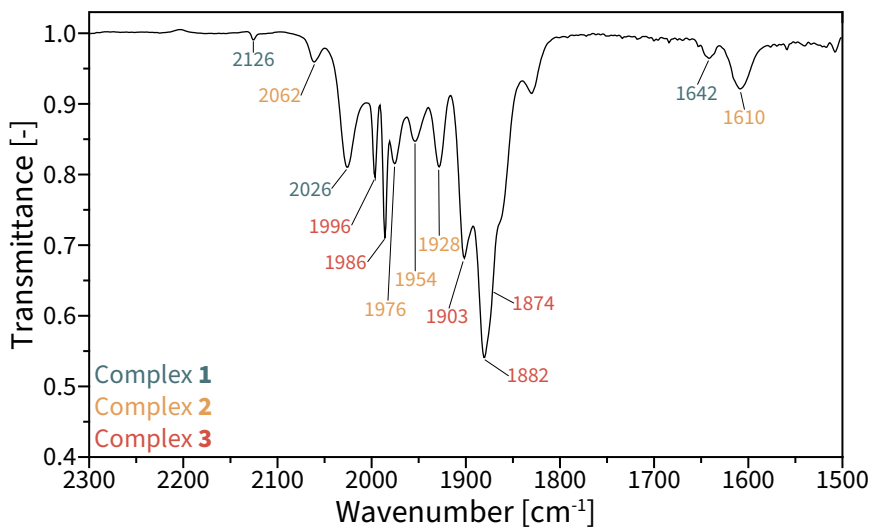


Figure 4.24. FTIR transmission spectrum after reaction of **2** with BEt_3 in THF.

Reaction optimisation and screening experiments

A general procedure for the reaction optimisation experiments is described below. Screening experiments were performed according to an analogous procedure.

To a 4.0 ml amber glass vial was loaded (in order) the appropriate amount of KOⁱPr as a stock solution in THF, a PTFE-coated stirring bar, 40 μ l *n*-dodecane, THF (so that the total mixture is Σ 2.0 ml), and 0.2 ml (1.0 mmol, 1.0 eq.) of a 0.5 M stock solution of K[Et₃B(OⁱPr)] in THF. The mixture was stirred and a 20 μ l aliquot was removed for pre-reaction GC-MS analysis. The appropriate amount of Mn(CO)₅Br was added to the mixture in 0.5 ml THF. The vials were capped and were stirred overnight (~16 h) at room temperature. Afterwards a second aliquot was removed from the mixture and the sample was analysed as described.

Analytical details

Measurements were performed on an Agilent 7890B gas chromatograph equipped with FID and Agilent 5977B MS detectors and a Restek Stabilwax-MS column (30 m, 0.32 mmID, 0.25 μ m film thickness). Method details: 50 °C (hold 1.0 min), ramp to 100 °C at 10 °C min⁻¹, ramp to 250 °C at 100 °C min⁻¹ (hold at 250 °C for 3.3 min). Products were identified using the retention times of analytically pure reference samples and by comparison of observed mass spectra and spectra of the authentic reference samples available in the NIST 17 and SDBS libraries.

Computational details

DFT calculations were performed by A.M. Krieger MSc using the hybrid PBE0-D3(BJ)-SMD(THF) exchange-correlation functional⁴³ as implemented in Gaussian 16 C.01.⁴⁴ Geometry optimisations were performed with the all-electron 6-311+g(d,p) basis set for all atoms. Vibrational analysis was then carried out for all structures at the same level of theory to identify the true nature of the stationary points. Neither structure had imaginary frequencies. Bulk solvent effects were accounted for by the solvation model based on density (SMD) with THF as the solvent.

Reaction energies (ΔE) were corrected for zero-point energy (ZPE) from the normal-mode frequency analysis. Standard reaction Gibbs free energies (ΔG) in the THF solution were computed with the results of the normal-mode analysis with the ideal gas approximation at a pressure of 1 atm and a temperature of 298 K.

Crystallographic details

X-ray diffraction studies were performed by dr. M. Lutz (Universiteit Utrecht). Crystallographic details are available in the electronic supporting information of the published work: *Organometallics* **2021**, *40*, 674–681, DOI: 10.1021/acs.organomet.0c00781. CCDC entry 2039376 (**3**) contains the supplementary data for this work.

4.9 References

1. Beller, M.; Wu, X.F., *Transition Metal Catalyzed Carbonylation Reactions: Carbonylative Activation of C-X Bonds*, Springer, Berlin and Heidelberg, Germany, **2013**; 13–52;
2. Hietala, J.; Vuori, A.; Johnsson, P.; Pollari, I.; Reutemann, W.; Kieczka, H., *Formic Acid - Ullmann's Encyclopedia of Industrial Chemistry*, Wiley-VCH Verlag GmbH & Co. kGaA, Weinheim, Germany, **2016**, 1–22;
3. Kalck, P.; Le Berre, C.; Serp, P., *Recent advances in the methanol carbonylation reaction into acetic acid*, *Coordination Chemistry Reviews* **2020**, 402, 213078;
4. Beller, M.; Wu, X.F., *Transition Metal Catalyzed Carbonylation Reactions: Carbonylative Activation of C-X Bonds*, Springer, Berlin and Heidelberg, Germany, **2013**; 1–11;
5. Wang, Z., *Repe Carbonylation - Comprehensive Organic Name Reactions and Reagents*, Wiley-VCH Verlag GmbH & Co. kGaA, Weinheim, Germany, **2010**, 2352–2357;
6. Kiss, G., *Palladium-Catalyzed Repe Carbonylation*, *Chemical Reviews* **2001**, 101 (11), 3435–3456;
7. Zhao, S.; Mankad, N.P., *Metal-catalysed radical carbonylation reactions*, *Catalysis Science & Technology* **2019**, 9 (14), 3603–3613;
8. Mizushima, E.; Hayashi, T.; Tanaka, M., *Palladium-catalysed carbonylation of aryl halides in ionic liquid media: high catalyst stability and significant rate-enhancement in alkoxycarbonylation*, *Green Chemistry* **2001**, 3 (2), 76–79;
9. Mägerlein, W.; Indolese, A.F.; Beller, M., *Development of new palladium catalysts for the alkoxycarbonylation of aryl chlorides*, *Journal of Organometallic Chemistry* **2002**, 641 (1), 30–40;
10. Sargent, B.T.; Alexanian, E.J., *Palladium-Catalyzed Alkoxycarbonylation of Unactivated Secondary Alkyl Bromides at Low Pressure*, *Journal of the American Chemical Society* **2016**, 138 (24), 7520–7523;
11. Xin, Z.; Gøgsig, T.M.; Lindhardt, A.T.; Skrydstrup, T., *An Efficient Method for the Preparation of Tertiary Esters by Palladium-Catalyzed Alkoxycarbonylation of Aryl Bromides*, *Organic Letters* **2012**, 14 (1), 284–287;
12. Minami, H.; Nogi, K.; Yorimitsu, H., *Palladium-Catalyzed Alkoxycarbonylation of Arylsulfoniums*, *Organic Letters* **2019**, 21 (8), 2518–2522;
13. Guo, W.; Lu, L.Q.; Wang, Y.; Wang, Y.N.; Chen, J.R.; Xiao, W.J., *Metal-Free, Room-Temperature, Radical Alkoxycarbonylation of Aryldiazonium Salts through Visible-Light Photoredox Catalysis*, *Angewandte Chemie International Edition* **2015**, 54 (7), 2265–2269;
14. Dolle, R.E.; Schmidt, S.J.; Kruse, L.I., *Palladium catalysed alkoxycarbonylation of phenols to benzoate esters*, *Journal of the Chemical Society, Chemical Communications* **1987**, 12, 904–905;
15. Cook, G.K.; Hornback, W.J.; Jordan, C.L.; McDonald, J.H.; Munroe, J.E., *Palladium-catalyzed chemistry of beta-lactam vinyl triflates: coupling with organostannanes and alkoxycarbonylation*, *The Journal of Organic Chemistry* **1989**, 54 (24), 5828–5830;
16. Xu, J.X.; Wu, X.F., *Cobalt-Catalyzed Alkoxycarbonylation of Epoxides to β -Hydroxyesters*, *The Journal of Organic Chemistry* **2019**, 84 (16), 9907–9912;
17. Murahashi, S.; Imada, Y.; Taniguchi, Y.; Higashiura, S., *Palladium(0)-catalyzed alkoxycarbonylation of allyl phosphates and acetates*, *The Journal of Organic Chemistry* **1993**, 58 (6), 1538–1545;
18. Li, C.L.; Jiang, X.; Lu, L.Q.; Xiao, W.J.; Wu, X.F., *Cobalt(II)-Catalyzed Alkoxycarbonylation of Aliphatic Amines via C–N Bond Activation*, *Organic Letters* **2019**, 21 (17), 6919–6923;

19. Zhang, H.; Shi, R.; Ding, A.; Lu, L.; Chen, B.; Lei, A., *Transition-Metal-Free Alkoxy carbonylation of Aryl Halides*, *Angewandte Chemie International Edition* **2012**, 51 (50), 12542–12545;
20. Dong, Y.; Sun, S.; Yang, F.; Zhu, Y.; Zhu, W.; Qiao, H.; Wu, Y.; Wu, Y., *Pd-catalyzed aminocarbonylation of alkynes with amines using $\text{Co}_2(\text{CO})_8$ as a carbonyl source*, *Organic Chemistry Frontiers* **2016**, 3 (6), 720–724;
21. Babjak, M.; Markovič, M.; Kandríková, B.; Gracza, T., *Homogeneous Cyclocarbonylation of Alkenols with Iron Pentacarbonyl*, *Synthesis* **2014**, 46 (06), 809–816;
22. Odell, L.R.; Russo, F.; Larhed, M., *Molybdenum Hexacarbonyl Mediated CO Gas-Free Carbonylative Reactions*, *Synlett* **2012**, 23 (05), 685–698;
23. Kondo, T.; Tsuji, Y.; Watanabe, Y., *Photochemical carbonylation of alkyl iodides in the presence of various metal carbonyls*, *Tetrahedron Letters* **1988**, 29 (31), 3833–3836;
24. Kondo, T.; Sone, Y.; Tsuji, Y.; Watanabe, Y., *Photo-, electro-, and thermal carbonylation of alkyl iodides in the presence of group 7 and 8–10 metal carbonyl catalysts*, *Journal of Organometallic Chemistry* **1994**, 473 (1), 163–173;
25. Fleischer, I.; Jennerjahn, R.; Cozzula, D.; Jackstell, R.; Franke, R.; Beller, M., *A Unique Palladium Catalyst for Efficient and Selective Alkoxy carbonylation of Olefins with Formates*, *ChemSusChem* **2013**, 6 (3), 417–420;
26. Qi, X.; Li, C.L.; Jiang, L.B.; Zhang, W.Q.; Wu, X.F., *Palladium-catalyzed alkoxy carbonylation of aryl halides with phenols employing formic acid as the CO source*, *Catalysis Science & Technology* **2016**, 6 (9), 3099–3107;
27. Ko, S.; Lee, C.; Choi, M.G.; Na, Y.; Chang, S., *Chelation-Accelerated Sequential Decarbonylation of Formate and Alkoxy carbonylation of Aryl Halides Using a Combined Ru and Pd Catalyst*, *The Journal of Organic Chemistry* **2003**, 68 (4), 1607–1610;
28. Wu, L.; Liu, Q.; Fleischer, I.; Jackstell, R.; Beller, M., *Ruthenium-catalysed alkoxy carbonylation of alkenes with carbon dioxide*, *Nature Communications* **2014**, 5 (1), 3091;
29. Zhang, X.; Shen, C.; Xia, C.; Tian, X.; He, L., *Alkoxy carbonylation of olefins with carbon dioxide by a reusable heterobimetallic ruthenium–cobalt catalytic system*, *Green Chemistry* **2018**, 20 (24), 5533–5539;
30. Walker, P.J.C.; Mawby, R.J., *Patterns of nucleophilic attack on tricarbonyl π -arene complexes of manganese(I)*, *Inorganica Chimica Acta* **1973**, 7, 621–625;
31. Johnson, R.W.; Pearson, R.G., *Kinetics and mechanism of the cleavage reactions of acylmanganese pentacarbonyl and methylmanganese pentacarbonyl*, *Inorganic Chemistry* **1971**, 10 (10), 2091–2095;
32. Lukehart, C.M.; Torrence, G.P.; Zeile, J.V., *Reactions on coordinated molecules. IV. Preparation of tris(cis-diacetyltetracarbonylmanganate)aluminum. Metalloacetylacetonate complex*, *Journal of the American Chemical Society* **1975**, 97 (23), 6903–6904;
33. Casey, C.P.; Bunnell, C.A., *Site of nucleophilic attack on acylpentacarbonylmanganese(I) compounds*, *Journal of the American Chemical Society* **1976**, 98 (2), 436–441;
34. Gladysz, J.A.; Williams, G.M.; Tam, W.; Johnson, D.L., *A convenient preparation of metal carbonyl monoanions by trialkylborohydride cleavage of metal carbonyl dimers; observation and reactions of a bimetallic manganese-formyl intermediate*, *Journal of Organometallic Chemistry* **1977**, 140 (1), C1–C6;
35. Selover, J.C.; Marsi, M.; Parker, D.W.; Gladysz, J.A., *Mononuclear anionic formyl complexes; synthesis and properties*, *Journal of Organometallic Chemistry* **1981**, 206 (3), 317–329;
36. Kovacs, I.; Hoff, C.D.; Ungvary, F.; Marko, L., *Kinetic investigation of the mixed-metal bimolecular*

- reductive eliminations in the reactions of $\text{EtOC(O)CH}_2\text{M(CO)}_n$ or EtOC(O)M(CO)_n ($M = \text{Co}$, $n = 4$; $M = \text{Mn}$, $n = 5$) with HCo(CO)_4 or HMn(CO)_5 , *Organometallics* **1985**, 4 (8), 1347–1350;
37. Bowen, D.H.; Green, M.; Grove, D.M.; Moss, J.R.; Stone, F.G.A., *Chemistry of the metal carbonyls. Part LXIX. Synthesis and reactions of complexes of manganese containing the substituted and unsubstituted 2,5-dioxacyclopentylidene ligand*, *Journal of the Chemical Society, Dalton Transactions* **1974**, 11, 1189–1194;
38. Andersen, J.A.M.; Moss, J.R., *Synthesis of an Extensive Series of Manganese Pentacarbonyl Alkyl and Acyl Compounds: Carbonylation and Decarbonylation Studies on $[\text{Mn(R)(CO)}_5]$ and $[\text{Mn(COR)(CO)}_5]$* , *Organometallics* **1994**, 13 (12), 5013–5020;
39. Casey, C.P.; Scheck, D.M., *Preferred kinetic migration of methyl and preferred thermodynamic migration of phenyl in conversion of cis-acetylbenzoyltetracarbonylrhenate(I) to cis-benzoylmethyltetracarbonylrhenate(I) and cis-acetylphenyltetracarbonylrhenate(I)*, *Journal of the American Chemical Society* **1980**, 102 (8), 2723–2728;
40. Álvarez, C.M.; Carrillo, R.; García-Rodríguez, R.; Miguel, D., *Intramolecular carboboration of carbonyl ligands to form boroxycarbenes*, *Chemical Communications* **2012**, 48 (62), 7705–7707;
41. Cole, T.E.; Haly, B.D., *Selective preparation of borinic esters from Grignard reagents and selected trialkoxyboranes*, *Organometallics* **1992**, 11 (2), 652–657;
42. Lindner, E.; Ossig, E.; Darmuth, M., *Darstellung und eigenschaften von und reaktionen mit metallhaltigen heterocyclen LXVIII. Phosphidomanganate als bausteine zur synthese von Phosphamanganacyclopropanen mit carben- und phosphiniden einheiten*, *Journal of Organometallic Chemistry* **1989**, 379 (1), 107–118;
43. Adamo, C.; Barone, V., *Toward reliable density functional methods without adjustable parameters: The PBE0 model*, *The Journal of Chemical Physics* **1999**, 110 (13), 6158–6170;
44. Frisch, M.J.; Trucks, G.W.; Schlegel, H.B.; Scuseria, G.E.; Robb, M.A.; Cheeseman, J.R.; Scalmani, G.; Barone, V.; Petersson, G.A.; Nakatsuji, H.; Li, X.; Caricato, M.; Marenich, A.V.; Bloino, J.; Janesko, B.G.; Gomperts, R.; Mennucci, B.; Hratchian, H.P.; Ortiz, J.V.; Izmaylov, A.F.; Sonnenberg, J.L.; Williams, Ding, F.; Lipparini, F.; Egidi, F.; Goings, J.; Peng, B.; Petrone, A.; Henderson, T.; Ranasinghe, D.; Zakrzewski, V.G.; Gao, J.; Rega, N.; Zheng, G.; Liang, W.; Hada, M.; Ehara, M.; Toyota, K.; Fukuda, R.; Hasegawa, J.; Ishida, M.; Nakajima, T.; Honda, Y.; Kitao, O.; Nakai, H.; Vreven, T.; Throssell, K.; Montgomery Jr., J.A.; Peralta, J.E.; Ogliaro, F.; Bearpark, M.J.; Heyd, J.J.; Brothers, E.N.; Kudin, K.N.; Staroverov, V.N.; Keith, T.A.; Kobayashi, R.; Normand, J.; Raghavachari, K.; Rendell, A.P.; Burant, J.C.; Iyengar, S.S.; Tomasi, J.; Cossi, M.; Millam, J.M.; Klene, M.; Adamo, C.; Cammi, R.; Ochterski, J.W.; Martin, R.L.; Morokuma, K.; Farkas, O.; Foresman, J.B.; Fox, D.J., *Gaussian 16 Rev. C.01*, Wallingford, CT, **2016**.



Chapter



Deactivation of Mn^I-NHC transfer hydrogenation catalysts

and its prevention

.....

“It doesn't make a difference how beautiful your guess is. It doesn't make a difference how smart you are, who made the guess, or what his name is. If it disagrees with experiments, it's wrong.”

Richard Feynman

Abstract

The Mn^I-NHC catalytic system described in **Chapter 3** deactivated extensively when it was used at low catalyst loading and elevated reaction temperature. Such irreversible catalyst deactivation is undesirable because it directly prevents a further decrease of catalyst concentration. The deactivation process was therefore studied in more detail with a combination of dedicated kinetic studies, a modelling campaign, stoichiometric reactivity studies, and multiple modes of spectroscopic investigations that focused on the redox behaviour of Mn^I. These combined works revealed that deactivation of the Mn^I-NHC transfer hydrogenation catalyst is a highly complex process that is not easily captured or investigated with current experimental methods. The dilute nature of realistic catalytic reaction mixtures severely complicated our studies, and we occasionally encountered boundaries of experimental detectability or representativeness.

EPR spectroscopy indicated that the active catalyst decomposes at elevated temperatures as a result of a base-induced side-reaction that produces extended, paramagnetic Mn^{III}-oxo clusters. This (partial) oxidation of the active Mn^I complex was also detected with preliminary *in situ* XANES measurements. Attempts to synthesise or isolate these clusters are ongoing and the exact structure of these materials therefore remains unclear at this time. Dedicated EXAFS experiments are expected to provide more information on the nature of these clusters once synchrotron beamtime becomes available.

Finally, a practical method was developed that suppressed the adverse deactivation reaction and enabled a further reduction of catalyst loading. Addition of small quantities of triethylborane significantly improved catalyst lifetime. These reaction mixtures contained the organo(alkoxy)borate salts that were first described in **Chapter 4** and effectively neutralised the hard and nucleophilic alkoxide base. The role of BEt₃ was further investigated. Spectroscopic studies revealed that potassium triethyl(alkoxy)borate salts were less reactive towards Mn^I complexes compared to ‘unprotected’ alkoxides, which suppressed the undesirable deactivation reaction. These results thus indicate that catalyst deactivation may be prevented by careful optimisation and design of the holistic catalytic system that includes the catalyst, additives, as well as reaction conditions.

.....

This chapter has been published as:

R. van Putten, E.A. Uslamin, D.M. Polykhov, A.S. Poryvaev, J. Benschop, R.P.W.M. Tielen, D. Ripepi, F.D. Tichelaar, M.V. Fedin, E.A. Pidko, *In preparation*

5.1 Introduction

The Mn^I-NHC complex **1** that was first described in **Chapter 3** is a potent precatalyst for the catalytic transfer hydrogenation of ketones with alcohol hydrogen donors. It showed good performance for the reduction of a variety of ketones and was synthetically useful at catalyst loadings as low as 75 ppm. A further reduction of metal content was prevented by pronounced catalyst deactivation.

Extensive and irreversible catalyst deactivation is undesirable because it directly increases catalyst consumption, produces additional waste, and drives operational cost. Each catalyst species that is removed from the active catalytic pool can no longer contribute to the target transformation and has—in the best case—effectively become an unproductive spectator. In the worst case, deactivated species also are catalytically active and cause a loss of (enantio)selectivity.¹ It is therefore critically important to understand and control catalyst deactivation in order to optimise performance. This is particularly relevant for the development of ‘high-turnover catalysts’ that are generally considered to have TONs exceeding one thousand.²

Deactivation of homogeneous catalysts is investigated less often compared to their heterogeneous counterparts. Most homogeneous catalysts are intended to be used once, whereas heterogeneous catalysts are often expected to remain active for months or even years.^{3–5} (Fluidic catalytic cracking catalysts are a notable exception that deactivate within seconds. The heat that is produced during oxidative regeneration is used to drive the reaction.) In fact, the origin of homogeneous catalyst deactivation is often not investigated in depth and is simply countered with an increased catalyst loading. This practise was explained by Poater and Cavallo⁶ (and later by Crabtree⁷), who wrote that: *“One of the reasons for this limited understanding [of catalyst deactivation] is that academic groups usually focus on the more rewarding improvement of activity and/or selectivity of a catalyst, since more or less rational strategies can be followed, rather than investing resources to follow catalyst deactivation along unexplored pathways.”*

Catalyst deactivation studies are difficult because many factors can lead to a loss of catalytic activity. For example, catalysts can stop working after the main ligand dissociates, reacts, or decomposes, after oxidation or reduction of the ligand and/or metal centre, nanoparticle or cluster formation, irreversible poisoning by impurities or mixture components, or photochemical or thermal decomposition. These processes often are specific to the catalytic system and may depend strongly on the reaction conditions and batch of chemicals used. This can make it difficult to predict, study, and resolve catalyst deactivation of homogeneous systems. A number of reports have dealt with the issue in more detail and have described specific methods that can be employed to study deactivation phenomena.^{7–8}

Several groups have investigated the specific deactivation behaviour of (transfer) hydrogenation catalysts. These catalyst were diverse and deactivated in different ways, including, *e.g.*, the formation of Rh-oxo or Rh- μ_3 -chloro clusters⁹, Ir-hydride/NHC clusters¹⁰⁻¹¹, well-defined Ir-alkoxides¹², bridging Ru-polyhydrides (and eventual ruthenium black)¹³, and inactive Fe-hydrides¹⁴ or Fe⁰-NHC clusters¹. The most compelling evidence for the structure of these deactivated states was usually provided with X-ray absorption spectroscopy methods such as XANES and EXAFS, or with X-ray single-crystal diffraction studies if representative, high-quality crystals could be obtained.

The mechanism of irreversible catalyst deactivation can generally be classified by one of three distinct regimes. In the first such modes, catalyst deactivation is a singular event that has a limited impact on the target transformation. This could for example occur if the catalyst reacts with a trace impurity or poison present inside the system. The remaining, unaffected catalyst portion can continue to operate once the poison has been neutralised. Purification of the starting materials could prevent or resolve this situation.

The second regime of deactivation is turnover-related and could for example occur if the catalyst is poisoned by the reaction's product. (Note that this situation is distinct from product inhibition, which is generally considered to be equilibrium-driven and therefore reversible.) In this case one would ideally use a more robust catalytic system that tolerates the poison. If this is not feasible, the catalyst can also be added in several portions to mitigate the worst impact of deactivation.

The third mode of catalyst deactivation is the most difficult to resolve and occurs if deactivation is an intrinsic and/or continuous process that is caused by the reaction conditions or the highly reactive nature of the catalyst. This could for example be the case if the active species dimerises and gets trapped in a (semi) inescapable thermodynamic well. The effects of such deactivation are necessarily most pronounced at low catalyst concentration because the initial catalytic pool is small and there is little headroom to compensate losses. In such a situation more drastic measures are required, and the conditions and catalyst design should be carefully analysed and optimised for the specific target transformation. Attention must be given to finding conditions that favour the target reaction over the background deactivation reaction. The deactivation of Mn^I-NHC **1** is believed to fit this category.

This chapter describes our efforts to characterise the deactivation behaviour of the Mn^I-NHC transfer hydrogenation catalyst first described in **Chapter 3**. This phenomenon was studied with a variety of techniques that include dedicated kinetic studies, a modelling campaign, stoichiometric reactivity studies, and multiple

modes of (*in situ*) spectroscopy. These combined works revealed that deactivation of the Mn^I-NHC transfer hydrogenation catalyst is a highly complex process that is not easily captured or investigated with contemporary experimental methods. Our current understanding of the deactivation process is still under development and the ideas presented in this chapter are part of our working hypothesis.

5.2 Kinetic study of deactivation phenomena

We started our investigation into the deactivation behaviour of **1** with a series of kinetic experiments. Kinetic studies often provide relevant and insightful data to study these phenomena and correlate macro-level effects to small changes in conditions. The preliminary kinetic study described in **Chapter 3** was therefore expanded. Experiments were performed at five different temperatures between 40 °C and 80 °C with varied catalyst loadings. These experiments were designed such that each 'temperature set' included both extensively- and minimally-deactivated traces, as well as several runs in between these extremes. These data are summarised in **Figure 5.1**.

The initial rate data enabled us to extract information on the catalyst reaction order and the apparent activation energy of the overall process. Kinetic parameters were determined and used as input for a dedicated modelling campaign. Experimental data were compared to the numerical solution of various kinetic models to estimate the concentration profiles of catalyst species that could not be measured directly by other means because of their low concentration.

Table 5.1. Extracted data from kinetic experiments with Mn^I-NHC precatalyst **1**.^{a)}

Entry	Temperature [°C]	Equilibrium conversion [%]	$K_{eq}^{b)}$ [-]	Apparent catalyst reaction order ^{c)} [-]
1	40	97.2	0.3407	0.98
2	50	97.4	0.3685	0.99
3	60	97.6	0.4008	1.00
4	70	97.8	0.4391	1.19
5	80	98.0	0.4850	1.64

a) Conditions: 0.5 mmol acetophenone, 25–5000 ppm **1**, 1.0 mol% KO^tBu, 3.82 ml 2-propanol, 40–80 °C. Yields were determined by GC-FID using *n*-dodecane as an internal standard. **b)** K_{eq} was calculated with **Equation 5.1**. A = acetophenone, B = 2-propanol, C = 1-phenylethanol, D = acetone, X = conversion. **c)** See **Figure 5.2**.

$$K_{eq} = \frac{k_f}{k_b} \approx \frac{C_C C_D}{C_A C_B} = \frac{C_A^0 X^2}{C_B^0 (1-X) + C_A^0 X(X-1)} \quad (5.1)$$

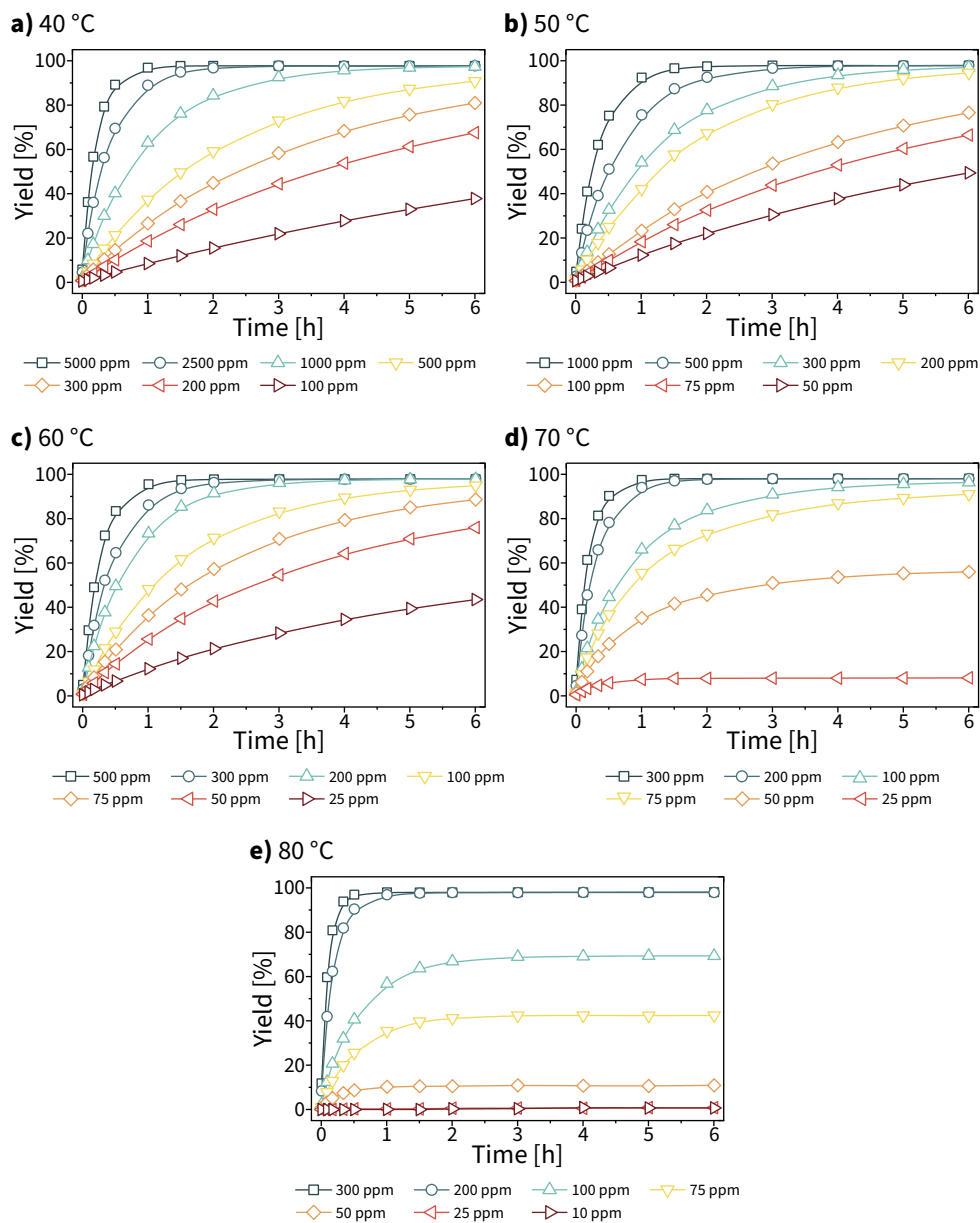


Figure 5.1. Kinetic traces of deactivation experiments at varied temperature and catalyst loading. Conditions: 0.5 mmol acetophenone, 25–5000 ppm **1**, 1.0 mol% KO^tBu, 3.82 ml 2-propanol, 40–80 °C. Yields were determined by GC-FID using *n*-dodecane as an internal standard.

Analysis of the kinetic data revealed that the apparent catalyst reaction order was temperature dependent (**Figure 5.2**). At temperatures below 60 °C, the reaction order in **1** was constant and approximately equal to 1.0. Increased reaction temperature led to apparent catalyst reaction orders above unity: 1.19 at 70 °C and 1.64 at 80 °C. Close inspection of the initial rate data indicated that this was caused by specific experiments that were performed at low catalyst concentrations (**Figure 5.2**, solid markers). The specific combination of high temperature and low catalyst loading probably induced catalyst deactivation and suppressed the observed initial reaction rate. Experiments at low catalyst concentration were more severely impacted because these had a smaller ‘active catalytic pool’ that made them more prone to catalyst deactivation. Omission of these specific points produced catalyst orders of 1.04 and 0.87 at 70 °C and 80 °C, respectively. Note that the fit at 80 °C is based on two points and may not be representative. This deviation from the anticipated result again suggests that deactivation of **1** strongly depends on reaction temperature and is most pronounced at low catalyst loadings.

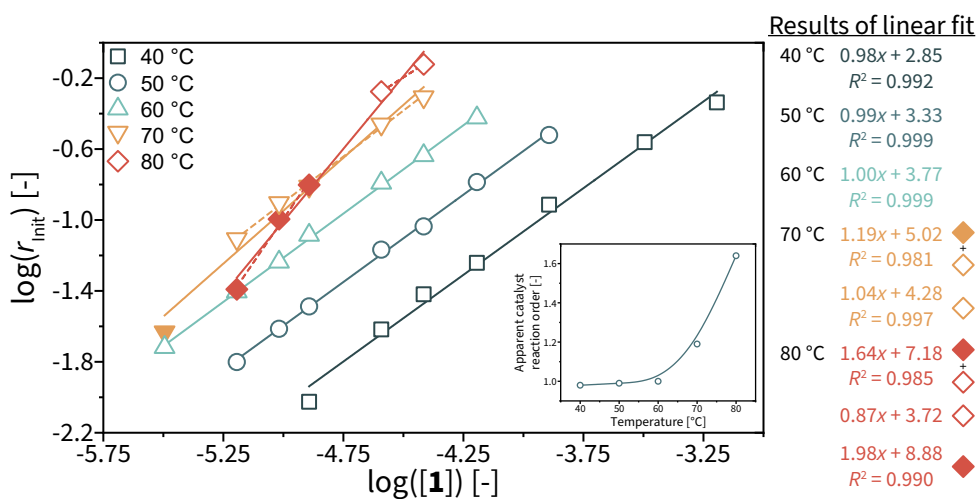


Figure 5.2. Apparent reaction order of **1** as a function of temperature. Conditions: 0.5 mmol acetophenone, 25–5000 ppm **1**, 1.0 mol% KO^tBu, 3.82 ml 2-propanol, 40–80 °C. Yields were determined by GC-FID using *n*-dodecane as an internal standard. Points labelled with solid markers had deactivated to some degree.

These data also allowed determination of the apparent activation energy. The abundance of kinetic data at identical catalyst concentration but varied temperature enabled us to perform the analysis several times. Data points previously determined to have suffered from catalyst deactivation in the initial phase of the reaction were excluded from the fit (*i.e.*, 50 ppm at 70 °C and all runs at 80 °C). Results of this analysis are summarised in **Figure 5.3** and **Table 5.2**.

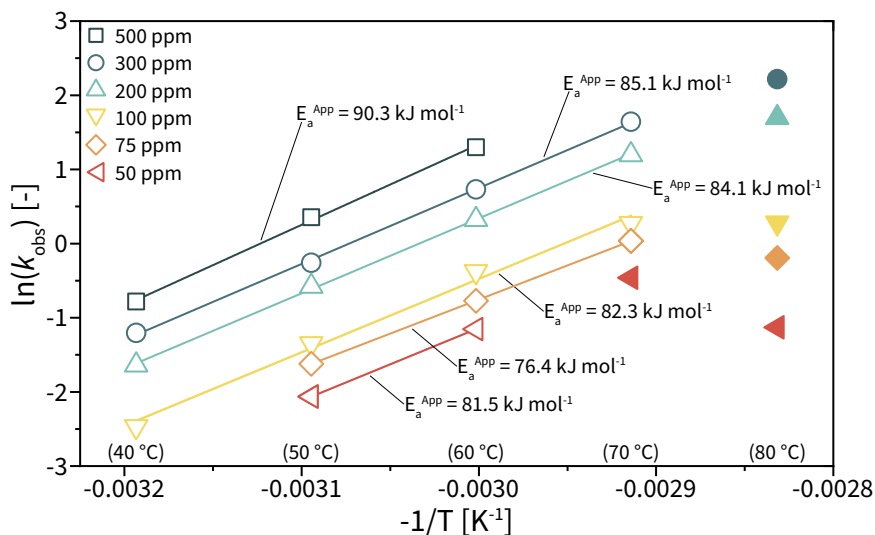


Figure 5.3. Arrhenius plot for acetophenone transfer hydrogenation with **1**. Conditions: 0.5 mmol acetophenone, 50–500 ppm **1**, 1.0 mol% KO^tBu, 3.82 ml 2-propanol, 40–80 °C. Yields were determined by GC-FID using *n*-dodecane as an internal standard. Points labelled with solid markers were excluded from fit because they had deactivated to some degree.

Table 5.2. Fit data accompanying Arrhenius plot in Figure 5.3.

Entry	Mn loading [ppm]	# Points in fit [-]	Intercept [-]	Slope [-]	R ² [-]	E _a ^{APP} [kJ mol ⁻¹]	A ^{a)} [a.u.]
1	500	3	33.9	10865.5	0.99876	90.3	5.47*10 ¹⁴
2	300	4	31.5	10235.1	0.99945	85.1	4.58*10 ¹³
3	200	4	30.7	10112.0	0.99949	84.1	2.10*10 ¹³
4	100	4	29.2	9900.6	0.99209	82.3	4.93*10 ¹²
5	75	3	26.8	9192.1	0.99999	76.4	4.58*10 ¹¹
6	50	2	28.3	9801.6	-	81.5	1.89*10 ¹²

a) Pre-exponential factor.

Analysis of the fits revealed an average E_a^{APP} of 83.3 kJ mol⁻¹, with a standard deviation of 4.2 kJ mol⁻¹. The pre-exponential factor showed an approximately linear dependence on concentration of the catalyst between 50 ppm and 300 ppm. There was a relatively large spread in the obtained values, which is attributed to the modest number of points available for each fit. Fits that were based on four data points (*i.e.*, at 300, 200, and 100 ppm) were more consistent and led to an apparent activation energy of 83.8 ± 1.1 kJ mol⁻¹ and A = 2.39*10¹³ ± 1.68*10¹³. The observed spread in values suggests that more points should be added in case more accurate results are required.

In conclusion, we have performed a detailed kinetic analysis of the Mn^I-NHC transfer hydrogenation system with precatalyst **1**. The effects of catalyst deactivation were most pronounced at catalyst concentrations below 100 ppm and/or high reaction temperatures at or above 70 °C. The reaction's sensitivity to temperature reveals that the activation energy for deactivation is probably higher than the activation energy of the target reaction. The fact that the catalyst deactivates under these conditions is unfortunate because operation at high temperature and low catalyst loading leads to systems that are more applicable for industrial use, where high temperature ensures good productivity and low catalyst concentration suppresses operational cost. We therefore sought to understand this behaviour with the goal to prevent or mitigate it. First, the experimental kinetic data were compared to results from kinetic modelling studies that explored different rate equations for the deactivation reaction and enabled us to understand critical process parameters. The results of these studies are described in the next section.

5.3 Kinetic modelling

Experimental kinetic data were compared to kinetic models that were composed of systems of ordinary differential equations (ODEs) and were solved numerically with packages available in MATLAB or Python. These equations describe the concentration of the individual components as a function of time for acetophenone (A), 2-propanol (B), 1-phenylethanol (C), acetone (D), as well as the Mn catalyst (Mn), as summarised in **Figure 5.4** and **Equation 5.2–5.6**. It was assumed that different Mn species (except irreversibly deactivated ones) readily interconvert and therefore are reasonably described by one bulk concentration. (Note that if this is not the case, concentrations of individual species could be included in the model to construct a so-called microkinetic model.)

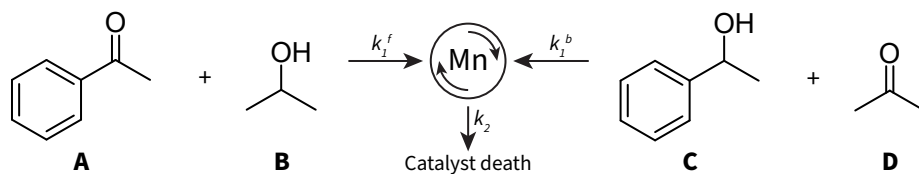


Figure 5.4. Reaction scheme for Mn-catalysed transfer hydrogenation with irreversible catalyst deactivation.

$$\frac{dC_A}{dt} = -k_1^f C_A C_B C_{Mn} + k_1^b C_C C_D C_{Mn} \quad (5.2)$$

$$\frac{dC_B}{dt} = -k_1^f C_A C_B C_{Mn} + k_1^b C_C C_D C_{Mn} \quad (5.3)$$

$$\frac{dC_C}{dt} = +k_1^f C_A C_B C_{Mn} - k_1^b C_C C_D C_{Mn} \quad (5.4)$$

$$\frac{dC_D}{dt} = +k_1^f C_A C_B C_{Mn} - k_1^b C_C C_D C_{Mn} \quad (5.5)$$

$$\frac{dC_{Mn}}{dt} = -k_2 C_{Mn}^n; \text{ with } n=0,1,2 \quad (5.6)$$

Our modelling campaign enabled us to qualitatively study the effect of transient catalyst deactivation on the transfer hydrogenation's reaction progress and the bulk composition. We assumed that deactivation is driven by a single, intrinsic process (*i.e.*, of the third kind) with reaction rate constant k_2 . Three different reaction rate models were investigated that considered this catalyst deactivation reaction as an irreversible zeroth, first, or second order process. These relatively simple models were selected to provide generalisable results and prevent fitting of 'better' but arbitrary models. Values for the reaction rate constants k_1^f and k_1^b were determined from experimental data and were assumed to follow Arrhenius behaviour (**Table 5.3**).

Table 5.3. Kinetic parameters used in modelling campaign.^{a)}

Entry	Temperature [°C]	k_1^f [l ² mol ⁻² h ⁻¹]	k_1^b [l ² mol ⁻² h ⁻¹]	$K_{eq}^{b)}$ [-]
1	40	9.06*10 ²	2.66*10 ³	0.3407
2	50	2.45*10 ³	6.66*10 ³	0.3685
3	60	6.25*10 ³	1.56*10 ⁴	0.4008
4	70	1.51*10 ⁴	3.44*10 ⁴	0.4391
5	80	3.47*10 ⁴	7.15*10 ⁴	0.4850

a) See **Table 5.2**. Input used: $A = 2.391 \cdot 10^{13}$, $E_a^{APP} = 83.8 \text{ kJ mol}^{-1}$. b) See **Table 5.1**.

The deactivation reaction rate constant k_2 was fit to experimental data in two different ways. First, k_2 was fit globally to experimental data obtained at identical temperature but different catalyst loading. In this case one global value for k_2 was obtained for a given 'temperature set' that sought to describe *all* kinetic traces at that temperature. Parameter k_2 was also fit to individual curves, which provided a series of values for k_2 at each temperature.

The fitting method that produced one global parameter k_2 for runs at different Mn concentrations but identical temperature arguably is the most realistic for the real-world system. (Because reaction rate constants predominantly change with temperature, and not, *e.g.*, concentration.) This constrained fit, however, could not capture the complex behaviour of the experimental concentration profiles. Individual fitting of each curve enabled us to obtain better fits and approximate the catalyst concentration profiles in more detail for each reaction.

Experimental data were first compared to a reference model that did not include terms for catalyst deactivation (*i.e.*, without **Equation 5.6**). This enabled us to understand the real system's divergence from the ideal situation (**Figure 5.5**). The observed deviation between experimental data and predicted yields (referred to as Δ) was characterised with L^2 norms that were determined for individual fits, where each point was weighed equally. The L^2 norm effectively computes the Euclidean distance between two points in space (**Equation 5.7**), where C_C^{Num} denotes the numerical solution and C_C^{Exp} the experimental value. The determined L^2 norms were summed so that one measure of error was obtained for each model at each temperature. Kinetic traces of the best performing deactivation models are shown in **Figure 5.6** (individual fit) and **Figure 5.7** (global fit). An overview of the obtained model errors is provided in **Figure 5.8**.

$$\Delta = \left\| C_C^{Num} - C_C^{Exp} \right\|_2 \quad (5.7)$$

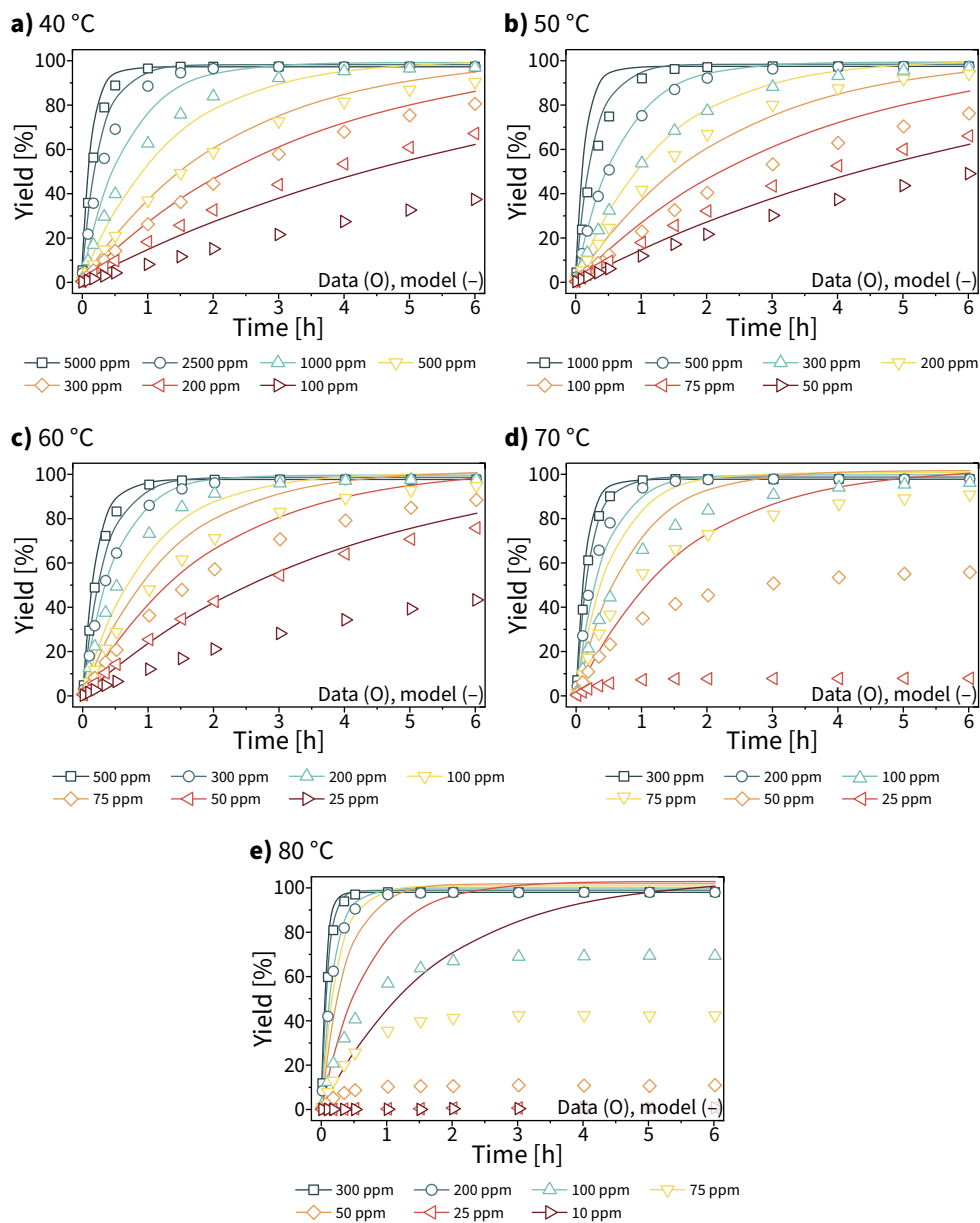


Figure 5.5. Kinetic traces of deactivation experiments at varied temperature and catalyst loading (O) versus model results (-). The reference model did not include any deactivation effects and the catalyst concentration was therefore constant. Experimental data from **Figure 5.1**.

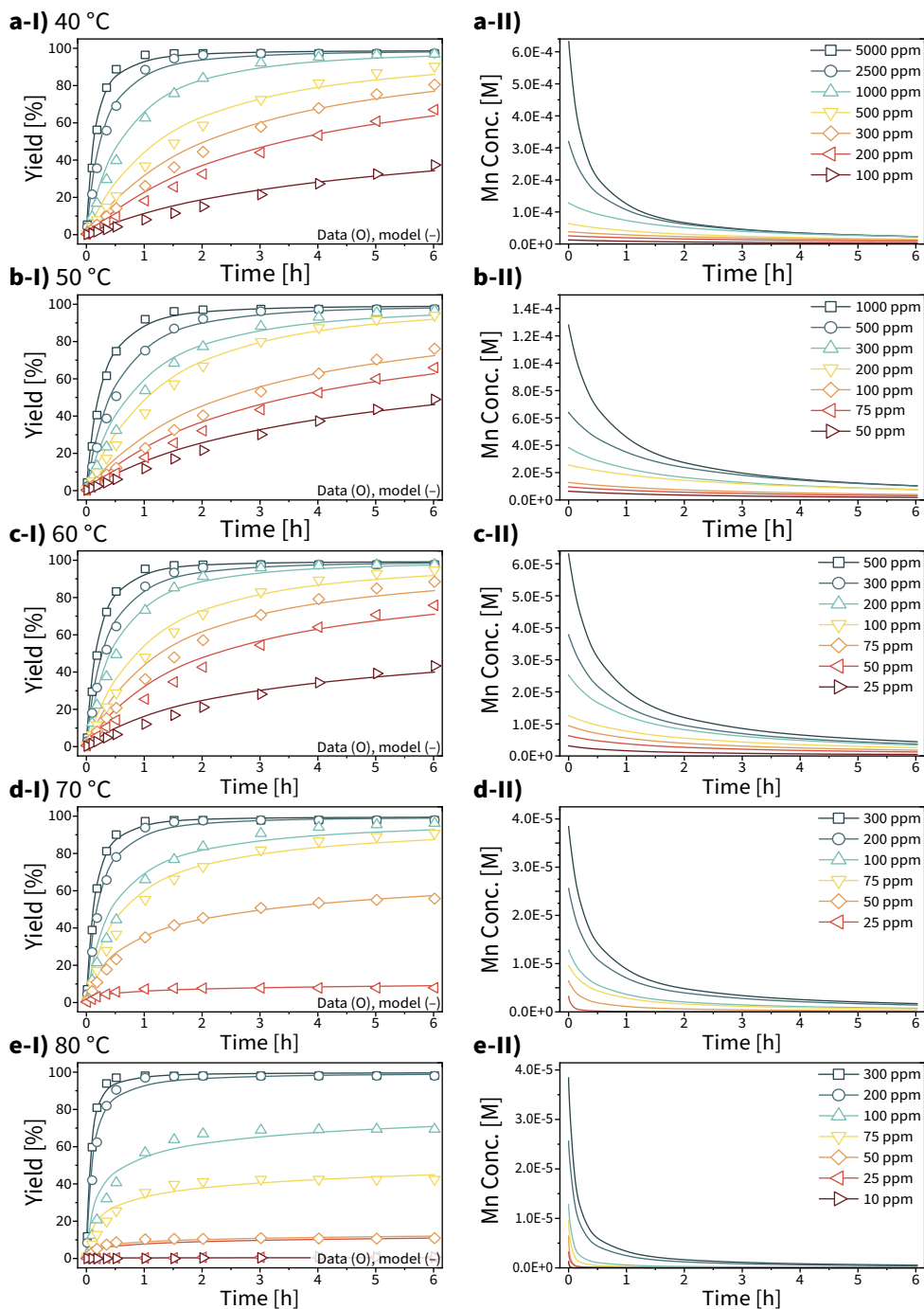


Figure 5.6. Plots I: Kinetic traces of deactivation experiments at varied temperature and catalyst loading (O) versus model results (-). The model used individually-fit values for k_2 and featured a second order catalyst deactivation reaction. Experimental data from **Figure 5.1**. Plots II: Numerical solution for catalyst concentration.

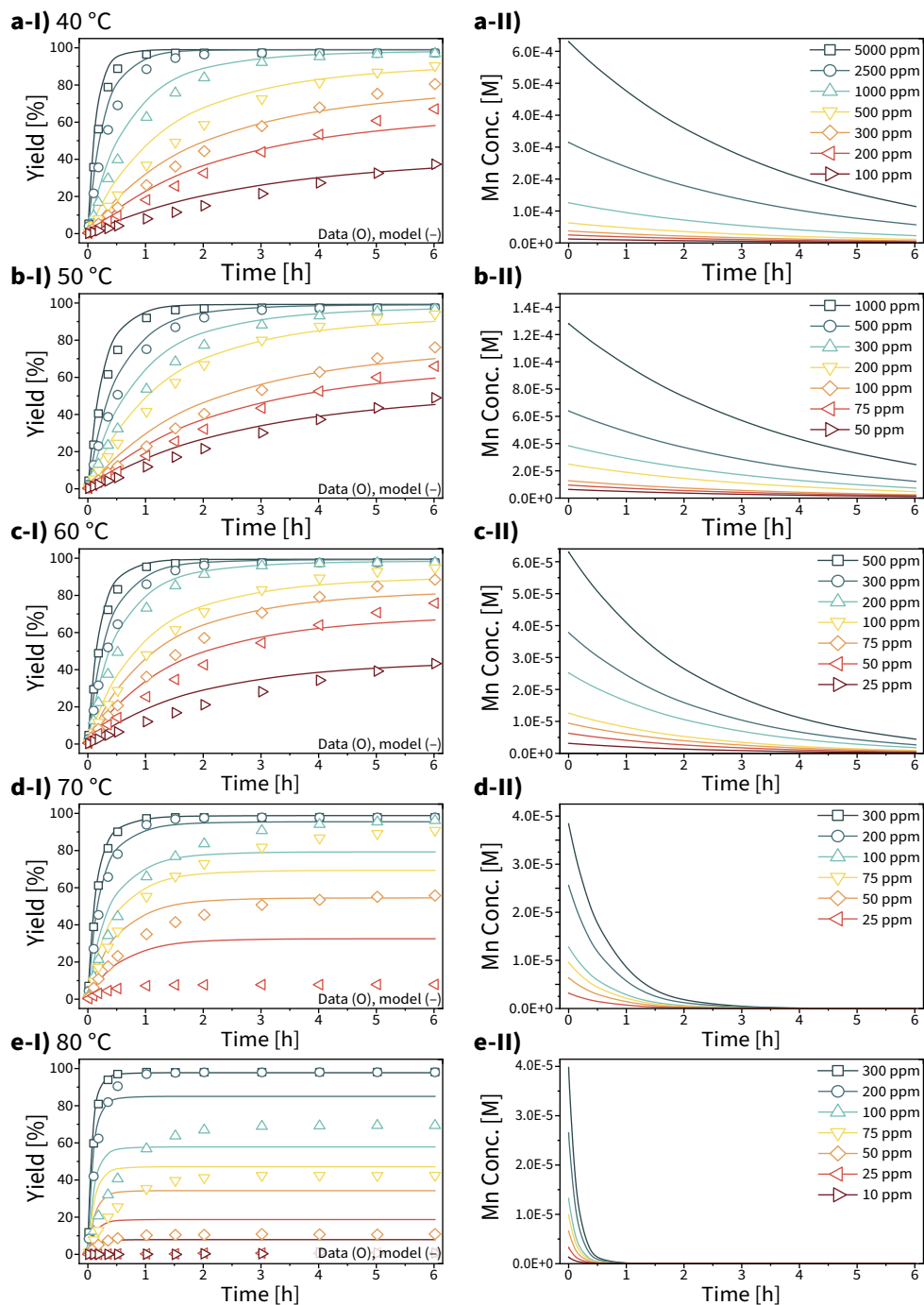


Figure 5.7. Plots I: Kinetic traces of deactivation experiments at varied temperature and catalyst loading (O) versus model results (-). The model used a globally-fit value for k_2 and featured a first order catalyst deactivation reaction. Experimental data from **Figure 5.1**. Plots II: Numerical solution for catalyst concentration profile.

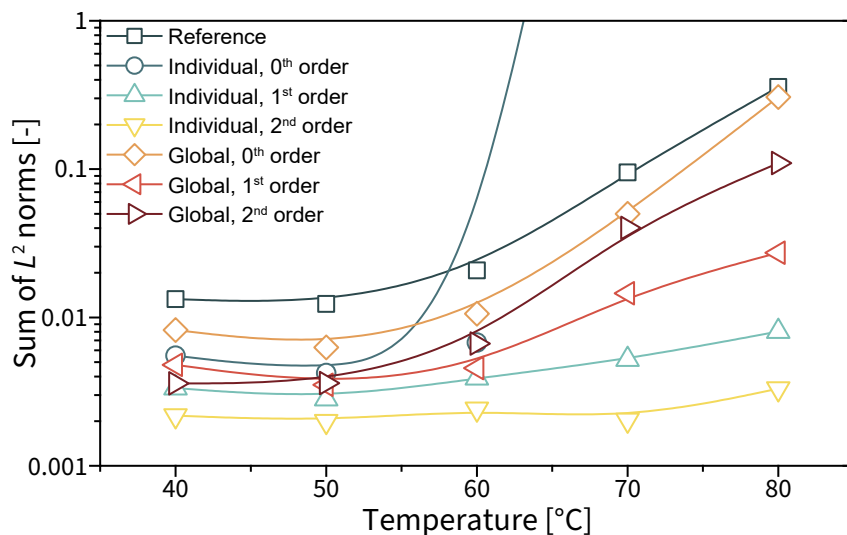


Figure 5.8. Summed L^2 norms that describe the error of the model compared to the experimental data. Note that the sum of L^2 norms is plotted logarithmically and that lower values indicate a better fit.

The reference model accurately described experiments at high catalyst concentration and/or low reaction temperature, but not those at reduced catalyst loading and/or at higher temperature (**Figure 5.5**). These results are in line with our previous finding that catalyst deactivation is most pronounced at low catalyst loading and high temperature. Our experiments at high catalyst concentration were designed to behave more or less ideally, while experiments performed with little catalyst were anticipated to deactivate quantitatively. This behaviour could not be captured by the reference model because it did not incorporate a catalyst deactivation term that would prevent the mixture from reaching the specified thermodynamic equilibrium.

Inclusion of a catalyst deactivation term universally improved model accuracy (**Figure 5.8**). The best agreement between data and model was obtained when parameter k_2 was fit to individual kinetic curves (**Figure 5.6**). This is reasonable because the globally-optimised solution occupies only a subset of the parameter space available to the individually-fit model. The additional degrees of freedom available to the individually-fit models translate to better fits. An individually-fit second order deactivation model resulted in the lowest overall deviation between the data and the model (**Figure 5.6**). The best globally-optimised model featured a first order catalyst deactivation reaction (**Figure 5.7**). Zeroth order models occasionally were numerically unstable and resulted in large absolute errors and negative catalyst concentrations.

Inclusion of a catalyst deactivation term thus unambiguously improved the kinetic model's accuracy. The total error, as characterised by the sum of L^2 norms, was reduced by an order of magnitude from $\Delta = 0.499$ for the reference model, to 0.012 for the second order (individual) model, and 0.055 for the first order (global) model. However, despite these large improvements, relatively large deviations were still observed that lead to two possible conclusions. First, it is possible that the kinetic models are accurate and representative, but that the experimental data is not. We propose that this scenario is unlikely; experimental reproducibility was verified frequently and no significant deviations were observed throughout the experimental campaigns described in this dissertation.

In the second situation the experimental data is accurate and the difference between it and the model is caused by an incorrect or insufficiently complex model. The deactivation rate equations were selected as general and representative examples, and no specific rationalisation can be provided to favour one model over the other. (This therefore also precludes fitting of 'better' but arbitrary functions.) It is thus reasonable to conclude that the decomposition process is not well-defined, or is governed by multiple simultaneous processes. We therefore concluded that detailed chemical insight into the nature of the catalytic cycle and deactivated species was required, and continued to perform such experiments.

5.4 NMR and FTIR stoichiometric reactivity studies

The chemistry of $\text{Mn}^{\text{I}}\text{-NHC } \mathbf{1}$ was further investigated with dedicated stoichiometric reactivity experiments that potentially enabled us to identify catalytically relevant species and resting states, as well as look for signs of deactivation. Mixtures were analysed with FTIR and, where possible, NMR spectroscopy. Similarly to the situation described in the previous two chapters, ^1H NMR spectra occasionally featured broad or noisy resonances that precluded exhaustive interpretation. FTIR spectroscopy did not suffer from this drawback and could be used more reliably to detect and identify new species.

Experiments were performed with standardised mixtures that contained the Mn complex and five equivalents of the respective reagent. Alcohols were generally present in large excess. These experiments also included a 'spectroscopy mix' that contained 50–100 equivalents of the acetophenone substrate and was designed to simulate catalytic conditions. Direct measurement of catalytic mixtures was unfeasible because of their very low Mn content; a typical experiment performed with 50 ppm $\mathbf{1}$ ($[\text{Mn}] = 6.4 \mu\text{M}$) contained only 12 μg of the complex. Such mixtures are not readily analysed with standard analytical methods and a compromise was therefore required. Mixtures were prepared in a glove box and were stirred for one

hour at room temperature, or were taken outside and heated at 70 °C for 3 hours. Afterwards, mixtures were immediately analysed without exposure to air.

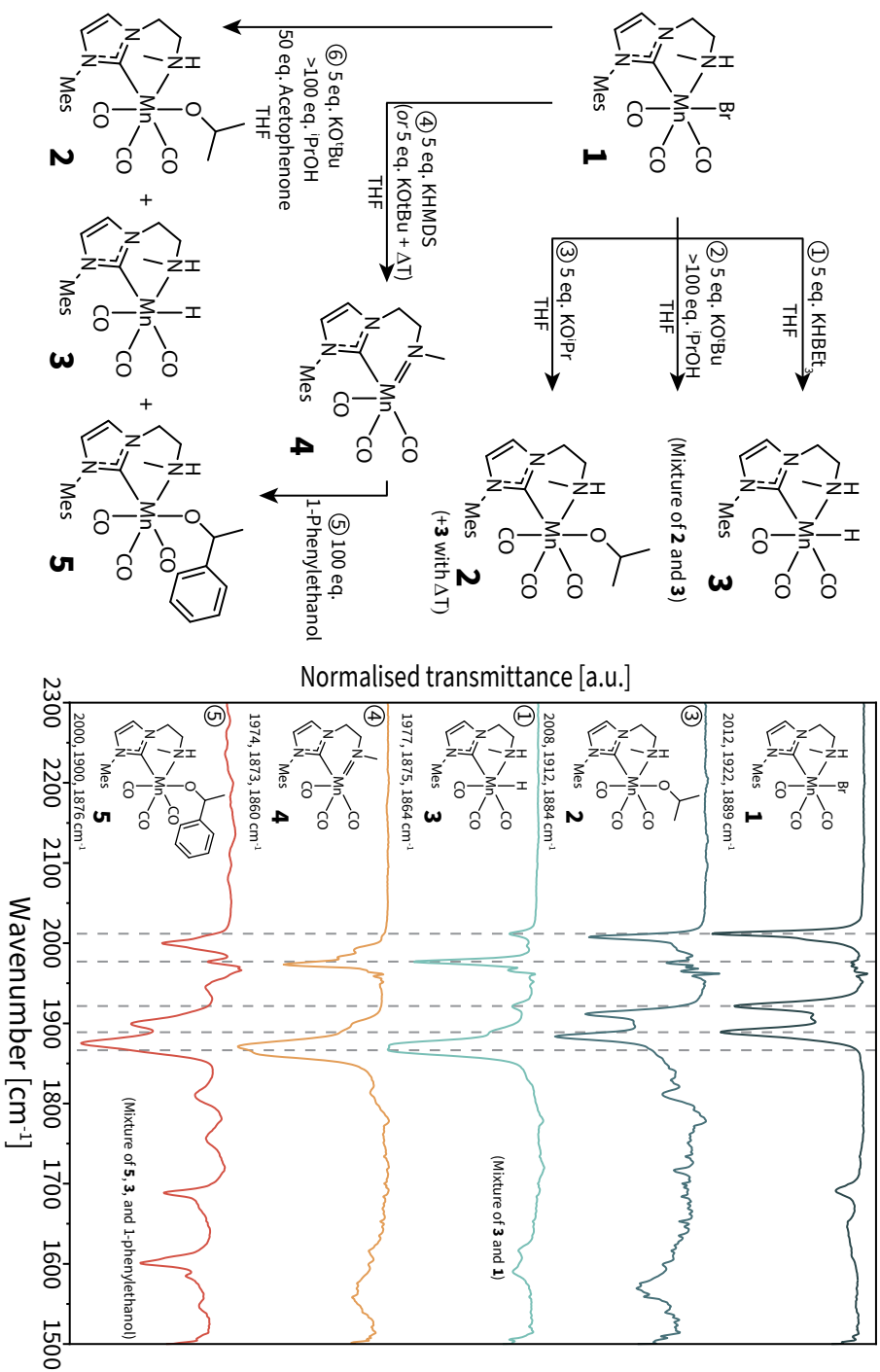
Precatalyst activation produced very similar FTIR spectra that each featured three sharp and intense bands in the Mn-carbonyl region (**Figure 5.9**). This pattern is characteristic for octahedral Mn^I tricarbonyl species. Peak location roughly correlated with electron density, with more electron-rich complexes appearing at lower wavenumbers (specifically complexes **3** and **4**). Occasionally mixtures were observed that contained multiple Mn compounds (as indicated in **Figure 5.9**).

Addition of an alkoxide base to a solution of **1** in 2-propanol led to a mixture of two new complexes that were assigned as Mn-isopropoxide **2** and Mn-hydride **3** (reaction 2). A third component was only present in trace quantities and could not be identified. The ability of **1** to form detectable hydrides at room temperature contrasts with the Mn^I-N,N' precatalyst that was described in **Chapter 2**, which was found to only produce the corresponding Mn-isopropoxide complex. This suggests that β -hydride elimination for the Mn^I-NHC system has a lower activation barrier compared to the Mn^I-N,N' complexes.

Manganese isopropoxide **2** is also formed directly from the reaction of Mn^I-NHC complex **1** with potassium isopropoxide in THF (**Figure 5.9**, reaction 3). Deprotonated Mn-amido complex **4** was observed if a non-nucleophilic (KHMDS) or sterically hindered (KO^tBu if heated) base was used to activate the precatalyst (reaction 4). This species featured a broadened ¹H NMR spectrum (not shown) and had a practically identical FTIR spectrum as that of Mn hydride **3**, in which the characteristic carbonyl bands shifted by only a few reciprocal centimetres. (Spectra were acquired at the maximum spectral resolution of 2 cm⁻¹. These minor shifts are of the same order of magnitude.) Addition of an alcohol (2-propanol or 1-phenylethanol) to the deprotonated complex led to the rapid formation of the corresponding Mn-alkoxide **2** or **5**, as was evidenced by the pronounced colour change from red/pink to bright yellow.

Mn-hydride **3** presumably is the catalytically active species that reduces the ketone substrate. Compound **3** was observed in several mixtures and could be obtained from the reaction of **1** with KHBET₃, or that with KOⁱPr, and KO^tBu in isopropanol. The Mn-hydride resonance appeared in the ¹H NMR spectrum as two sharp singlets at $\delta = -4.07$ and $\delta = -4.45$ ppm (see **Figure 3.9**). Addition of acetophenone to a mixture that contained Mn-hydride **3** led to the corresponding 1-phenylethanol product, acetone, and Mn complex **5**, which was identified as Mn-1-phenylethoxide. The chemistry of Mn^I-NHC complex **1** thus is conceptually similar to that of the Mn^I-N,N' precatalysts described in **Chapter 2**, and most probably operates *via* the well-established Noyori-Ikariya mechanism.

Figure 5.9. Summary of observed reactivity for Mn-NHC **1** towards various reagents, and corresponding transmission FTIR spectra of selected reactions.



Measurements were finally performed on the standardised ‘spectroscopy mix’ that was designed to be compatible with multiple analytical techniques. Mixtures were stirred at room temperature for 1 hour or heated to 70 °C for 3 hours before analysis with FTIR, ^1H NMR, and ESI-MS. The major (and in fact only observable) Mn-species was Mn-isopropoxide **2**. This is reasonable because of the large excess of 2-propanol present in the system (**Figure 5.10**). Spectral intensity of the heated mixture was somewhat lower compared to the room temperature mixture, which might have been caused by a marginally higher dilution factor or the formation of FTIR-invisible species.

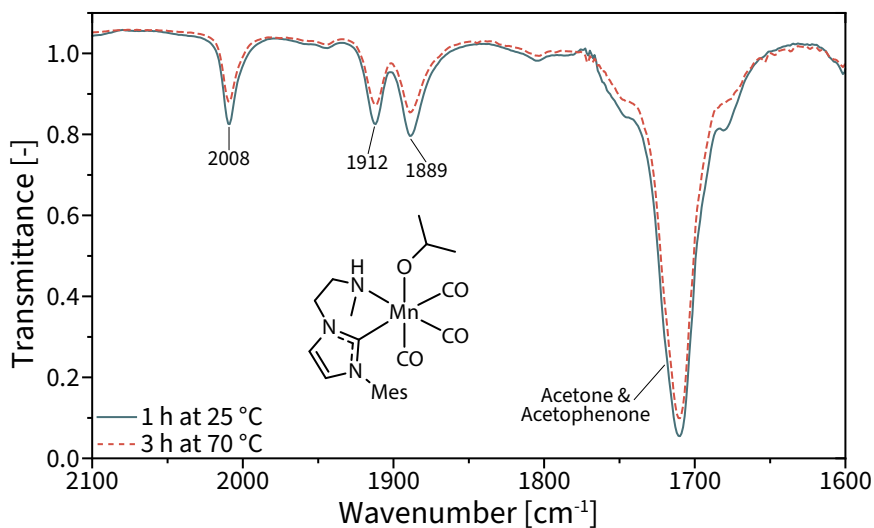


Figure 5.10. FTIR spectrum of ‘spectroscopy mix’ after reactions.

^1H NMR and ESI-MS did not produce useful information. ^1H NMR spectra featured very large peaks originating from isopropanol, acetophenone, and 1-phenylethanol that obstructed further interpretation. No new species were observed with ESI-MS. (Ionisation of Mn carbonyl species is difficult, or at least inconsistent. This means that ESI-MS often can only detect species that already contain a charge (*i.e.*, cationic or anionic complexes with an ionic counterion).)

In summary, a stoichiometric reactivity study was performed with Mn^I-NHC precatalyst **1**. This study provided insight into the formation of a series of octahedral Mn^I tricarbonyl species that are suspected intermediates in the catalytic cycle. No intermediates were observed that could directly be associated with the catalyst deactivation process, and our efforts to detect such species were hampered by the very low Mn content of such mixtures. (Which, although unfortunate, is not surprising; catalyst deactivation, by its very nature, is a minor phenomenon that is

easily masked by major components of a reaction mixture or catalyst resting states.) We did, however, observe that ^1H NMR spectral broadening was most pronounced when base was present in the mixture. These conditions also led to a relative loss of signal intensity in FTIR, which could indicate the formation of paramagnetic or NMR-silent species that was further investigated with EPR spectroscopy.

5.5 Electron paramagnetic resonance spectroscopy

The broadened ^1H NMR resonances hindered spectral interpretation and hinted at the presence of paramagnetic species. (Paramagnetic NMR spectroscopy has several applications that are discussed elsewhere.¹⁵) The formation of paramagnetic complexes would probably be the result of redox chemistry that takes place at the Mn^{I} centre. For example, oxidation or disproportionation of Mn^{I} could produce paramagnetic Mn^{II} that is no longer catalytically active.

Mn^{I} has a d^6 electron configuration and almost exclusively exists as diamagnetic, octahedral complexes. This low oxidation state of manganese requires stabilisation by strong field ligands that favour low-spin complexes, notably CO, NO, or carbenes. (There are some reports of high-spin Mn^{I} complexes, but these are rare.¹⁶) The formation of paramagnetic species from diamagnetic Mn^{I} can be rationalised with crystal field theory (**Figure 5.11**). Crystal field theory provides a simplified but generally applicable model with fair predictive power. More accurate evaluation of electronic and geometric properties requires dedicated quantum chemical calculations at the cost of generalisability.

Complexes with similar ligands but alternative electronic configurations or geometries can be diamagnetic or paramagnetic (**Figure 5.11**). Practically all Mn^{II} (d^5), Mn^0 (d^7), and $\text{Mn}^{-\text{I}}$ (d^8) complexes are paramagnetic if one assigns electrons in accordance with the Aufbau principle, Hund's first rule, and the Pauli exclusion principle. A trigonal bipyramidal d^8 species is an exception that is predicted to be diamagnetic. Most significant electronic and geometric changes to Mn^{I} species might thus result in detectable paramagnetic species.

Electron paramagnetic resonance spectroscopy (EPR, occasionally called ESR for *electron spin resonance*) is the most important tool for the characterisation of paramagnetic compounds. (The other being the measurement of magnetic susceptibility using a Gouy balance.) It is significantly more sensitive than NMR techniques, which makes it particularly useful to study the structure of (short-lived) organic radicals, metalloenzyme catalysts, and transition metal complexes at relatively low concentrations.^{17–19} EPR spectroscopy therefore is one of the most promising techniques to study (minor) deactivation products of Mn^{I} catalysts.

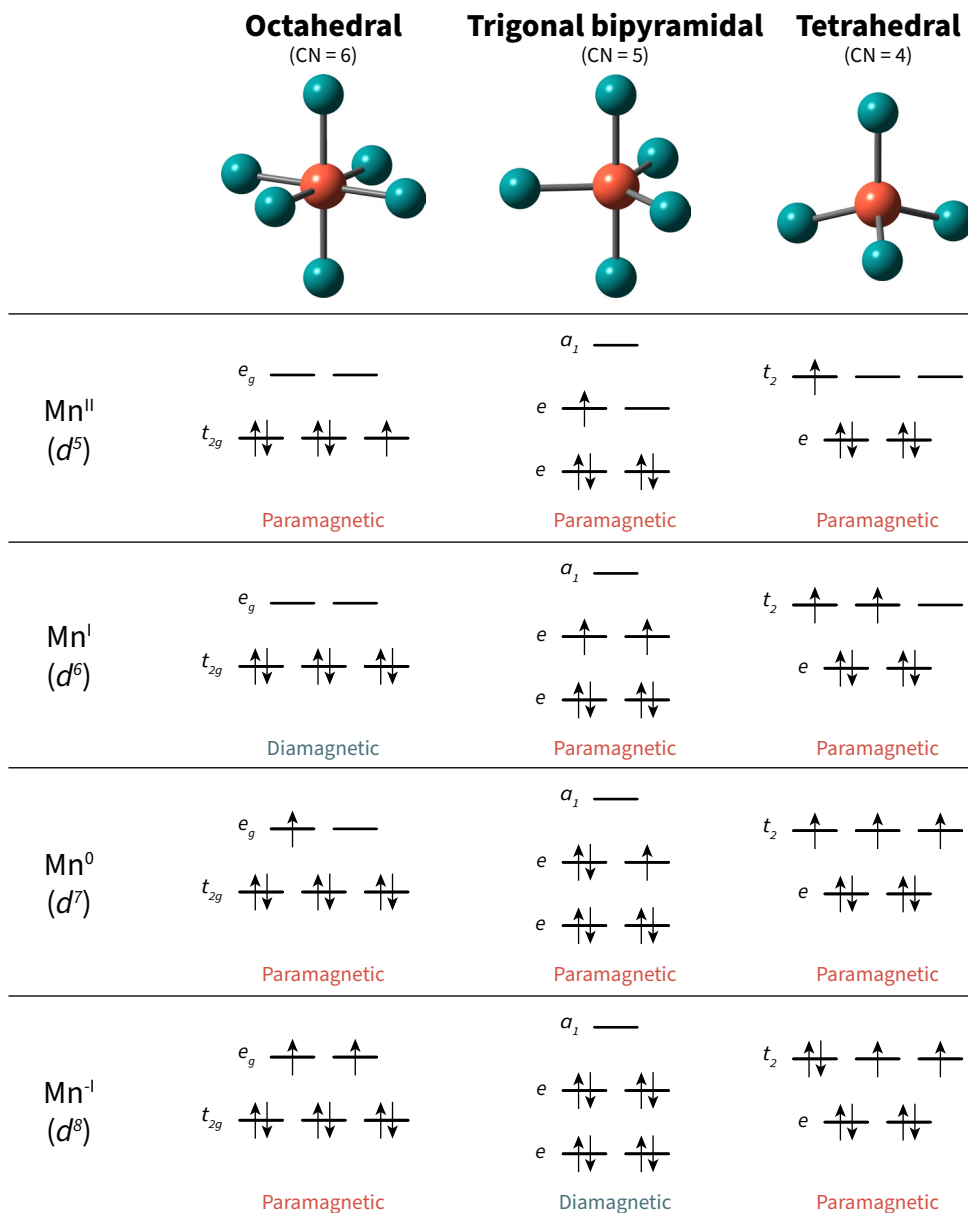


Figure 5.11. Expected crystal field d orbital splitting for Mn complexes of different geometries with strong field ligands.

EPR spectroscopy has been used before to solve similar problems. For example, it was instrumental for the elucidation of the structure of the manganese cluster that is responsible for photosynthetic water oxidation in plants.²⁰⁻²² The reactive centre of this oxygen evolving complex is now thought to consist of an Mn_4CaO_n

cluster that contains mixed oxidation states between Mn^{II} and Mn^{IV}, depending on the specific enzyme and state in the catalytic cycle.^{20,23}

The paramagnetic behaviour of Mn is complex and can manifest itself in different ways. ⁵⁵Mn is the only naturally occurring isotope of manganese and has a nuclear spin of $I = 5/2$, which leads to a six-fold hyperfine splitting of the EPR resonance.²⁴ However, hyperfine splitting of transition metal complexes is predominantly controlled by electronic spin, and thus also depends on the oxidation state and specific geometry of the nucleus under study. For example, high-spin Mn^{II}, Mn^{III}, and Mn^{IV} ions have electronic spins of $S = 5/2$, 2, and 3/2, respectively, that split the signal in $|2S+1|$ lines.²⁰ Signal intensity theoretically scales with $S(S+1)$. The total number of lines *in principle* is a function of the number of paramagnetic nuclei, their spins, and the specific coupling between those centres. In practise, however, it is not possible to *a priori* predict which transitions will be observed. Mononuclear complexes often have well-defined and characteristic hyperfine structures, while multinuclear Mn species frequently give complex spectra that don't necessarily have well-resolved hyperfine features. Interpretation of such spectra therefore is significantly more challenging.

The open literature describes only a very small number of EPR studies of low oxidation state Mn (carbonyl) complexes.^{25–29} Most of these works describe the detection of paramagnetic species after oxidation from Mn⁰ or Mn^I (and thus investigated Mn^{II}). To the best of our knowledge there is only one study that acquired EPR spectra of a paramagnetic pentacoordinate square pyramidal Mn⁰ complex.²⁵ The spectrum of this Mn⁰ monoradical featured six lines centred around $g = 2.0755$. Its square pyramidal structure was confirmed with single-crystal XRD.

The deactivation reaction of Mn^I complex **1** was studied with EPR spectroscopy. X-band EPR measurements were performed in continuous-wave (CW) mode at room temperature on the standardised spectroscopy mixture that was described previously. We first sought to confirm the (previously only suspected) formation of paramagnetic species under the reaction conditions. Three samples were measured. The first contained a solution of precatalyst **1** in 2-propanol and was included as a control. The second and third samples contained the precatalyst and 5 eq. KO^tBu in 2-propanol and were kept at room temperature and 70 °C, respectively. The resulting spectra are summarised in **Figure 5.12**.

The initial measurements revealed the presence of a broad signal for the samples that contained precatalyst **1** and base. The signal was centred at 340.8 mT ($g_{\text{iso}} = 2.024$), had a full width at half maximum of about 80 mT, and had a line shape that was approximately Lorentzian. No hyperfine structure could be resolved. The signal was considerably more intense in the sample that was heated overnight

at 70 °C, while it was practically absent in the control sample. This suggests that paramagnetic species form after reaction of **1** with base and that this is an activated process that is expedited at elevated temperature. Our experiments thus confirmed the formation of paramagnetic species depending on the reaction conditions.

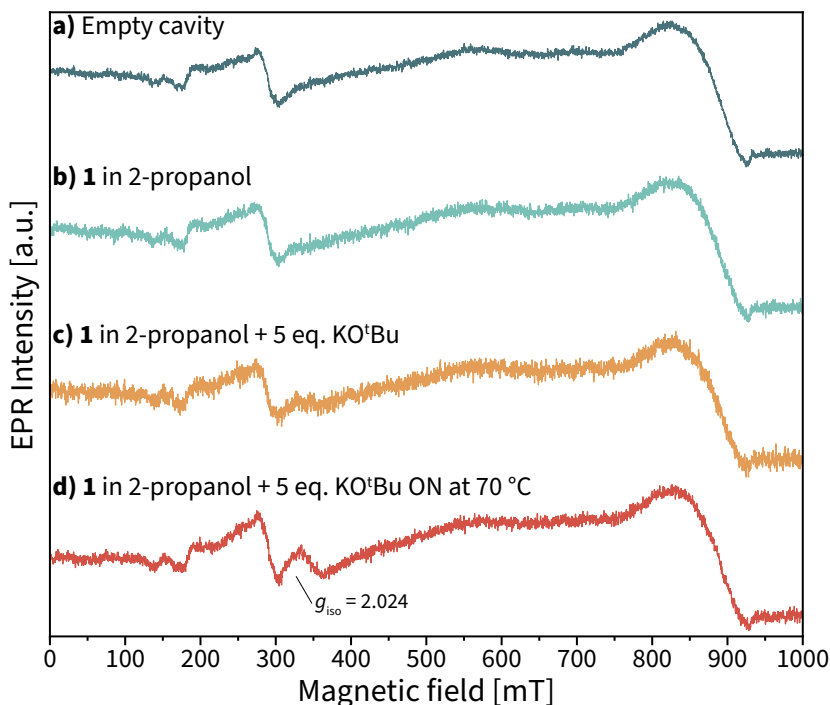


Figure 5.12. CW X-band room temperature EPR spectra of mixtures of **1**. The broad signal between 800–900 mT originates from dioxygen inside the EPR cavity. **a)** Empty cavity. **b)** Complex **1** in 2-propanol (2.36 mM). **c)** Complex **1** in 2-propanol (2.36 mM) with 5 eq. KO^tBu. **d)** Complex **1** in 2-propanol (2.36 mM) with 5 eq. KO^tBu, heated overnight at 70 °C.

Follow-up studies were conducted to understand the formation of the paramagnetic species and to potentially gain structural information. A kinetic study was performed with a mixture that contained precatalyst **1**, 5 eq. KO^tBu, and approximately 57 equivalents of acetophenone in 2-propanol ([Mn] = 1.35 mM). This allowed us to measure spectroscopy on the mixture under actual catalytic transfer hydrogenation conditions, albeit at a low substrate-to-catalyst ratio. (A further reduction of the Mn content resulted in insufficient signal intensity.) The sample was kept in liquid nitrogen and was heated to 70 °C for the indicated amount of time. CW X-band EPR was measured of the glass sample at 200 K (-73.15 °C) at the indicated time (**Figure 5.13**). Spectral intensity was normalised to the signal at 176 mT that originated from an established baseline (Mo^{III}) feature. The absence of *g* anisotropy was confirmed with Q-band EPR on the final sample.

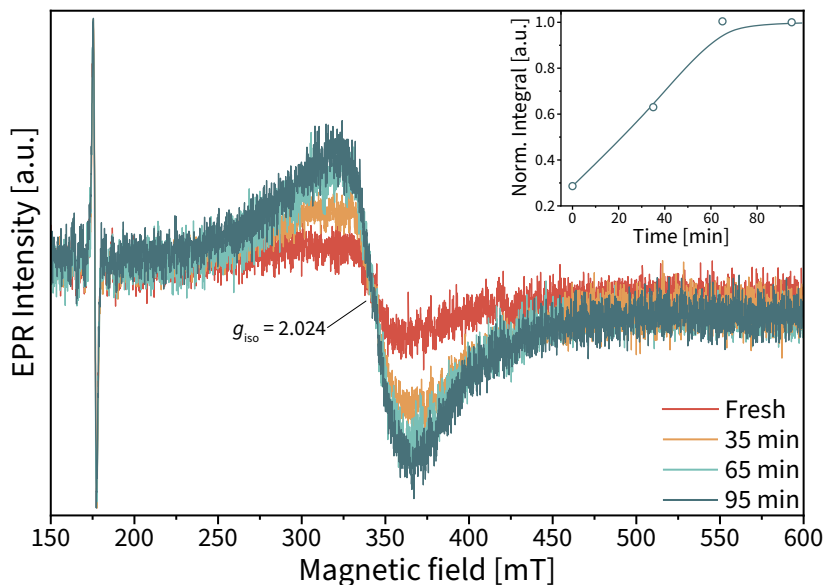


Figure 5.13. CW X-band EPR spectra of mixtures of **1** measured at 200 K at the indicated times. Microwave frequency $\nu_{mw} \approx 9.66$ GHz. Spectra were normalised to the baseline signal at 176 mT. Data obtained after overnight heating was omitted for clarity. Inset: normalised integral of broad signal centred around 340.8 mT.

The intensity of the broad signal increased for approximately 1 hour and levelled-off afterwards. This suggested that the paramagnetic species in the heated samples formed gradually and on a timescale that is similar to that of deactivation. The final ‘deactivated’ state was investigated with variable-temperature CW X-band EPR spectroscopy between 10 K and 200 K, which provided specific information on the energetics of the system. The results of these experiments are summarised in **Figure 5.14–5.15**.

The resonance at 340.8 mT showed strong temperature-dependent behaviour. It was most intense at 200 K and gradually became less so at lower temperatures. The signal disappeared at temperatures below approximately 20 K. These results suggest that the paramagnetic centres were strongly antiferromagnetically coupled and that the (energetically elevated) high-spin state was thermally populated.³⁰ The results were fit with the Boltzmann distribution function, which correlates the probability that a certain energy level is populated to the temperature of the system (**Equation 5.8** and **Figure 5.15**). ΔE represents the energy difference (in kJ mol^{-1}) between the ground and elevated states, where n_0 is the population of the lower state, and n is the population of the higher energy level. This energy can be converted to the wavenumber of a single photon with **Equation 5.9** (N_A is Avogadro’s number, h is Planck’s constant, and c is the speed of light in a vacuum). The energy difference was determined from the fit at $1.2 \pm 0.3 \text{ kJ mol}^{-1}$ or $106 \pm 24 \text{ cm}^{-1}$.

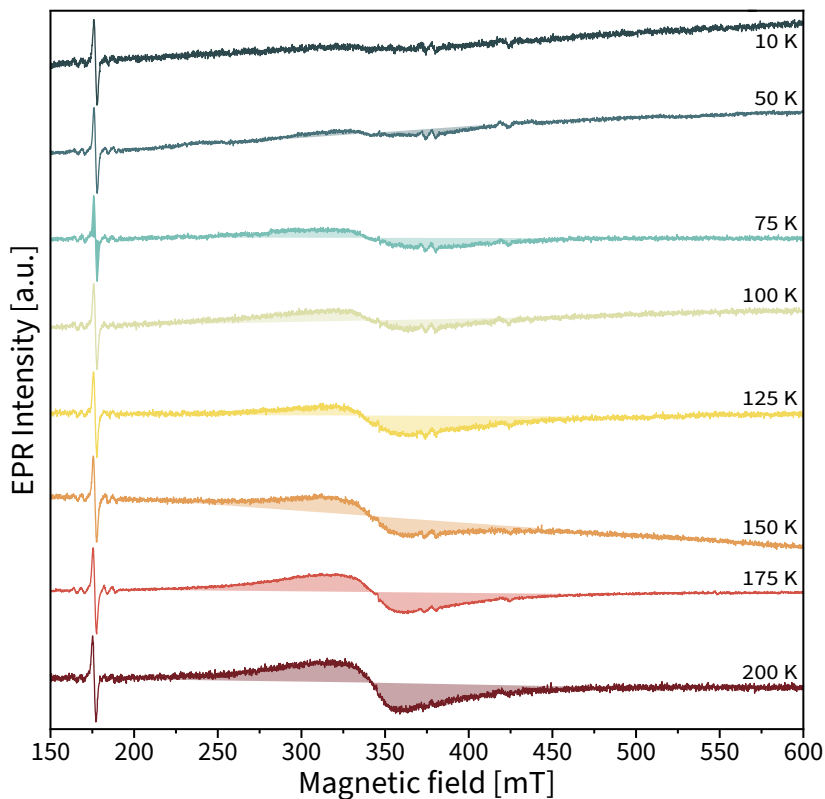


Figure 5.14. CW X-band EPR spectra of final deactivated mixture of **1** measured at the indicated temperature in the range of 10 K–200 K. Spectra were normalised to the baseline signal at 176 mT.

$$\frac{n}{n_0} = e^{-\frac{\Delta E}{RT}} \quad (5.8)$$

$$\nu = \frac{\Delta E}{N_A hc} \quad (5.9)$$

These data also allowed an estimation of the total number of spins inside the system. Integration was relatively inaccurate due to the broad nature of the signal and should therefore only be considered an estimate. A total of 330 nmol of spins were found in the tube, compared to a theoretical Mn loading of 135 nmol. However, direct comparison of these numbers is difficult because signal intensity depends strongly on the (currently unknown) spin state of the material and its specific electronic transitions.

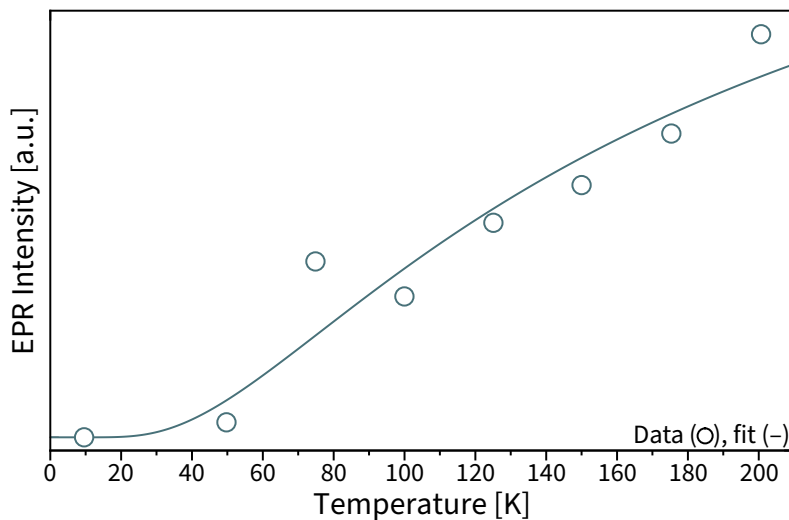


Figure 5.15. Temperature dependence of normalised spectral intensity. Accompanying data in **Figure 5.14**.

The observed broad signals that lacked resolved hyperfine structures are consistent with those of extended networks of structurally undefined, paramagnetic clusters. This is supported by several features of the presented data. First, larger clusters—even relatively small tri- or tetranuclear paramagnetic centres—often exhibit broad and complex resonances that are the combination of many sharper transitions.³⁰ (Although other broadening mechanisms also exist.³⁰) Numerous literature reports indicate that it is probably reasonable to assume that well-defined, mononuclear Mn centres would have sharp lines with observable hyperfine splitting. The absence of such hyperfine structure thus probably means that the paramagnetic centres are not mononuclear and/or well-defined.

Secondly, the antiferromagnetic coupling constant determined from temperature dependence studies ($J = 106 \pm 24 \text{ cm}^{-1}$) is of a similar order of magnitude as those reported for high-spin Mn-oxo and Fe-oxo clusters.^{30–31} The tendency of Mn (and Fe) to form antiferromagnetically coupled clusters with μ_{22} chalcogen or halogen bridges has been described in detail in the open literature.^{30,32–38} These species most often consist of mixed oxidation state Mn clusters that are linked by oxygen bridges. This bridging allows for antiferromagnetic coupling between the nuclei because there is good overlap between the Mn d_{xy} and oxygen p orbitals.³⁰

The observed g_{iso} value of 2.024 is fairly close to that of the free electron ($g = 2.002$), which suggests that the Mn centre most probably resides in an oxidation state of II or lower. (A gradually increasing value of g would be expected for higher oxidation states once d orbitals become occupied.) To the best of our knowledge there are no examples in the open literature of extended, low-oxidation state Mn clusters

(i.e., Mn⁴²). The well-defined (diamagnetic) Mn- μ_2 -isopropoxy dimer described in **Chapter 4** perhaps is the best demonstration of the feasibility of such chemistry. Unfortunately, structural elucidation on basis of EPR spectroscopy is not straightforward and is best performed in conjunction with dedicated modelling efforts. Such modelling strongly relies on the availability of *a priori* hypotheses of the species' nature, because specific structures must be calculated and small structural differences can lead to largely different spectra. Such calculations were therefore not performed because insufficient knowledge was available on the structure of the observed clusters. Instead, further (spectroscopic) investigations were performed to study the structure and oxidation state of the deactivated species. These experiments included TEM, X-ray photoelectron spectroscopy, and X-ray absorption measurements, and are described below.

5.6 Transmission electron microscopy

The potential formation of Mn-containing clusters prompted us to look for such species with high-resolution transmission electron microscopy. Even though this technique has not yet found extensive use in the study of homogeneous catalysts, it *in principle* is sensitive enough to resolve low-nuclearity, sub-nm clusters.³⁹ To give a sense of scale: most reports on Mn-oxo clusters describe Mn-Mn distances of 2.80 Å and 3.51 Å for μ_2 -oxo and μ_1 -oxo bridges, respectively.⁴⁰ An intermanganese distance of 2.855 Å was found for the Mn- μ_2 -isopropoxy dimer described in **Chapter 4**. Small clusters may thus already be large enough to be detectable with high-resolution electron microscopy.

Electron microscopy has—for obvious reasons—not found extensive use in the characterisation of homogeneous catalytic systems. Perhaps the most prominent application of electron microscopy in the field of homogeneous catalysis has been to distinguish between homogeneous and heterogeneous modes of catalysis.^{1,41–46} Here, TEM was used to characterise metallic nanoparticles of Fe, Ru, Rh, Pt, or Pd that formed from well-defined mononuclear complexes under the reaction conditions. In some cases these metallic nanoparticles were identified as the catalytically active component, instead of the ‘homogeneous catalysts’ that were added to the reaction mixture.^{42,45–46}

It should be noted that, even though electron microscopy is a very powerful characterisation technique, it also has a number of disadvantages or pitfalls that one should be aware of. This is particularly true when it is applied to non-standard problems. (Like the one described in this chapter.) The presence or absence of particulate matter cannot by itself be proof for or against the formation of nanoparticles or clusters, let alone their relevance for catalysis—the absence

of evidence is not the same as evidence of absence. Statistics are also important. Unless TEM is used to analyse large ensembles of particles (like those found in heterogeneous catalysts that contain deposited nanoparticles), one cannot guarantee that the analysis was representative for the bulk material. Electron radiation has further been reported to produce nanoparticles from homogeneous samples, even at low acceleration voltages.⁴⁵⁻⁴⁹ However, with these limitations and pitfalls in mind, electron microscopy can be a useful technique for the characterisation of post-reaction catalytic mixtures.

Three samples were submitted for HR-(S)TEM-EDX analysis. EDX (*electron-dispersive X-ray spectroscopy*) mapping was used to measure the particle's elemental composition. This enabled us to distinguish Mn-containing materials from other solids, such as KBr, and remains of molecular sieves (a zeolite-based drying agent). The first two samples were used as controls and contained the 2-propanol solvent and a solution of **1** in 2-propanol, respectively. The third grid was loaded with a solution of the standardised, heated reaction mixture that had also been used in previous analyses.

TEM micrographs of the isopropanol solvent revealed a number of large (>>100 nm) agglomerates that predominantly consisted of Na, K, Al, Si, and O (**Figure 5.16**). This elemental composition is in line with that of the zeolite drying agent, which the manufacturer claims has a composition of $0.6 \text{ K}_2\text{O} : 0.4 \text{ Na}_2\text{O} : 1 \text{ Al}_2\text{O}_3 : 2.0 \pm 0.1 \text{ SiO}_2 : x \text{ H}_2\text{O}$.⁵⁰ This sample did not contain significant quantities of Mn, and a background level was established at approximately <0.3 at%.

The solution of precatalyst **1** in 2-propanol contained similar particulate matter as the clean solvent (**Figure 5.17a**). One particle was observed that had a high manganese content of 10 at% in the EDX analysis (**Figure 5.17b**). This particle had relatively sharp faces and its elemental composition was consistent with that of precatalyst **1**. It was therefore identified as a crystal of **1**. Peaks were observed in the EDX spectrum that could be assigned to phosphorus and fluorine, which suggested that the material potentially contained a minor residual hexafluorophosphate impurity from the synthetic procedure (see **Chapter 3**). The combination of the two control samples indicated that some large particles were present in the solvent that had a distinct elemental composition, and that it did not contain small, well-dispersed, Mn-rich solids.

The heated reaction mixtures had rather different EM micrographs compared to the control samples, and contained both smaller and larger particles (**Figure 5.18**). The small particles were approximately 50 nm or less in diameter and were comparatively numerous. Several clusters were investigated in more detail and their elemental composition was mapped with EDX (**Figure 5.19–5.20**).

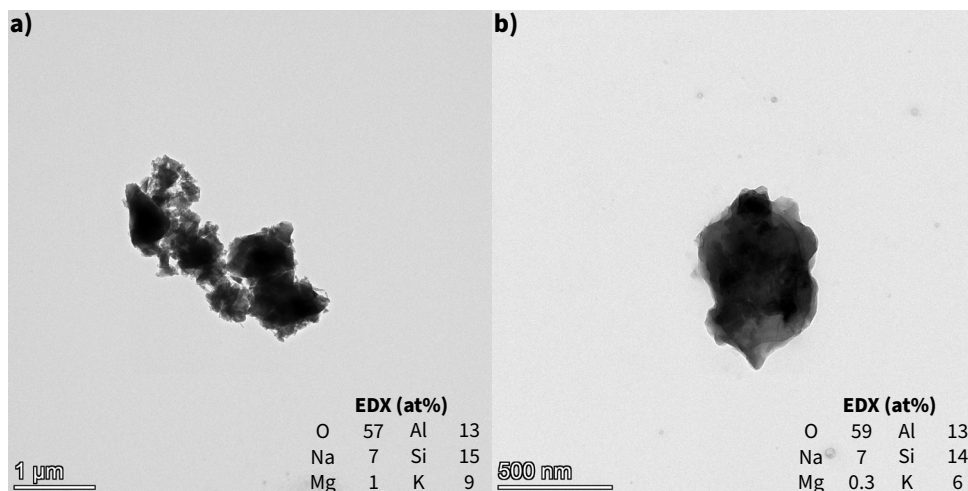


Figure 5.16. TEM micrographs and EDX results of (zeolite) particles found in the control sample that contained 2-propanol.

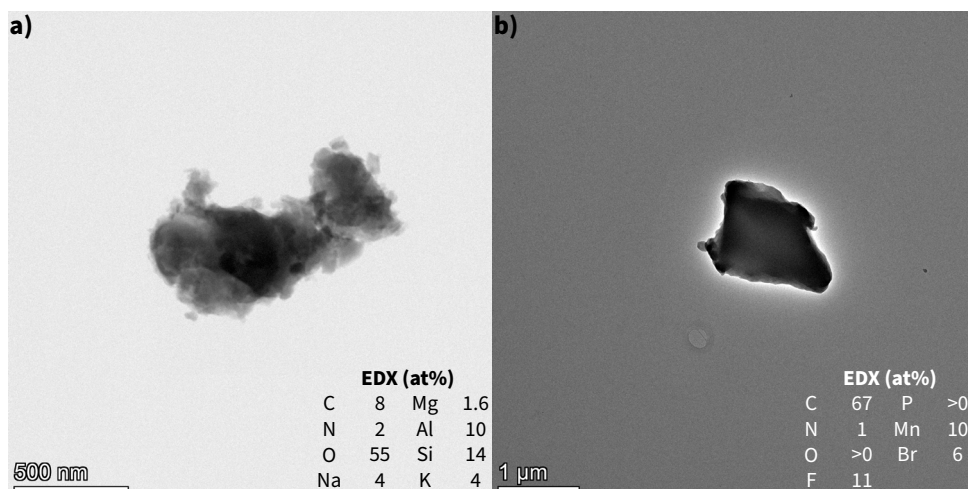


Figure 5.17. TEM micrographs and EDX results of particles found in the control sample that contained **1** and 2-propanol. **a)** Zeolite particle similar to those in **Figure 5.16.** **b)** Mn-containing particle that is most probably a crystal of the Mn precatalyst.

The aggregates predominantly contained potassium and bromine. It therefore seems reasonable to conclude that many of the observed particles consisted of potassium bromide. This salt is believed to have formed in the activation reaction of **1** with KO^tBu. These particles measured approximately 50 nm in diameter. Other elements were also observed. Manganese, potassium, and oxygen were distributed fairly even over the sample grid. Samples contained $0.9 \leq \text{at\% Mn} \leq 1.6$, which, although low, is meaningfully higher than that of the control sample

that contained only ≤ 0.3 at% Mn. If zeolite particles were present there was some apparent correlation between the location of particles and detection of these elements (**Figure 5.20**). It is possible that these porous particles effectively functioned as a deposition site during sample drying.

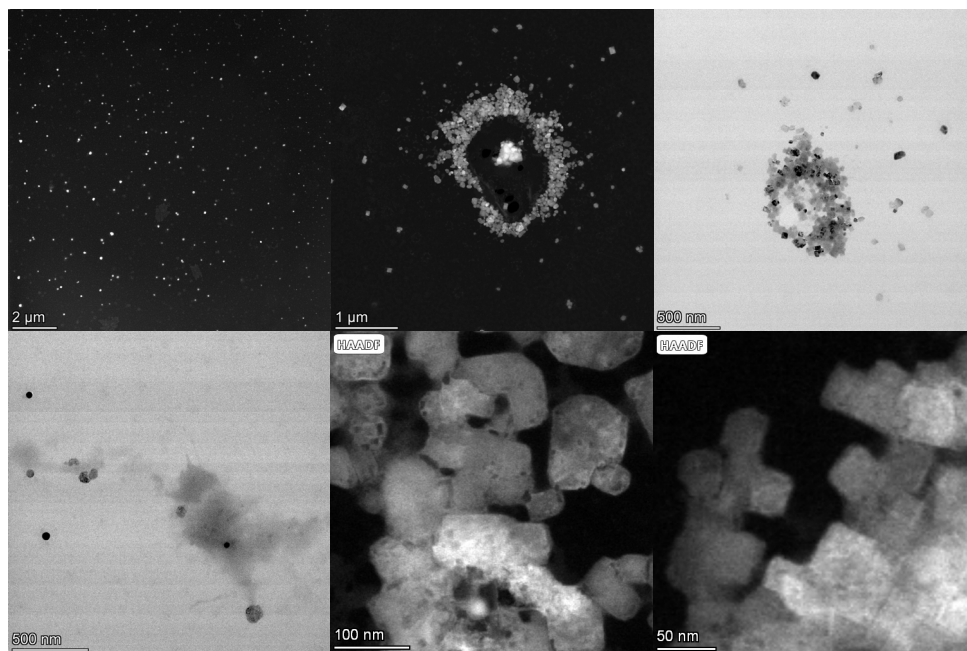


Figure 5.18. Overview of (HAADF/ADF)-TEM micrographs of particles found in sample that contained **1**, KO'Bu, acetophenone, and 2-propanol, and was heated overnight at 70 °C.

While the reaction indeed produced significant particulate matter, it remains unclear whether the observed agglomerates were formed in solution, as a result of drying during sample preparation, or upon exposure to the electron beam. The anticipated individual or small Mn-oxo particles could not directly be observed. Instead, most particles were identified as KBr or the aluminosilicate zeolite that was used to dehydrate the solvent. STEM-EDX was not sufficiently powerful to spatially resolve the smaller features, which is probably a consequence of the low local material loading. The obtained results are consistent with the hypothesised formation of small Mn-oxo clusters and did not provide evidence against it (*e.g.*, with the explicit observation of (metallic) nanoparticles^{1,41-46}).

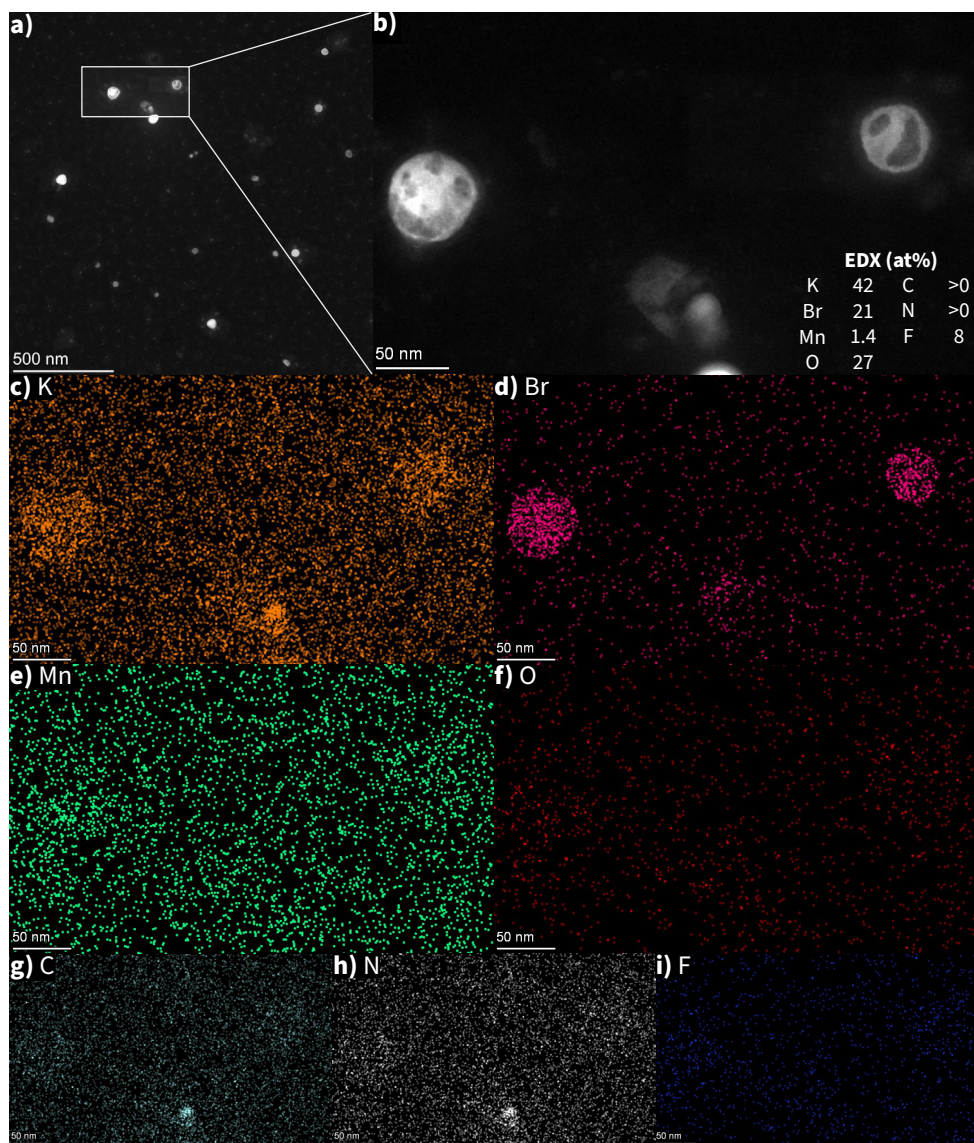


Figure 5.19. TEM micrographs and EDX results of particles found in sample that contained **1**, KO^tBu, acetophenone, and 2-propanol, and was heated overnight at 70 °C. **a)** ADF-TEM micrograph. **b)** HAADF-TEM micrograph. **c–i)** EDX intensity maps of indicated element.

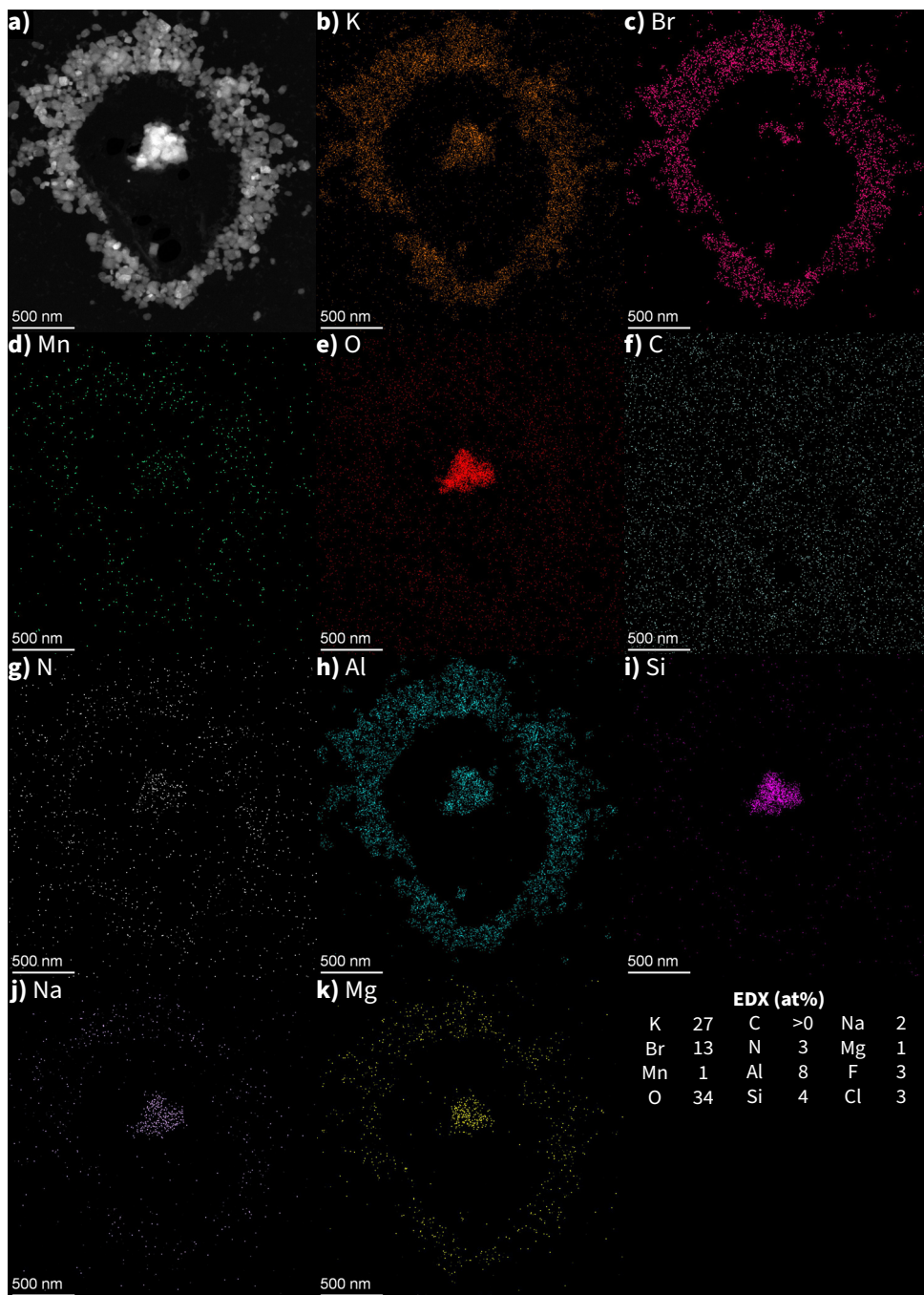


Figure 5.20. TEM micrographs and EDX results of particles found in sample that contained **1**, KO^tBu, acetophenone, and 2-propanol, and was heated overnight at 70 °C. **a)** HAADF-TEM micrograph. **b-k)** EDX intensity maps of indicated element.

5.7 X-ray photoelectron spectroscopy

Our EPR spectroscopy studies revealed the gradual formation of paramagnetic species under relevant reaction conditions. Such materials most probably are the result of redox chemistry that takes place at the Mn^I nucleus. These EPR experiments, however, could not provide further information on the precise structure and oxidation state of these clusters. Further investigations with X-ray techniques were therefore performed to determine these properties and to probe what chemistry could potentially lead to the deactivated catalyst state.

X-ray photoelectron spectroscopy (XPS) is an advanced surface characterisation technique that is highly sensitive to the sample's elemental composition, oxidation state, and coordination environment. It is used extensively to characterise heterogeneous catalysts and various other inorganic materials, but hasn't found widespread and universal application for the characterisation of transition metal complexes and homogeneous (pre)catalysts. This is probably because the interpretation of XPS spectra can be difficult and requires the use of standards that might be challenging to procure. Transition metal complexes often are sufficiently small and well-behaved that they are more conveniently characterised with other, more accessible methods. However, in this particular case such methods are not available and XPS might provide useful information on the nature and oxidation state of deactivated Mn species.

XPS spectra of Mn often are complex because of the multitude of possible oxidation states, overlapping binding energies, and potential multiplet splitting for paramagnetic materials.⁵¹⁻⁵² There is also an ongoing debate in the open literature regarding XPS's capacity to accurately determine oxidation states from either the Mn $2p_{3/2}$ or Mn 3s peaks.^{51,53-55} Finally, literature data on reference binding energies and peak fitting is sparse for Mn^{±II}, although it is known that higher oxidation states *in principle* should be observed at increased binding energies.⁵⁶⁻⁵⁷ We therefore decided to perform these measurements and to start building the knowledge base.

Standards were measured that contained Mn in oxidation states of -I, 0, I, and II (**Figure 5.21**). The volatile Mn₂(CO)₁₀ could not be measured due to sublimation inside the high-vacuum environment of the XPS. Powders were deposited directly onto double-sided carbon tape and were transferred into the XPS load lock without exposure to air. Measurements were performed using a flood gun to prevent excessive charging of the sample, and binding energies are therefore uncorrected. Mn's $2p_{3/2}$ peak at approximately 640 eV was the most sensitive and was used throughout this work. Data were fit with the minimum number of components against a Shirley baseline.

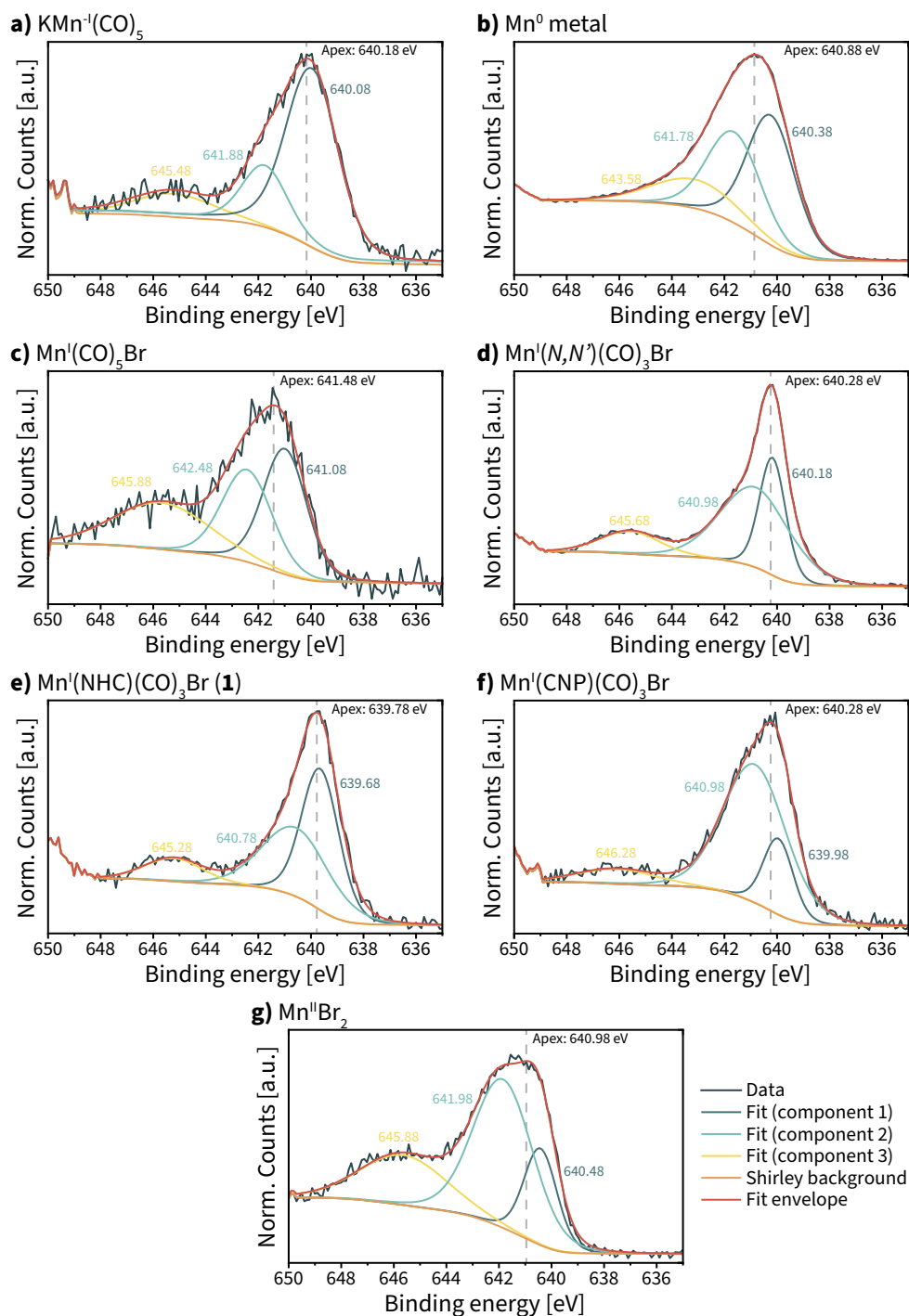


Figure 5.21. XPS spectra, fits, and fit envelopes of Mn standards. Numbers indicate peak apexes.

All spectra could be reasonably fit with three components, albeit with varying peak location and relative size (**Figure 5.21**). Peak locations of these fits did not universally agree with reported literature values for the metal (reported: 638.7 eV⁵² and 640.9 eV⁵⁶) and MnBr₂ (reported: 642.1 eV⁵⁶). Our sample of metallic manganese was used as received and potentially contained an oxide coating (reported binding energy of 641.4 eV⁵²). Mn^I standards were observed within a range of ~1 eV.

We believe that the accuracy of these measurements can be improved upon introduction of accurate charge referencing. Such charge corrections were not currently performed because of extensive overlap of the samples (and carbon tape) with the accepted charge correction standard of adventitious carbon at 284.8 eV. This made charge correction against adventitious carbon unreliable and future application of improved methods desirable (*e.g.*, referencing against Au's 4f_{7/2} peak at 84.0 eV).

Finally, two unknown samples were measured that contained the previously-defined spectroscopy mix and a real, deactivated reaction mixture (**Figure 5.22**). Samples were prepared inside the glove box by evaporating the corresponding solutions onto a piece of aluminium foil that could be transferred to the XPS's high-vacuum environment. The real mixture contained only 0.5 µg Mn (on ~2 cm²), and signal intensity was approximately 1000-fold lower than for the other samples. Spectra were therefore accumulated for as long as reasonably possible (*i.e.*, several hours compared to minutes).

Spectra of deactivated samples clearly featured a peak at higher binding energy that was not observed in the Mn^I(NHC)(CO)₃Br standard (**Figure 5.22**). This indicates that the deactivated mixture and its individual components have a distinct XPS spectrum from the original Mn^I-NHC precatalyst, and that the technique might become a viable method to characterise very dilute, spent reaction mixtures. The location of the new peak/component suggests that it might correspond to an Mn species that resides in a different (probably increased) oxidation state. Ideally, a reference spectrum of such deactivated species is acquired to confirm this peak assignment. However, such a standard is not available at this time, and we therefore sought to independently verify this oxidation state change with XAS measurements.

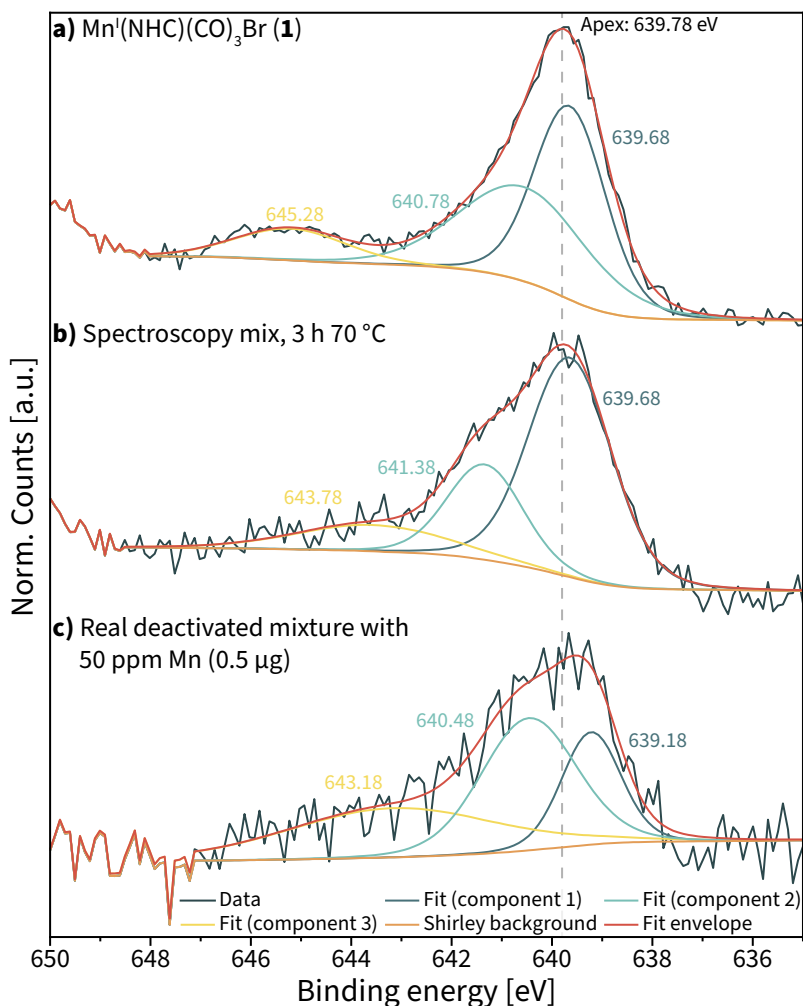


Figure 5.22. XPS spectra, fits, and fit envelopes of deactivated samples. Numbers indicate peak apexes. **a)** $\text{Mn}^{\text{I}}(\text{NHC})(\text{CO})_3\text{Br}$ standard. **b)** Evaporated spectroscopy mix after 3 h at 70 °C on Al foil. **c)** Evaporated solution of deactivated catalytic experiment that contained 50 ppm Mn on Al foil.

5.8 X-ray absorption spectroscopy

X-ray absorption spectroscopy (XAS) techniques nowadays provide a way to study transition metal complexes under realistic, liquid-phase reaction conditions.^{58–60} Similarly to XPS, XAS is sensitive to changes in oxidation state and the coordination environment that surrounds the metal centre under study. These properties can be measured with XANES and EXAFS, which are two types of X-ray absorption spectroscopy that focus on specific energy regions and provide complementary

information. XAS has previously been used to elucidate the structure of complex, multinuclear Mn-oxo clusters⁶¹⁻⁶², where higher oxidation states were generally shifted to higher edge energies.⁶³⁻⁶⁴ Clusters with metal nuclei in multiple oxidation states could be resolved and quantified with XAS techniques after calibration with proper standards.⁶⁵ This is important because it should allow us to distinguish, *e.g.*, disproportionation of Mn^I to a mixture of Mn⁰ and Mn^{II}, and direct oxidation of Mn^I to Mn^{II}. X-ray absorption thus is a very powerful technique that can provide a complete picture of catalytic systems under realistic, *operando* reaction conditions.

The major disadvantage of XAS is its reliance on very bright X-rays that are only available at synchrotron particle accelerators. Access to these facilities is often very limited and is regulated on basis of research proposals. Despite repeated attempts, we have not yet been able to secure dedicated beamtime for this project. We have, however, been able to measure a small number of samples that serve as a proof-of-concept and provide an idea of future data still to come. (Beamline scientists generally believe that the concentration of Mn is too low to allow for accurate measurements. Our preliminary data suggests otherwise, and we therefore believe that our proposal will eventually be accepted.)

Technical problems with the detector resulted in loss of information in the EXAFS region of the spectrum. This is unfortunate because this region captures structural information around the Mn nucleus that would have allowed us to extract average coordination numbers and internuclear distances. *In situ* XANES spectroscopy nevertheless provided valuable information on the redox chemistry of Mn^I under these reaction conditions.

Experiments were performed at the Mn K-edge with the previously-defined spectroscopy mixture (although THF was used as the solvent). The monochromator edge was calibrated with Mn⁰ foil. Three samples were measured that contained Mn^I-NHC precatalyst **1**, a mixture of **1**, KO^tBu, and acetophenone at room temperature right after addition, and a complete mixture that was heated to 100 °C. This last mixture was measured twice: immediately after heating had started, and after 3 h. This reaction temperature was selected for practical reasons at the beamline, even though it deviated from other experiments described in this chapter. The results of these measurements are summarised in **Figure 5.23**.

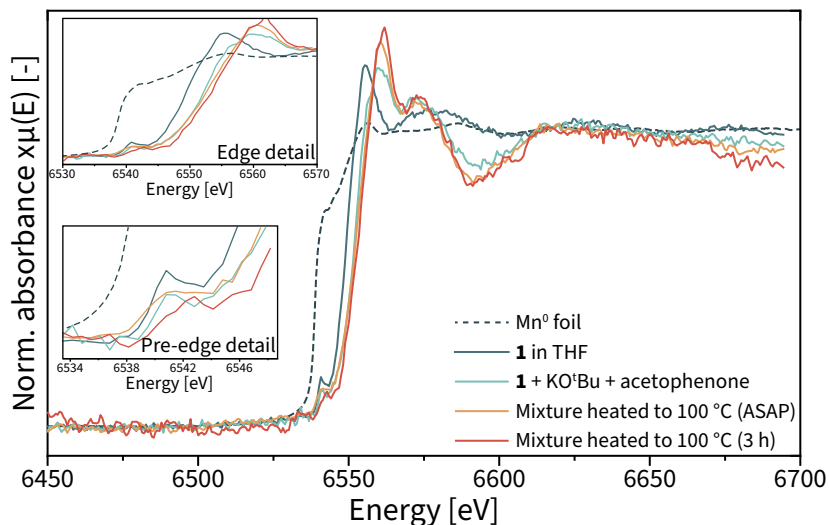


Figure 5.23. Overview of observed XANES spectra of Mn-containing solutions in THF.

The initial Mn^I-NHC complex featured a low-intensity pre-edge peak at approximately 6540 eV. The formation of pre-edge features is associated with the transition of electrons from 1s to 3d orbitals.^{65–67} This transition is formally forbidden, but is enabled by mixing of 3d_{z²} and 4p_z orbitals upon (axial) distortion of the octahedral ligand environment. The observed pre-edge feature for **1** is in line with the strongly asymmetric ligand environment of the octahedral complex. The main edge position of **1** is shifted to higher energy compared to Mn metal and was observed at 6549 eV. This energy is close to the reported energy of Mn^{II} compounds⁶⁸, which demonstrates that ligand properties have a strong impact on absolute edge energies.⁶⁹ Further calibration experiments are required to determine typical edge energies for this class of Mn compounds.

Addition of base and substrate caused the main edge to shift to higher energy by 4 eV, and occurred with a concomitant loss of intensity in the pre-edge region. A new feature also appeared at the white line (the most intense peak). These spectral changes might reasonably be attributed to elimination of the bromide ligand and the formation of a six-coordinate, octahedral species with higher symmetry. Heating of the solution for extended time caused a further shift of the main edge and development of its features. The first differential of the XANES region shows the sequential transition of the edge position from 6549 eV for **1** to 6553 eV and 6558 eV (**Figure 5.24**).

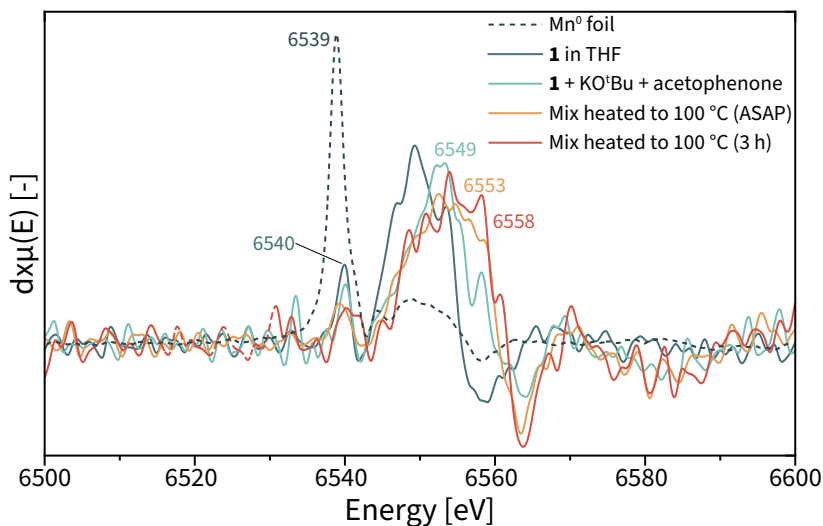


Figure 5.24. First derivative of XANES region that reveals edge positions.

The shifting main edge peak location suggests that the original Mn^{I} complex is transformed into a mixture of Mn species with increased oxidation states. This process is expedited by heating and activation with a base, and is presumably the result of direct oxidation of Mn^{I} to Mn^{II} or disproportionation of two Mn^{I} nuclei to Mn^{0} and Mn^{II} . *In principle* it is possible to distinguish these two cases with XAS techniques, provided that the right standards are measured or available in literature. (Which is not the case at the moment.) Our future experiments will therefore include measurement of these standards, as well as acquisition of spectral data in the EXAFS region to understand the structure of the observed Mn clusters. The herein presented data nevertheless provide insight into the redox behaviour of Mn^{I} transfer hydrogenation catalyst under deactivating conditions.

5.9 The origin and mitigation of catalyst deactivation

Our studies revealed that catalyst deactivation is probably associated with redox chemistry of the catalytically active Mn^{I} centre, that the deactivation process is initiated by base, and that it is accelerated at elevated reaction temperatures. Interestingly, a solution of precatalyst **1** in THF or 2-propanol was stable at 70 °C for extended periods of time and did not deactivate. This specific combination of conditions therefore suggests that the (coordinatively-unsaturated) base-activated catalyst undergoes a thermally-activated deactivation reaction that leads to the formation of paramagnetic Mn-oxo clusters. The reaction mechanism of this transformation, however, remains unclear at this time, and ideas presented in the next section should be considered part of the working hypothesis.

We propose that ligand-loss is the most sensible origin of the observed catalyst deactivation. Ligand-loss is a well-known deactivation pathway for homogeneous catalysts that could be the result of many different processes, including, *e.g.*, photochemical CO loss, thermal ligand dissociation or decomposition, or the reaction between a carbonyl and a hard nucleophile (like the Hieber base reaction or the chemistry described in **Chapter 4**). The resulting coordinatively-unsaturated species often exhibit increased reactivity because of their altered electronic and steric properties. It is imperative that such undesirable reactivity is limited as much as possible to prevent catalyst deactivation or other parallel chemistry.

A recent study from our group demonstrated that introduction of a tridentate CNP ligand to $\text{Mn}(\text{CO})_5\text{Br}$ resulted in a highly active and stable ketone reduction catalyst.⁷⁰ The ligand scaffold of this complex was very similar to that of **1**, but featured an additional phosphine donor group that is believed to stabilise the active catalyst by preventing the formation of a highly reactive, five-coordinated state. This Mn^{I} -CNP complex could be used at low catalyst loading and was more tolerant to elevated reaction temperatures. It showed high activity for the hydrogenation of ketones under molecular hydrogen, but was also active in transfer hydrogenation. The reduction of acetophenone in 2-propanol with 50 ppm Mn^{I} -CNP at 70 °C produced 1-phenylethanol in approximately 40% yield after 6 hours, compared to 55% with Mn^{I} -NHC **1** under identical conditions. However, despite this lower activity, the tridentate complex deactivated slower and ultimately achieved 80% conversion after 23 hours. This again indicates that activity and stability often represent a trade-off that can be optimised by tuning of electronic and steric parameters.

The loss of one or more ligands could lead to highly reactive coordinatively-unsaturated species that can, *e.g.*, disproportionate, react, or dimerise to become trapped in an inescapable thermodynamic well. Such chemistry of Mn^{I} is not exhaustively understood and the properties of selected coordinatively-unsaturated Mn^{I} species were therefore investigated with preliminary DFT calculations. Experimental studies were performed that investigated the prevention of catalyst deactivation by means of changing conditions, bases, and additives.

We hypothesised that the loss of (strong) ligands would destabilise the electron-rich Mn^{I} nucleus and lead to reactive species. This is supported by the fact that, to the best of our knowledge, there are no examples of carbonyl- or nitrosyl-free Mn^{I} complexes (NO is isoelectronic with CO). DFT calculations were performed in different molecular geometries and spin states with CO and MeCN as reasonable representatives of strong field and weak field ligands. Similar to our earlier exploration of crystal field theory in **Chapter 5.5**, these calculations provided a general understanding of the chemistry and electronic properties of such Mn^{I} compounds. The results of these calculations are summarised in **Figure 5.25**.

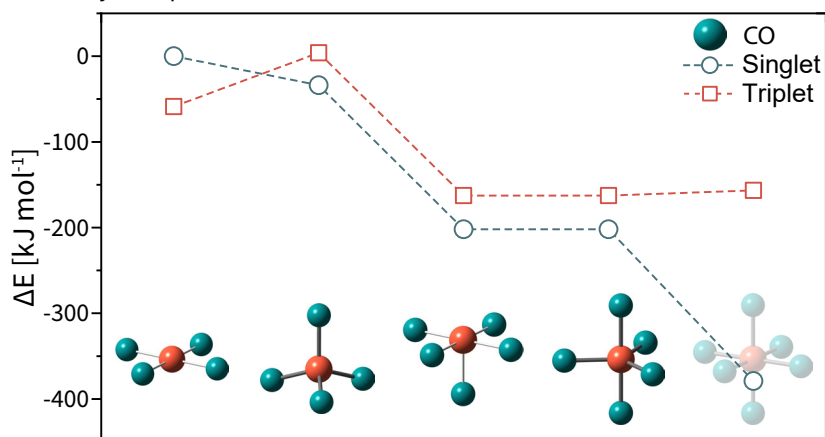
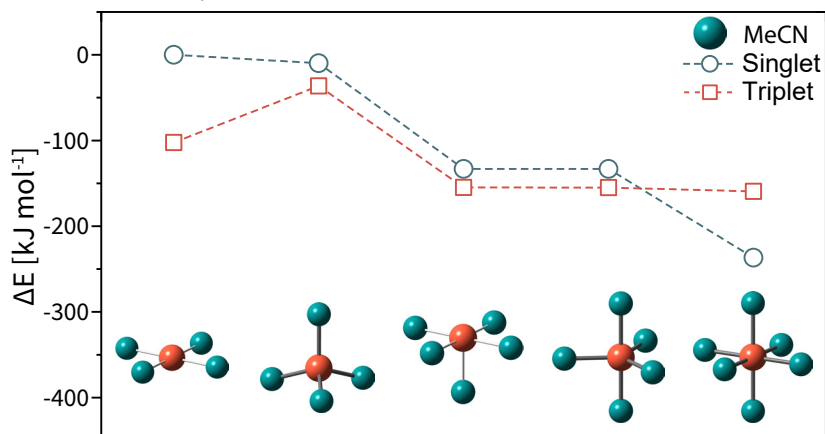
a) Mn^I carbonyl complexesb) Mn^I acetonitrile complexes

Figure 5.25. Computed relative energies for Mn^I complexes in varied geometry and spin state with carbonyl (a) and acetonitrile (b) ligands. All complexes had a charge of +1.

Our DFT calculations revealed two discrete trends (**Figure 5.25**). First, complexes generally became more stable when more ligands surrounded the metal centre. Carbonyl complexes were more stable than their acetonitrile analogues and predominantly favoured the singlet state. A square planar Mn^I(CO)₄⁺ complex is an exception that was predicted to prefer the triplet state as its ground state. Interestingly, the trend reversed for analogous complexes with weak field acetonitrile ligands; here the triplet state was most energetically favourable, except for octahedral Mn^I(MeCN)₆⁺ (**Figure 5.25b**).

These calculations suggest that loss and/or substitution of strong field carbonyl ligand(s) could produce complexes with an energetically accessible and potentially reactive triplet state. The most obvious candidates to replace such carbonyl ligands are the hard, oxygen-centred nucleophiles that are present in the reaction mixture and are weak field ligands (*i.e.*, the alcohol solvent and alkoxide base required to activate precatalyst **1** by forming (reactive) five-coordinated Mn-amido species **4**). Reaction of such an activated species with a component of the mixture or another Mn^I complex could induce oxidation/disproportionation and form the observed Mn-oxo clusters. This suggests that the balance between catalyst life and death is very delicate and could be a matter of low-incidence encounters of rare species.

After these theoretical insights, we finally tried to find experimental conditions that prevented or mitigated the detrimental catalyst deactivation reaction by excluding potentially destabilising factors. Our experiments first probed the effect of preheating, exposure to daylight, and the nature of the ketone substrate. All three parameters could reasonably lead to catalyst deactivation; preheating might cause thermal decomposition if an unstable intermediate is formed, light—particularly UV—could induce photochemical decarbonylation, and the presence of certain (aromatic) ketones could initiate radical chemistry that is detrimental to the Mn catalyst.^{71–74} Experiments were performed under deactivating conditions inside a glove box (kinetics) or an oil bath (batch) in regular or amber glass vials.

Preheating of the solution did not lead to increased catalyst deactivation, except when precatalyst **1**, KO^tBu, and acetophenone were preheated together in toluene instead of 2-propanol (**Figure 5.26a–c**). Mixtures that were preheated in toluene without acetophenone did not deactivate extensively, and the lower yield of these experiments is more reasonably attributed to the necessarily more dilute solution. The results indicate that deactivation probably is not related to catalytic turnover, and is instead caused by the specific combination of pre-activated **1**, the substrate, and heat. This is in line with the stoichiometric reactivity studies described in **Chapter 5.4**, which showed that heating of a solution of precatalyst **1** with base led to formation of Mn-amido **4**. (Although it is possible that these mixtures contained spectroscopically silent species.)

Similar results were obtained when the reaction was performed in daylight or in the dark, or when acetophenone was substituted for 2-octanone (**Figure 5.26d**). Addition of approximately 50 equivalents of BHT relative to the catalyst (an established radical scavenger commonly used as an antioxidant) did not impact the reaction and did not lead to diminished deactivation. We therefore concluded that radical chemistry is probably not the cause of deactivation, and proceeded to test the impact of different bases. (It is reasonable to assume that base nucleophilicity changes in different solvents and therefore also impacts the deactivation reaction.)

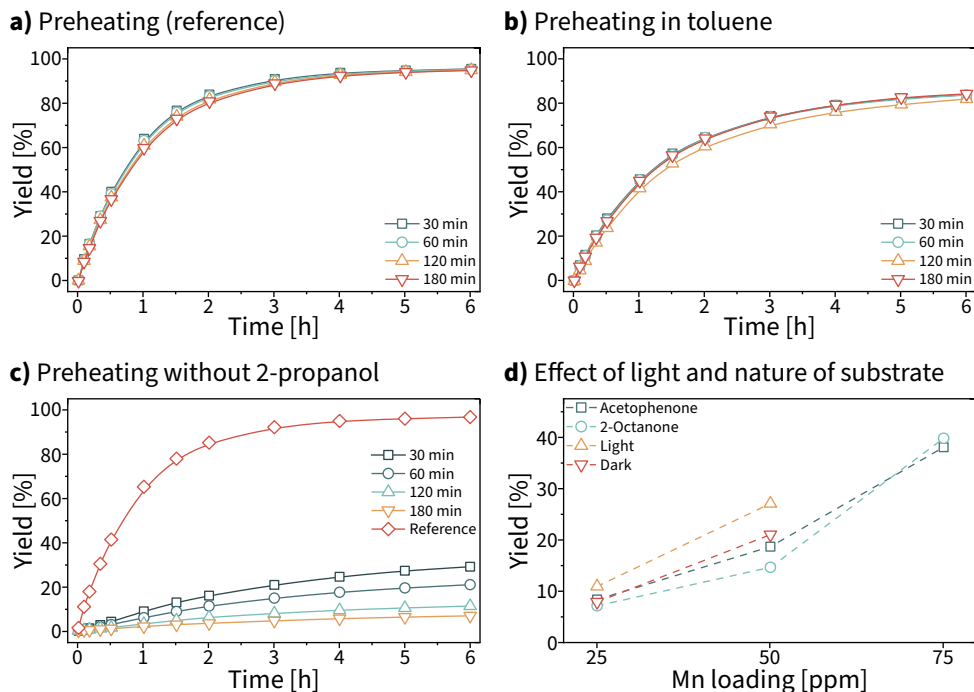


Figure 5.26. Condition and additive screening to prevent or mitigate catalyst deactivation. Mixtures were preheated for the indicated time. Conditions unless indicated otherwise: 0.5 mmol acetophenone, 75 ppm **1**, 1.0 mol% KO^tBu, 3.82 ml 2-propanol, 70 °C. Yields were determined by GC-FID using *n*-dodecane as an internal standard. **a)** Effect of preheating (without acetophenone) in 2-propanol (reference). **b)** Effect of preheating in toluene. **c)** Effect of preheating of complete mixture (without 2-propanol) in toluene. **d)** Effect of daylight and nature of the substrate. Reactions in batch with 25–75 ppm **1** after 16 h.

Base screening experiments were performed in batch under deactivating conditions at varied catalyst loading (**Figure 5.27**). Product alcohol yield was used as a proxy for the degree of deactivation. We propose that this is reasonable because the reaction time was much longer than the timescale of deactivation, which means that catalysts had quantitatively lost their activity at the time of analysis. The screening included a variety of alkoxide bases and hydride sources that were added as solutions in 2-propanol. (Which means that triethylborohydrides were actually present as the corresponding triethyl(isopropoxy)borate salts, see **Chapter 4**.)

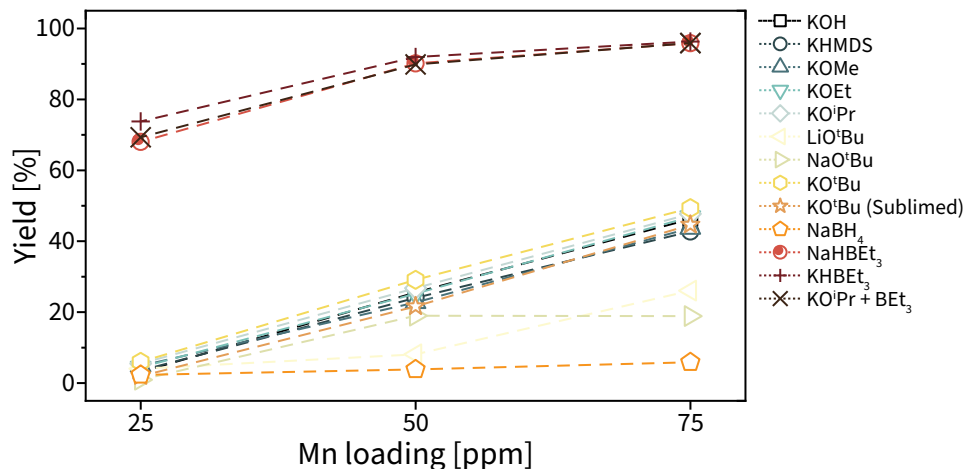


Figure 5.27. Base screening to prevent or mitigate catalyst deactivation. Conditions: 0.5 mmol acetophenone, 25–75 ppm **1**, 1.0 mol% base, 3.82 ml 2-propanol, 70 °C, 16 h. Yields were determined by GC-FID using *n*-dodecane as an internal standard.

Analysis of the base screening results revealed two distinct performance classes, as well as some additional poorly-performing systems. Potassium alkoxides, KOH, and KHMDS were in the first class and all gave practically identical yields of the target alcohol. The reaction with NaO'Bu, LiO'Bu, and NaBH₄ was less successful and resulted in alcohol yields that did not exceed 26%. The fact that all potassium bases gave similar yields is interesting because their properties are vastly different in terms of steric size and base strength. This suggests that the nature of the base is not very important for the deactivation process.

The second performance class exclusively contained triethyl(isopropoxy)borate salts. Addition of these compounds enabled an approximate 13-fold increase in yield and turnover number at 25 ppm **1**. At 50 ppm it improved the maximum turnover number achieved by **1** from 17.300 in **Chapter 3** to over 30.000. This reiterates that deactivation probably is not directly caused by catalytic turnover and thus is a process of the third kind (as introduced in **Chapter 5.1**). Identical performance was obtained with a solution of KHBET₃ in 2-propanol and an independently prepared solution of KOiPr and BEt₃. A base-free reaction mixture that contained BEt₃ (but not KOiPr) was not catalytically active, which confirms that the triethyl(isopropoxy)borate anion was the critical additive required to achieve the described performance gains. We propose that addition of BEt₃ effectively 'captured' the hard nucleophile and reduced its reactivity.

Kinetic experiments were performed to further study the role of $\text{K}[\text{Et}_3\text{B}(\text{O}^i\text{Pr})]$ on catalytic performance and to distinguish whether it increased the initial reaction rate or mitigated the deactivation reaction. This distinction is important because it potentially provides insight into the mechanism of deactivation. Unfortunately, our established and validated method for kinetic measurements gave significantly lower yields compared to when the reaction was performed in batch (results not shown). This difference was reproduced several times and is believed to be caused by the repeated opening of the vial (which is required for the kinetic measurements). It is reasonable to propose that such opening enables a critical volatile component to leave the reaction mixture and causes the mixture to deactivate, just as it would have without this beneficial volatile component. Kinetics were therefore performed with a series of batch experiments that contained identical reaction mixtures and were quenched at the appropriate time (**Figure 5.28**).

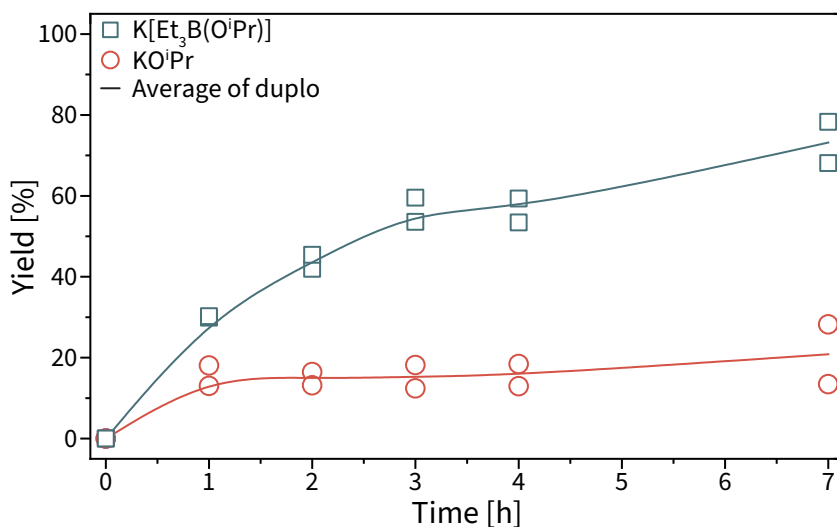


Figure 5.28. ‘Batch kinetics’. Conditions: 0.5 mmol acetophenone, 50 ppm **1**, 1.0 mol% base, 3.82 ml 2-propanol, 70 °C. Solutions were preheated for 30 min without acetophenone before the start of the experiment. Yields were determined by GC-FID using *n*-dodecane as an internal standard.

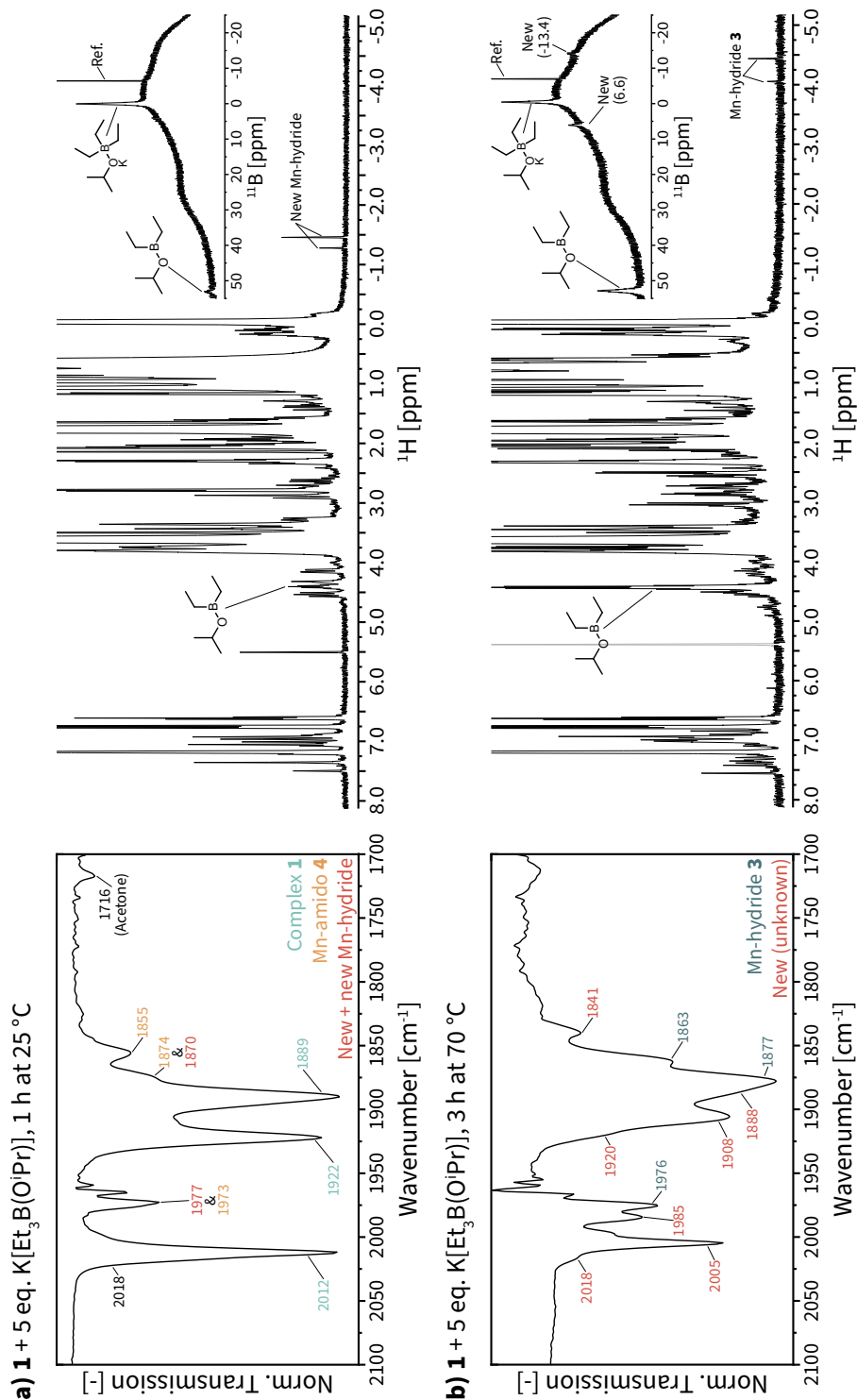
The ‘batch kinetics’ method was considerably less precise than the established kinetic experimentation method and could not resolve whether the initial reaction rate was enhanced or deactivation was slowed. Reproducibility was poor for experiments at the short reaction times required for accurate determination of initial reaction rates. We have not yet been able to obtain the required high-resolution data. Methodological improvements are underway that are expected to make such phenomena measurable. (Application of the data-rich experimentation systems described in **Part II** of this dissertation has not yet been successful for this particular problem.)

Finally, we carried out a stoichiometric reactivity study to better understand the divergent reactivity of the 'naked' alkoxide base and its triethyl(alkoxy)borate salt, as well as its implications on precatalyst activation. Complex **1** was dissolved in THF and 5 equivalents of pre-contacted $\text{K}[\text{Et}_3\text{B}(\text{O}^i\text{Pr})]$ were added as a 0.5 M THF solution. Mixtures were stirred at room temperature for 1 h or heated to 70 °C for 3 h, and were analysed with transmission FTIR and $^1\text{H}/^{11}\text{B}$ NMR spectroscopy (**Figure 5.29**). NMR experiments were performed in $\text{THF-}d_8$ with a flame-sealed glass reference tube (see **Chapter 4**).

The room temperature reaction between Mn^{I} -NHC precatalyst **1** and $\text{K}[\text{Et}_3\text{B}(\text{O}^i\text{Pr})]$ was very slow compared to that with KO^iPr , which was practically instantaneous under these conditions. The solution did not significantly change colour upon addition and remained bright yellow. (Which is again different from the situation with KO^iPr , where the solution very rapidly turned from bright yellow to bright red with the formation of the deprotonated species.) Spectroscopic analysis revealed that the reaction of **1** and $\text{K}[\text{Et}_3\text{B}(\text{O}^i\text{Pr})]$ led to a mixture that predominantly contained **1**, as well as Mn-amido **4**, and a new species that closely resembled Mn-hydride **3** (**Figure 5.29a**).

The ^1H NMR spectrum of the room temperature solution was relatively clean and narrow, and featured two new hydride resonances at $\delta = -1.27$ ppm and $\delta = -1.46$ ppm. These hydrides were present in an approximate 1:3 ratio. The downfield shift of the two hydride resonances indicates that they are significantly more deshielded compared to Mn-hydride **3**, which could for example be the result of partial coordination of the electron-deficient boron nucleus. ^1H and ^{11}B NMR also revealed the presence of diethyl(isopropoxy)borane (^1H : 4.41 ppm, ^{11}B : 53.2 ppm). This species was probably formed after alkyl-transfer from the potassium triethyl(isopropoxy)borate salt to a suitable acceptor. (Although the anticipated isopropyl propionate product was not observed.)

The reaction at 70 °C produced a range of species, of which some remain unidentified at the time of writing. FTIR indicated that Mn-hydride **3** was one of the major components, together with one or two unidentified species that also appear to be octahedral Mn^{I} tricarbonyl complexes. NMR studies confirmed the presence of Mn-hydride **3** and revealed the extensive formation of diethyl(isopropoxy) borane. ^{11}B NMR further indicated the presence of $\text{K}[\text{Et}_3\text{B}(\text{O}^i\text{Pr})]$ and two new, small resonances at 6.6 ppm and -13.4 ppm. Free BEt_3 was not observed.



The combined results demonstrate that the reaction of **1** with $\text{K}[\text{Et}_3\text{B}(\text{O}^i\text{Pr})]$ is complex and results in a range of new Mn complexes. This reaction is much slower than that of **1** with KO^iPr , and probably produces Mn-hydride **3** via a divergent chemical pathway. We speculate that the reduced nucleophilicity of the borate anion moderates the association reaction and prevents the formation of highly reactive, five-coordinated Mn^{I} intermediates that can react unfavourably and/or disproportionate. Coordination of triethylborane further impacts the β -hydride elimination reaction that is critical to obtain reactive intermediate **3**. The formation of (presumably unreactive) diethyl(isopropoxy)borane effectively neutralises one equivalent of the hard nucleophilic base that might induce side-reactions.

In summary, we have demonstrated that the specific combination of **1**, base, substrate, and heat leads to undesirable deactivation chemistry. Although its mechanism remains unclear at this time, we propose that deactivation is initiated by ligand-loss from base-activated **1** and produces (partially oxidised) Mn-oxo clusters through direct oxidation or disproportionation. This undesirable chemistry can be moderated by addition of triethylborane. Preliminary stoichiometric reactivity studies suggest that the borane slows the catalyst activation steps, potentially prevents the formation of five-coordinated species, and leads to catalytically active Mn-hydride **3** via a new and currently unidentified Mn species.

5.10 Conclusion

We have performed an extensive study of the deactivation of Mn^{I} -NHC precatalyst **1** and have analysed the resulting mixtures with a multitude of techniques that include kinetic experiments, modelling efforts, stoichiometric reactivity studies, and several modes of (*in situ*) spectroscopy. The detailed kinetic studies indicate that catalyst deactivation is strongly dependent on catalyst concentration and reaction temperature, and is caused by intrinsic chemistry that is unrelated to catalytic turnover. The deactivation reaction could not be adequately modelled with simple catalyst deactivation models, which suggests that the deactivation reaction is poorly defined or the result of multiple simultaneous processes.

EPR and XANES spectroscopy provided invaluable insight and indicated that the deactivation reaction produces large, antiferromagnetically coupled, paramagnetic Mn-oxo clusters that contain oxidised Mn nuclei (presumably Mn^{II}). We propose that deactivation is the result of direct oxidation or disproportionation of highly reactive five-coordinated Mn^{I} species that are formed in the presence of base. Attempts to synthesise or isolate these clusters have so far been unsuccessful and their exact nature is not yet clear. EXAFS experiments are expected to provide more detailed information on these clusters once beamtime becomes available.

Our experimental efforts were significantly impaired by the homoeopathic concentrations of Mn used in this work. Most analytical techniques were not sufficiently sensitive to detect small quantities of Mn or changes to its environment. To give a sense of scale: the described XPS analysis of a real, deactivated reaction mixture was performed on a sample that contained approximately 0.5 μg Mn. (With ~ 0.3 ng Mn inside the spot area.) This was possible because XPS is a surface-sensitive technique and post-reaction concentration was possible. Volume- or concentration-dependent methods, however, most often were at the limit of their capabilities when used with our artificial ‘spectroscopy mix’ that contained Mn concentrations that were several orders of magnitude higher than the real catalytic mixtures. Analysis of real mixtures clearly is not currently practical or feasible. Development of next-generation high-turnover catalytic systems will therefore require simultaneous advances of analytical techniques.

Finally, a practical method was developed that mitigated the deactivation reaction and enabled a further reduction of catalyst loading by approximately one third. A base screening revealed that addition of triethylborane to catalytic reaction mixtures in the form of the triethyl(alkoxy)borate anion significantly improved catalyst lifetime and regularly enabled turnover numbers as high as 30.000. We propose that the organo(alkoxy)borate salt, which was first described in **Chapter 4** of this dissertation, effectively is a moderated analogue of the alkoxide activator. Spectroscopic studies revealed that $\text{K}[\text{Et}_3\text{B}(\text{O}^i\text{Pr})]$ was significantly less reactive towards Mn^{I} -NHC complex **1** compared to ‘unprotected’ alkoxides and might prevent the formation of unstable intermediates that lead to deactivation. The combined results reiterate that catalyst deactivation may be prevented by careful optimisation and design of the holistic catalytic system that includes the catalyst, additives, as well as reaction conditions.

5.11 Experimental section

General considerations

All manipulations were, unless stated otherwise, performed under an inert atmosphere in an Ar-filled Inert glove box or using standard Schlenk techniques. Manipulations involving Mn complexes were performed in the dark or in amber glass to prevent exposure to light. Anhydrous solvents were dispensed from an Inert PureSolv solvent purification system or were dried using 3 or 4 Å molecular sieves. Solvents were degassed before use. Chemicals were purchased from Sigma-Aldrich, Strem, or TCI, and were dried and/or degassed before use. Air and/or moisture sensitive materials were stored in the glove box. Deuterated solvents were purchased from Eurisotop, dried using molecular sieves, degassed, and stored in the glove box.

NMR spectra were recorded on an Agilent 400-MR DD2 400 MHz spectrometer equipped with a 5 mm ONE NMR probe. ^1H NMR chemical shifts were referenced to residual solvent peaks (3.58 ppm THF- d_8). ^{11}B NMR spectra were referenced to a solution of NaBPh_4 in THF- d_8 (-6.42 ppm) inside a flame-sealed glass insert (see experimental section of **Chapter 4**). When ^1H NMR spectra could not be referenced to the residual solvent peak (*i.e.*, when protium-THF was present and/or measurements were performed with a PRESAT pulse sequence), spectra were referenced to the centre resonance of NaBPh_4 in THF- d_8 inside the glass insert tube (6.84 ppm, itself referenced against THF- d_8 at 3.58 ppm). FTIR was measured in transmission mode on a Bruker Alpha II spectrometer with KBr or CaF_2 windows and 250 or 500 μm PTFE spacers (16 scans, 2 cm^{-1} resolution, approximately 0.5 mg Mn ml^{-1}). Peak locations were determined from second derivative maxima of measured spectra.

Catalytic (kinetic) experiments

Inside the Ar-filled glove box, a 4 ml glass vial was loaded (in order) with a PTFE-coated magnetic stirring bar, *n*-dodecane, solvent and/or 2-propanol, precatalyst, base (both as stock solutions), and substrate. The vial was capped, placed inside a preheated oil bath, stirred at 500 rpm, and was heated for the desired reaction time. Negligible heating time was assumed because of the small diameter vials inside the large heat basin and the relatively long reaction times.

Kinetic experiments were performed inside the glove box. For these experiments the substrate was withheld from the main solution, and was added after the main solution was preheated for 30 minutes inside a metal heating block. A 50 μl aliquot was removed from the reaction mixtures at the appropriate time. Samples were immediately quenched by their addition to 100 μl of a 2 wt% solution of acetic acid in 2-propanol. The mixture was diluted with 1.0 ml 2-propanol and was analysed as described.

Typical loadings: 25.0 μl *n*-dodecane, 3.82 ml 2-propanol, 0.114 mg **1** (0.25 μmol , 0.05 mol%, 500 ppm), 0.56 mg KO^tBu (5.0 μmol , 1.0 mol%), and 58.4 μl acetophenone (0.5 mmol, initial concentration 0.128 M).

Analytical details

Measurements were performed on an Agilent 6890 gas chromatograph equipped with an FID detector and an Agilent CP-Chirasil-Dex CB column (25 m, 0.25 mmID, 0.25 μm film thickness). Method details: 120 $^\circ\text{C}$ (hold 1.0 min), ramp to 180 $^\circ\text{C}$ at 20 $^\circ\text{C min}^{-1}$ (hold 2.0 min). Products were identified using the retention times from analytically pure reference samples. Mass balances were calculated using *n*-dodecane as an internal standard and were verified to be within 90%–110% for all experiments.

Electron paramagnetic resonance spectroscopy (EPR)

Measurements were performed by dr. D.M. Polyukhov, dr. A.S. Poryvaev, and prof. dr. M.V. Fedin (International Tomography Center, Novosibirsk, Russian Federation). Samples were prepared inside an Ar-filled glove box and were transferred to a quartz EPR tube (OD 3.8 mm) without exposure to air. Sample tubes were frozen in liquid nitrogen, evacuated, and sealed using an oxyhydrogen flame. Samples were kept at room temperature unless indicated otherwise.

Room and liquid nitrogen temperature EPR measurements were performed in continuous wave mode on a Bruker EMX X-band spectrometer equipped with an Oxford Instruments temperature control system. Variable temperature EPR measurements were performed in continuous wave mode on a Bruker ELEXSYS E580 X/Q-band spectrometer equipped with an Oxford flow helium cryostat temperature control system.

High-resolution transmission electron microscopy (HR-(S)TEM-EDX)

Measurements were performed by dr. F.D. Tichelaar. Reaction mixtures were prepared as described and were transferred to Quantifoil carbon-foil Cu grids. Samples were prepared in an Ar-filled glove box and were kept under Ar. Measurements were performed using a C_s -corrected FEI Titan 80–300 electron microscope. HAADF-(S)TEM images were obtained with a camera length of 145 mm. EDX was measured with a ThermoFisher Scientific ChemiSTEM detector.

X-ray photoelectron spectroscopy (XPS)

Powdered samples were placed on double-sided carbon tape and introduced to the spectrometer load lock without exposure to air. Aliquots of the deactivated reaction mixture were dispensed on a piece of Al foil that was attached to double-sided carbon tape. Volatiles were removed at 70 °C and a mild vacuum ($\sim 10^{-3}$ mbar) before introduction to the spectrometer load lock without exposure to air.

Measurements were performed on a ThermoFisher Scientific K-Alpha spectrometer using an Al K α X-ray source (1486.68 eV), a Rowland circle monochromator, and a nominal spot size of 400 μ m. Measurements were performed with a flood gun to prevent excessive charging. Charges are uncorrected and were fit against a Shirley background with CasaXPS.

X-ray absorption spectroscopy (XAS)

Measurements were performed by dr. E.A. Uslamin at the P65 beamline (PETRA-III, DESY, Hamburg, Germany). The beamline utilised an undulator high-flux X-ray source equipped with a fixed-exit Si(111) double-crystal monochromator and a Si plane mirror for harmonic rejection. Spectra were collected in transmission and fluorescence mode at the Mn K-edge, which corresponds to an energy of 6.539

keV. The intensity of X-rays was measured using two ionisation chambers, placed before and after the sample, and a Si-PIPS diode fluorescence detector. Manganese foil was used as a standard to calibrate the monochromator edge.

Samples were prepared inside an Ar-filled glove box and transferred to the flow cell without exposure to air. During measurements the reaction mixture was circulated through a thin-walled quartz capillary (Hilgenberg, 10 μm wall thickness, \varnothing 3.0 mm) installed on a sample stage. A chemically-inert gear pump (HNP Mikrosysteme) was used to circulate the liquid through the heated system.

Computational details

DFT calculations were performed by prof. dr. E.A. Pidko using the hybrid PBE0 exchange-correlation functional⁷⁵ as implemented in the Gaussian 16 C.01 program.⁷⁶ Geometry optimisations were performed with the all-electron 6-311+G(d,p) basis set for all atoms.

5.12 References

1. Sonnenberg, J.F.; Morris, R.H., *Distinguishing homogeneous from nanoparticle asymmetric iron catalysis*, *Catalysis Science & Technology* **2014**, 4 (10), 3426–3438;
2. Kozuch, S.; Martin, J.M.L., “Turning Over” Definitions in Catalytic Cycles, *ACS Catalysis* **2012**, 2 (12), 2787–2794;
3. Moulijn, J.A.; van Diepen, A.E.; Kapteijn, F., *Catalyst deactivation: is it predictable?: What to do?*, *Applied Catalysis A: General* **2001**, 212 (1), 3–16;
4. Argyle, M.D.; Bartholomew, C.H., *Heterogeneous Catalyst Deactivation and Regeneration: A Review*, *Catalysts* **2015**, 5 (1);
5. Oudar, J.; Wise, H., *Deactivation and poisoning of catalysts*, Academic Press Inc., **1985**;
6. Poater, A.; Cavallo, L., *Deactivation of Ru-benzylidene Grubbs catalysts active in olefin metathesis*, *Theoretical Chemistry Accounts* **2012**, 131 (3), 1155;
7. Crabtree, R.H., *Deactivation in Homogeneous Transition Metal Catalysis: Causes, Avoidance, and Cure*, *Chemical Reviews* **2015**, 115 (1), 127–150;
8. van Leeuwen, P.W.N.M.; Chadwick, J.C., *Homogeneous Catalysts: Activity - Stability - Deactivation*, Wiley-VCH Verlag GmbH & Co. kGaA, Weinheim, Germany, **2011**;
9. Alberico, E.; Möller, S.; Horstmann, M.; Drexler, H.J.; Heller, D., *Activation, Deactivation and Reversibility Phenomena in Homogeneous Catalysis: A Showcase Based on the Chemistry of Rhodium/Phosphine Catalysts*, *Catalysts* **2019**, 9 (7);
10. Sharninghausen, L.S.; Crabtree, R.H., *Activation, Deactivation and Reversibility in a Series of Homogeneous Iridium Dehydrogenation Catalysts*, *Israel Journal of Chemistry* **2017**, 57 (10–11), 937–944;
11. Crabtree, R.H., *Transfer Hydrogenation with Glycerol as H-Donor: Catalyst Activation, Deactivation and Homogeneity*, *ACS Sustainable Chemistry & Engineering* **2019**, 7 (19), 15845–15853;
12. Sherborne, G.J.; Chapman, M.R.; Blacker, A.J.; Bourne, R.A.; Chamberlain, T.W.; Crossley, B.D.; Lucas, S.J.; McGowan, P.C.; Newton, M.A.; Screen, T.E.O.; Thompson, P.; Willans, C.E.; Nguyen, B.N., *Activation and Deactivation of a Robust Immobilized Cp*Ir-Transfer Hydrogenation Catalyst: A Multielement in Situ X-ray Absorption Spectroscopy Study*, *Journal of the American Chemical Society* **2015**, 137 (12), 4151–4157;
13. Hall, A.M.R.; Dong, P.; Codina, A.; Lowe, J.P.; Hintermair, U., *Kinetics of Asymmetric Transfer Hydrogenation, Catalyst Deactivation, and Inhibition with Noyori Complexes As Revealed by Real-Time High-Resolution FlowNMR Spectroscopy*, *ACS Catalysis* **2019**, 9 (3), 2079–2090;
14. Lagaditis, P.O.; Sues, P.E.; Lough, A.J.; Morris, R.H., *Exploring the decomposition pathways of iron asymmetric transfer hydrogenation catalysts*, *Dalton Transactions* **2015**, 44 (27), 12119–12127;
15. Pell, A.J.; Pintacuda, G.; Grey, C.P., *Paramagnetic NMR in solution and the solid state*, *Progress in Nuclear Magnetic Resonance Spectroscopy* **2019**, 111, 1–271;
16. Housecroft, C.E.; Sharpe, A.G., *Inorganic Chemistry*, 4th ed., Pearson, **2001**, 745;
17. Roessler, M.M.; Salvadori, E., *Principles and applications of EPR spectroscopy in the chemical sciences*, *Chemical Society Reviews* **2018**, 47 (8), 2534–2553;
18. Levanon, H.; Möbius, K., *Advanced EPR spectroscopy on electron transfer processes in photosynthesis and biomimetic model systems*, *Annual Review of Biophysics and Biomolecular Structure* **1997**, 26 (1), 495–540;

19. Goswami, M.; Chirila, A.; Rebreyend, C.; de Bruin, B., *EPR Spectroscopy as a Tool in Homogeneous Catalysis Research, Topics in Catalysis* **2015**, 58 (12), 719–750;
20. Peloquin, J.M.; Britt, R.D., *EPR/ENDOR characterization of the physical and electronic structure of the OEC Mn cluster, Biochimica et Biophysica Acta (BBA) - Bioenergetics* **2001**, 1503 (1), 96–111;
21. Kim, D.H.; Britt, R.D.; Klein, M.P.; Sauer, K., *The manganese site of the photosynthetic oxygen-evolving complex probed by EPR spectroscopy of oriented photosystem II membranes: the $g = 4$ and $g = 2$ multiline signals, Biochemistry* **1992**, 31 (2), 541–547;
22. Peloquin, J.M.; Campbell, K.A.; Randall, D.W.; Evanchik, M.A.; Pecoraro, V.L.; Armstrong, W.H.; Britt, R.D., *^{55}Mn ENDOR of the S_2 -State Multiline EPR Signal of Photosystem II: Implications on the Structure of the Tetranuclear Mn Cluster, Journal of the American Chemical Society* **2000**, 122 (44), 10926–10942;
23. Kanady, J.S.; Tsui, E.Y.; Day, M.W.; Agapie, T., *A Synthetic Model of the Mn_3Ca Subsite of the Oxygen-Evolving Complex in Photosystem II, Science* **2011**, 333 (6043), 733;
24. NIST, *Atomic Data for Manganese (Mn)*, <https://physics.nist.gov/PhysRefData/Handbook/Tables/manganesetable1.htm> (accessed 29 January 2021);
25. Agnew, D.W.; Moore, C.E.; Rheingold, A.L.; Figueroa, J.S., *Kinetic Destabilization of Metal–Metal Single Bonds: Isolation of a Pentacoordinate Manganese(0) Monoradical, Angewandte Chemie International Edition* **2015**, 54 (43), 12673–12677;
26. Bourrez, M.; Orio, M.; Molton, F.; Vezin, H.; Duboc, C.; Deronzier, A.; Chardon-Noblat, S., *Pulsed-EPR Evidence of a Manganese(II) Hydroxycarbonyl Intermediate in the Electrocatalytic Reduction of Carbon Dioxide by a Manganese Bipyridyl Derivative, Angewandte Chemie International Edition* **2014**, 53 (1), 240–243;
27. Radosevich, A.T.; Melnick, J.G.; Stoian, S.A.; Bacciu, D.; Chen, C.H.; Foxman, B.M.; Ozerov, O.V.; Nocera, D.G., *Ligand Reactivity in Diarylamido/Bis(Phosphine) PNP Complexes of $\text{Mn}(\text{CO})_3$ and $\text{Re}(\text{CO})_3$, Inorganic Chemistry* **2009**, 48 (19), 9214–9221;
28. Berends, H.M.; Kurz, P., *Investigation of light-triggered carbon monoxide release from two manganese photoCORMs by IR, UV–Vis and EPR spectroscopy, Inorganica Chimica Acta* **2012**, 380, 141–147;
29. Rattinger, G.B.; Belford, R.L.; Walker, H.; Brown, T.L., *EPR-derived electronic characteristics of zerovalent manganese carbonyl di(tertiary phosphine) radicals, Inorganic Chemistry* **1989**, 28 (6), 1059–1066;
30. Bencini, A.; Gatteschi, D., *Electron Paramagnetic Resonance of Exchange Coupled Systems*, Springer-Verlag, Heidelberg & Berlin, Germany, **1990**;
31. Osadchii, D.Y.; Olivos-Suarez, A.I.; Szécsényi, Á.; Li, G.; Nasalevich, M.A.; Dugulan, I.A.; Crespo, P.S.; Hensen, E.J.M.; Veber, S.L.; Fedin, M.V.; Sankar, G.; Pidko, E.A.; Gascon, J., *Isolated Fe Sites in Metal Organic Frameworks Catalyze the Direct Conversion of Methane to Methanol, ACS Catalysis* **2018**, 8 (6), 5542–5548;
32. Golombek, A.P.; Hendrich, M.P., *Quantitative analysis of dinuclear manganese(II) EPR spectra, Journal of Magnetic Resonance* **2003**, 165 (1), 33–48;
33. Barra, A.L.; Caneschi, A.; Gatteschi, D.; Sessoli, R., *High-Frequency EPR Spectra for the Analysis of Magnetic Anisotropy in Large Magnetic Clusters, Journal of the American Chemical Society* **1995**, 117 (34), 8855–8856;
34. Goldberg, D.P.; Caneschi, A.; Lippard, S.J., *A decanuclear mixed-valent manganese complex with a*

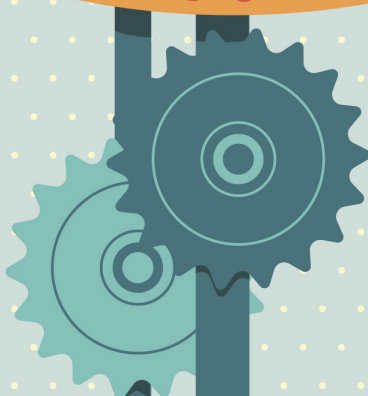
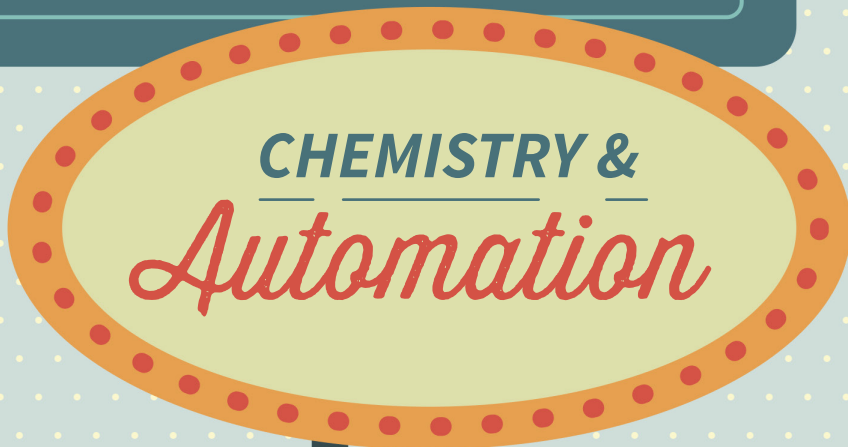
- high spin multiplicity in the ground state, *Journal of the American Chemical Society* **1993**, 115 (20), 9299–9300;
35. Ribas, J.; Albela, B.; Stoeckli-Evans, H.; Christou, G., *Synthesis and Magnetic Properties of Six New Trinuclear Oxo-Centered Manganese Complexes of General Formula $[Mn_3O(X\text{-benzoato})_6L_3]$ ($X = 2\text{-F}, 2\text{-Cl}, 2\text{-Br}, 3\text{-F}, 3\text{-Cl}, 3\text{-Br}$; $L = \text{Pyridine or Water}$) and Crystal Structures of the 2-F, 3-Cl, and 3-Br Complexes*, *Inorganic Chemistry* **1997**, 36 (11), 2352–2360;
 36. Kessissoglou, D.P., *Homo- and mixed-valence EPR -active trinuclear manganese complexes*, *Coordination Chemistry Reviews* **1999**, 185–186, 837–858;
 37. Anderton, K.J.; Ermert, D.M.; Quintero, P.A.; Turvey, M.W.; Fataftah, M.S.; Abboud, K.A.; Meisel, M.W.; Čížmár, E.; Murray, L.J., *Correlating Bridging Ligand with Properties of Ligand-Templated $[Mn^II_3X_3]^{3+}$ Clusters ($X = Br^-, Cl^-, H^-, MeO^-$)*, *Inorganic Chemistry* **2017**, 56 (19), 12012–12022;
 38. Liu, X.; Wang, F., *Transition metal complexes that catalyze oxygen formation from water: 1979–2010*, *Coordination Chemistry Reviews* **2012**, 256 (11), 1115–1136;
 39. ScienceDirect, *High-Resolution Transmission Electron Microscopy*, <https://www.sciencedirect.com/topics/materials-science/high-resolution-transmission-electron-microscopy> (accessed 3 February 2021);
 40. Chen; Collomb, M.N.; Duboc, C.; Blondin, G.; Rivière, E.; Faller, J.W.; Crabtree, R.H.; Brudvig, G.W., *New Linear High-Valent Tetranuclear Manganese-Oxo Cluster Relevant to the Oxygen-Evolving Complex of Photosystem II with Oxo, Hydroxo, and Aqua Coordinated to a Single Mn(IV)*, *Inorganic Chemistry* **2005**, 44 (25), 9567–9573;
 41. Zalesskiy, S.S.; Ananikov, V.P., *$Pd_2(dba)_3$ as a Precursor of Soluble Metal Complexes and Nanoparticles: Determination of Palladium Active Species for Catalysis and Synthesis*, *Organometallics* **2012**, 31 (6), 2302–2309;
 42. Phan, N.T.S.; Van Der Sluys, M.; Jones, C.W., *On the Nature of the Active Species in Palladium Catalyzed Mizoroki–Heck and Suzuki–Miyaura Couplings – Homogeneous or Heterogeneous Catalysis, A Critical Review*, *Advanced Synthesis & Catalysis* **2006**, 348 (6), 609–679;
 43. Higman, C.S.; Lanterna, A.E.; Marin, M.L.; Scaiano, J.C.; Fogg, D.E., *Catalyst Decomposition during Olefin Metathesis Yields Isomerization-Active Ruthenium Nanoparticles*, *ChemCatChem* **2016**, 8 (15), 2446–2449;
 44. Stein, J.; Lewis, L.N.; Gao, Y.; Scott, R.A., *In Situ Determination of the Active Catalyst in Hydrosilylation Reactions Using Highly Reactive Pt(0) Catalyst Precursors*, *Journal of the American Chemical Society* **1999**, 121 (15), 3693–3703;
 45. Jaska, C.A.; Manners, I., *Catalytic Dehydrocoupling of Amine-Borane and Phosphine-Borane Adducts: The Mechanism Is Heterogeneous in One Case and Homogeneous in the Other*, *Journal of the American Chemical Society* **2004**, 126 (5), 1334–1335;
 46. Bayram, E.; Linehan, J.C.; Fulton, J.L.; Roberts, J.A.S.; Szymczak, N.K.; Smurthwaite, T.D.; Özkaz, S.; Balasubramanian, M.; Finke, R.G., *Is It Homogeneous or Heterogeneous Catalysis Derived from $[RhCp^*Cl]_2$? In Operando XAFS, Kinetic, and Crucial Kinetic Poisoning Evidence for Subnanometer Rh_4 Cluster-Based Benzene Hydrogenation Catalysis*, *Journal of the American Chemical Society* **2011**, 133 (46), 18889–18902;
 47. Hagen, C.M.; Widegren, J.A.; Maitlis, P.M.; Finke, R.G., *Is It Homogeneous or Heterogeneous Catalysis? Compelling Evidence for Both Types of Catalysts Derived from $[Rh(\eta^5\text{-C}_5\text{Me}_5)_2Cl]_2$ as a Function of*

- Temperature and Hydrogen Pressure, Journal of the American Chemical Society* **2005**, 127 (12), 4423–4432;
48. Schmid, G., *Large clusters and colloids. Metals in the embryonic state, Chemical Reviews* **1992**, 92 (8), 1709–1727;
49. Aiken, J.D.; Finke, R.G., *A review of modern transition-metal nanoclusters: their synthesis, characterization, and applications in catalysis, Journal of Molecular Catalysis A: Chemical* **1999**, 145 (1), 1–44;
50. Sigma-Aldrich, *Sigma-Aldrich Molecular Sieves - Technical Information Bulletin*, <https://www.sigmaaldrich.com/chemistry/chemical-synthesis/learning-center/technical-bulletins/al-1430/molecular-sieves.html> (accessed 4 February 2021);
51. XPS fitting, *X-ray Photoelectron Spectroscopy (XPS) Reference Pages*, <http://www.xpsfitting.com/search/label/Manganese> (accessed 15 March 2021);
52. Thermo Scientific, XPS, <https://xpssimplified.com/elements/manganese.php> (accessed 15 March 2021);
53. Cerrato, J.M.; Hochella, M.F.; Knocke, W.R.; Dietrich, A.M.; Cromer, T.F., *Use of XPS to Identify the Oxidation State of Mn in Solid Surfaces of Filtration Media Oxide Samples from Drinking Water Treatment Plants, Environmental Science & Technology* **2010**, 44 (15), 5881–5886;
54. Nelson, A.J.; Reynolds, J.G.; Roos, J.W., *Core-level satellites and outer core-level multiplet splitting in Mn model compounds, Journal of Vacuum Science & Technology A* **2000**, 18 (4), 1072–1076;
55. Ilton, E.S.; Post, J.E.; Heaney, P.J.; Ling, F.T.; Kerisit, S.N., *XPS determination of Mn oxidation states in Mn (hydr)oxides, Applied Surface Science* **2016**, 366, 475–485;
56. NIST, *Data on Mn*, https://srdata.nist.gov/xps/EngElmSrchQuery.aspx?EType=PE&CSOpt=Retri_ex_dat&Elm=Mn (accessed 15 March 2021);
57. Avanzino, S.C., *Bonding In Inorganic Compounds: A Study By X-Ray Photoelectron Spectroscopy*, University of California, Berkeley, **1978**;
58. Bauer, M.; Gastl, C., *X-Ray absorption in homogeneous catalysis research: the iron-catalyzed Michael addition reaction by XAS, RIXS and multi-dimensional spectroscopy, Physical Chemistry Chemical Physics* **2010**, 12 (21), 5575–5584;
59. Sherborne, G.J.; Nguyen, B.N., *Recent XAS studies into Homogeneous metal catalyst in fine chemical and pharmaceutical syntheses, Chemistry Central Journal* **2015**, 9, 37;
60. Tromp, M., *Catalysis seen in action, Philosophical Transactions of the Royal Society A: Mathematical, Physical and Engineering Sciences* **2015**, 373 (2036), 20130152;
61. Tsui, E.Y.; Tran, R.; Yano, J.; Agapie, T., *Redox-inactive metals modulate the reduction potential in heterometallic manganese–oxido clusters, Nature Chemistry* **2013**, 5 (4), 293–299;
62. Pizarro, S.A.; Glatzel, P.; Visser, H.; Robblee, J.H.; Christou, G.; Bergmann, U.; Yachandra, V.K., *Mn oxidation states in tri- and tetra-nuclear Mn compounds structurally relevant to photosystem II: Mn K-edge X-ray absorption and K β X-ray emission spectroscopy studies, Physical Chemistry Chemical Physics* **2004**, 6 (20), 4864–4870;
63. Stueben, B.L.; Cantrelle, B.; Sneddon, J.; Beck, J.N., *Manganese K-edge XANES studies of Mn speciation in Lac des Allemands as a function of depth, Microchemical Journal* **2004**, 76 (1), 113–120;
64. Kubin, M.; Guo, M.; Kroll, T.; Löchel, H.; Källman, E.; Baker, M.L.; Mitzner, R.; Gul, S.; Kern, J.; Föhlisch, A.; Erko, A.; Bergmann, U.; Yachandra, V.; Yano, J.; Lundberg, M.; Wernet, P., *Probing the*

- oxidation state of transition metal complexes: a case study on how charge and spin densities determine Mn L-edge X-ray absorption energies, Chemical Science* **2018**, 9 (33), 6813–6829;
65. Chalmin, E.; Farges, F.; Brown, G.E., *A pre-edge analysis of Mn K-edge XANES spectra to help determine the speciation of manganese in minerals and glasses, Contributions to Mineralogy and Petrology* **2009**, 157 (1), 111–126;
 66. Cartier, C.; Verdaguer, M.; Menage, S.; Girerd, J.; Tuchagues, J.; Mabad, B., *Xanes of Manganese Coordination Complexes, Journal de Physique Colloques* **1986**, 47 (C8), C8–623–C628–625;
 67. Roemelt, M.; Beckwith, M.A.; Duboc, C.; Collomb, M.N.; Neese, F.; DeBeer, S., *Manganese K-Edge X-Ray Absorption Spectroscopy as a Probe of the Metal–Ligand Interactions in Coordination Compounds, Inorganic Chemistry* **2012**, 51 (1), 680–687;
 68. Vezin, H.; Lamour, E.; Routier, S.; Villain, F.; Bailly, C.; Bernier, J.L.; Catteau, J.P., *Free radical production by hydroxy-salen manganese complexes studied by ESR and XANES, Journal of Inorganic Biochemistry* **2002**, 92 (3), 177–182;
 69. Feth, M.P.; Bolm, C.; Hildebrand, J.P.; Köhler, M.; Beckmann, O.; Bauer, M.; Ramamonjisoa, R.; Bertagnolli, H., *Structural Investigation of High-Valent Manganese–Salen Complexes by UV/Vis, Raman, XANES, and EXAFS Spectroscopy, Chemistry – A European Journal* **2003**, 9 (6), 1348–1359;
 70. Yang, W.; Chernyshov, I.Y.; van Schendel, R.K.A.; Weber, M.; Müller, C.; Filonenko, G.A.; Pidko, E.A., *Robust and efficient hydrogenation of carbonyl compounds catalysed by mixed donor Mn(I) pincer complexes, Nature Communications* **2021**, 12 (1), 12;
 71. Ashby, E.C., *Single-electron transfer, a major reaction pathway in organic chemistry. An answer to recent criticisms, Accounts of Chemical Research* **1988**, 21 (11), 414–421;
 72. Gentry, E.C.; Knowles, R.R., *Synthetic Applications of Proton-Coupled Electron Transfer, Accounts of Chemical Research* **2016**, 49 (8), 1546–1556;
 73. Barham, J.P.; Coulthard, G.; Emery, K.J.; Doni, E.; Cumine, F.; Nocera, G.; John, M.P.; Berlouis, L.E.A.; McGuire, T.; Tuttle, T.; Murphy, J.A., *KO^oBu: A Privileged Reagent for Electron Transfer Reactions?, Journal of the American Chemical Society* **2016**, 138 (23), 7402–7410;
 74. Nocera, G.; Young, A.; Palumbo, F.; Emery, K.J.; Coulthard, G.; McGuire, T.; Tuttle, T.; Murphy, J.A., *Electron Transfer Reactions: KO^oBu (but not NaO^oBu) Photoreduces Benzophenone under Activation by Visible Light, Journal of the American Chemical Society* **2018**, 140 (30), 9751–9757;
 75. Adamo, C.; Barone, V., *Toward reliable density functional methods without adjustable parameters: The PBE0 model, The Journal of Chemical Physics* **1999**, 110 (13), 6158–6170;
 76. Frisch, M.J.; Trucks, G.W.; Schlegel, H.B.; Scuseria, G.E.; Robb, M.A.; Cheeseman, J.R.; Scalmani, G.; Barone, V.; Petersson, G.A.; Nakatsuji, H.; Li, X.; Caricato, M.; Marenich, A.V.; Bloino, J.; Janesko, B.G.; Gomperts, R.; Mennucci, B.; Hratchian, H.P.; Ortiz, J.V.; Izmaylov, A.F.; Sonnenberg, J.L.; Williams, D.; Ding, F.; Lipparini, F.; Egidi, F.; Goings, J.; Peng, B.; Petrone, A.; Henderson, T.; Ranasinghe, D.; Zakrzewski, V.G.; Gao, J.; Rega, N.; Zheng, G.; Liang, W.; Hada, M.; Ehara, M.; Toyota, K.; Fukuda, R.; Hasegawa, J.; Ishida, M.; Nakajima, T.; Honda, Y.; Kitao, O.; Nakai, H.; Vreven, T.; Throssell, K.; Montgomery Jr., J.A.; Peralta, J.E.; Ogliaro, F.; Bearpark, M.J.; Heyd, J.J.; Brothers, E.N.; Kudin, K.N.; Staroverov, V.N.; Keith, T.A.; Kobayashi, R.; Normand, J.; Raghavachari, K.; Rendell, A.P.; Burant, J.C.; Iyengar, S.S.; Tomasi, J.; Cossi, M.; Millam, J.M.; Klene, M.; Adamo, C.; Cammi, R.; Ochterski, J.W.; Martin, R.L.; Morokuma, K.; Farkas, O.; Foresman, J.B.; Fox, D.J., *Gaussian 16 Rev. C.01*, Wallingford, CT, **2016**.



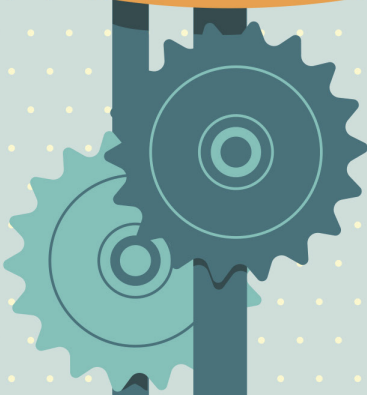
Part II





Chapter

6



Automation-guided reaction development

of high-pressure gas-liquid catalytic reactions
in oscillatory microflow

.....

*“If you're walking down the right path and you're willing to keep walking,
eventually you'll make progress.”*

Barack Obama

Abstract

Automated microfluidic tools potentially offer fast, efficient, and focused screening and optimisation of categorical and continuous variables. Here we describe the application of an oscillatory microfluidic platform to the development of high-pressure gas-liquid catalytic reactions. A microfluidic screening platform was engineered to enable its stable and safe operation under relatively harsh reaction conditions. The system was used for the automated discovery and development of complex catalytic hydrogenation chemistry.

The platform's capabilities were demonstrated with a challenging Ru-catalysed asymmetric hydrogenation of a base-sensitive β -aminoketone. A promising catalytic system was identified in a screening of discrete precatalysts under different conditions. The reaction was finally scaled-up in a batch autoclave system that produced multigram quantities of the enantiopure γ -aminoalcohol product, which was isolated as the corresponding hydrochloride salt. The platform ultimately enabled the discovery and scale-up of a challenging chiral reaction in less than a week of total experimental time.

This chapter has been published as:

R. van Putten, N.S. Eyke, L.M. Baumgartner, V.L. Schultz, G.A. Filonenko,
K.F. Jensen, E.A. Pidko, *In preparation*

6.1 Introduction

High-throughput experimentation (HTE) is a critical enabling technology for the fine-chemical industry, where it is used to rapidly identify catalysts and reaction conditions for a target chemical transformation.¹⁻⁴ These reaction development campaigns are often complicated by the vast parameter space that governs catalytic performance, as well as the relatively unpredictable reactivity of many catalytic systems. These complications can make rational navigation of the available parameter space difficult, tedious, and time-consuming. In these situations it can be more attractive to rationally screen (a section of) the available parameter space instead.

HTE is particularly powerful in situations where fundamental theories are underdeveloped, predictive power is low, and/or time constraints are present. If time-to-market is critical, a more pragmatic and brute-force method is required to quickly obtain answers and prevent bottlenecking of the project. While the exact technical implementation of HTE can vary depending on the chemistry under study, the approaches are similar.^{1-2,5-8}

The initial phase of HTE-based reaction development campaigns usually consists of broad screenings that aim to capture as much of the available parameter space as possible. The primary goal of this phase is to identify catalytic systems that *in principle* could promote the desired reaction. Hits from the first stage are then promoted to a secondary stage screening, where a reduced number of systems are studied in more detail. These first stages are customarily performed in parallel reactor systems, with reaction volumes that range from several hundred microlitres up to several (tens of) millilitres.^{1-2,5-7}

Although these systems are highly effective, there are also several disadvantages due to the parallelised nature of such experimentation. For example, material consumption can be high, which is particularly problematic in the early phases of development when the substrate material is both scarce and in high demand. Operational limitations of the equipment can also severely restrict experimental design. Most systems offer only limited—if any—control over temperature and pressure for different reactor zones. Multiple runs are therefore required to screen different reaction conditions. Because of this relative inflexibility, parallel HTE approaches cannot practically cover the available parameter space at high resolution. This limitation can lead to 'missing-out' of more favourable catalytic systems under conditions that were not experimentally evaluated. A good example of such a situation was described in **Chapter 3** of this dissertation, where a 10 °C reduction of the reaction temperature led to a more than five-fold increase of catalyst lifetime.

This chapter describes our efforts to develop an automated microfluidic reaction development platform for high-pressure gas-liquid catalytic chemistry. MIT's existing microfluidic oscillatory flow system was modified to enable safe operation at the target reaction conditions. The system was validated and demonstrated with a Ru-catalysed asymmetric ketone hydrogenation reaction that is known to suffer from condition-dependent side-product formation.

6.2 Microfluidic oscillatory flow platforms

Chemical synthesis in (continuous) microflow can have significant benefits compared to conventional approaches such as batch reactors and continuously stirred tank reactors. These improvements originate from the specific geometries and length scales of microreactors, and lead to enhanced heat and mass transfer rates and better safety characteristics due to the constrained absolute physical dimensions of such microfluidic systems.^{9–13} These properties render microreactors particularly attractive for multiphase reactions that require hazardous gases such as hydrogen or carbon monoxide.

Jensen and co-workers have developed an automated microfluidic oscillatory flow platform that combined good experimental throughput with high-quality chromatographic analysis (**Figure 6.1**).^{14–22} The introduction of a mixed-integer non-linear optimisation algorithm improved the system's ability to optimise reaction conditions in non-trivial parameter spaces that are relevant for catalytic reactions. This capability has recently been demonstrated with catalytic applications in Suzuki-Miyaura cross-couplings²⁰ and Buchwald-Hartwig aminations.²²

The oscillatory microfluidic flow platform consists of a liquid handling robot placed inside an argon-filled glove bag, four syringe pumps, a custom-made aluminium reactor block, and an on-line HPLC system (**Figure 6.1**). The reactions are performed inside FEP (*fluorinated ethylene propylene*) or PFA (*perfluoroalkoxy alkane*) polymer tubing. Discrete reaction mixtures (*e.g.*, to screen different precatalysts) are automatically prepared by the liquid handling robot according to a computer-generated experimental design. The solution is then thoroughly mixed and a single 17 μl droplet is injected into the gas-filled system. The droplet is moved through the system by the slow infusion of the carrier gas syringe pump. The droplet that contains the reaction mixture is then oscillated inside the temperature-controlled reactor for the target reaction time. Afterwards the mixture is quenched and/or diluted and analysed with on-line HPLC. Key performance indicators such as reagent conversion and product yield are finally computed, and the optimisation algorithm is updated with the new information. This cycle is repeated until an optimal solution is found. The system is fully automated and

is controlled by software written in LabVIEW (process control) and MATLAB (optimisation algorithm). The implementation of such feedback-driven automated experimentation is an important advantage of this platform that enables the efficient optimisation of discrete reagents and reaction conditions.

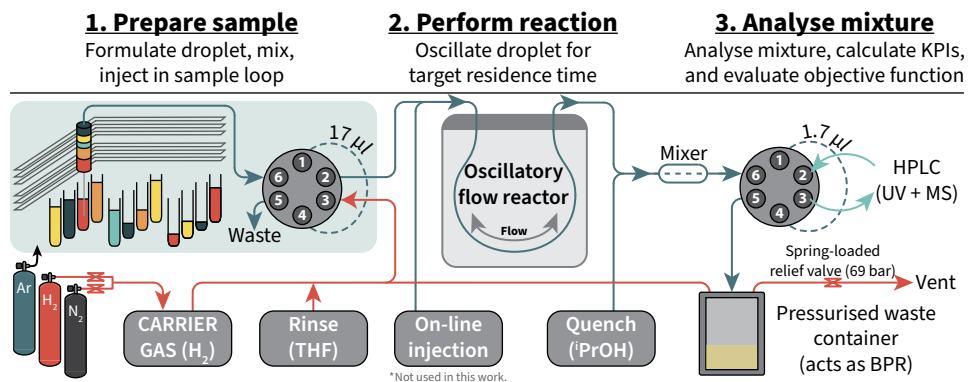


Figure 6.1. Automated microfluidic oscillatory flow platform used in this work.

The continuous movement of the droplet through the reactor is critical to reach the desired Taylor flow pattern and its associated mass transfer rates. (This specific regime is also known as *segmented flow*, *slug flow*, *bubble train flow*, or *intermittent flow*.^{23–25}) Taylor flow is characterised by a strong internal circulation that continuously 'refreshes' the gas-liquid interface. The oscillating motion of the liquid inside the reactor decouples its mixing with the gas-phase from its residence time.¹⁴ This ensures that experiments with vastly different residence times can be performed inside the same reactor. (Which would otherwise require several reactors of different lengths.)

The position of the mixture inside the aluminium reactor is controlled with an optical detection system (**Figure 6.2**). A visible light source is configured such that its beam passes through the optically transparent inlet and outlet tubing. The droplet is detected with the photodetector once it moves through the beam, and the direction of the carrier flow is reversed to keep the droplet inside the reactor.

The automated optimisation campaign proceeds through two distinct but related phases.^{20,26} (The optimisation algorithm was not modified significantly for this work and is described for reference and completeness only. The minor changes that were made are described in the experimental section.) The system first generates a D-optimal experimental design that aims to explore the user-defined parameter space. The model that is used to create the D-optimal design assumes a quadratic model for all variables (including linear terms and interaction effects), as well as first-order interaction terms for distinct catalysts and the reaction temperature.

Several duplicate experiments are performed to estimate the model's uncertainty. The experiments are then performed in randomised order and the results are used to construct the objective function response surface.

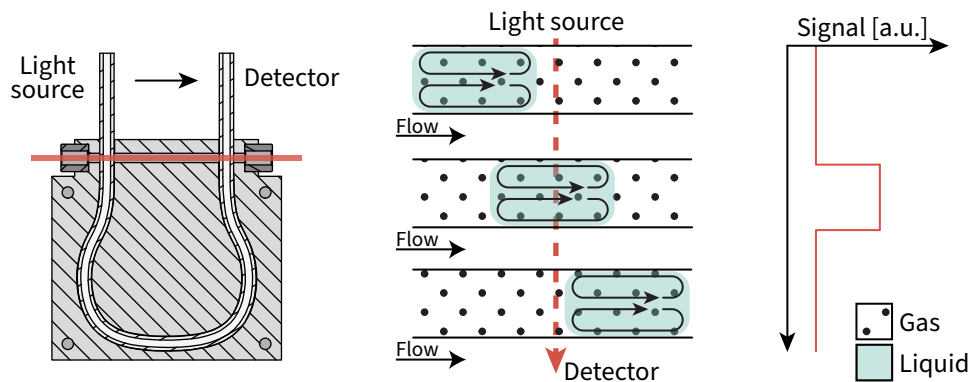


Figure 6.2. Reactor configuration and its optical droplet detection system.

The second phase of the optimisation campaign is based on a G-optimal design. This procedure aims to refine the model by minimising the variance of the objective function response surface. Lower performing discrete parameters (*e.g.*, precatalysts) are sequentially removed from the model once it becomes statistically improbable that their performance exceeds the global optimum. New experiments are added to the queue until no more discrete variables can be removed from the model, and the latest n experiments have not led to improvements of the objective function. (Parameter n is defined by the user and is usually set to 3 or 4.)

6.3 High-pressure oscillatory flow

A number of system modifications were required to enable high-pressure operation with hazardous gases. Thus far only one example of such a system has been described in the open literature. Abolhasani and co-workers were able to perform hydroformylation reactions at 95 °C and 30 bar syngas pressure.^{27–29} Their tube-in-tube reactor incorporated a gas-permeable membrane that enclosed the inner, liquid-containing, reaction tube. Instead, we sought to modify the existing oscillatory flow platform and perform the multiphase reaction inside a single, perfluorinated reactor cavity (*i.e.*, not with a tube-in-tube design).

Such an approach presented a number of challenges. Commercially available PFA or FEP tubing is typically pressure tested with water and air at room temperature³⁰, which resulted in ratings of 138 bar for the desired system tubing (FEP, 1/16" OD x

0.02" ID)³¹, and 34 bar for the reactor tubing (PFA, 1/8" OD x 1/16" ID)³². Ratings for operation at elevated temperature were not available. (Materials are conventionally rated at ~20% of the room temperature burst pressure.³⁰) Experiments were therefore performed to understand the behaviour of these materials above ambient temperature and pressure. The original (non-modified) reactor was subjected to 69 bar nitrogen gas and the temperature of the reactor was slowly increased. While the system was stable at room temperature, elevated temperature (~50 °C) caused the tubing to fail. This failure took place where the aluminium reactor body no longer supported the tubing (**Figure 6.3a**).

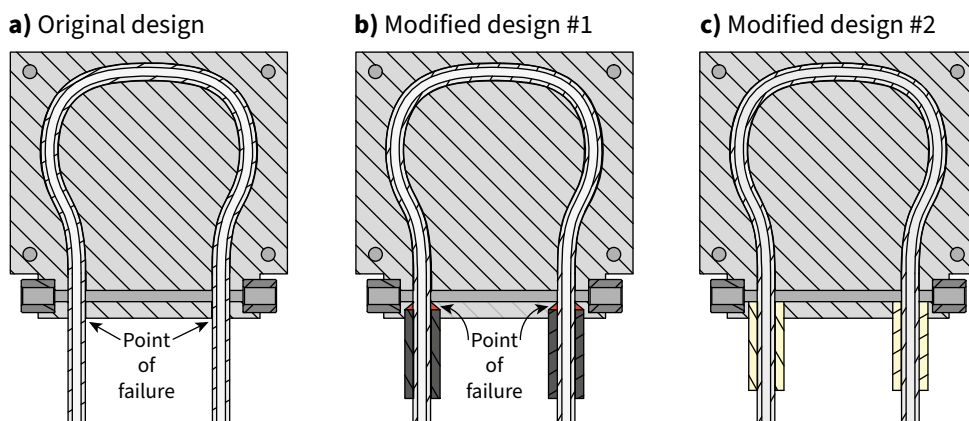
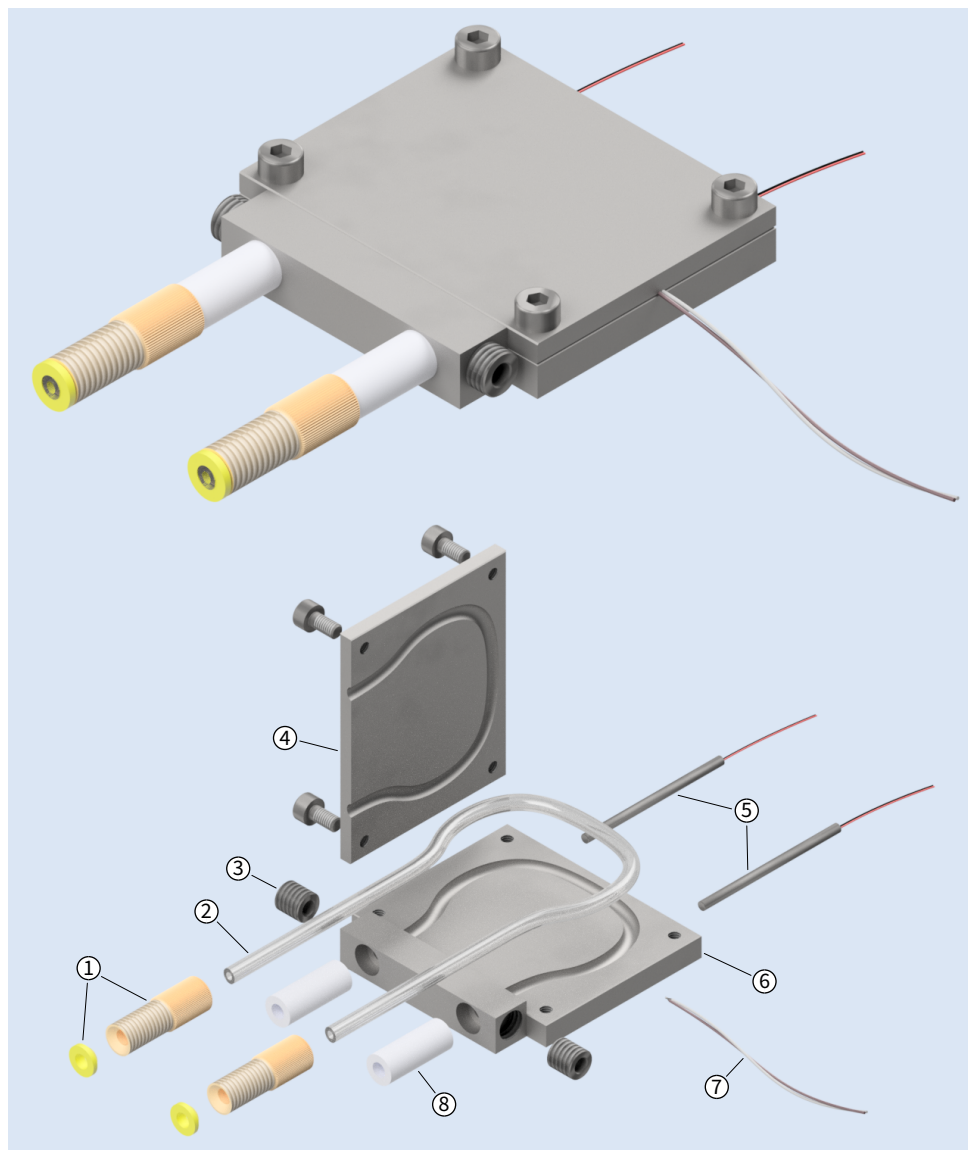


Figure 6.3. Reactor design iterations. **a)** Original reactor design. **b)** Modified design #1 was unsuccessful and failed at the locations indicated in red. **c)** Modified design #2.

We hypothesised that the root cause of this failure was the sharp boundary between the heated reactor body and the colder, unsupported, tubing just outside it. A ¼" (6.35 mm) hole was therefore drilled into the reactor body and a stainless steel annular ring was press-fit into it to provide back pressure for the tubing. This also physically distanced the unsupported tubing from the heated assembly. The experiment was repeated with the modified design.

The new design had a failure mode that was similar to that of the original design. The leak had occurred between the aluminium reactor body and the stainless steel annular ring (**Figure 6.3b**). This small area had been left unsupported because a regular (*i.e.*, angled) drill bit had been used for the modification. This situation was corrected with the corresponding plunging end mill. The stainless steel annular ring was replaced by a PTFE analogue to further reduce thermal conductivity from the aluminium reactor block to the unsupported sections (**Figure 6.3c**). A schematic overview of the final reactor design is provided in **Figure 6.4**.



- | | |
|---|---|
| ① Flangeless flat-bottom fitting (PEEK) | ⑤ Watlow FIREROD® 60 W cartridge heater |
| ② Reactor tubing (PFA, 1/8" OD, 1/16" ID) | ⑥ Aluminium reactor body |
| ③ Thread adapter from optical fiber to reactor body | ⑦ Type K thermocouple |
| ④ Aluminium reactor lid with hex socket bolts | ⑧ Annular ring (PTFE) |

Figure 6.4. Rendering of the high-pressure microfluidic oscillatory flow reactor used in this work.

The second design enabled sustained operation at 75 °C and 69 bar for at least three hours. Further heating to 85 °C caused the system to fail after an additional 1.5 hours. This failure occurred in the small gap between the PTFE annular ring (item 8 in **Figure 6.4**) and the PEEK fitting (item 1 in **Figure 6.4**) and was probably delayed by the relatively non-conductive PTFE ring.

The conditions that could be reached with the new design were adequate for the chiral demonstration chemistry and no further modifications were made. Operational limits were set at 70 °C and 40 bar. (Higher temperature or pressure *in principle* are possible, but not simultaneously.) The absolute temperature limit was determined by PFA's glass transition temperature. PFA softened at ~85 °C ($T_g = 90$ °C) and, when pressurised internally, extruded when it was not adequately supported. The system's maximum operating pressure was determined by the syringe pump's linear force limits. These motors provided approximately 34 kg of linear force. When 8 ml stainless steel syringes were employed, this force limit translated to a maximum pressure of 47 bar. (Use of a smaller 2.5 ml syringe could *in principle* allow operation at up to 188 bar. High-force syringe pumps are also available from the same supplier.)

Finally, changes were made to the setup and its enclosure to facilitate safe operation. The ventilation rate of the cabinet was improved following the installation of a large-diameter exhaust tube and removal of several 90° bends. The volumetric flow rate was verified to be sufficient to prevent the build-up of hydrogen gas in case of a reasonably-sized leak. A gas detector was installed at the top of the same enclosure to provide early warning of a potential (small) leak. A spring-loaded overpressure relief valve was installed that was connected directly to the exhaust and was set to an opening pressure of 69 bar (1000 psi).

6.4 Demonstration chemistry

We decided to demonstrate the system's capabilities with a challenging asymmetric hydrogenation reaction. We selected the chiral reduction of β -aminoketone **1** as a representative model reaction that could be encountered in a typical reaction development campaign in the pharmaceutical or fine-chemical industry (**Figure 6.5**). The resulting chiral γ -aminoalcohol is an important building block for the synthesis of several antidepressants and is a potential intermediate *en route* enantiopure Fluoxetine (which is marketed under the name of Prozac by Eli Lilly and Co.)³³⁻³⁶

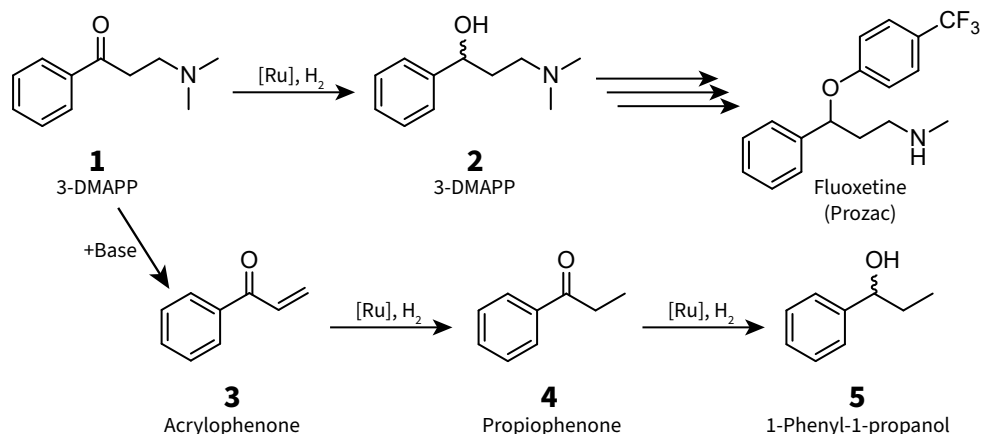


Figure 6.5. Asymmetric hydrogenation of β -aminoketone **1** to chiral γ -aminoalcohol **2** en route Fluoxetine. The reaction of Mannich base **1** with bases leads to (further reducible) acrylophenone **3**.

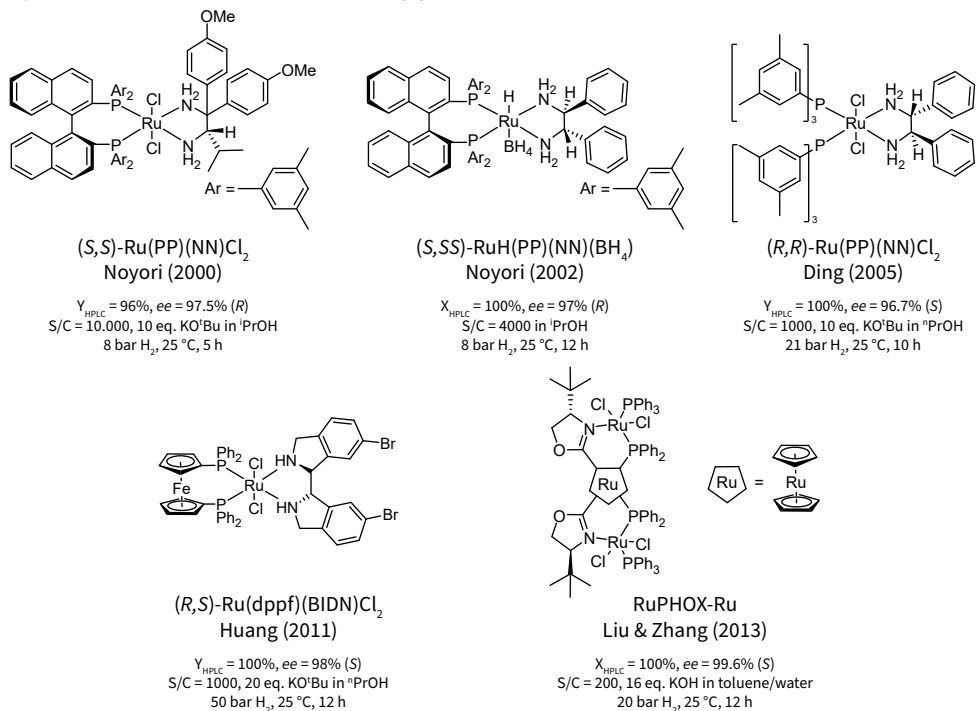
Substrate **1** is incompatible with almost all transition metal ketone hydrogenation catalysts. Most precatalysts for these reactions (which are almost exclusively Ru^{II} chloride complexes) require the addition of a basic activator. This base converts the precatalyst into a deprotonated complex that can form catalytically active Ru-hydrides under hydrogen pressure. The requirement for basic conditions is problematic for Mannich bases such as **1**, because exposure to bases leads to undesirable elimination reactions and degradation of the substrate, which itself results in poor yields and/or product selectivity.

Several groups have reported the catalytic (asymmetric) hydrogenation of **1**.^{37–46} These reactions were performed with Rh^I or Ru^{II} precatalysts and resulted in similar yields of **2**. Two strategies have been devised that work around the base sensitivity of **1**: *i*) activation with a minimum amount of base to reduce its impact, and *ii*) reaction with a pre-activated (stable) borohydride complex. The best performing catalytic systems are summarised in **Figure 6.6a**. Under optimised conditions all catalytic systems provided **2** in excellent yields at very high enantioselectivity.

We assembled a modest library of structurally-related complexes that were both commercially available and that had not been used before for the target reaction (**Figure 6.6b**). The precatalysts were activated *in situ* with the addition of five equivalents of NaBH₄ or NaHBet₃. Addition of the hydride reagent to a solution of the precatalyst in THF resulted in a pronounced and rapid colour change to golden yellow (from either green or yellow, depending on the precatalyst). Ultimately the use of NaHBet₃ was preferred because of its high solubility in organic solvents. (Use of NaBH₄ resulted in a finely dispersed suspension that would occasionally block the microfluidic system.) The *in situ* pre-activation protocol allowed us

to efficiently and conveniently screen a series of Ru^{II} precatalysts without the additional workload of (pre)catalyst isolation.

a) Literature overview of 3-DMAPP (**1**) reductions



b) Precatalysts used in this work

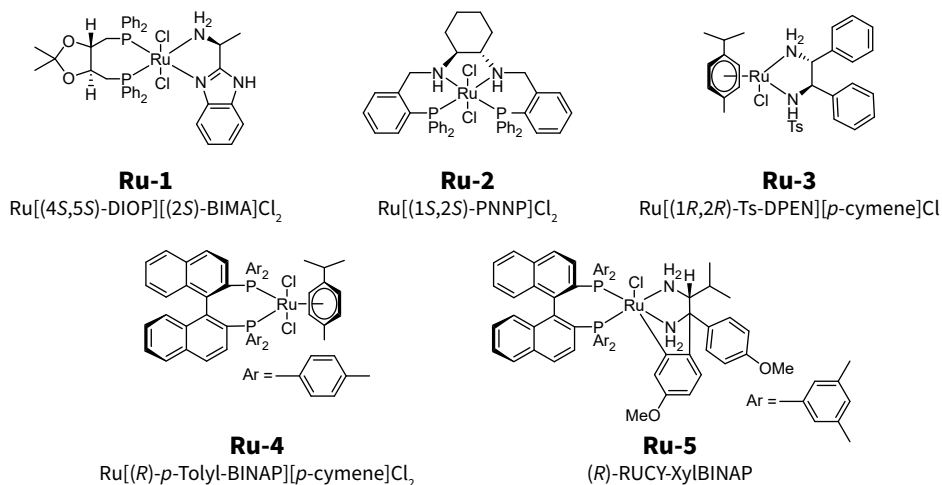
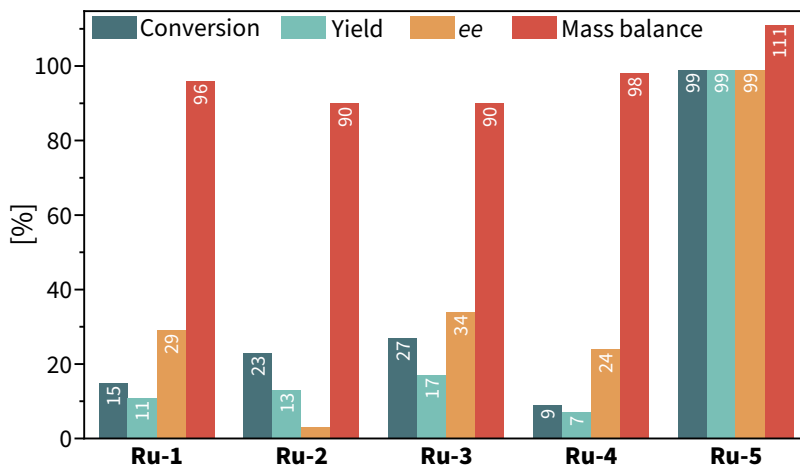


Figure 6.6. a) Selected literature examples of the catalytic asymmetric reduction of **1**. b) Selection of Ru^{II} precatalysts used in this work.

6.5 Reaction screening and optimisation

The reaction development campaign was started with a user-defined pre-screening. This phase was used to scout the experimental parameter space without the use of the optimisation algorithm. We estimated that a catalyst loading of 3 mol% Ru would allow the evaluation of catalytic performance in approximately 30 minutes per experiment. Two sets of conditions were employed for each catalytic system: *i*) a 'long' run of 30 minutes at 30 °C, and *ii*) a 'short' run of 15 minutes at 60 °C. The results of these experiments are summarised in **Figure 6.7**.

a) 30 min at 30 °C



b) 15 min at 60 °C

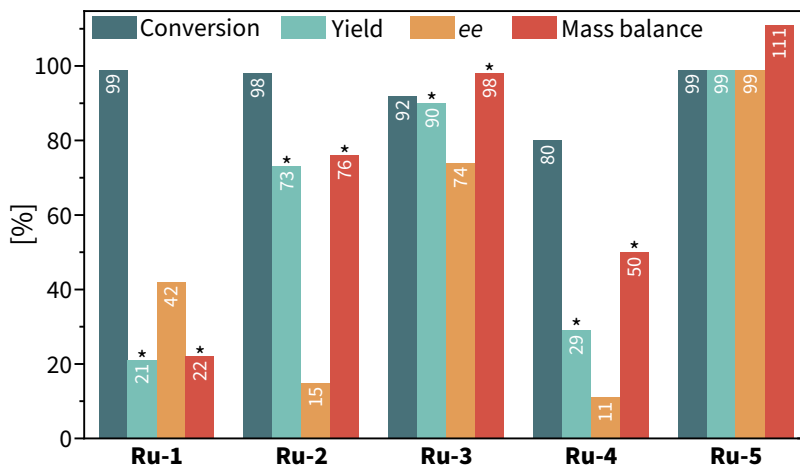


Figure 6.7. Asymmetric hydrogenation of β -aminoketone **1** to chiral γ -aminoalcohol **2** with catalysts **Ru-1–Ru-5**. Conditions: 0.1 M **1** in 2-propanol, 3 mol% activated Ru, 15–30 min, 30–60 °C, 30 bar H₂. *Unresolved side-product present in chromatogram. Peak integration is unreliable.

At 30 °C, catalytic systems **Ru-1** to **Ru-4** exhibited similar activity and selectivity. RUCY catalyst **Ru-5** performed significantly better and provided **2** in excellent yield and enantiomeric excess. Our first experiments thus immediately identified suitable conditions for the target transformation. The experiments at 60 °C indicated that catalytic performance depended strongly on the reaction temperature. Mixtures that contained catalysts **Ru-1** to **Ru-4** all featured significantly higher conversion of the starting material, and, at first glance, improved product enantiomeric excess. Closer inspection revealed that a chromatographically-unresolved side-product was present that had been automatically integrated with the target product. This side-product was later identified as 1-phenyl-1-propanol (**5**) and had been absent at 30 °C. The compound overlapped with (*S*)-**2** in the chromatogram and increased the apparent *ee* and yield of the target product because the automated integration algorithm failed to differentiate the two overlapping peaks. Acrylophenone **3** and propiophenone **4** were not detected in the HPLC analysis. Product **5** was not observed after reaction with **Ru-5** at 60 °C, and a practically identical reaction mixture was obtained under both conditions.

These results neatly demonstrate that automation is a very powerful tool that enables operators or experts to spend time on other tasks. It is also more accurate, reproducible, and can be operated (semi-)continuously to shorten development times. However—as this case demonstrates—it is not a proverbial 'silver bullet'. The automated system must be provided with a flawless chromatographic method and its actions should be closely monitored by the operator.

The obtained results led to a number of conclusions regarding the (catalytic) chemistry under study. Firstly, the reaction rate of the retro-Mannich reaction was negligible at 30 °C, and was comparable to the rate of the target reaction at 60 °C in the presence of **Ru-1** to **Ru-4**. (It is possible that the retro-Mannich reaction also occurred with **Ru-5**, but this was masked by the system's extraordinarily high activity for the desired reduction of **1** to **2**.) Secondly, because **3** and **4** were not observed in the chromatograms, this probably means that they were more readily reduced than substrate **1**. Finally, it can be concluded that activated complex **Ru-5** is a highly active and selective catalyst for the target reaction. It was therefore selected for the scale-up reaction to multigram quantities.

(Note that we intended to demonstrate the system's ability to automatically navigate the non-trivial reaction parameter space with catalysts **Ru-1** to **Ru-4**. These experiments unfortunately could not be performed at the time and a follow-up visit has since been hindered by the COVID-19 pandemic.)

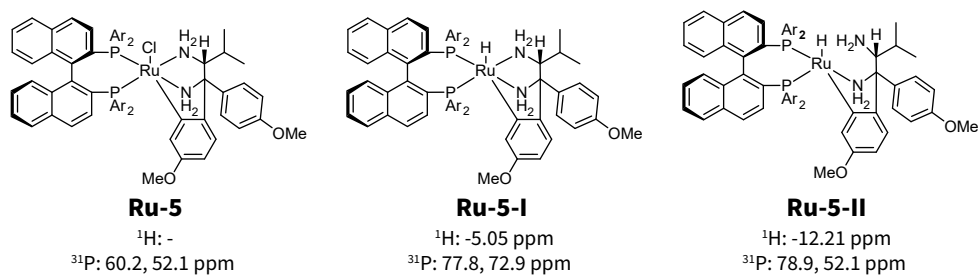
6.6 Scale-up to multigram quantities

The catalyst activation process was studied in more detail to support optimisation of the targeted reaction scale-up. The transformation of the precatalyst upon activation was studied with ^1H and ^{31}P NMR spectroscopy. The reaction of (*R*)-RUCY-XylBINAP **Ru-5** with 5 eq. NaHBET_3 in $\text{THF-}d_8$ resulted in a rapid and pronounced colour change from green to golden yellow. Spectra were acquired immediately after mixing, after approximately 3 hours at room temperature, and after a night at room temperature (**Figure 6.8**).

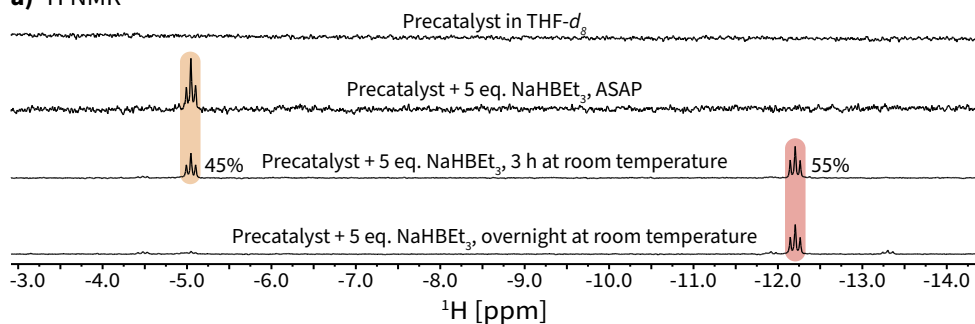
Treatment of the Ru^{II} chloride precursor **Ru-5** with NaHBET_3 gave rise to two new Ru-hydride species. Directly after mixing the solution contained **Ru-5-I** as the major species. This complex was characterised by the hydride resonance in the ^1H NMR spectrum at $\delta = -5.05$ ppm. The phosphorus nuclei of this complex appeared in the ^{31}P NMR spectrum as two doublets at 77.8 ppm and 72.9 ppm ($^2J_{\text{pp}} = 43.6$ Hz).

After 3 hours at room temperature the spectrum had changed significantly and a second Ru-hydride species **Ru-5-II** was observed. The two hydride complexes were present in approximately the same amount (45% **Ru-5-I** and 55% **Ru-5-II** by ^1H NMR). The hydride resonance of **Ru-5-II** appeared significantly upfield compared to the first Ru-H complex, at $\delta = -12.21$ ppm. One of the two doublets in the ^{31}P NMR was also shifted upfield (78.9 ppm and 52.1 ppm with $^2J_{\text{pp}} = 26.6$ Hz). After one night at room temperature the solution contained **Ru-5-II** as the major species.

The spectra of complexes **Ru-5-I** and **Ru-5-II** were consistent with reports from Matsumura *et al*, who activated **Ru-5** with 1 atm H_2 in the presence of KO^tBu and characterised the two species with multidimensional NMR experiments (**Figure 6.8**).⁴⁷ **Ru-5-I** is an octahedral ruthenium hydride complex that is highly active for the (asymmetric) hydrogenation of ketones. Pentaligated complex **Ru-5-II** was considerably less catalytically active, which was attributed to the decoordination of the (potentially reactive) amino group. We therefore concluded that the activated precatalyst solution was best used as soon as possible after mixing.



a) ^1H NMR



b) ^{31}P NMR

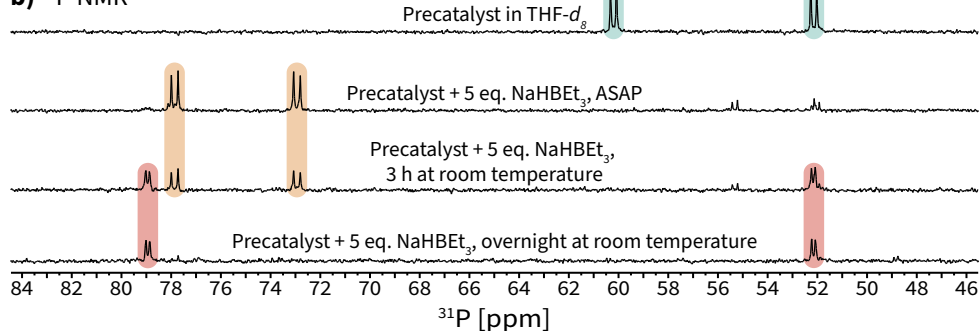


Figure 6.8. NMR study into activation of (*R*)-RUCY-XylBINAP with 5 eq. NaHBET_3 in THF at room temperature. Approximate reaction times are indicated in the figure. Assignment of Ru hydrides **Ru-5-I** and **Ru-5-II** are from K. Matsumura *et al.*⁴⁷ **a)** ^1H NMR spectrum in $\text{THF-}d_8$ (400 MHz). **b)** ^{31}P NMR spectrum in $\text{THF-}d_8$ (162 MHz).

The asymmetric hydrogenation reaction was performed twice at different catalyst loadings and reaction scales (**Figure 6.9**). Reactions were performed in a stainless steel autoclave that was fitted with a custom-built automatic sampling system. This autosampler system was designed for automated high-resolution kinetic measurements and it is described in detail in **Chapter 7**.

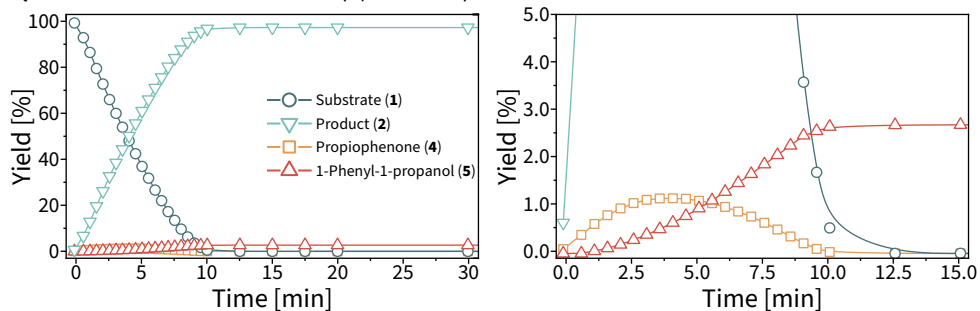
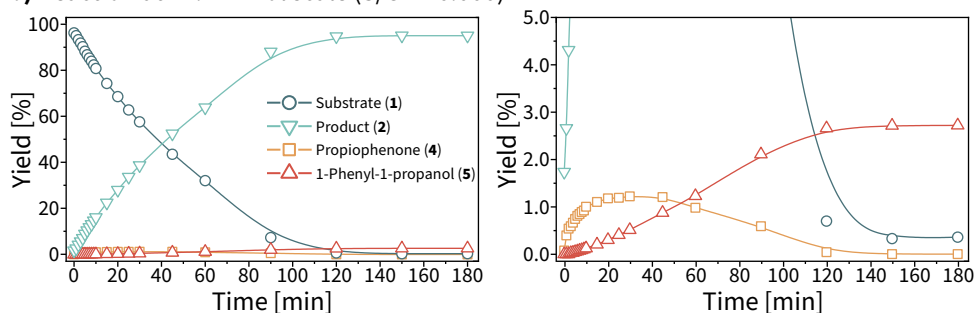
a) Reaction at 7.5 mmol scale (S/C = 5000)**b) Reaction at 44.7 mmol scale (S/C = 10.000)**

Figure 6.9. Kinetic profiles of the asymmetric hydrogenation of **1** to **2** with **Ru-5**. Yields were determined by GC-FID using *n*-dodecane as an internal standard. **a)** Conditions: 7.5 mmol **1** in 20 ml 2-propanol, 0.02 mol% activated **Ru-5** (S/C = 5000), 29 °C, 30 bar H₂. **b)** Conditions: 44.7 mmol **1** in 20 ml 2-propanol, 0.01 mol% activated **Ru-5** (S/C = 10.000), 29 °C, 30 bar H₂.

The reaction with 0.02 mol% Ru (S/C = 5000) was very fast and completed within 15 minutes at 29 °C (**Figure 6.9a**). Product **2** was formed in 97% yield. Product *ee* (not shown) was constant throughout the reaction at >99% (*S*)-**2**. Our kinetic analysis also allowed the detection of the minor propiophenone (**4**) and 1-phenyl-1-propanol (**5**) products. Acrylophenone (**3**) presumably was too reactive and could not be observed by GC-FID or HPLC analysis. (Also note that the mixture was sampled at excessive temporal resolution to demonstrate the autosampler's capabilities. This was not required for the chemistry at hand and actually quite severely diminished the isolated yield of (*S*)-**2**.)

The reaction's final scale-up was performed at 0.01 mol% **Ru-5** with 44.7 mmol (~8 g) **1** (kinetic traces in **Figure 6.9b**). This reaction was considerably slower than that at S/C = 5000 and completed in just under 3 hours. (*S*)-**2** was obtained in 97% GC-yield at >99% *ee*. The fully hydrogenated side-product **5** was formed in approximately 3% yield. This up-scaled reaction consumed a significant quantity of gas from the reactor headspace, which decreased the hydrogen pressure inside the autoclave system appreciably. The target product was isolated as its hydrochloride

salt. Additional purification by recrystallisation ultimately provided 5.81 g of the chemically and enantiomerically pure (*S*)-**2**·HCl product. This represents a 65% isolated yield of the initial substrate loading, and 84% isolated yield based on the residual reaction mixture after sampling (*i.e.*, 19% of the material was removed during sampling).

Our automation-guided approach successfully identified a suitable catalytic system from a set of (previously untested) commercially available precatalysts. This use case is relevant in a number of situations, *e.g.*, when catalyst consumption is too high and increased performance is required, when production costs should be decreased, or when there are restrictions on the use of intellectual property and specific compounds cannot be used. This catalytic system outperformed the state-of-the-art catalytic system for this transformation³⁹ and ultimately provided the target γ -aminoalcohol product in comparable yield at an identical catalyst loading, approximately halved reaction time, and improved product *ee* (>99% *versus* 97.5%).

6.7 Conclusion

Automated microfluidic tools potentially offer fast, efficient, and focused screening and optimisation of discrete and continuous variables. We have described the modification of an existing oscillatory flow platform that enabled high-pressure gas-liquid catalytic chemistry inside chemically inert perfluorinated tubing. The application of back pressure was critical for system stability and integrity, and ultimately enabled continuous operation at 70 °C and 40 bar.

The platform's capabilities were demonstrated with a challenging Ru-catalysed asymmetric hydrogenation reaction of a highly sensitive β -aminoketone. Favourable reaction conditions were identified with the screening and optimisation tool, which were used to perform the reaction at a synthetically useful scale. These reactions were performed automatically and only required minor involvement from the operator once the system was started.

The scale-up reaction was performed in a batch autoclave system and afforded multigram quantities of the enantiopure compound as its hydrochloride salt. Reaction kinetics were measured automatically with a custom-built sampling system that is described in more detail in **Chapter 7**. Our automation-guided reaction development approach ultimately enabled the discovery and scale-up of a challenging chiral reduction in less than a week of total experimental time.

6.8 Experimental section

General considerations

All manipulations were, unless stated otherwise, performed under an inert atmosphere in an Ar-filled Inert glove box or using standard Schlenk techniques. Anhydrous solvents were dispensed from an Inert PureSolv solvent purification system or were dried using 3 or 4 Å molecular sieves. Solvents were degassed before use. Chemicals were purchased from Sigma-Aldrich, Strem, TCI, or Key Organics and were dried and/or degassed before use. Air and/or moisture sensitive materials were stored in the glove box. Deuterated solvents were purchased from Eurisotop, dried using molecular sieves, degassed, and stored in the glove box.

NMR spectra were recorded on an Agilent 400-MR DD2 400 MHz spectrometer equipped with a 5 mm ONE NMR probe. ^1H and ^{13}C chemical shifts were referenced to residual solvent peaks (^1H : 3.58 ppm THF- d_6 , 7.26 ppm CDCl_3 , ^{13}C : 67.21 ppm THF- d_6 , 77.16 ppm CDCl_3). ^{31}P NMR spectra were referenced *via* the IUPAC absolute chemical shift ($\Xi = 40.480742$).

Synthetic procedures

Complex **Ru-2** was prepared according to literature procedure.^{48–49}

1 – 3-(Dimethylamino)propiophenone

Compound **1** was freebased from the commercially available hydrochloride salt *via* the procedure below, or was prepared *via* a Mannich reaction following an adapted procedure from Almutairi *et al.*⁵⁰

To a 500 ml flask was added 24.0 g acetophenone (200 mmol, 1.0 eq.), 22.0 g dimethylamine hydrochloride (270 mmol, 1.35 eq.), 8.1 g paraformaldehyde (270 mmol, 1.35 eq.), 1.0 ml concentrated aqueous HCl, and 200 ml anhydrous ethanol. The mixture was refluxed overnight in air.

Afterwards volatiles were removed *in vacuo*, the resulting solids were filtered off, washed with cold acetone, and dried under vacuum to give 35.6 g of the crude product as a white solid. At this stage the main contamination was residual dimethylamine hydrochloride.

The hydrochloride salts were dissolved in 200 ml water and were cooled to 0 °C. To the solution was added dropwise a 3.65 M solution of KOH in water at 0 °C until the pH reached >12. The product was extracted with diethyl ether (4 x 50 ml). Combined organic phases were dried over MgSO_4 and the solvent was removed *in vacuo* to

obtain the product as a clear liquid that was further purified by crystallisation. The liquid was cooled to -20 °C to induce crystallisation. The large colourless crystals were filtered off, briefly dried under vacuum, and transferred to the glove box for storage. The title compound was obtained as a colourless and slightly viscous liquid. Yield: 23.7 g (67%). Purity: 99.3% (GC relative area%).

^1H NMR (400 MHz, CDCl_3): δ 7.94–7.88 (m, aryl H , 2H), 7.53–7.47 (m, aryl H , 1H), 7.44–7.36 (m, aryl H , 2H), 3.09 (t, $J = 7.3$ Hz, CH_2 , 2H), 2.70 (d, $J = 7.9$ Hz, CH_2 , 2H), 2.23 (s, $\text{N}(\text{CH}_3)_2$, 6H).

^{13}C NMR (101 MHz, CDCl_3): all resonances are singlets: δ 199.0, 136.9, 133.0, 128.6, 128.0, 54.4, 45.5, 36.9.

2 - (S)-3-(Dimethylamino)-1-phenyl-1-propanol hydrochloride

After the asymmetric hydrogenation was complete (see procedure below) the crude reaction mixture was dried over MgSO_4 , and 22.5 ml of a 4.0 M HCl solution in 1,4-dioxane (90.0 mmol, 2.0 eq.) was slowly added. The mixture was stirred for approximately 10 minutes and volatiles were removed *in vacuo* to yield the crude product as a yellow oil. The oil was triturated for 1 h with 15 ml anhydrous THF to give the product as a white solid. The solids were collected, dried, and recrystallised from ethanol/diethyl ether at -20 °C to give the analytically pure title compound as white crystals. Yield: 5.81 g (65% of initial loading, 84% of residual reaction mixture after sample withdrawal; 19% of the material was removed during sampling).

^1H NMR (400 MHz, D_2O): δ 7.55–7.36 (m, aryl H , 5H), 4.90–4.82 (m, 1H), 3.36–3.22 (m, 1H), 3.22–3.09 (m, 1H), 2.89 (s, $\text{N}(\text{CH}_3)_2$, 6H), 2.30–2.11 (m, CH_2 , 2H).

^{13}C NMR (101 MHz, D_2O): all resonances are singlets: δ 142.5, 129.0, 128.4, 125.9, 71.3, 55.3, 43.0, 42.7, 32.4.

Screening and optimisation experiments

Experiments were performed using a modified version of the automated microfluidic oscillatory flow platform that has been described in previous works.^{15–22,51} Modifications were made to the reactor block to enable sustained operation at elevated temperature and pressure (see **Chapter 6.3**). Microfluidic tubing and connectors were purchased from IDEX Health and Services (system: FEP 1/16" OD x 0.02" ID, reactor: PFA 1/8" OD x 1/16" ID). The system and optimisation campaign were controlled with software written in MATLAB R2016a and LabVIEW 2016, which have been described in the cited works.

Precatalysts were activated at room temperature inside an N₂-filled glove box by the addition of 5.0 eq. NaHBET₃ (1 M in THF) to a solution of the Ru complex in THF. The mixtures were stirred in the glove box for ≥1 h. Immediately upon addition the colour of the mixtures changed from yellow to golden orange.

Note: NaBH₄ was initially used for catalyst activation and resulted in similar catalytic activity as NaHBET₃. Use of these suspensions occasionally led to blockages of the microfluidic system, while filtration caused diminished catalytic performance. The procedure based on NaHBET₃ was more convenient and reproducible, and was therefore preferred over activation with NaBH₄.

Stock solutions of precisely-known concentrations were prepared of the catalysts in 2-propanol, and of substrate **1** in 2-propanol with 1-fluoronaphthalene as an internal standard. The solutions were transferred to conical glass vials, capped with a silicone septum, and taken out of the glove box. The vials were placed inside a vial rack inside the liquid handler module (Gilson GX-241), which itself was placed inside a gas-tight glove bag. 2-Propanol was used as the liquid handler's transfer solvent and the pump was primed. The bag was then purged with Ar until the atmosphere inside measured <0.1 vol% O₂ (measured with a Honeywell GasAlert MicroClip X3 gas detector located inside the bag).

Stainless steel high-pressure syringes (8 ml, Harvard Apparatus) were filled with the appropriate solvent while inside the glove box (THF in rinse, 2-propanol in quench, injection not used), taken outside without exposure to air, placed inside the syringe pumps (Harvard Apparatus PHD Ultra), and were primed. The microfluidic system was thoroughly purged of air through a series of gas-exchange cycles, during which: *i*) the system was pressurised with 30 bar N₂, *ii*) the carrier syringe was fully withdrawn, *iii*) the gas supply was closed, *iv*) the carrier syringe volume was infused into the system, and *v*) the system was depressurised *via* the waste valve. The cycle was repeated twice more with N₂, after which the procedure was repeated thrice with 30 bar H₂. Experiments were then started and proceeded through phases of sample preparation, reaction, and analysis.

Four 15 µl rinse slugs were injected before each experiment to clean the system and to minimise carry-over between experiments. Reaction mixtures were prepared by the liquid handling robot. A total volume of 40 µl was prepared, which was thoroughly mixed inside the liquid handler, and was injected into a 17 µl sample loop that was connected to a 6-port 2-position valve inside the glove bag. Once the system was clean and empty, the liquid handler switched the valve and injected the droplet into the H₂-filled system. The slug was then transported to the reactor by slow gas infusion from the carrier syringe. The droplet's location inside the system was tracked with a number of phase sensors (Optek OCB350L062Z).

Once inside the reactor, the droplet was oscillated for the target residence time. The position of the droplet was tracked using a photodetector. This sensor signalled when the droplet was about to exit the reactor and when the carrier flow had to be reversed. Temperature of the custom-made aluminium reactor block was controlled to ± 2.0 °C with cartridge heaters and a fan. After the reaction the droplet was diluted two-fold with 2-propanol, thoroughly mixed, and injected into a 1.7 μl sample loop that was connected to a 6-port 2-position valve. The sample was injected into the on-line HPLC system and was analysed as described.

HPLC results were imported into MATLAB, and conversion, yield, and product enantiomeric excess were calculated. The natural logarithm of the absolute value of product enantiomeric excess was used for the optimisation objective function (**Equation 6.1**).

$$f_{obj} = \ln |ee| = \ln \left| \frac{Y_{(R)} - Y_{(S)}}{Y_{(R)} + Y_{(S)}} \right| \quad (6.1)$$

This was required because *a priori* knowledge on product stereoselectivity for a given catalyst's absolute configuration is not usually available (*i.e.*, predicting what enantiomer forms preferentially from a given catalyst). Use of absolute enantiomeric excess enabled the maximisation of *ee* without the need to assign a target enantiomer. The desired absolute configuration can be accessed with the corresponding catalyst after the screening and optimisation phase. A yield criterion of 0.9 was used to prioritise product *ee* over total yield. No further changes were made to the published optimisation algorithm.²⁰

Activation of (*R*)-RUCY-XylBINAP for large scale hydrogenation

Inside the glove box, 14.2 mg (*R*)-RUCY-XylBINAP (12.0 μmol , 1.0 eq.) was dissolved in 4.0 ml THF. To the stirred solution was added 60.0 μl of a 1 M NaHBET₃ solution in THF (60.0 μmol , 5.0 eq.). The mixture was stirred at room temperature in the glove box for ≥ 1 h. Immediately upon addition the colour of the solution rapidly changed from green/yellow to golden orange.

Large scale hydrogenation of 1

Reactions were performed in a 60 ml stainless steel Parr autoclave, equipped with a Julabo CF30 thermostat and a gas burette system that enabled monitoring of gas consumption. Samples were periodically removed from the system with a custom-made automated sampling system (see **Chapter 7**). Before the experiment, the autoclave was evacuated at 80 °C for ≥ 1 h, cooled to 30 °C, and refilled with Ar.

Inside the glove box, a glass vial was loaded with 250 μl *n*-dodecane, 20.0 ml 2-propanol, and 7.92 g **1** (44.7 mmol). A separate vial was loaded with 1.490 ml of the pre-activated catalyst solution (4.47 μmol Ru, S/C = 10.000, see section above). The two mixtures were transferred to the autoclave without exposure to air. The substrate solution was added to the main reactor vessel, and the catalyst solution was placed inside a separate stainless steel compartment that was fluidically decoupled from the reactor with a ball valve.

Stirring was engaged at 700 rpm and the reaction mixture was preheated for 5 minutes until it reached the desired temperature ($T_{\text{Set}} = 30\text{ }^{\circ}\text{C}$, $T_{\text{Internal}} = 29\text{ }^{\circ}\text{C}$, measured with an internal thermocouple). Hydrogen pressure was applied (30 bar) and the reaction was started following the addition of the catalyst solution to the reaction mixture. Samples were periodically removed from the reaction mixture and were analysed as described. Afterwards the reactor was depressurised, purged with Ar, and the crude reaction mixture was worked-up as described.

Analytical details - GC-FID

Measurements were performed on an Agilent 7890B gas chromatograph equipped with FID and Agilent 5977B MS detectors and an Restek Stabilwax-MS column (30 m, 0.32 mmID, 0.25 μm film thickness). Method details: 100 $^{\circ}\text{C}$ (hold 0.5 min), ramp to 250 $^{\circ}\text{C}$ at 30 $^{\circ}\text{C min}^{-1}$ (hold at 250 $^{\circ}\text{C}$ for 3.0 min). Products were identified using the retention times of analytically pure reference samples and by comparison of observed mass spectra and spectra of the authentic reference samples available in the NIST 17 and SDBS libraries. Mass balances were calculated using *n*-dodecane as an internal standard and were verified to be within 90%–110% for all experiments.

Analytical details - HPLC

Measurements were performed on an Agilent 1260 Infinity HPLC or Waters Acquity UPLC. Systems were equipped with UV detectors and were used at 220 nm and 275 nm. Agilent: measurements were performed with a Phenomenex Lux Cellulose-2 column (100 mm, 4.6 μm , 5 mm) at 30 $^{\circ}\text{C}$. Samples were eluted at 2.0 ml min^{-1} with *n*-heptane/2-propanol/diethylamine (*v/v*) as the eluent. Method details: 95/5/0.1 for 0.2 min, ramp to 60/40/0.1 in 4.3 min, hold 0.5 min, ramp to 95/5/0.1 in 0.1 min, hold 0.9 min (total runtime 6.0 min). Waters: measurements were performed with a Phenomenex Lux Cellulose-2 column (250 mm, 4.6 μm , 5 mm) at 30 $^{\circ}\text{C}$. Samples were eluted at 1.5 ml min^{-1} with *n*-heptane/2-propanol/diethylamine (*v/v*) as the eluent. Method details: ramp from 95/5/0.1 to 60/40/0.1 in 10.0 min, hold 2.0 min, ramp to 95/5/0.1 in 0.1 min, hold 2.9 min (total runtime 15.0 min). Products and absolute configuration were identified using the retention times of analytically pure reference samples. Mass balances were calculated using 1-fluoronaphthalene as an internal standard and were verified to be within 90%–110% for all experiments.

6.9 References

1. de Vries, J.G.; de Vries, A.H.M., *The Power of High-Throughput Experimentation in Homogeneous Catalysis Research for Fine Chemicals*, *European Journal of Organic Chemistry* **2003**, 2003 (5), 799–811;
2. de Vries, J.G.; Lefort, L., *Development of Asymmetric Hydrogenation Catalysts via High Throughput Experimentation*, *Oil Gas Sci. Technol. – Rev. IFP Energies nouvelles* **2013**, 68 (3), 519–528;
3. Krska, S.W.; DiRocco, D.A.; Dreher, S.D.; Shevlin, M., *The Evolution of Chemical High-Throughput Experimentation To Address Challenging Problems in Pharmaceutical Synthesis*, *Accounts of Chemical Research* **2017**, 50 (12), 2976–2985;
4. Mennen, S.M.; Alhambra, C.; Allen, C.L.; Barberis, M.; Berritt, S.; Brandt, T.A.; Campbell, A.D.; Castañón, J.; Cherney, A.H.; Christensen, M.; Damon, D.B.; Eugenio de Diego, J.; García-Cerrada, S.; García-Losada, P.; Haro, R.; Janey, J.; Leitch, D.C.; Li, L.; Liu, F.; Lobben, P.C.; MacMillan, D.W.C.; Magano, J.; McInturff, E.; Monfette, S.; Post, R.J.; Schultz, D.; Sitter, B.J.; Stevens, J.M.; Strambeanu, I.I.; Twilton, J.; Wang, K.; Zajac, M.A., *The Evolution of High-Throughput Experimentation in Pharmaceutical Development and Perspectives on the Future*, *Organic Process Research & Development* **2019**, 23 (6), 1213–1242;
5. Shultz, C.S.; Krska, S.W., *Unlocking the Potential of Asymmetric Hydrogenation at Merck*, *Accounts of Chemical Research* **2007**, 40 (12), 1320–1326;
6. Allen, C.L.; Leitch, D.C.; Anson, M.S.; Zajac, M.A., *The power and accessibility of high-throughput methods for catalysis research*, *Nature Catalysis* **2019**, 2 (1), 2–4;
7. Jäkel, C.; Paciello, R., *High-Throughput and Parallel Screening Methods in Asymmetric Hydrogenation*, *Chemical Reviews* **2006**, 106 (7), 2912–2942;
8. Isbrandt, E.S.; Sullivan, R.J.; Newman, S.G., *High Throughput Strategies for the Discovery and Optimization of Catalytic Reactions*, *Angewandte Chemie International Edition* **2019**, 58 (22), 7180–7191;
9. Plutschack, M.B.; Pieber, B.; Gilmore, K.; Seeberger, P.H., *The Hitchhiker's Guide to Flow Chemistry*, *Chemical Reviews* **2017**, 117 (18), 11796–11893;
10. Porta, R.; Benaglia, M.; Puglisi, A., *Flow Chemistry: Recent Developments in the Synthesis of Pharmaceutical Products*, *Organic Process Research & Development* **2016**, 20 (1), 2–25;
11. Hessel, V.; Kralisch, D.; Kockmann, N.; Noël, T.; Wang, Q., *Novel Process Windows for Enabling, Accelerating, and Uplifting Flow Chemistry*, *ChemSusChem* **2013**, 6 (5), 746–789;
12. Webb, D.; Jamison, T.F., *Continuous flow multi-step organic synthesis*, *Chemical Science* **2010**, 1 (6), 675–680;
13. Rogers, L.; Jensen, K.F., *Continuous manufacturing – the Green Chemistry promise?*, *Green Chemistry* **2019**, 21 (13), 3481–3498;
14. Abolhasani, M.; Bruno, N.C.; Jensen, K.F., *Oscillatory three-phase flow reactor for studies of bi-phasic catalytic reactions*, *Chemical Communications* **2015**, 51 (43), 8916–8919;
15. Abolhasani, M.; Coley, C.W.; Xie, L.; Chen, O.; Bawendi, M.G.; Jensen, K.F., *Oscillatory Microprocessor for Growth and in Situ Characterization of Semiconductor Nanocrystals*, *Chemistry of Materials* **2015**, 27 (17), 6131–6138;
16. Reizman, B.J.; Jensen, K.F., *Simultaneous solvent screening and reaction optimization in microliter slugs*, *Chemical Communications* **2015**, 51 (68), 13290–13293;
17. Reizman, B.J.; Wang, Y.M.; Buchwald, S.L.; Jensen, K.F., *Suzuki–Miyaura cross-coupling optimization*

- enabled by automated feedback, *Reaction Chemistry & Engineering* **2016**, 1 (6), 658–666;
18. Coley, C.W.; Abolhasani, M.; Lin, H.; Jensen, K.F., *Material-Efficient Microfluidic Platform for Exploratory Studies of Visible-Light Photoredox Catalysis*, *Angewandte Chemie International Edition* **2017**, 56 (33), 9847–9850;
 19. Hwang, Y.J.; Coley, C.W.; Abolhasani, M.; Marzinzik, A.L.; Koch, G.; Spanka, C.; Lehmann, H.; Jensen, K.F., *A segmented flow platform for on-demand medicinal chemistry and compound synthesis in oscillating droplets*, *Chemical Communications* **2017**, 53 (49), 6649–6652;
 20. Baumgartner, L.M.; Coley, C.W.; Reizman, B.J.; Gao, K.W.; Jensen, K.F., *Optimum catalyst selection over continuous and discrete process variables with a single droplet microfluidic reaction platform*, *Reaction Chemistry & Engineering* **2018**, 3 (3), 301–311;
 21. Hsieh, H.W.; Coley, C.W.; Baumgartner, L.M.; Jensen, K.F.; Robinson, R.I., *Photoredox Iridium–Nickel Dual-Catalyzed Decarboxylative Arylation Cross-Coupling: From Batch to Continuous Flow via Self-Optimizing Segmented Flow Reactor*, *Organic Process Research & Development* **2018**, 22 (4), 542–550;
 22. Baumgartner, L.M.; Dennis, J.M.; White, N.A.; Buchwald, S.L.; Jensen, K.F., *Use of a Droplet Platform To Optimize Pd-Catalyzed C–N Coupling Reactions Promoted by Organic Bases*, *Organic Process Research & Development* **2019**, 23 (8), 1594–1601;
 23. Angeli, P.; Gavriilidis, A., *Encyclopedia of Microfluidics and Nanofluidics*, Springer US, Boston, Massachusetts, United States of America, **2008**; 1971–1976;
 24. Kreutzer, M.T., *Hydrodynamics of Taylor Flow in Capillaries and Monolith Reactors*, Ph.D. Dissertation, Delft University of Technology, **2003**;
 25. Bianchi, P.; Williams, J.D.; Kappe, C.O., *Oscillatory flow reactors for synthetic chemistry applications*, *Journal of Flow Chemistry* **2020**, 10 (3), 475–490;
 26. Baumgartner, L.M., MSc thesis, Technische Universität München, **2017**;
 27. Zhu, C.; Raghuvanshi, K.; Coley, C.W.; Mason, D.; Rodgers, J.; Janka, M.E.; Abolhasani, M., *Flow chemistry-enabled studies of rhodium-catalyzed hydroformylation reactions*, *Chemical Communications* **2018**, 54 (62), 8567–8570;
 28. Raghuvanshi, K.; Zhu, C.; Ramezani, M.; Menegatti, S.; Santiso, E.E.; Mason, D.; Rodgers, J.; Janka, M.E.; Abolhasani, M., *Highly Efficient 1-Octene Hydroformylation at Low Syngas Pressure: From Single-Droplet Screening to Continuous Flow Synthesis*, *ACS Catalysis* **2020**, 10 (14), 7535–7542;
 29. Han, S.; Kashfipour, M.A.; Ramezani, M.; Abolhasani, M., *Accelerating gas–liquid chemical reactions in flow*, *Chemical Communications* **2020**, 56 (73), 10593–10606;
 30. Personal communication with IDEX representative, **2018**;
 31. IDEX FEP Tubing 1/16" OD x 0.020" ID, <https://www.idex-hs.com/store/fluidics/fluidic-connections/tubing/fep-tubing-1-16-od-x-020-id-natural-100ft.html> (accessed 24 December 2020);
 32. IDEX PFA Tubing High Purity 1/8" OD x 1/16" ID, <https://www.idex-hs.com/store/pfa-tubing-high-purity-1-8-od-x-1-16-id-x-50ft.html> (accessed 24 December 2020);
 33. Molloy, B.B.; Schmiegel, K.K., *Substituted Phenoxyphenylpropyl dimethylamines*, US4584404A, **1983**;
 34. Wong, D.T.; Horng, J.S.; Bymaster, F.P.; Hauser, K.L.; Molloy, B.B., *A selective inhibitor of serotonin uptake: Lilly 110140, 3-(p-Trifluoromethylphenoxy)-n-methyl-3-phenylpropylamine*, *Life Sciences* **1974**, 15 (3), 471–479;
 35. Molloy, B.B.; Schmiegel, K.K., *Aryloxyphenylpropylamines in treating depression*, US4018895A, **1977**;
 36. Wenthur, C.J.; Bennett, M.R.; Lindsley, C.W., *Classics in Chemical Neuroscience: Fluoxetine (Prozac)*,

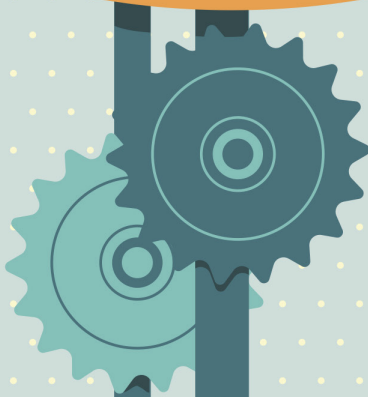
- ACS Chemical Neuroscience **2014**, 5 (1), 14–23;
37. Takahashi, H.; Sakuraba, S.; Takeda, H.; Achiwa, K., *Asymmetric reactions catalyzed by chiral metal complexes. Highly efficient asymmetric hydrogenation of amino ketone derivatives leading to practical syntheses of (S)-propranolol and related compounds*, *Journal of the American Chemical Society* **1990**, 112 (15), 5876–5878;
 38. Devocelle, M.; Agbossou, F.; Mortreux, A., *Asymmetric Hydrogenation of α , β , and γ -Aminoketones Catalyzed by Cationic Rhodium(I){AMPP} Complexes*, *Synlett* **1997**, 1997 (11), 1306–1308;
 39. Ohkuma, T.; Ishii, D.; Takeno, H.; Noyori, R., *Asymmetric Hydrogenation of Amino Ketones Using Chiral RuCl₂(diphosphine)(1,2-diamine) Complexes*, *Journal of the American Chemical Society* **2000**, 122 (27), 6510–6511;
 40. Ohkuma, T.; Koizumi, M.; Muñiz, K.; Hilt, G.; Kabuto, C.; Noyori, R., *trans-RuH(η -BH₂)(binap) (1,2-diamine): A Catalyst for Asymmetric Hydrogenation of Simple Ketones under Base-Free Conditions*, *Journal of the American Chemical Society* **2002**, 124 (23), 6508–6509;
 41. Jing, Q.; Zhang, X.; Sun, J.; Ding, K., *Bulky Achiral Triarylphosphines Mimic BINAP in Ru(II)-Catalyzed Asymmetric Hydrogenation of Ketones*, *Advanced Synthesis & Catalysis* **2005**, 347 (9), 1193–1197;
 42. Ngo, H.L.; Lin, W., *Development of 4,4'-Substituted-XylBINAP Ligands for Highly Enantioselective Hydrogenation of Ketones*, *The Journal of Organic Chemistry* **2005**, 70 (4), 1177–1187;
 43. de Koning, P.D.; Jackson, M.; Lennon, I.C., *Use of Achiral (Diphosphine)RuCl₂(Diamine) Precatalysts as a Practical Alternative to Sodium Borohydride for Ketone Reduction*, *Organic Process Research & Development* **2006**, 10 (5), 1054–1058;
 44. Zhu, Q.; Shi, D.; Xia, C.; Huang, H., *Ruthenium Catalysts Containing Rigid Chiral Diamines and Achiral Diphosphanes for Highly Enantioselective Hydrogenation of Aromatic Ketones*, *Chemistry – A European Journal* **2011**, 17 (28), 7760–7763;
 45. Wang, J.; Liu, D.; Liu, Y.; Zhang, W., *Asymmetric hydrogenation of β -amino ketones with the bimetallic complex RuPHOX-Ru as the chiral catalyst*, *Organic & Biomolecular Chemistry* **2013**, 11 (23), 3855–3861;
 46. Xu, W.; Langer, R., *Probing the effect of heterocycle-bonding in PNX-type ruthenium pre-catalysts for reactions involving H₂*, *Dalton Transactions* **2015**, 44 (38), 16785–16790;
 47. Matsumura, K.; Arai, N.; Hori, K.; Saito, T.; Sayo, N.; Ohkuma, T., *Chiral Ruthenabicyclic Complexes: Precatalysts for Rapid, Enantioselective, and Wide-Scope Hydrogenation of Ketones*, *Journal of the American Chemical Society* **2011**, 133 (28), 10696–10699;
 48. Wong, W.K.; Chik, T.W.; Hui, K.N.; Williams, I.; Feng, X.; Mak, T.C.W.; Che, C.M., *Preparation of chiral diimino- and diaminodiphosphine ligands and their Cu^I and Ag^I complexes. X-ray crystal structures of [Cu(1S,2S-cyclohexyl-P₂N₂)] [PF₆]⁻ and [Ag(1R,2R-cyclohexyl-P₂N₂H₂)] [BF₄]⁻*, *Polyhedron* **1996**, 15 (24), 4447–4460;
 49. Wong, W.K.; Chen, X.P.; Pan, W.X.; Guo, J.P.; Wong, W.Y., *Synthesis, Chemistry, and Catalytic Activity of Ruthenium Diaminodiphosphane Complexes – Crystal Structures of trans-[RuCl₂{ κ^2 -Ph₂PC₆H₄CH=NC₆H₁₀N(H)CH₂C₆H₄PPh₂}(PPh₃)] and cis-[RuCl₂{ κ^4 -Ph₂PC₆H₄CH=NC₆H₁₀N(H)CH₂C₆H₄PPh₂}]*, *European Journal of Inorganic Chemistry* **2002**, 2002 (1), 231–237;
 50. Almutairi, M.S.; Jayasheela, K.; Periandy, S.; Al-Ghamdi, A.R.; Sebastian, S.; Xavier, S.; Kadi, A.A.; Abdelhameed, A.S.; Attia, M.I., *Structural, spectroscopic, Hirshfeld surface and charge distribution analysis of 3-(1H-imidazole-1-yl)-1-phenylpropan-1-ol complemented by molecular docking predictions: An integrated experimental and computational approach*, *Journal of Molecular Structures* **2019**, 1196,

578–591;

51. Abolhasani, M.; Jensen, K.F., *Oscillatory multiphase flow strategy for chemistry and biology, Lab on a Chip* **2016**, 16 (15), 2775–2784.



Chapter



Automation and information sciences for catalysis R&D

.....

"Failure is always an option."

Adam Savage

Abstract

Recent developments in data-driven technologies, specifically machine learning, have greatly impacted a wide range of scientific disciplines and continue to hold great promise. However, the application of such methods to predict reactivity and reaction rates in the field of homogeneous catalysis so far remains limited. We propose that this is—at least in part—due to the difficulty and cost associated with acquiring sufficiently-sized and descriptive experimental data sets. Experimental efforts are limited because conventional high-throughput equipment usually does not provide the kinetic data that is critical for the development of the desired predictive catalytic activity models.

Herein we describe several (automated) approaches that aim to provide such data. Our efforts were focused on three specific aspects. First, an experimental sampling system was developed that automated the acquisition of high-quality kinetic data at high temporal resolution. This autosampler system was incorporated into a powerful and flexible reaction analysis platform capable of producing high-quality data. The platform's capacity to produce such data was demonstrated by studying a fast Claisen-Schmidt condensation reaction with simultaneous kinetic measurements and multiple representative modes of *operando* spectroscopy. Secondly, data management and analytics tools were developed to reproducibly store, visualise, and gain insight from the produced data. Finally, a number of remaining challenges were identified and a novel integral experimental and computational work flow was proposed. This work flow is aimed at achieving predictive capabilities for homogeneous catalysis research and has the potential to unlock the power of machine learning for contemporary catalysis R&D.

.....

Patent protection has been requested for parts of this chapter:

R. van Putten[‡], E.A. Uslamin[‡], E.A. Pidko, *Sampling arrangement*, NL2024908 (PCT/NL2021/050091), filed 14 February 2020

Parts of this chapter have been included in grant applications:

R. van Putten[‡], E.A. Uslamin[‡], E.A. Pidko, *Autonomous high-resolution sampling of (bio-) chemical reactions for kinetic analysis and quality control*, NWO Take-Off I, *Granted*

R. van Putten, F. Meirer, E.A. Pidko, *Computer-aided catalyst design: development of an automated microfluidic platform for next-generation data-driven catalysis R&D (AUTOKAT)*, NWO ENW-M-2, *Submitted*

7.1 Introduction

Recent advances in data-driven methods, specifically machine learning (ML), have enabled large developments in a multitude of domains, including, *e.g.*, gameplay¹⁻², protein structure prediction³⁻⁴, diagnostic medicine⁵⁻⁷, or finance⁸⁻¹⁰. ML has also significantly impacted the fields of chemistry and catalysis¹¹⁻¹⁴, where it has led to the development of, *e.g.*, computer-aided (retro)synthetic planning¹⁵⁻¹⁷, and the acceleration of (quantum chemical) calculations¹⁸⁻²⁰. However, despite these advances in the chemical domain, data-driven methods have not yet universally been able to accurately predict reaction rates of homogeneously catalysed reactions. We propose that this is—at least in part—due to the difficulty and costs associated with the collection of sufficiently large and descriptive experimental (and to some degree computational) data sets. This means that the required data are not currently available, but also cannot realistically be obtained with present methods. New tools are therefore necessary that can provide such data.

Modern data-driven techniques require input that satisfies at least five requirements, which can be described by the ‘*Five V’s of big-data*’: *volume*, *velocity*, *variety*, *veracity*, and *volatility*.²¹⁻²² Close inspection of conventional work flows in homogeneous catalysis reveals that these requirements cannot realistically be met using either sequential or parallel approaches. This is true for experimental and computational efforts, although their specific limitations are fundamentally different.

Sequential experimentation (*e.g.*, kinetic studies) provides high-quality data (*veracity*), at the expense of low *volume*, and, more importantly, *velocity* (*i.e.*, new data are not available quickly, **Figure 7.1a**). Parallelised high-throughput approaches on the other hand trade quality for quantity, and data value is reduced to (thermodynamic) properties such as product yield and selectivity (**Figure 7.1b**). This omission of transient or kinetic information is particularly problematic for the field of catalysis, which concerns *reaction rates* and is to a large degree governed by kinetic limitations rather than thermodynamics. For example, ML-models based only on final composition data (*i.e.*, yields) cannot be expected to accurately predict reaction rates, because this information was not captured by the original input (**Figure 7.1a**, *e.g.*, point A and B). Instead, ML might incorrectly infer from the yields at point B that the catalysts share similar catalytic activity. New methods are therefore required that combine beneficial aspects of sequential and parallel approaches to provide data of sufficient volume and density.

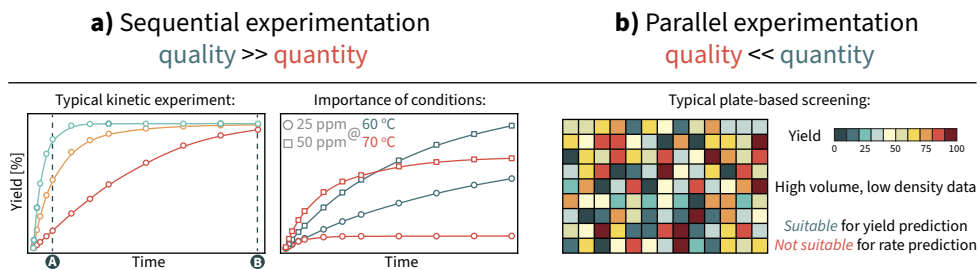


Figure 7.1. Implications of conventional experimental work flows for data-driven catalysis R&D.

This chapter describes our recent efforts to develop (automated) tools that provide the transient and rich data required for the successful prediction of catalytic reaction rates. Our work focused on three areas. First, an automated sampling system was developed that was incorporated into an *operando* reaction analysis platform. This system provided high-quality kinetic data with multiple modes of representative *operando* spectroscopy. A data management platform was developed that could be scaled to store large volumes of data. This platform was coupled to a desktop application and an advanced data visualisation suite. Finally, a novel experimental and computational work flow was proposed that has the capacity to provide the data that is required for the construction of predictive catalytic activity models. We anticipate that the combination of such dense experimental data and quantum chemical calculations will lead to predictive structure-activity relationships in homogeneous catalysis.

7.2 Autosampler technology

The development, detailed study, or scale-up of (novel) reactions almost always requires the availability of kinetic data. This information is then used to construct mathematical models that describe the rate of a chemical reaction as a function of its conditions. These data are also useful for mechanistic works, where they can provide insight into, *e.g.*, resting states, product selectivity, or catalyst deactivation phenomena.^{23–25} However, despite its importance and potential for new insights, kinetic experimentation is not always straightforward or universally applied as a routine measurement. (As was described by Blackmond: “*Experimental kinetic studies are often regarded by organic chemists as being too tedious, tough, and time-consuming to become standard practise for the initial report of a new reaction.*”)

A number of academic groups and companies have tried to reduce this perceived barrier and have developed tools that greatly simplify kinetic experimentation. Blackmond and co-workers have developed a convenient graphical system (named reaction progress kinetic analysis) that helps non-experts distinguish and

rationalise complex kinetic behaviours. Others have worked on practical aspects and have disclosed the (automated) measurement of kinetics in flow (sometimes combined with Design of Experiments, clever temperature and flow-rate ramps, and statistical methods)^{26–28}, with *in situ* or *operando* spectroscopy, gas uptake measurements or calorimetry^{23–25,29}, or with automated sampling systems^{30–33}. The latter are important because they closely mimic regular kinetic experiments that are familiar to experimental chemists. These autosampler systems effectively automate the tedious task of sampling while remaining conceptually similar.

However, despite these significant advances, neither of the few commercially available stand-alone sampling systems could meet the needs of our specific research in homogeneous catalysis. Most of these systems were prohibitively expensive and their operational window was relatively narrow (*e.g.*, the sampling volume that could be withdrawn or the maximum allowable pressure from which could be sampled). We therefore decided to develop a completely new autosampler for use in our laboratory.

7.3 Autosampler system design and construction

A number of target specifications and capabilities were set for the new autosampler system:

- i) Sampling frequency $\geq 1 \text{ min}^{-1}$ with high reproducibility;
- ii) Compatibility with harsh reaction conditions ($\geq 200 \text{ }^\circ\text{C}$ and $\geq 50 \text{ bar}$ with excellent chemical resistance to organic solvents and bases);
- iii) Flexible sample and diluent volume (in the range of μl – ml);
- iv) Option to add a quenching solution within seconds of sample withdrawal;
- v) Immediate sample dilution to chromatography-ready concentrations;
- vi) Fully automated operation.

A suitable system was developed around the functionality of two multi-position valves (**Figure 7.2–7.3**). This system can be used stand-alone or as part of a more capable reaction analysis platform, and allows sampling from pressurised or atmospheric vessels. (Sampling from atmospheric reactors may require the use of a pump.) Samples of the desired volume are automatically withdrawn from the reaction mixture and are diluted and/or quenched with a solvent portion. The samples are then routed to a sample holder that contains standardised glass chromatography vials. This procedure saves a tedious and error-prone pipetting step and provides the desired chromatography-ready samples without input from the operator.

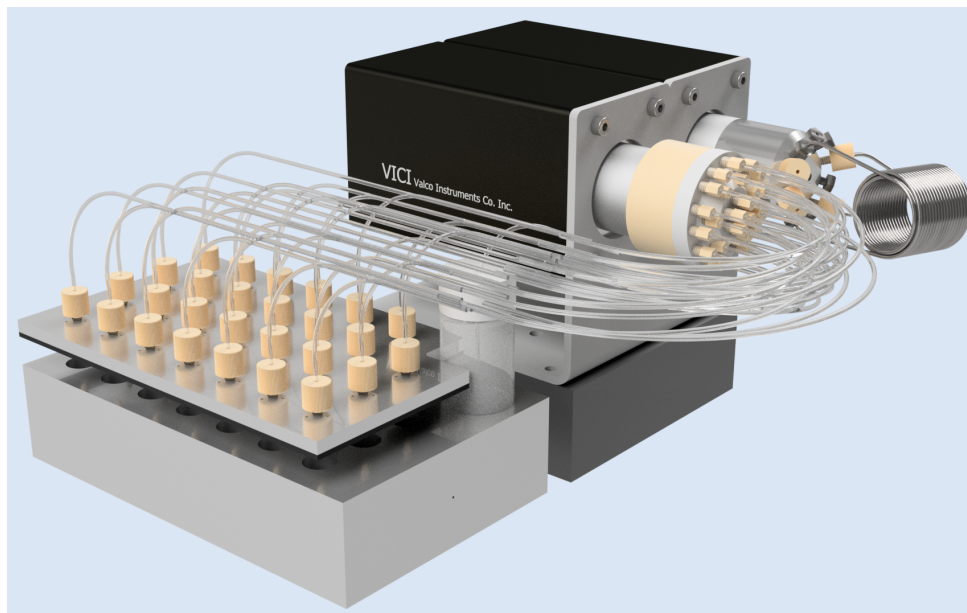


Figure 7.2. Rendering of (part of) the autosampler MKI system.

The autosampler system is designed to have two discrete operational modes. The first operational mode is used to acquire the sample, while the second operational mode is required to dispense and dilute the sample to the desired location. In the first operational mode (**Figure 7.3**, dashed lines in switching valve), the reactor is fluidically coupled to the switching valve through a sample loop. At the same time a pressurised solvent reservoir is connected to the switching valve through a solvent loop. The solvent reservoir is pressurised by an external gas supply and contains the diluent and/or quench solution.

In the second operational mode (**Figure 7.3**, solid lines), the switching valve is configured to provide fluidic contact between, successively, the gas supply, the solvent loop, the sample loop, and the sample container. This empties the sample loop, rinses it with the diluent (or quenching solution), and tails it with gas. After the sample is dispensed, the system is reset and prepared for the next sample.

The system was largely constructed with commercially available components. Wetted parts inside the autosampler system were made of chemically resistant materials that include stainless steel and a number of perfluorinated polymers. Both the sampling volume and diluent volume can be modified by the user within minutes, and samples are directly dispensed into standardised chromatography vials. This is important because it eliminates a tedious, repetitive, and error-prone pipetting step that is required for commercially available systems.

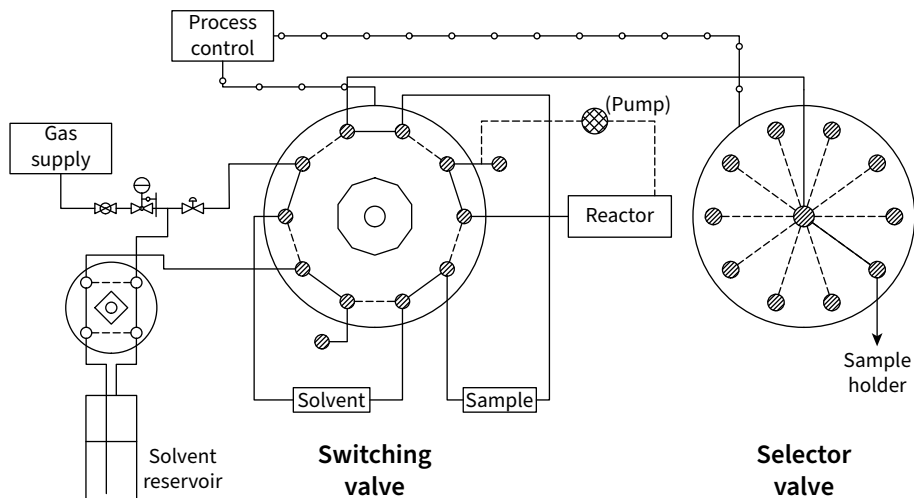


Figure 7.3. Schematic drawing of the autosampler system (adapted from patent application).

The success of the initial device led us to develop a next-generation autosampler MKII system. This iteration further expanded the operational window and allowed for its direct integration with *operando* spectroscopy tools. The improved version featured a heating system for the valve assembly and its transfer lines, as well as a solid-state cooling system for the sample tray (**Figure 7.4**). The heating system was incorporated in order to prevent heat-loss of the reaction mixture while it was circulated to-and-from the sampling system (the heating system is not shown in **Figure 7.4**). Heat is applied with a resistive heat tracing that is wrapped around the to-be-heated components. The temperature of these lines is monitored with a type K thermocouple and is maintained at the desired set point with a PID-controller located inside an electrical box.

A cooling system was fitted to the sample tray to enable storage of (semi-)volatile materials. Such cooling is important to ensure that (quenched) samples stay representative over prolonged amounts of time and that volatile components do not evaporate. An important application of this system is unattended overnight sampling. The sample holder was CNC-machined from a solid block of aluminium and was equipped with a thermoelectric cooling system (**Figure 7.4–7.5**). The aluminium sample tray is placed on a copper heat spreader that had machined-out slots for two 60W Peltier modules. Heat is removed from the Peltier elements with a set of off-the-shelf CPU coolers that are bolted to the copper plate and are connected with a thermally-conductive compound. The cooling assembly is enclosed in a block of thermally-insulating expanded polyurethane foam (**Figure 7.4**). The current configuration achieves a maximum cooling temperature of approximately $-10\text{ }^{\circ}\text{C}$ (although cooling below the dew point is not recommended).

The electrical hardware that is required to operate and control the system is placed inside a protective electrical box that is installed in the back of a fume hood or electrical cabinet.

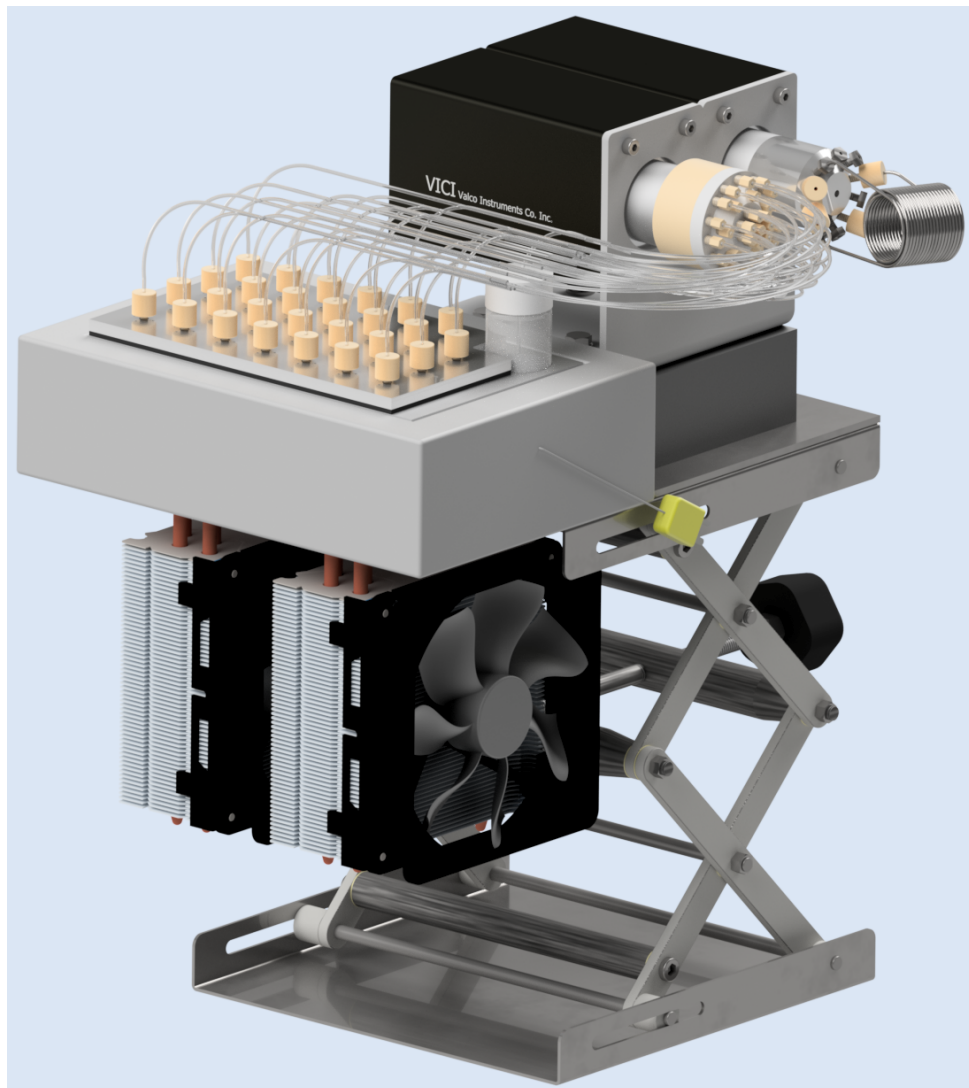


Figure 7.4. Rendering of (part of) the autosampler MKII system.

The autosampler system is fully automated and is controlled with custom-made software written in LabVIEW 2019 (**Figure 7.6**). The software displays a number of status indicators and allows the user to edit the sample queue. Before an experiment is started, the desired sampling times are edited in a text or spreadsheet editor. These times are then imported into LabVIEW and the sample queue is generated.

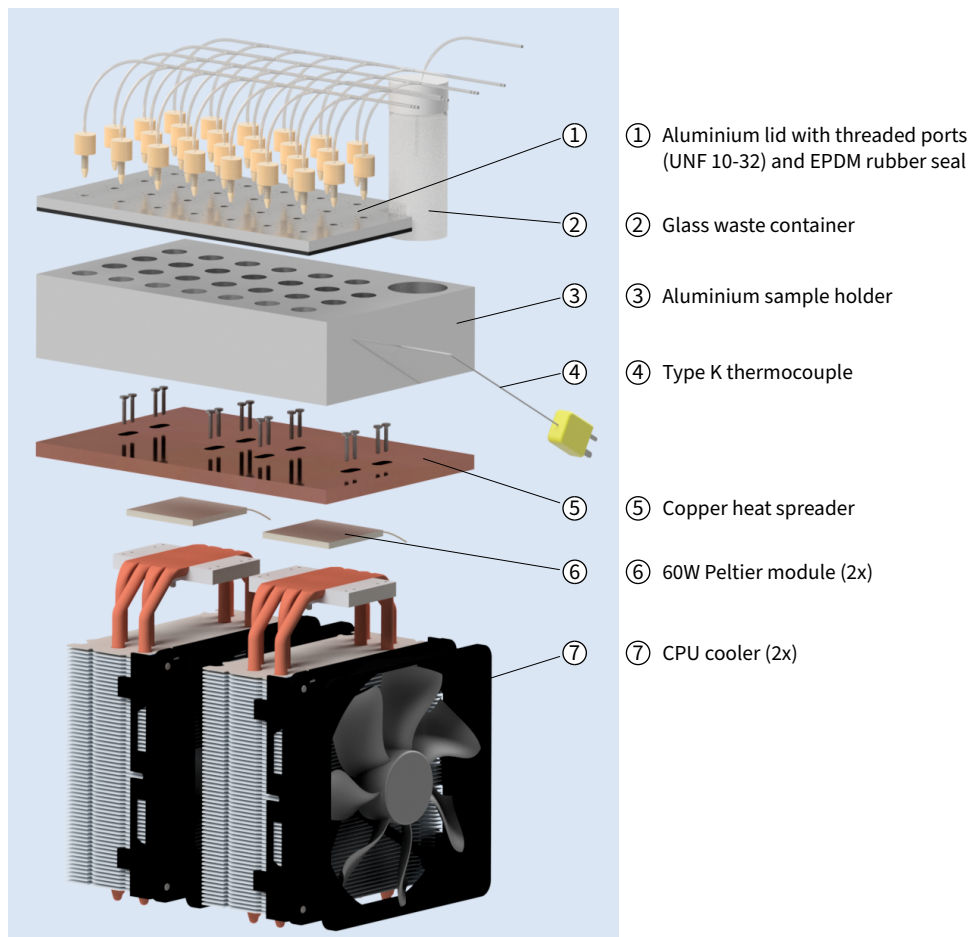


Figure 7.5. Exploded view of the thermoelectric cooling system, as implemented in the autosampler MKII. The polyurethane thermal insulation has been omitted for clarity.

When the software is started, the user is asked to confirm that the system is ready by pressing the corresponding button. The PC then starts the communication protocol with the autosampler system and initialises the equipment. Valves are returned to their initial position and set points are changed for the temperature-control systems. The system is now prepared for operation. Once both the system and the user are ready, the user initiates the kinetic experiment by pressing the blinking ‘*start experiment*’ button. A countdown timer appears on screen to aid the user with the accurate/timely injection of reagents to start the experiment exactly at $t = 0$. This is important because the autosampler supports high-frequency sampling that could otherwise become inaccurate.

A number of timers become operational once the experiment is started. From this moment the autosampler is fully automated and does not require additional input from the user. The internal clock references the current time to the programmed sample time and acts accordingly. An autosave file is generated/updated after each sample and contains the exact acquisition parameters, as well as the exact sample time compared to $t = 0$. The sample queue can be edited whilst an experiment is in progress. After completion of the last sample in the queue, a pop-up window is shown and the user is requested to stop the experiment or to add additional samples using the main interface. Slower or faster than expected experiments can thus easily be accommodated with the autosampler system and experiments do not need to be reset. The user is finally requested to clean the autosampler system. This cleaning and rinsing is implemented in the software and can be performed automatically without user intervention.

The autosampler met all our needs and its specifications exceeded the minimum requirements (**Table 7.1**). A very high sampling frequency could be obtained that depended on the specific use case. A higher frequency could be achieved if the reaction mixture was circulated through the system with a pump compared to when the sampling was pressure-fed. Most specifications depend on the supplier's rating and can be improved if required.

Table 7.1. Autosampler MKII specifications (state December 2020, subject to change).

Property	Specification
Sampling frequency	≤ 3 samples min^{-1} (from autoclave) ≤ 5 samples min^{-1} (with circulation)
Temperature range (reaction mixture) ^{a)}	Sub-zero – 250 °C
Pressure range (reaction mixture) ^{a)}	Vacuum – 345 bar
Sample/solvent loop volume ^{b,c)}	10 μl – 10 ml
Dead volume ^{d)}	≤ 50 μl
Heating system temperature range	Ambient – 250 °C
Cooling system temperature range ^{e)}	-10 °C – Ambient

a) Estimated or based on supplier specification. **b)** Ideally $V_{\text{Solvent}} \gg V_{\text{Sample}}$. **c)** Increased volume may negatively impact the minimum sampling interval under certain conditions. **d)** Reactor to sampling system. Should ideally not exceed sample volume. **e)** Preferably $T_{\text{Set}} > T_{\text{Dew}}$ in condensing atmosphere.

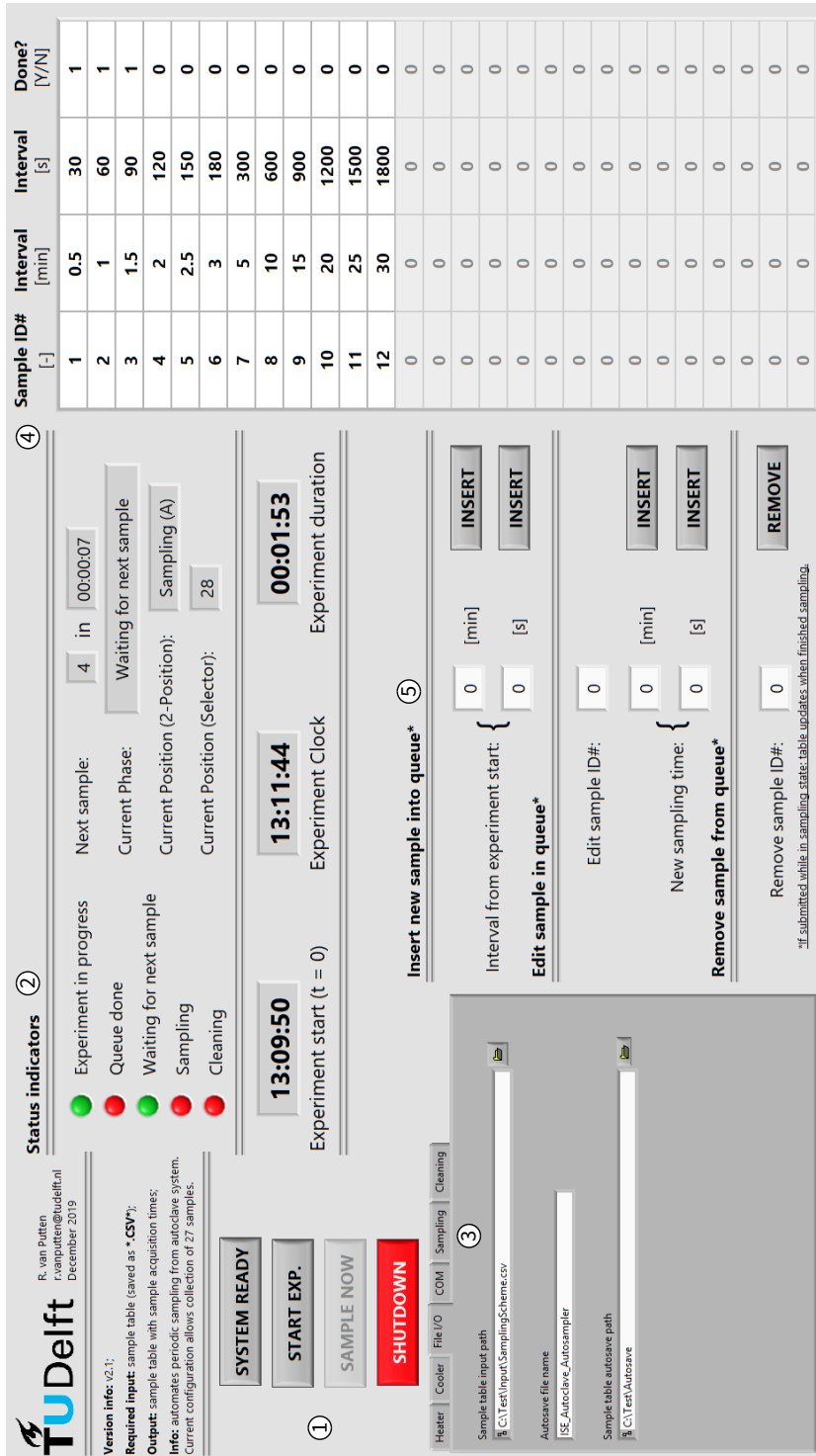


Figure 7.6. Overview of the autosampler software (v2.1, LabVIEW 2019).

The system's specifications were compared to two commercially available autosamplers: *i*) Mettler Toledo's EasySampler 1210³¹, and *ii*) Parr's 4878 Automated liquid sampler³³ (**Figure 7.7**). The EasySampler system is used extensively in the pharmaceutical industry for process development and reaction characterisation. Information on use of the Parr system was unavailable. We concluded that our autosampler MKII system outperforms the commercially available systems by some margin and offers a larger operational window and better flexibility.

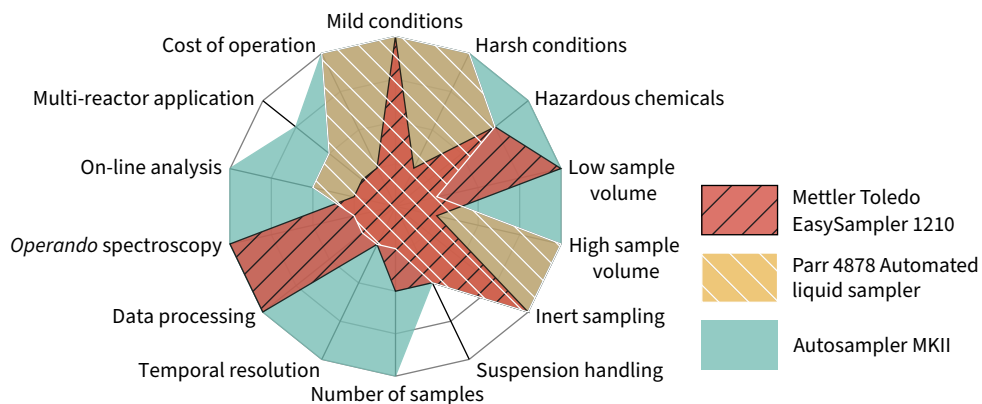


Figure 7.7. Comparison of commercially available autosampler systems to our autosampler MKII.

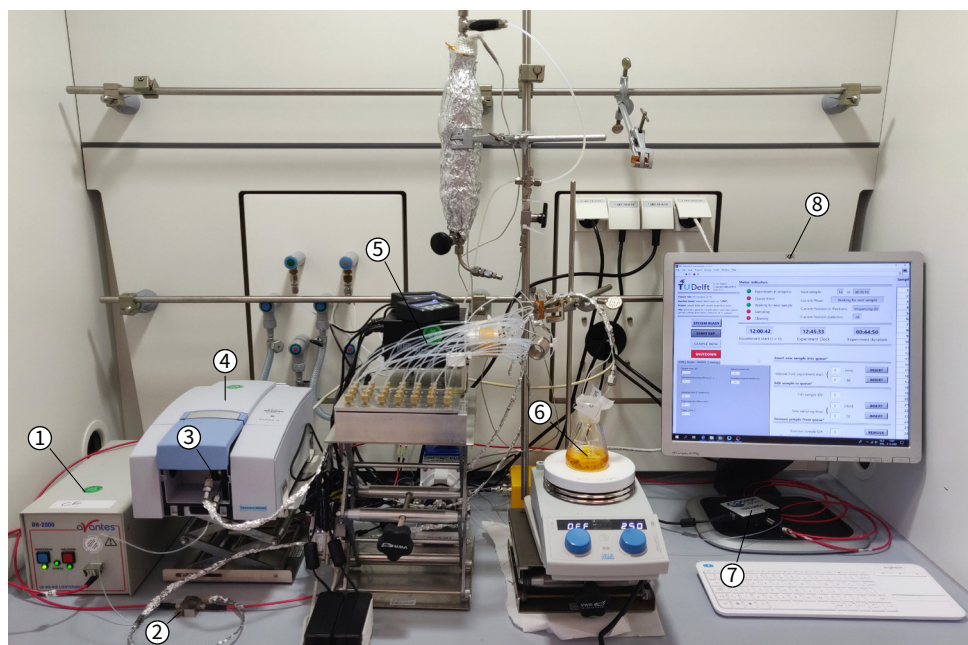
Initial steps have been taken towards commercialisation of our system. A patent application was submitted in early 2020 that describes the autosampler system and its sample acquisition method. The patent is currently pending. We have recently been awarded funding by the Dutch research council (NWO) to perform a feasibility study on a start-up's commercial viability (NWO Take-Off Phase I grant). This feasibility study will be performed in the second and third quarter of 2021.

7.4 Autosampler system validation

The autosampler system was first deployed in **Chapter 6**, where it was used to study the asymmetric hydrogenation of a base-sensitive β -aminoketone. The sampling system enabled the automated acquisition of reaction kinetics under conditions where manual sampling would have been challenging because the reaction rate was very high, the vessel was pressurised with hydrogen gas, and only small amounts of the side-product were formed that could easily have been overlooked.

After this first successful demonstration the autosampler system was incorporated into a (high-pressure capable) reaction analysis platform that integrated several modes of *operando* spectroscopy (**Figure 7.8**). This system facilitated simultaneous

sampling of the reaction mixture and *operando* monitoring of the catalytic reaction using FTIR and UV-Vis spectroscopy in (high-pressure) flow cells. The reaction mixture was continuously circulated from the reactor through the system and was returned to the reactor after analysis. This same setup was later used by colleagues to study dilute homogeneous catalysts under relevant reaction conditions at 100 °C and 50 bar H₂. These catalytic reactions were performed in a Parr autoclave with a magnetically-coupled gear pump.



- | | |
|--|--|
| ① Avantes DH-2000 UV-Vis-NIR light source | ⑤ Autosampler system (MKI) |
| ② UV-Vis flow cell with fused silica windows | ⑥ Reaction vessel on magnetic stirring plate |
| ③ IR flow cell with CaF ₂ windows | ⑦ Ocean Optics USB2000+ UV-Vis spectrometer |
| ④ Bruker Alpha II FTIR spectrometer | ⑧ PC for process control and spectra acquisition |

Figure 7.8. *Operando* reaction analysis platform used in this work.

The capabilities of the platform were evaluated with the Claisen-Schmidt condensation of benzaldehyde and acetone (**Figure 7.9**). This model reaction was selected because it could conveniently be analysed with GC-FID and because its products could be observed with IR and/or UV-Vis spectroscopy; product **4** absorbs UV-A radiation very strongly (and is in fact used in sunscreen).³⁴ Finally, the reaction was selected because it was known to produce coloured side-products that would potentially be observable with UV-Vis spectroscopy.

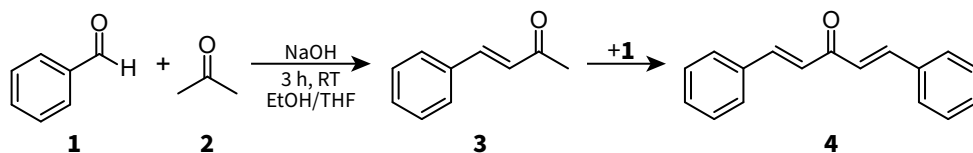


Figure 7.9. Claisen-Schmidt condensation of benzaldehyde and acetone.

The reaction was performed in air at room temperature. The solution rapidly changed from colourless to yellow after the reaction was started, which indicated the formation of **4**. The solution became darker over time and ultimately turned golden yellow/orange. The reaction was observed for a total of three hours, during which samples were periodically removed and spectra were acquired continuously. Samples were analysed with GC-FID/MS.

Reaction progress was neatly captured by the autosampler system and spectroscopic tools, which indicated that the target reaction was complete after approximately one hour (**Figure 7.10**, circles). The kinetic data that were obtained from sampling were fit with a simple system of ordinary differential equations (**Equation 7.1–7.4**). Acetone (**2**) was not quantified experimentally and its concentration was instead estimated from the numerical solution. This solution was in very good agreement with the experimental results ($R^2 = 0.993$) and provided estimations for the two reaction rate constants k_1 ($0.526 \pm 0.025 \text{ m}^3 \text{ kmol}^{-1} \text{ min}^{-1}$) and k_2 ($1.076 \pm 0.104 \text{ m}^3 \text{ kmol}^{-1} \text{ min}^{-1}$).

$$\frac{dC_1}{dt} = r_1 = -k_1 C_1 C_2 - k_2 C_1 C_3 \quad (7.1)$$

$$\frac{dC_2}{dt} = r_2 = -k_1 C_1 C_2 \quad (7.2)$$

$$\frac{dC_3}{dt} = r_3 = +k_1 C_1 C_2 - k_2 C_1 C_3 \quad (7.3)$$

$$\frac{dC_4}{dt} = r_4 = +k_2 C_1 C_3 \quad (7.4)$$

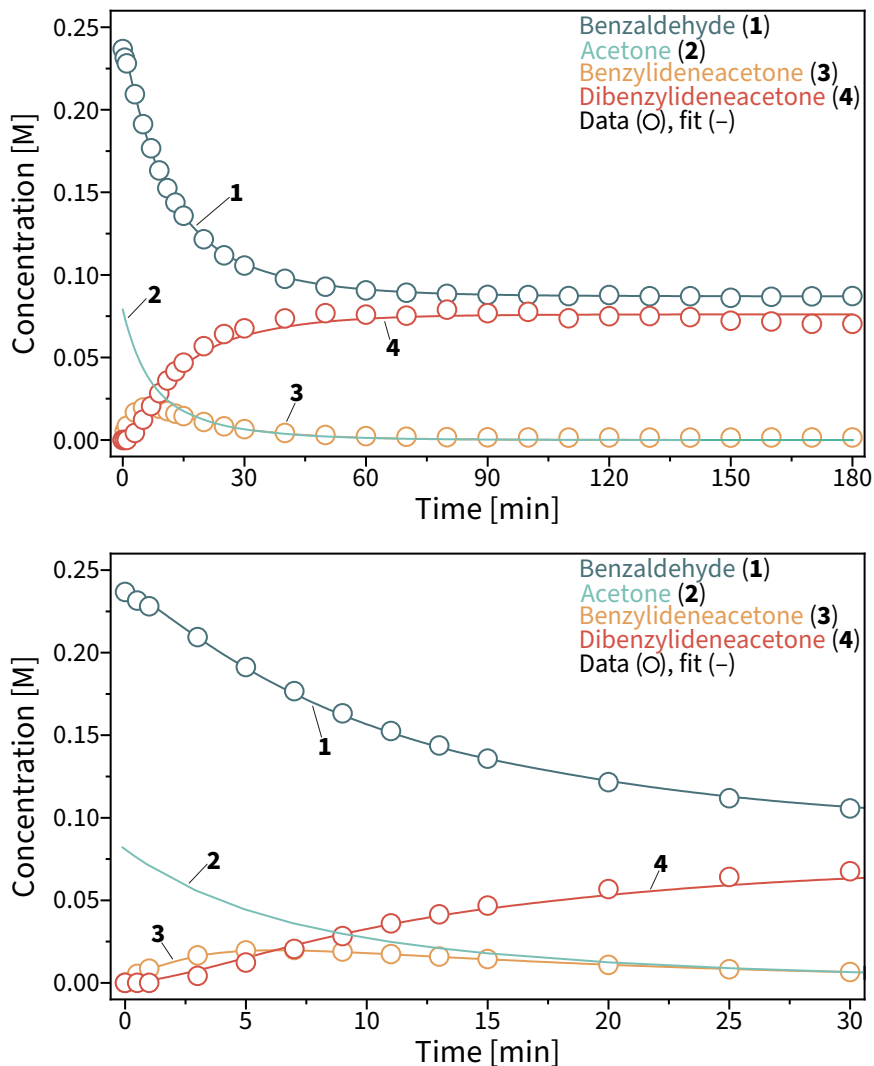


Figure 7.10. Kinetic traces from samples (O) and fit (-) of Claisen-Schmidt condensation reaction. Details on the numerical solution/fit are provided in the main body.

Data of similar fidelity were also obtained with continuous *operando* FTIR and UV-Vis spectroscopy (**Figure 7.11–7.14**). FTIR clearly indicated the consumption of benzaldehyde (1) and production of dibenzylideneacetone (4). Acetone (2) and the transient benzylideneacetone (3) product could not be observed with FTIR because their bands overlapped with those of benzaldehyde and dibenzylideneacetone. The normalised kinetic traces obtained from sampling and FTIR (time-series at 1705 cm^{-1} and 1624 cm^{-1}) were practically identical and could be superimposed, which indicated that our method and system could accurately track the reaction's

progress (**Figure 7.11**). This again confirmed that the yield of **4** was highest after approximately one hour and that it decreased slightly after that time, presumably because it was converted into a side-product.

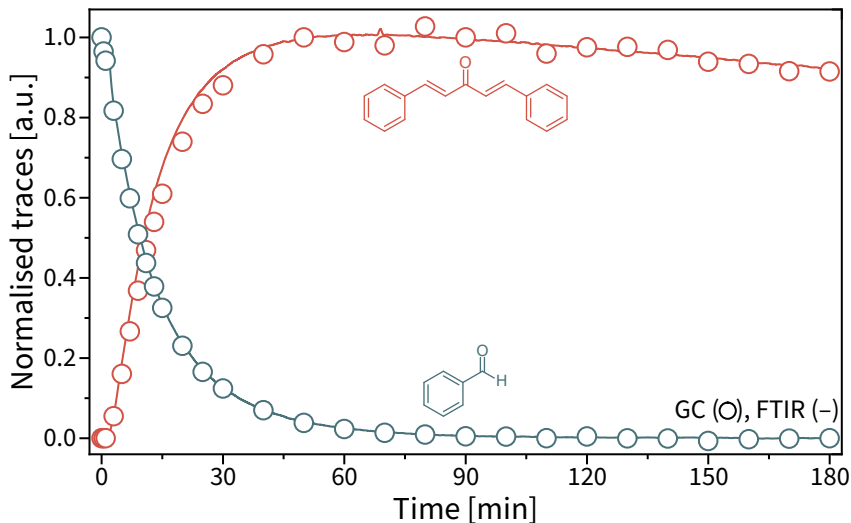


Figure 7.11. Normalised kinetic traces from GC samples (O) and FTIR (-) of Claisen-Schmidt condensation reaction.

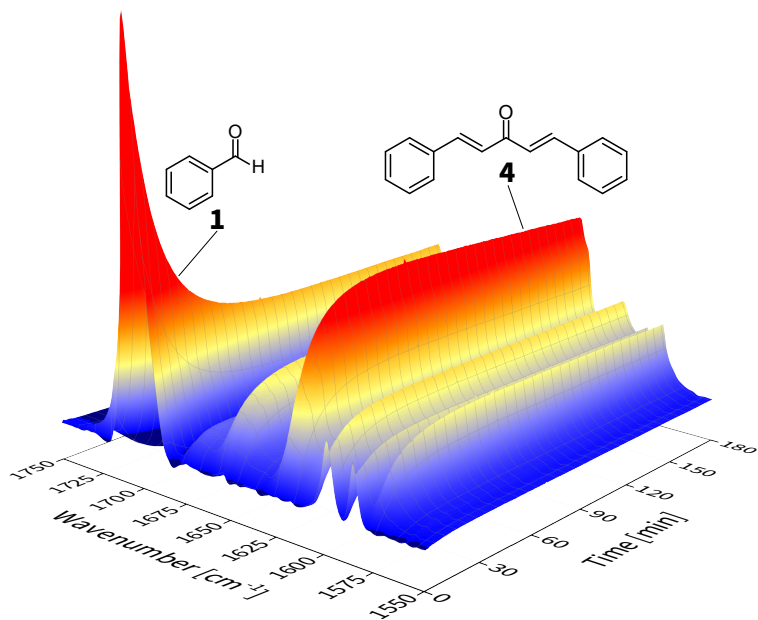


Figure 7.12. Time series of FTIR spectra of Claisen-Schmidt condensation – 3D plot.

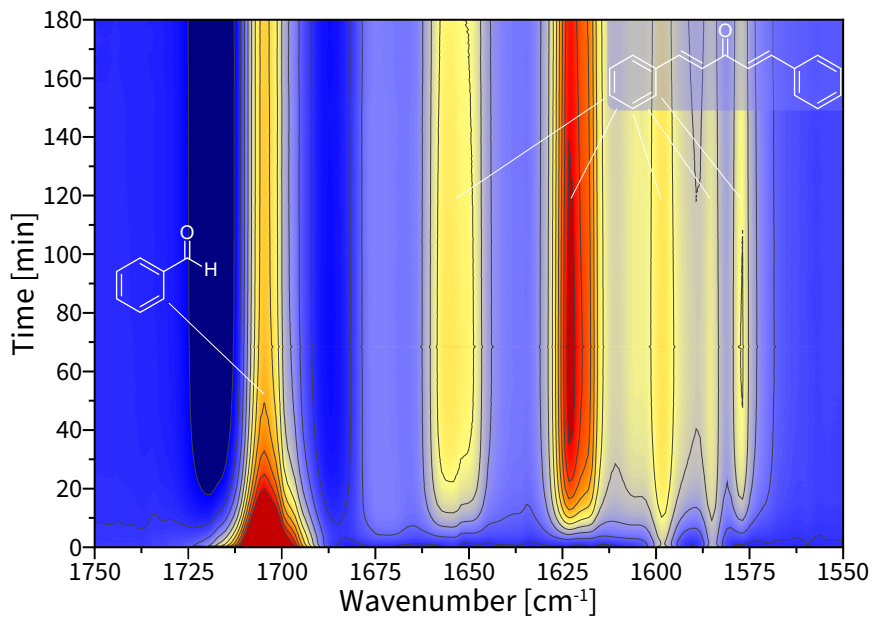


Figure 7.13. Time series of FTIR spectra of Claisen-Schmidt condensation – contour plot.

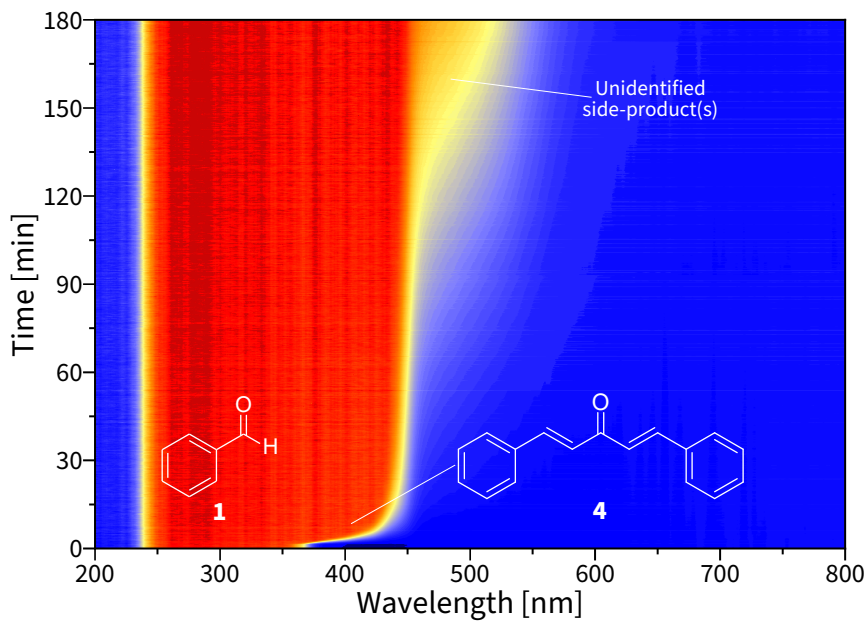


Figure 7.14. Time series of UV-Vis spectra of Claisen-Schmidt condensation – contour plot.

UV-Vis spectroscopy was used to monitor the formation of **4** and of an unidentified side-product. The available flow cell had a fixed optical path length of 10.0 mm that proved too long for the chemistry at the selected concentration. This led to quantitative absorption of light between 240 nm and 365 nm for the initial mixture that contained benzaldehyde. However, components that absorbed in this region could also be tracked with FTIR and were therefore deprioritised for UV-Vis.

As observed before, dibenzylideneacetone **4** was formed quickly after the reaction was started, which resulted in a pronounced colour change from colourless to bright yellow. This was apparent in the UV-Vis spectrum from the appearance of a strong (saturated) signal up to 450 nm. Product **4** absorbs UV-A (315–400 nm) radiation most strongly and absorbs significantly up to approximately 450 nm (and therefore has a yellow appearance).

UV-Vis spectroscopy also revealed the progressive formation of a side-product that was not detected with GC-FID/MS. This product formed while the reaction mixture turned golden yellow/orange and absorbed light between approximately 450–500 nm. This product probably was relatively dilute and was not identified. GC-FID/MS analysis did not reveal additional components in the mixture. We hypothesise that **4** was transformed into the orange product because our kinetic traces indicated that target product **4** was consumed while the side-product formed. The structure of this new product is not clear, but is believed to *not* be the reasonably anticipated dimerisation product of **4**. This dimeric compound has been reported to be a colourless material with maximum absorption in the deep UV region.³⁵

In summary, we have developed an automatic sampling system that has been applied to study several diverse chemistries. The sampling system was incorporated into a versatile *operando* reaction analysis platform that was validated with the Claisen-Schmidt condensation of benzaldehyde and acetone. This system provides data-rich experimentation that is promising for future data-driven scientific discoveries and developments in the chemical domain.

7.5 Data management and analytics platform

The advent of modern data-driven technologies and their deployment to social media platforms has brought increased attention to the intrinsic value of data. This is also the case within the scientific community, where there have been calls to transition to ‘*open science*’ and open-access publishing—at least for publicly-funded research. Funding agencies, policymakers, and universities have been keen to promote data sharing to maximise data value and utilisation. Achieving this, however, is not trivial and requires much more than a place to store data.

Some of the challenges are discipline-specific and relate to the content of the data: what exactly is stored, in what format, how was the data measured or obtained, and how does it relate to other objects and concepts in the database. (The latter might benefit from the availability of a suitable and community-supported ontology. The development of ontologies is complex and deserves dedicated efforts.) Other challenges are more general. For example: who owns the data that is deposited? Who is responsible for its content and its veracity? Will the data set be curated, and if so, by whom, using what criteria? Many of these issues remain open questions at the time of writing. However, it is clear that generalised ‘one-size-fits-all’ solutions are unlikely to succeed and that more dedicated, agile, and community-led initiatives are needed.

This section describes our recent efforts to construct a data management platform for use in our research group at TU Delft. The intended purpose of this ‘*data lake*’ was twofold: *i*) to create a repository that our group could use to pool results for specific classes of (catalytic) experiments, and gain insights from them, and *ii*) to provide a secure, robust, and scalable platform equipped to store the diverse data produced with the automated techniques that are under development in our lab. (Disclaimer: the data management platform that is described in this chapter is by no means finished, or claimed as such. However, we found it worthwhile to describe its development and capabilities in this chapter. For the purpose of this discussion we will assume that most of the general challenges have been addressed.)

7.6 Database and platform architecture

One important characteristic of well-managed data is that it is ‘FAIR’: *Findable, Accessible, Interoperable, and Reusable*.³⁶ In practise this roughly means that data has to be classified or indexed (to make it findable), stored and hosted somewhere so that it can be used (accessible), stored and published in a standardised and preferably open-source format (interoperable), and documented such that it is valuable for further use (reusable). Academic institutions have been working towards these goals and have, *e.g.*, started to publish data sets and dissertations in publicly available, purpose-built repositories.^{37–38} Such uninhibited access to data is believed to potentially improve research quality, prevent redundant work, and accelerate discovery and ideation.

Adequate data management solutions could also simply be necessary to handle the sheer volume or velocity of data. For example, YouTube’s servers have been reported to ingest more than 500 hours of footage *per minute*.³⁹ YouTube does not publish details about their technical infrastructure, but these numbers nevertheless make

it possible to get a sense of scale. If one assumes that a typical cinematic full HD video demands approximately 3 GB h⁻¹ at a reasonable compression and bit rate of 8 Mbps, the reported 500+ h min⁻¹ translates to a staggering ~788 PB of footage per year. It is obvious that manual management of these data is not feasible and that automated solutions are needed.

YouTube's data velocity admittedly is a worst-case scenario. Almost all (scientific) data sets are orders of magnitude smaller. Data streams relevant for the chemical sciences often are in the MB–GB range, and currently rarely exceed TBs (and should therefore probably not be referred to as 'big-data'). However, the advent of modern data-rich experimentation has the potential to lead to a paradigm shift that necessitates automated management. For example, the *operando* reaction analysis platform described in the previous section has the capacity to produce approximately 300 FTIR and 13.000 UV-Vis spectra per hour. These data were saved as two-dimensional arrays that required 47 kB and 29 kB per spectrum, respectively. Data was thus produced at a velocity of approximately 400 MB h⁻¹, excluding chromatographs or processed data. Future methods (like the one described in **Chapter 7.8**) will almost certainly have higher data velocities that require robust data storage and management systems.

The general structure of our data management solution is summarised in **Figure 7.15**. A combination of hardware and software was required to obtain the targeted functionality. (The software package is described in more detail in the next section.) The required technological infrastructure was deployed in TU Delft's data centre. This had three large benefits compared to the use of standalone servers: *i*) fast 10 Gbps connectivity inside the data centre, *ii*) automated daily off-site back-ups, and *iii*) the ability to use our IT department's existing security infrastructure. Servers are protected by the institutional firewall and are only accessible where required (potentially with a VPN). Remote server management is possible over SSH after authentication to a bastion host.

Four servers were deployed in the data centre (**Figure 7.15**). The first was a commercial NAS solution (*Network-Attached Storage*) that fulfilled several key roles. The system provided secure cloud storage for our group (16 TB configured in RAID5), allowed convenient data ingestion into the data centre with the commercial synchronisation software, and enabled us to automatically aggregate data from measurement PCs into one centralised data lake to facilitate further processing. This functionality is important because these PCs are not necessarily located in the same lab or building. Data on this server is backed-up daily to a second (virtual) machine. This provides an off-site copy of the data and ensures its safe and robust long-term storage in accordance with the 3–2–1 data storage principle.

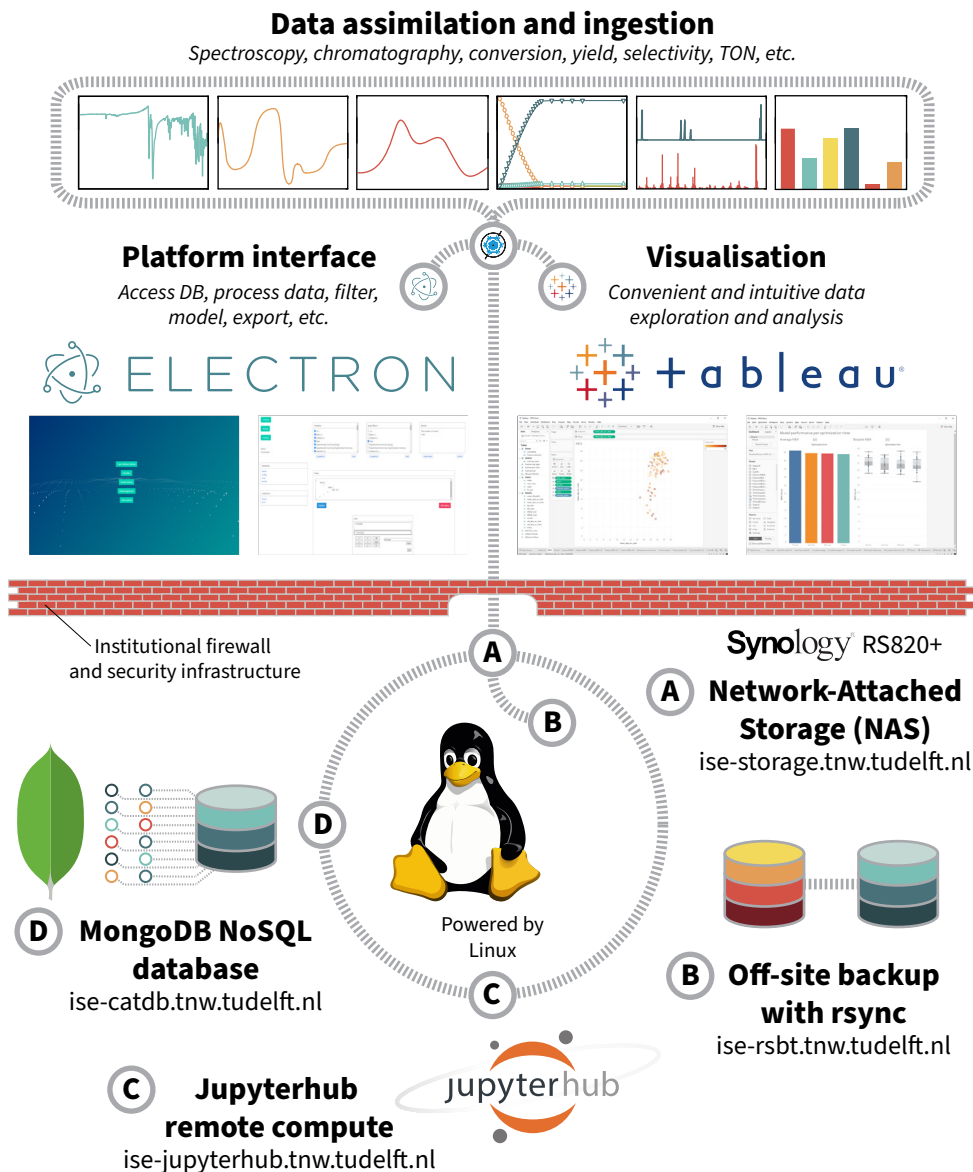


Figure 7.15. Global overview of the data management solution described in this work.

The remaining two servers were used to provide remote computational capabilities and to host the database. Jupyterhub was selected as the platform to host the kernel or application of choice.⁴⁰ (We are running IPython. Others such as IRkernel and IJulia are available.⁴¹) This allowed us to provide computational resources to the data management platform's users and to ensure a smooth user-experience. Users can operate individual Notebooks *via* a browser or run calculations from the

platform's desktop application (see next section). The current configuration runs on a virtualised 10-core machine that can conveniently be expanded if required. The connection between the app and (browser-based) Jupyterhub is managed through Puppeteer, which is an API that can control headless instances of Chrome and perform virtually any task that can be performed in a normal browser.⁴¹

A fourth server hosted the database application. We selected MongoDB's implementation of NoSQL because it was open-source and allowed the storage of many different data types inside one pooled data lake. This is important because the structure of our data is diverse and includes, *e.g.*, text, numerical values, but also (multidimensional) arrays. The specific 'document-oriented' architecture of MongoDB made it particularly well-suited to store these data without the additional complexity of operating multiple databases.

(Two general database formats exist: SQL and NoSQL. The first is a so-called structured or relational database that has well-defined cells or fields and is very similar to the way spreadsheet software works. NoSQL does not require a strict schema and can therefore be optimised to the specific structure of the data. Many implementations exist that each are geared towards specific applications.)

7.7 Analytics platform

The analytics platform of the data management solution is distributed to the users as a desktop application that runs on the local machine. Two iterations currently exist. The first version of the platform was programmed in the R programming language, and the accompanying visualisation app was made with RShiny. The R language is particularly suitable for data analysis and statistical computing.⁴² Data was transferred to the MongoDB database from Excel templates on the user's local machine and could be edited, searched, filtered, and visualised in the application. The construction of these (interactive) graphs and plots, however, was burdensome because it required explicit pieces of code for each analysis type.

A second-generation platform was therefore constructed that aimed to improve the first version. Functionalities that related to database interaction and data visualisation were decoupled and were implemented separately (**Figure 7.15**). The data management platform was constructed in Electron and was combined with commercial data visualisation software. Electron is a powerful cross-platform desktop construction tool based on JavaScript, CSS, and HTML, and has been used to create, *e.g.*, WhatsApp, Slack, and Twitch.⁴³ The app is coupled to Tableau's strong and intuitive visualisation software, which completely eliminated the need for hardcoding (an impression is provided in **Figure 7.16**). The data management

platform requires the installation of Tableau desktop on the local machine. Academic researchers can use this software free of charge.⁴⁴

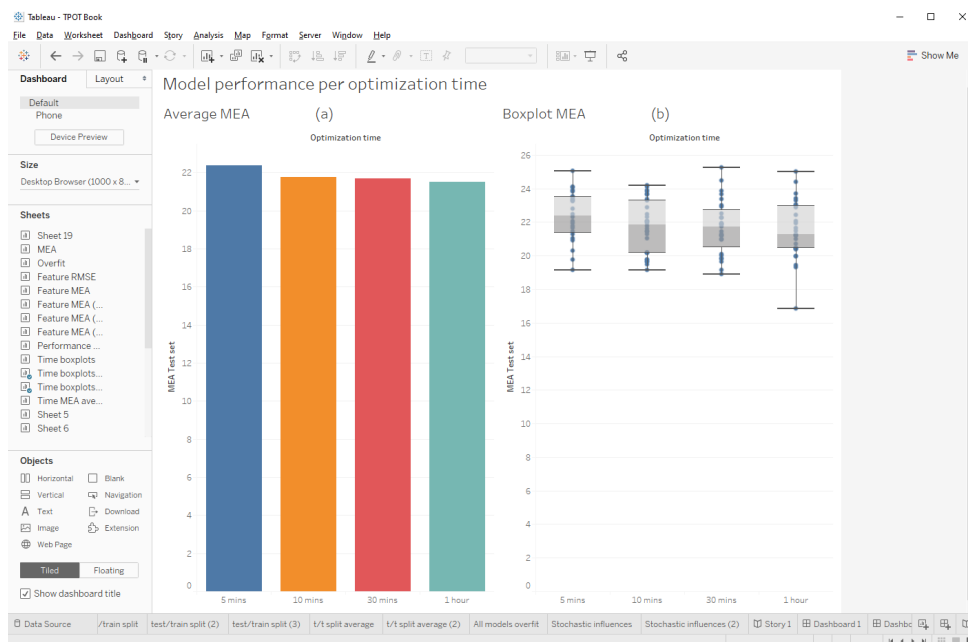


Figure 7.16. Impression of Tableau visualisation suite that is used in the data management platform.

The platform currently enables data to be created, read, updated, and deleted (operations that are customarily described as CRUD). Data can also be filtered, extracted, and visualised. Data are uploaded from the NAS to the MongoDB database server *via* template spreadsheets. The use of Excel (or any spreadsheet software package) was preferred over a custom submission form or panel because it provided better flexibility, scalability and accessibility. Data is identified with a persistent identifier such as an unique experiment number and uploads are checked for duplicate entries before they are added to the database. Additional columns can be added when required without the need to retroactively provide data for existing entries, ensuring that the platform stays relevant even as needs evolve.

Two specific data types required additional measures. Chemical structures were encoded with extended SMILES, as implemented in the commercial MarvinSketch software (version 20.21).⁴⁵ This format was selected over standard SMILES notation because it offers several advantages and supports more dense encoding. For example, extended SMILES can be used to add the metal centre oxidation state, describe different ligands, their hapticity and donor atoms (and specific geometry

if ligands are mapped, as in the example below), and supports the description of dative bonds that are common in transition metal complexes. A comparison of regular and extended SMILES for an arbitrary example is provided in **Figure 7.17**.

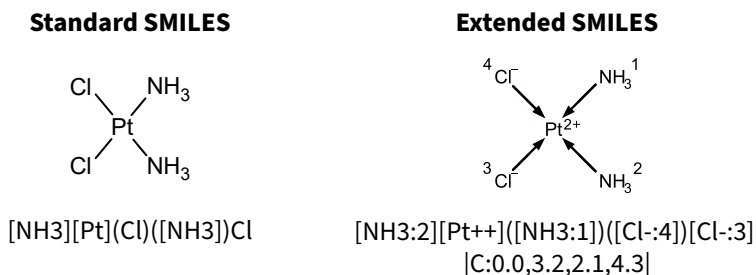


Figure 7.17. Comparison of regular and extended SMILES notation for Cisplatin.

Data that was shaped in arrays (usually spectra or chromatograms) presented other issues. These data were stored as ‘arrays-in-arrays’ such that spectra belonging to a specific experiment could be stored together with other data of that same experiment. The reproducible and convenient storage of series of arrays in database systems is not trivial, but was required to support our development of the data-rich experimentation approach that is described in this chapter. The ability to store arrays as documents (in JSON) is an important feature of MongoDB’s implementation of NoSQL that eliminated the need for different databases to store our different types of data.

In conclusion, we have developed a data management platform for use in our research group. The platform runs on several Linux servers that were deployed in TU Delft’s data centre. These servers interfaced with a custom-built desktop app that provided both CRUD functionalities as well as convenient and intuitive visualisations using Tableau’s desktop software suite. The system enabled the safe and robust storage of these data in a pooled data lake. The data management application described in this chapter remains under development and continuously gains functionalities. We ultimately envisage a situation where equipment in the lab is connected to the centralised platform and experiments are ‘announced’ to the system by the user. The system will then continuously look for new data, and import and process the results as they become available. We believe that such an automated system has the capacity to unburden researchers and help focus attention and resources to more meaningful work.

7.8 AUTOKAT – Computer-aided catalyst design

The *operando* reaction analysis platform described in **Chapter 7.3** of this dissertation is suitable for the in-depth study of a limited number of (sequential) experiments. Its data is of superior quality and density, but lacks the volume and velocity required for the construction of the desired predictive catalytic activity models. Alternative methods to acquire such data in sufficient volume do not currently exist. A new and highly automated ‘AUTOKAT’ work flow was therefore designed that integrates the best of sequential and parallelised approaches for both experimental and computational methods (**Figure 7.18**). AUTOKAT will establish a ground truth for catalyst development and deliver data suitable for the development of predictive catalytic activity models.

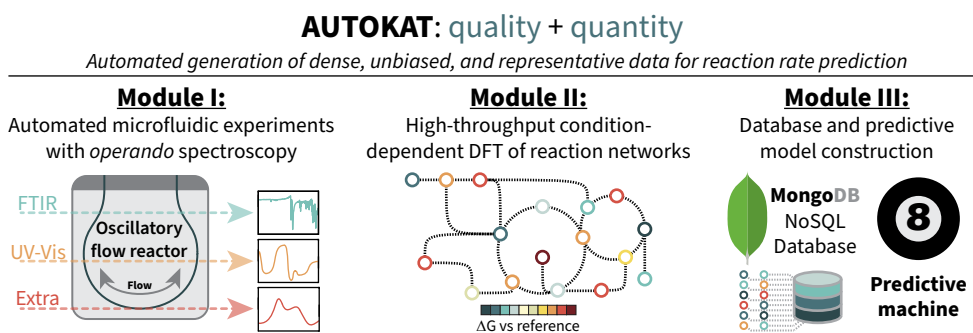


Figure 7.18. Proposed AUTOKAT work flow to enable the automated generation of dense, unbiased, and representative data.

The AUTOKAT project is based on three modules. The experimental and computational modules (I and II) will enable the generation of dense, unbiased, and representative data on catalytic activity that satisfies the ‘Five V’s’. The third module (III) is more future-facing and focuses on predictive model development. Details on the proposed project modules are described in this section. (Project funding was requested from the Dutch research council (NWO) in early 2021. The application is under review at the time of writing.)

7.9 AUTOKAT – Experimental work flow

The proposed experimental approach of the AUTOKAT work flow will provide an automated microfluidic system that produces data of similar quality and density as the reaction analysis platform, while also enabling significantly higher experimental throughput. This will be achieved by the integration of multiple modes of *operando* spectroscopy to the microfluidic oscillatory flow system that

was described in **Chapter 6**. Spectroscopy will be incorporated at fixed locations in the system, at which the droplet temporarily (<1 s) stops for spectral acquisition (**Figure 7.19**).

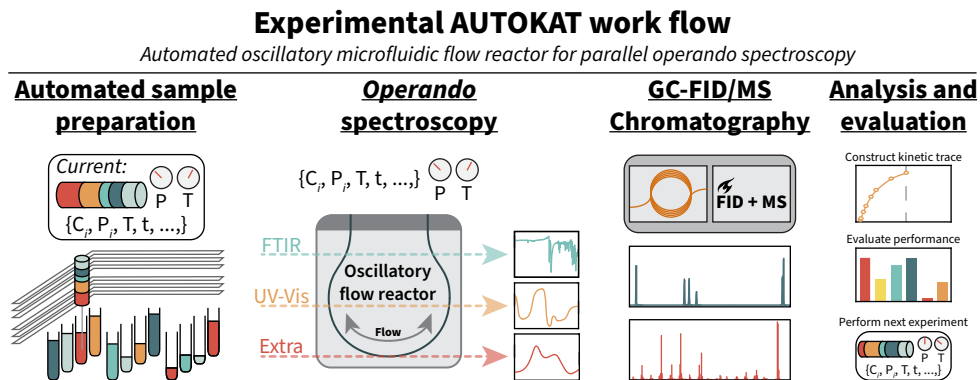


Figure 7.19. Proposed experimental work flow of AUTOKAT: a microfluidic oscillatory flow platform for parallel operando spectroscopy.

The specific type of automated and feedback-driven sequential experimentation enabled by the microfluidic oscillatory flow platform is important for the project to succeed, because it allows a more thorough and focused evaluation of the available condition space. Catalyst performance is known to be a function of variables such as the concentration and nature of reaction components, promoters, temperature, and pressure. Practical limitations, however, constrain the number of possible permutations in conventional approaches and lead to sparse sampling of the parameter space. This forces the selection of idealised ‘model conditions’, under which performance is evaluated for different molecular catalysts.⁴⁶ As a consequence, potentially strong-performing catalytic systems under other conditions cannot be identified with conventional approaches. AUTOKAT is not limited by such constraints and offers much more representative sampling of the available condition space.

Data produced with AUTOKAT will not only be more representative of the chemical system under certain conditions, it will also be of higher quality and density compared to conventional approaches. The specific combination of FTIR and UV-Vis spectroscopy covers a broad range of liquid-phase chemical applications and is well-equipped to detect minor changes in product composition at high temporal resolutions, as well as structural changes of the metal catalyst under study. Fast gas chromatography with combined FID and MS detectors enables rapid analysis of the reaction mixtures that allows improved experimental throughput compared to HPLC. (It is noted that implementation of UPLC would probably afford a similar acceleration.)

The proposed platform is highly modular and can accommodate alternative techniques when required. Such flexibility is an important aspect of the proposed AUTOKAT experimentation that will allow rapid modification of the system to host the best combination of available techniques, *e.g.*, a combination of FTIR, UV-Vis, and GC for project A, or Raman, UV-Vis, and HPLC for project B. Techniques can be embedded into the system when they are required by future projects, or as they become available (*e.g.*, flow-NMR). This will ensure that the system is used to its maximal capability and stays relevant as technology matures.

Integration of multiple modes of *operando* spectroscopy is the critical aspect of AUTOKAT experimentation that will provide the rich data that is required as a ground truth to train ML models. The capability to adapt the spectroscopic solution to the chemistry under study within the same platform is innovative and enables our proposed holistic approach to investigate complex catalytic systems under realistic reaction conditions. The combination of spectroscopy with on-line chromatography further improves data density and enables product quantification and (side-)product identification with mass spectroscopy.

Implementation of the experimental AUTOKAT work flow is further expected to improve data veracity. Experimental and data-driven techniques are highly sensitive to minor procedural variations, which can lead to undesirable outcomes and irreproducibility.^{13,47-51} For example, a small (unrecognised) temperature gradient in plate-based high-throughput experimentation can result in reactor-coordinate dependent catalytic activity. To address these issues, we will define procedural and experimental standards, collect metadata, and facilitate bias-free experimentation by extensive automation and reaction-environment control that is enabled by microfluidics. AUTOKAT will thus be well-placed to provide data that satisfies the ‘*Five V’s of big-data*’ and establish an experimental ground-truth to support the construction of predictive models.

7.10 AUTOKAT – Computational work flow

We propose to integrate the experimental microfluidic platform with a complementary computational work flow. The envisaged computational AUTOKAT system will address two important challenges that currently limit the widespread application of quantum chemical calculations for the prediction of catalytic reaction rates. The first challenge is the practical difficulty of calculating condition-dependent activity descriptors that are required for comprehensive predictive models. Quantum chemical calculations are generally performed under static conditions with a particular solvent model. Results are then corrected for temperature and pressure on basis of the ideal gas approximation. The results of

these calculations often are insightful, but rarely capture the complexity of real mixtures. Our group has recently developed and demonstrated the use of COSMO-RS-based models that describe the chemistry of complex and reactive multicomponent and multiphase catalytic mixtures.^{52–53} This approach enabled the calculation of concentration- and condition-dependent (thermodynamic) properties that were used to identify and rationalise condition-dependent deactivation pathways in catalytic CO₂ hydrogenations. The computational AUTOKAT project will continue to develop these tools and will introduce an automated work flow that enables high-throughput calculation of condition-dependent catalytic activity descriptors.

The second challenge is more fundamentally distinct from those encountered in experimental campaigns, but can also be addressed by automation. Computational work generally demands *a priori* hypothesis formation before calculations are submitted and analysed. This is important because the calculations will always return a result, but do not provide context: “*The answer is 42!*”. The researcher therefore not only has to know *what* to calculate, but also *why*, and *how* (*i.e.*, with what method). (This is in fact a much larger challenge in computational chemistry. Much like wave-particle duality in quantum mechanics, if one is not careful, DFT calculations can provide different answers depending on how the problem is approached.) Experiments, in contrast, can *in principle* be performed without such knowledge and will provide a more or less clear and contextual result. For example: when DFT calculations are employed to study the feasibility of a particular reaction mechanism, the researcher has to explicitly formulate intermediates and look for transition states. Pathways that are not considered or imagined cannot be explored because they are unknown unknowns. The results will therefore be biased to what is imaginable by the researcher.

To overcome this bias, we instead propose to automatically generate chemical structures within the reactivity network that *in principle* are accessible within specified constraints (*e.g.*, a maximum energy difference relative to the initial state). The first steps towards such automated reaction network analysis are currently being made in our group. AUTOKAT will build on this work and will be combined with the condition-dependent models. This integration will enable the automated high-throughput calculation of all feasible structures in the reaction mixture, as well as their properties under realistic conditions.

The proposed computational AUTOKAT work flow is summarised in **Figure 7.20**. A number of platform components still need to be developed to allow the automated calculation of input features for ML-methods.^{49,54–56} We envisage that a separate subsystem will be integrated and complemented with a user-friendly GUI to drive widespread adoption.

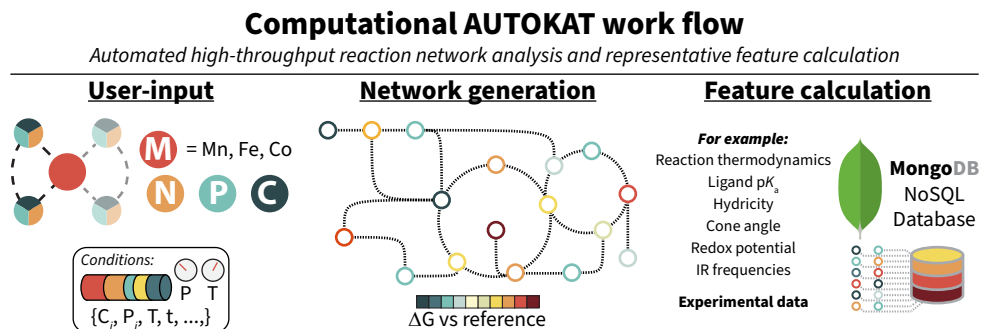


Figure 7.20. Proposed computational work flow of AUTOKAT: automated high-throughput reaction network analysis and feature calculation for predictive catalytic activity models.

The computational AUTOKAT project will start with the development of an automated submission and analysis system for the targeted condition-dependent (quantum chemical) calculations. This automated submission procedure is relatively straightforward and primarily requires bash-scripting. Extraction of target information will be implemented in Python. We will construct an interface that enables users to select the parameters that are required and what computational methods and corrections should be used. A number of diverse methods will be implemented in the software tool in the form of a library. This library can be used in parallel to enable cross-validation of different computational methods for a given problem. Cross-validation will increase our system's flexibility and robustness. It is noted that some of the proposed calculations might require non-trivial computational resources. These calculations will be performed on high-performance computing facilities available to our group.

As soon as the automated submission and analysis capabilities are complete, we will focus on the development of the proposed integral AUTOKAT work flow (**Figure 7.20**). First, the user provides information about the (catalytic) system under study, which will be used as a starting point for further calculations. This user-input includes chemical information about, *e.g.*, the precatalyst, the solvent, reagents, promoters (all in a machine-readable structural format that is already under development in our group). Additional information on the reaction conditions and their boundaries should also be provided at this stage. If the precatalyst under study is not well-defined (*e.g.*, when an *in situ* generated catalyst is used), the system will generate all possible structure and select the most likely candidates on basis of user-defined criteria (*e.g.*, 'the five most thermodynamically stable candidates', or 'only one multidentate ligand per complex').

Once the reaction input is complete and initial structures have been computed, the information is transferred to the second stage of the computational AUTOKAT work flow. Here, an automated reaction network analysis tool scouts the reaction's potential energy surface and generates permutations of the input structure in accordance with some cut-off criterion (*e.g.*, ± 120 kJ mol⁻¹ relative to the initial structure). Initial efforts towards such an algorithm are underway in our group, but currently are significantly less automated and advanced as imagined here. The envisaged automated reaction network analysis tool provides an overview of species that *in principle* are accessible under the reaction conditions. It will provide an unbiased overview of transient phenomena in the complex reaction mixture and will be particularly useful for the study of precatalyst activation or irreversible catalyst deactivation. Importantly, the procedure is automated and does not need *a priori* hypothesis formation to function. Automated reaction network analysis therefore is a critical aspect of the AUTOKAT work flow that enables bias-free and more generalised data acquisition and generation.

In the last step of the computational AUTOKAT work flow, condition-dependent activity descriptors and molecular features are calculated on basis of structures identified during the reactivity network analysis. The number of species in the network could be relatively large ($O(10^2-10^3)$), and subsequent processing necessitates the use of automated submission and analysis tools that have been described earlier. Calculations are submitted using the user-defined settings and the results are parsed to a document-based database. The output format(s) of these calculations could be highly diverse (*i.e.*, single values, arrays, but also multidimensional arrays). We therefore intend to use the well-established document-based database structure that is implemented in MongoDB (that has been described in more detail in this chapter). This database will also host results from the experimental AUTOKAT module and will function as our data lake.

7.11 AUTOKAT – Model construction

Once a sufficient body of data has been generated using the AUTOKAT platform, we will start model construction using all statistical and empirical methods that are available to us, with the ultimate goal of achieving predictive capabilities. These efforts will include, *e.g.*, but are not limited to, Bayesian optimisation, (non-) linear regression, random forests, support-vector machines, and/or reinforcement learning. Because the required data for such models are currently both unavailable and inaccessible, we do not yet know what model(s) will work best. We will therefore, for the time being, assume to use a wide range of models. For example, the prospect of using reinforcement learning is attractive, which could, *e.g.*, be implemented to train the model(s) on basis of the experimental ground truth.

Design of Experiments (DoE) and principal component analysis (PCA) will be used to efficiently map the available parameter space and build understanding of, *e.g.*, the effects of promoters, solvents, and conditions on catalytic activity, stability, and selectivity.^{46, 57} Data imputation will be used to enrich and supplement the available data set (*e.g.*, from response surfaces fitted from DoE). The proposed project does not intend to develop custom machine learning algorithms and will instead rely on ‘off-the-shelf’ libraries available in R, Python, and KNIME (*e.g.*, TPOT, CARET, randomForest, Skikit-learn, and TensorFlow). KNIME will predominantly be used for cheminformatics and to handle, *e.g.*, translation and incorporation of 3D structures. Tableau and R will be used for rapid data exploration and visualisation. Ultimately, the platform’s functionalities and access to the database will be streamlined and incorporated into a GUI-based system that is programmed in Electron. This will provide a convenient and user-friendly experience to drive rapid and widespread system adoption.

We intend to demonstrate the capabilities of the AUTOKAT work flow with the non-noble metal catalyst carbonyl reduction chemistry that has been described in detail in this dissertation and is currently being developed in our group (**Figure 7.21**).^{52, 58-62} Carbonyl hydrogenation chemistry is highly relevant for the production of a wide range of fine and bulk chemicals such as pharmaceuticals, flavours, fragrances, (bio)fuels, and lubricants.⁶¹⁻⁶³ Recent efforts have focused on replacing toxic, expensive, and scarce noble metals (Ru, Ir, Os) for more sustainable alternatives such as Fe and Mn.^{62, 64-66} Although large steps have been made, the performance of 3d transition metal catalysts generally lags behind that of the noble metals, and has predominantly been achieved by translation of established ligand platforms from noble to non-noble metals. Recent findings, however, indicate that 3d metals exhibit divergent reactivity that could potentially enable new and distinct chemistries (such as, *e.g.*, Mn-catalysed hydroformylation). We expect that the proposed AUTOKAT work flow will greatly benefit the development of non-noble metal catalysts. Tailoring of complex reaction environments to suit first-row metal catalysts is a current challenge in the field that holds great promise to improve green synthetic methods.

Green hydrogenation of carboxylic acid derivatives

Amides, (fatty) esters, ketones, imines, etc.

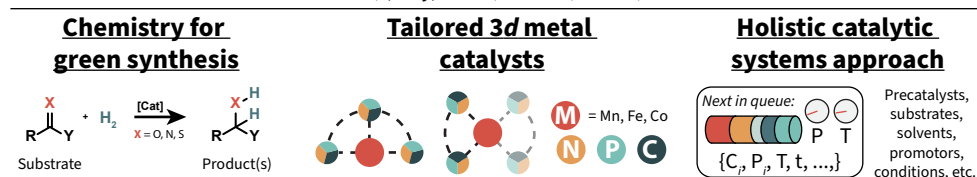


Figure 7.21. Hydrogenation of carboxylic acid derivatives and catalyst examples to be studied with AUTOKAT.

In summary, we propose to adopt a holistic approach to catalyst performance description and to study the integrated catalytic system that is comprised of molecular catalysts, conditions, promoters, and other components that are in the mixture. AUTOKAT will enable automated screening of categorical variables (*e.g.*, precatalysts, promoters, substrates) and continuous variables (*e.g.*, temperature, pressure, and time) to better sample the available condition space and thus improve understanding. This automated screening is performed experimentally and *in silico*. AUTOKAT will be able to provide data for predictive models by generating rich data under relevant and representative conditions. Our integral approach that focuses on catalytic systems, rather than catalysts, will provide fundamental insight that is not currently available. The rich data that is produced by the microfluidic platform will be combined with high-throughput calculations that are more representative and informative than conventional calculations. We believe that AUTOKAT will enable the accurate prediction of catalytic reaction rates and will strongly impact the field of homogeneous catalysis.

7.12 Conclusion

Recent developments in data-driven technologies such as machine learning have greatly impacted a wide range of scientific disciplines and continue to hold great promise. The application of such methods to predict reaction rates in the field of homogeneous catalysis, however, remains limited. We propose that this is—at least in part—due to the difficulty and cost associated with acquiring sufficiently-sized and descriptive experimental data sets.

In this chapter we have presented several (automated) tools that aim to provide and handle such data. An experimental sampling system was developed for the automated acquisition of high-quality kinetic data. This autosampler system was incorporated into a powerful and flexible reaction analysis platform that was used to study a fast Claisen-Schmidt condensation reaction with simultaneous kinetic measurements and several representative modes of *operando* spectroscopy. Initial steps were taken towards commercialisation of the developed autosampler system.

A data management and analytics tool was developed to reproducibly store, visualise, and gain insight from the produced data. This system was comprised of several (virtualised) Linux servers that were installed inside TU Delft's data centre. These servers were used to host the database, provide remote compute resources, and enable user-friendly interaction with the system through a commercial NAS solution. A front-end application was developed in Electron that provided convenient interaction with the database and was paired with the strong and intuitive visualisation suite of Tableau Desktop. The database and analytics tool is

currently being deployed in our group to store results of catalytic experiments and pool them into one centralised data lake.

Finally, a novel integral experimental and computational ('AUTOKAT') work flow was proposed that is aimed at achieving predictive capabilities for homogeneous catalysis research. We proposed a holistic approach to catalyst performance evaluation and description that aims to study *catalytic systems* rather than *catalysts*. The combined experimental and computational AUTOKAT projects aim to provide rich data that is relevant and representative for complex catalytic systems under realistic process conditions. Such data are not currently available or accessible by practical means, which limits the application of data-driven techniques in the field of homogeneous catalysis. We expect that AUTOKAT will provide data that are suitable for the prediction of catalytic activity and will help unlock the power of machine learning in catalysis R&D.

7.13 Experimental section

General considerations

All manipulations were performed in air. Chemicals and solvents were purchased from Sigma-Aldrich, TCI, and Biosolve and were dried and/or degassed before use.

Operando reaction analysis platform

Reactions were performed in air at 20 °C inside a 100 ml conical flask that was equipped with a PTFE-coated magnetic stirring bar. The flask was connected to the spectroscopic flow cells with FEP tubing (1/16" OD x 0.03" ID) and a Fluid Metering Q pump (GC400 pump assembly with RH0 ceramic pump head module, giving $1 \leq \Phi_v \leq 16 \text{ ml min}^{-1}$). The reactor was connected to, in order, the pump, IR flow cell, UV-Vis flow cell, and the autosampler system. This configuration provided the most stable flow through the flow cells. Background spectra were measured with empty flow cells. Mixture components were added sequentially whilst the spectrometers were running to acquire spectra of the individual components. FTIR was measured in absorption mode with a Bruker Alpha II spectrometer and a high-pressure flow cell that was equipped with CaF₂ windows and a 250 μm PTFE spacer (16 scans, 2 cm⁻¹ resolution, ~2 spectra min⁻¹). UV-Vis was measured in absorption mode on an Ocean Optics USB2000+ spectrometer, with an Avantes DH-2000 deuterium-halogen light source, and a high-pressure stainless steel flow cell that was equipped with 5 mm fused silica windows and had a 10.0 mm optical path length (10 scans, 6.78 μs integration time, ~220 spectra min⁻¹). Spectra were processed with Python. Solvent background spectra were subtracted and individual spectra were combined into one file. Spectra were visualised with OriginPro 2019. The least squares method was used for fitting, as implemented in the symfit module for Python.

Claisen-Schmidt condensation of benzaldehyde and acetone

To the reactor was added 0.21 g NaOH (5.3 mmol, 1.4 eq.), 1.0 ml water, and 20 ml ethanol. The suspension was sonicated until a clear solution was obtained. Circulation and spectroscopy were started and the system was checked for leaks and bubbles. To the circulating liquid was added a solution of 1.09 g benzaldehyde (10.3 mmol, 2.6 eq.) and 250 μ l *n*-dodecane in 20 ml THF. Once the solutions were well-mixed, a 50 μ l aliquot was removed for pre-reaction GC analysis. The reaction was started with the addition of a solution of 265 μ l acetone (3.9 mmol, 1.0 eq.) in 500 μ l THF. Upon addition the solution immediately turned yellow and later coloured golden yellow/orange. Spectra were acquired continuously. Samples (50 μ l) were removed at the indicated times with the autosampler system and were diluted and quenched with approximately 1.0 ml THF that contained 2 eq. acetic acid relative to NaOH. Samples were analysed as described.

Analytical details

Measurements were performed on an Agilent 7890B gas chromatograph equipped with FID and Agilent 5977B MS detectors and an Restek Stabilwax-MS column (30 m, 0.32 mmID, 0.25 μ m film thickness). Method details: 50 $^{\circ}$ C (hold 3.0 min), ramp to 250 $^{\circ}$ C at 100 $^{\circ}$ C min⁻¹ (hold at 250 $^{\circ}$ C for 20.0 min). Products were identified using the retention times of analytically pure reference samples and by comparison of observed mass spectra and spectra of the authentic reference samples available in the NIST 17 and SDBS libraries.

7.14 References

1. Silver, D.; Huang, A.; Maddison, C.J.; Guez, A.; Sifre, L.; van den Driessche, G.; Schrittwieser, J.; Antonoglou, I.; Panneershelvam, V.; Lanctot, M.; Dieleman, S.; Grewe, D.; Nham, J.; Kalchbrenner, N.; Sutskever, I.; Lillicrap, T.; Leach, M.; Kavukcuoglu, K.; Graepel, T.; Hassabis, D., *Mastering the game of Go with deep neural networks and tree search*, *Nature* **2016**, 529 (7587), 484–489;
2. Schrittwieser, J.; Antonoglou, I.; Hubert, T.; Simonyan, K.; Sifre, L.; Schmitt, S.; Guez, A.; Lockhart, E.; Hassabis, D.; Graepel, T.; Lillicrap, T.; Silver, D., *Mastering Atari, Go, chess and shogi by planning with a learned model*, *Nature* **2020**, 588 (7839), 604–609;
3. Senior, A.W.; Evans, R.; Jumper, J.; Kirkpatrick, J.; Sifre, L.; Green, T.; Qin, C.; Žídek, A.; Nelson, A. W.R.; Bridgland, A.; Penedones, H.; Petersen, S.; Simonyan, K.; Crossan, S.; Kohli, P.; Jones, D.T.; Silver, D.; Kavukcuoglu, K.; Hassabis, D., *Improved protein structure prediction using potentials from deep learning*, *Nature* **2020**, 577 (7792), 706–710;
4. Mulnaes, D.; Porta, N.; Clemens, R.; Apanasenko, I.; Reiners, J.; Gremer, L.; Neudecker, P.; Smits, S. H.J.; Gohlke, H., *TopModel: Template-Based Protein Structure Prediction at Low Sequence Identity Using Top-Down Consensus and Deep Neural Networks*, *Journal of Chemical Theory and Computation* **2020**, 16 (3), 1953–1967;
5. Rajkomar, A.; Dean, J.; Kohane, I., *Machine Learning in Medicine*, *New England Journal of Medicine* **2019**, 380 (14), 1347–1358;
6. *IBM Artificial intelligence in medicine*, <https://www.ibm.com/watson-health/learn/artificial-intelligence-medicine> (accessed 8 January 2021);
7. McKinney, S.M.; Sieniek, M.; Godbole, V.; Godwin, J.; Antropova, N.; Ashrafian, H.; Back, T.; Chesus, M.; Corrado, G.S.; Darzi, A.; Etemadi, M.; Garcia-Vicente, F.; Gilbert, F.J.; Halling-Brown, M.; Hassabis, D.; Jansen, S.; Karthikesalingam, A.; Kelly, C.J.; King, D.; Ledsam, J.R.; Melnick, D.; Mostofi, H.; Peng, L.; Reicher, J.J.; Romera-Paredes, B.; Sidebottom, R.; Suleyman, M.; Tse, D.; Young, K.C.; De Fauw, J.; Shetty, S., *International evaluation of an AI system for breast cancer screening*, *Nature* **2020**, 577 (7788), 89–94;
8. Dixon, M.F.; Halperin, I.; Bilokon, P., *Machine Learning in Finance*, 1st ed., Springer International Publishing, **2020**;
9. Culkun, R. *In Machine Learning in Finance : The Case of Deep Learning for Option Pricing*, **2017**;
10. De Spiegeleer, J.; Madan, D.B.; Reyners, S.; Schoutens, W., *Machine learning for quantitative finance: fast derivative pricing, hedging and fitting*, *Quantitative Finance* **2018**, 18 (10), 1635–1643;
11. Pflüger, P.M.; Glorius, F., *Molecular Machine Learning: The Future of Synthetic Chemistry?*, *Angewandte Chemie International Edition* **2020**, 59 (43), 18860–18865;
12. Strieth-Kalthoff, F.; Sandfort, F.; Segler, M.H.S.; Glorius, F., *Machine learning the ropes: principles, applications and directions in synthetic chemistry*, *Chemical Society Reviews* **2020**, 49 (17), 6154–6168;
13. Kitchin, J.R., *Machine learning in catalysis*, *Nature Catalysis* **2018**, 1 (4), 230–232;
14. Toyao, T.; Maeno, Z.; Takakusagi, S.; Kamachi, T.; Takigawa, I.; Shimizu, K.I., *Machine Learning for Catalysis Informatics: Recent Applications and Prospects*, *ACS Catalysis* **2020**, 10 (3), 2260–2297;
15. Coley, C.W.; Green, W.H.; Jensen, K.F., *Machine Learning in Computer-Aided Synthesis Planning*, *Accounts of Chemical Research* **2018**, 51 (5), 1281–1289;
16. Coley, C.W.; Barzilay, R.; Jaakkola, T.S.; Green, W.H.; Jensen, K.F., *Prediction of Organic Reaction*

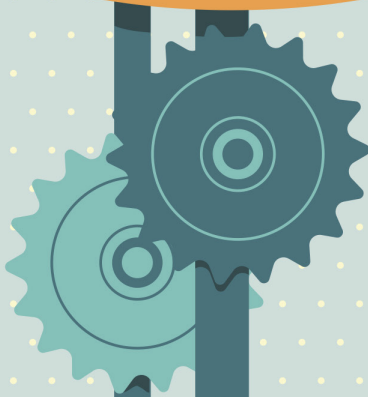
- Outcomes Using Machine Learning*, *ACS Central Science* **2017**, 3 (5), 434–443;
17. Fortunato, M.E.; Coley, C.W.; Barnes, B.C.; Jensen, K.F., *Data Augmentation and Pretraining for Template-Based Retrosynthetic Prediction in Computer-Aided Synthesis Planning*, *Journal of Chemical Information and Modeling* **2020**, 60 (7), 3398–3407;
 18. Ramakrishnan, R.; Dral, P.O.; Rupp, M.; von Lilienfeld, O.A., *Big Data Meets Quantum Chemistry Approximations: The Δ -Machine Learning Approach*, *Journal of Chemical Theory and Computation* **2015**, 11 (5), 2087–2096;
 19. Nandy, A.; Duan, C.; Janet, J.P.; Gugler, S.; Kulik, H.J., *Strategies and Software for Machine Learning Accelerated Discovery in Transition Metal Chemistry*, *Industrial & Engineering Chemistry Research* **2018**, 57 (42), 13973–13986;
 20. Kulik, H.J., *Making machine learning a useful tool in the accelerated discovery of transition metal complexes*, *WIREs Computational Molecular Science* **2020**, 10 (1), e1439;
 21. Philip Chen, C.L.; Zhang, C.Y., *Data-intensive applications, challenges, techniques and technologies: A survey on Big Data*, *Information Sciences* **2014**, 275, 314–347;
 22. Medford, A.J.; Kunz, M.R.; Ewing, S.M.; Borders, T.; Fushimi, R., *Extracting Knowledge from Data through Catalysis Informatics*, *ACS Catalysis* **2018**, 8 (8), 7403–7429;
 23. Blackmond, D.G., *Reaction Progress Kinetic Analysis: A Powerful Methodology for Mechanistic Studies of Complex Catalytic Reactions*, *Angewandte Chemie International Edition* **2005**, 44 (28), 4302–4320;
 24. Blackmond, D.G., *Kinetic Profiling of Catalytic Organic Reactions as a Mechanistic Tool*, *Journal of the American Chemical Society* **2015**, 137 (34), 10852–10866;
 25. Wei, B.; Sharland, J.C.; Lin, P.; Wilkerson-Hill, S.M.; Fullilove, F.A.; McKinnon, S.; Blackmond, D.G.; Davies, H.M.L., *In Situ Kinetic Studies of Rh(II)-Catalyzed Asymmetric Cyclopropanation with Low Catalyst Loadings*, *ACS Catalysis* **2020**, 10 (2), 1161–1170;
 26. McMullen, J.P.; Jensen, K.F., *Rapid Determination of Reaction Kinetics with an Automated Microfluidic System*, *Organic Process Research & Development* **2011**, 15 (2), 398–407;
 27. Taylor, C.J.; Booth, M.; Manson, J.A.; Willis, M.J.; Clemens, G.; Taylor, B.A.; Chamberlain, T.W.; Bourne, R.A., *Rapid, Automated Determination of Reaction Models and Kinetic Parameters*, *Chemical Engineering Journal* **2020**, 127017;
 28. Aroh, K.C.; Jensen, K.F., *Efficient kinetic experiments in continuous flow microreactors*, *Reaction Chemistry & Engineering* **2018**, 3 (1), 94–101;
 29. Mettler Toledo ReactIR 702L, https://www.mt.com/int/en/home/products/L1_AutochemProducts/ReactIR/ReactIR-702L.html (accessed 2 January 2021);
 30. Nunn, C.; DiPietro, A.; Hodnett, N.; Sun, P.; Wells, K.M., *High-Throughput Automated Design of Experiment (DoE) and Kinetic Modeling to Aid in Process Development of an API*, *Organic Process Research & Development* **2018**, 22 (1), 54–61;
 31. Mettler Toledo EasySampler 1210, https://www.mt.com/int/en/home/products/L1_AutochemProducts/EasySampler/easysampler-1210.html (accessed 2 January 2021);
 32. *Unchained Labs Optimization Sampling Reactor (OSR)*, https://www.unchainedlabs.com/wp-content/uploads/2016/09/17_OSR_spec_sheet.pdf (accessed 2 January 2021);
 33. Parr 4878 Automated Liquid Sampler, <https://www.parrinst.com/products/specialty-custom-systems/4878-automated-liquid-sampler/> (accessed 2 January 2021);
 34. Huck, L.A.; Leigh, W.J., *A Better Sunscreen: Structural Effects on Spectral Properties*, *Journal of Chemical*

- Education* **2010**, 87 (12), 1384–1387;
35. Rao, G.N.; Janardhana, C.; Ramanathan, V.; Rajesh, T.; Kumar, P.H., *Photochemical Dimerization of Dibenzylideneacetone. A Convenient Exercise in [2+2] Cycloaddition Using Chemical Ionization Mass Spectrometry*, *Journal of Chemical Education* **2006**, 83 (11), 1667;
 36. *FAIR Principles*, <https://www.go-fair.org/fair-principles/> (accessed 16 January 2021);
 37. *TU Delft research repository*, <https://repository.tudelft.nl/islandora/search/?collection=research> (accessed 16 January 2021);
 38. *4TU.ResearchData Repository*, <https://data.4tu.nl/info/en/> (accessed 16 January 2021);
 39. *YouTube by the numbers*, <https://blog.youtube/press> (accessed 19 January 2021);
 40. *Project Jupyter - Jupyterhub*, <https://jupyter.org/hub> (accessed 20 January 2021);
 41. *Puppeteer*, <https://developers.google.com/web/tools/puppeteer> (accessed 20 January 2021);
 42. *What is R?*, <https://www.r-project.org/about.html> (accessed 21 January 2021);
 43. *Electron*, <https://www.electronjs.org/> (accessed 20 January 2021);
 44. *Tableau Academic Programs*, <https://www.tableau.com/academic> (accessed 21 January 2021);
 45. *ChemAxon Extended SMILES and SMARTS*, <https://docs.chemaxon.com/display/docs/chemaxon-extended-smiles-and-smarts-cxsmiles-and-cxsmarts.md> (accessed 21 January 2021);
 46. Murray, P.M.; Tyler, S.N.G.; Moseley, J.D., *Beyond the Numbers: Charting Chemical Reaction Space*, *Organic Process Research & Development* **2013**, 17 (1), 40–46;
 47. Hutson, M., *Artificial intelligence faces reproducibility crisis*, *Science* **2018**, 359 (6377), 725;
 48. *Ensuring reproducibility in computational catalysis*, *Nature Catalysis* **2018**, 1 (4), 229–229;
 49. Ahneman, D.T.; Estrada, J.G.; Lin, S.; Dreher, S.D.; Doyle, A.G., *Predicting reaction performance in C–N cross-coupling using machine learning*, *Science* **2018**, 360 (6385), 186;
 50. Chuang, K.V.; Keiser, M.J., *Comment on “Predicting reaction performance in C–N cross-coupling using machine learning”*, *Science* **2018**, 362 (6416), eaat8603;
 51. Estrada, J.G.; Ahneman, D.T.; Sheridan, R.P.; Dreher, S.D.; Doyle, A.G., *Response to Comment on “Predicting reaction performance in C–N cross-coupling using machine learning”*, *Science* **2018**, 362 (6416), eaat8763;
 52. Liu, C.; van Putten, R.; Kulyaev, P.O.; Filonenko, G.A.; Pidko, E.A., *Computational insights into the catalytic role of the base promoters in ester hydrogenation with homogeneous non-pincer-based Mn-P,N catalyst*, *Journal of Catalysis* **2018**, 363, 136–143;
 53. Kuliaev, P.O.; Pidko, E.A., *Operando Modeling of Multicomponent Reactive Solutions in Homogeneous Catalysis: from Non-standard Free Energies to Reaction Network Control*, *ChemCatChem* **2020**, 12 (3), 795–802;
 54. Meyer, B.; Sawatlon, B.; Heinen, S.; von Lilienfeld, O.A.; Corminboeuf, C., *Machine learning meets volcano plots: computational discovery of cross-coupling catalysts*, *Chemical Science* **2018**, 9 (35), 7069–7077;
 55. Zahrt, A.F.; Henle, J.J.; Rose, B.T.; Wang, Y.; Darrow, W.T.; Denmark, S.E., *Prediction of higher-selectivity catalysts by computer-driven work flow and machine learning*, *Science* **2019**, 363 (6424), eaau5631;
 56. Reid, J.P.; Sigman, M.S., *Holistic prediction of enantioselectivity in asymmetric catalysis*, *Nature* **2019**, 571 (7765), 343–348;
 57. Fey, N., *Lost in chemical space? Maps to support organometallic catalysis*, *Chemistry Central Journal*

- 2015**, 9 (1), 38;
58. van Putten, R.; Benschop, J.; de Munck, V.J.; Weber, M.; Müller, C.; Filonenko, G.A.; Pidko, E.A., *Efficient and Practical Transfer Hydrogenation of Ketones Catalyzed by a Simple Bidentate Mn-NHC Complex*, *ChemCatChem* **2019**, 11 (21), 5232–5235;
59. van Putten, R.; Uslamin, E.A.; Garbe, M.; Liu, C.; Gonzalez-de-Castro, A.; Lutz, M.; Junge, K.; Hensen, E.J.M.; Beller, M.; Lefort, L.; Pidko, E.A., *Non-Pincer-Type Manganese Complexes as Efficient Catalysts for the Hydrogenation of Esters*, *Angewandte Chemie International Edition* **2017**, 56 (26), 7531–7534;
60. Filonenko, G.A.; Aguila, M.J.B.; Schulpen, E.N.; van Putten, R.; Wiecko, J.; Müller, C.; Lefort, L.; Hensen, E.J.M.; Pidko, E.A., *Bis-N-heterocyclic Carbene Aminopincer Ligands Enable High Activity in Ru-Catalyzed Ester Hydrogenation*, *Journal of the American Chemical Society* **2015**, 137 (24), 7620–7623;
61. Pritchard, J.; Filonenko, G.A.; van Putten, R.; Hensen, E.J.M.; Pidko, E.A., *Heterogeneous and homogeneous catalysis for the hydrogenation of carboxylic acid derivatives: history, advances and future directions*, *Chemical Society Reviews* **2015**, 44 (11), 3808–3833;
62. Filonenko, G.A.; van Putten, R.; Hensen, E.J.M.; Pidko, E.A., *Catalytic (de)hydrogenation promoted by non-precious metals – Co, Fe and Mn: recent advances in an emerging field*, *Chemical Society Reviews* **2018**, 47 (4), 1459–1483;
63. Werkmeister, S.; Junge, K.; Beller, M., *Catalytic Hydrogenation of Carboxylic Acid Esters, Amides, and Nitriles with Homogeneous Catalysts*, *Organic Process Research & Development* **2014**, 18 (2), 289–302;
64. Garbe, M.; Junge, K.; Beller, M., *Homogeneous Catalysis by Manganese-Based Pincer Complexes*, *European Journal of Organic Chemistry* **2017**, 2017 (30), 4344–4362;
65. Kallmeier, F.; Kempe, R., *Manganese Complexes for (De)Hydrogenation Catalysis: A Comparison to Cobalt and Iron Catalysts*, *Angewandte Chemie International Edition* **2018**, 57 (1), 46–60;
66. Gorgas, N.; Kirchner, K., *Isoelectronic Manganese and Iron Hydrogenation/Dehydrogenation Catalysts: Similarities and Divergences*, *Accounts of Chemical Research* **2018**, 51 (6), 1558–1569.



Chapter



Outlook



“No man should escape our universities without knowing how little he knows.”

Robert Oppenheimer

8.1 Introduction

Contemporary science is progressing at an astonishing pace. What once started as a pursuit of curiosity for the fortunate few has now transformed into a global enterprise that literally reaches beyond our solar system. Because progress is so fast, it makes sense to briefly look beyond the specific work described in this dissertation, and to take a moment to speculate about the developments that might be on the horizon. Some of these advances were already alluded to in previous chapters of this work, while other insights are more high-level and general.

This chapter follows a similar structure as the rest of the dissertation. First, an outlook is provided on the development of high-turnover, non-noble metal catalysts, and their application. This is followed by a discussion of recent trends in automation and modern data-science tools, as well as their projected impact on catalyst development in the near future. The chapter closes with a brief outlook on the changing culture of academia.

8.2 High-turnover non-noble metal catalysts

Chemical transformations—particularly catalytic ones—are still becoming increasingly sophisticated, and undoubtedly many improvements remain to be discovered. Researchers and engineers in both academia and industry are leveraging these new technologies to manufacture their products in smarter, cleaner, cheaper, safer, or generally better ways. Continuous improvement and development of novel and existing techniques is therefore highly desirable. It also makes sense to think about factors that drive adoption of these technologies such that their impact and reach can be maximised.

This comes back to the main question that we attempted to address in this dissertation: how to improve catalytic systems such that they can be operated at lower loading (and thus become practically applicable and cost-effective)? One of the goals of this work was to understand irreversible catalyst deactivation. Historically, this has been very successful and has resulted in non-noble metal catalysts that approach the performance of their more privileged, noble metal counterparts. (Although catalyst lifetime often remains significantly shorter for most non-noble metal systems.) The study of catalyst deactivation phenomena is therefore expected to become increasingly important. These investigations are further supported by the advanced *in situ* and *operando* tools that are currently being developed and can help extend catalyst lifetime to drastically reduce operational costs.

In order to drive adoption of advanced catalytic technologies, it makes sense to study catalytic systems that are already best-in-class and thus closest to commercial implementation. Often this will mean that noble metal catalysts should be studied, instead of the first-row transition metal systems that were predominantly used in **Part I** of this work. The properties of these noble metal complexes often are (but not always) more favourable compared to ostensibly attractive non-noble metal systems; their reactivity is more predictable, robust, and better understood. This all contributes to more convenient use and potentially lower costs.

Other purported benefits (cost, natural abundance, and toxicity) are also not necessarily in favour of the first-row metals. There is no cost advantage of using the highly popularised Mn. In fact, $\text{Mn}(\text{CO})_5\text{Br}$ is ~60% *more expensive* per mole than $\text{RuCl}_3 \cdot x\text{H}_2\text{O}$, which is the most common precursor into ruthenium chemistry (€10.900 mol⁻¹ *versus* €6900 mol⁻¹, prices for largest standard quantity at Strem in early 2021). Furthermore, metal precursor price only constitutes a small fraction of total system cost once the ligand, complexation and purification, packaging, storage, distribution, and overhead are accounted for. At the end of the day, the only cost that matters to the end-user is that of the targeted transformation, not that of a specific component.

Finally, there is a potential issue surrounding the limited natural abundance of certain metals. Arguably, however, this constrained supply of noble metals is a non-issue with regard to homogeneous catalysis. Noble metals are valuable precisely because of their scarcity, and are therefore often recycled. (Which is made easier by their particular inertness and physical properties.) To the best of our knowledge, such dedicated recycling infrastructure does not currently exist for non-noble metals such as Mn. For the foreseeable future it might therefore be more sustainable to use low loadings of recycled noble metals instead.

In conclusion, we expect that catalytic routes will see increased adoption by synthetic users. This will prevent the formation of large amounts of waste and potentially bring significant cost savings. Research into catalytic technologies will likely continue to increase, and would ideally be focused on the study of deactivation phenomena in order to understand and prevent premature catalyst death. A significant portion of these resources should be used to develop next-generation noble metal catalytic systems that can be operated at truly low and cost-competitive catalyst loadings in order to drive (industrial) adoption and maximise impact.

8.3 Automation and data-driven development

Automation and data-driven tools such as machine learning have received significant attention over the past years and continue to hold great promise. They have revolutionised certain aspect of data gathering and analysis, and have greatly improved the quality of insight that can be obtained from a given data set. As described in **Chapter 7**, the statistical tools used in machine learning generally only thrive with the availability of large amounts of—ideally high quality—data. These data have occasionally been difficult to procure in the (sometimes archaic) chemical sciences. Knowledge is often passed on to the next-generation directly and experimental design is occasionally considered more art than science. Experimental procedures and results have long been communicated in mostly unstructured or varying formats, which has limited the application of machine learning to (combinations of) very large data sets (*e.g.*, Reaxys), computationally-generated data sets, or experimental data sets that were produced using high-throughput experimentation (and thus were designed to be internally consistent).

Slowly this is changing. Advanced tools and electronic lab notebooks (ELNs) are coming online that produce and store unprecedented amounts of high-quality data, as well as record metadata that establishes context and consistency such that data can be mixed, matched, and reused. Initiatives that recognise the need for proper data repositories and management systems are also gaining traction, which will probably increase the value of these data (*e.g.*, **Chapter 7** of this dissertation, the Open Reaction Database project, and the German NFDI4Chem consortium). These efforts will undoubtedly benefit greatly from the development of a community-supported ontology, which can be used to standardise protocols and increase the value of derived properties such as turnover frequency and turnover number. Unfortunately, this apparently Herculean task of standardisation will be mission critical to the success of these ventures and cannot be avoided (and might therefore more reasonably be described as Sisyphean).

An integrated experimental and computational work flow was presented in **Chapter 7** of this dissertation that aims to address many of these issues. Ultimately it is expected that extensive automation and data-driven work flows will provide unprecedented insight and accelerate discovery and ideation. Importantly, this won't render skilled operators, chemists, and engineers obsolete. On the contrary; a premium will likely be placed on individuals that can bridge the two disciplines and provide judgement and interpretation. In this case, resource allocation, experimental design, planning, execution, analysis, and interpretation might become unified in one (online/app-based) platform that serves as 'mission control' for the lab's operations and unlocks significant productivity gains.

8.4 Concluding remarks

As a final note, it is important to place this dissertation in the appropriate context. The work described herein represents a very small advance of the state-of-the-art, despite it summarising several years of work of a team of people. At times this can feel disheartening, and it can therefore be useful to take a step back and to realise that many scientific advances were—and still are—achieved by lengthy, large-scale initiatives that combine forces and harness individual strengths, foster healthy competition, and, most importantly, enable the relentless work of countless unnamed researchers around the world. Many hands proverbially make light work, and the present generation truly stand on the shoulders of those that went before them. As a whole, this system leads to progress and drives innovation; project by project, paper by paper—no matter how small or apparently insignificant the contribution at the time. It is important to be patient and keep track of the bigger picture; Rome wasn't built in a day (and, in fact, neither was the first nitrogen fixation plant).

Unfortunately, this is easily forgotten in a hypercompetitive academic community that is busy with high-impact publishing and working of citation metrics to sustain hard-fought careers. This not only wastes precious resources that could be used more productively, but it also stifles growth and further distances academia from society. Thankfully, it appears that times are changing and that support is gathering for a more sustainable academic culture—a culture where contributions are evaluated on more than *h*-indices or the number of papers in *Nature* or *Science*. Although progress is slow, I believe it is vitally important to support such initiatives and to be vocal about the need for change. We should demand it from our institutions, each other, and from ourselves. Good things come to those who are fascinated by what they do and are excited to get back to work the next day. For it is endless curiosity and the belief in progress that drives so many of us, as well as the hope that our modest contribution to the greater body of human knowledge will someday lead to something tangible and good.



Appendix

A-C



Appendix



“Lord, grant me the humility to Google the things I do not know, the courage to pester my friends about the things I cannot Google, and the wisdom to know the difference.”

Uri Bram

(Adaptation of Reinhold Niebuhr's 'Serenity Prayer', as published in 1843 Magazine on 5 January 2018.)

Acknowledgements

Dordrecht, July 2021

So many things have happened over the past three and a half years. I can see how much I've changed during this time, both professionally and personally; I've become more mature, better balanced, and perhaps even a bit wiser. I'm proud of the work that we've done and the book that lies before you. This dissertation is the product of countless interactions, conversations, discussions, arguments, and collaborations with so many nice, smart, and gifted people, and this book genuinely couldn't have been without them. This makes me incredibly thankful to everyone that was involved—thank you! This section is for you.

First and foremost, I'd like to thank my promotors. Evgeny, you and I go way back, and I've genuinely enjoyed our working together ever since. I vividly remember how at some point (which must have been late 2014 or early 2015) you asked Erik and me into your office to talk about our future. Little did I know how seven (!) years later we'd still be working together. Thank you for all the support that you've given over the years, the opportunities that you've created, and the leeway that you've allowed me to find my own way. I've learned so much from you and am thankful to have you as a supervisor, advisor, and friend. I really appreciate our tête-à-têtes where we can talk about life and all sorts of things besides work. Evgeny, it's been a pleasure to work with you, and I hope we can find some way to continue doing so in the future.

Klavs, thank you for everything that you've done over the years, first at MIT and now as promotor. Thank you for taking me into your lab. I'm incredibly grateful to have had the chance to work with you and your group, and to have become a (very small) part of the MIT community. It's a shame that the pandemic prevented us from finishing the project properly. I have come to know you as an incredibly kind, generous, and patient leader, and I can't thank you enough for all the wisdom and experience that you've shared. Big thanks also for generously inviting us into your home for Thanksgiving that year—you're great chefs and the turkey and pecan pie were easily the best I've ever had. Thanks, Klavs, it's been a privilege.

I would like to sincerely thank the committee members for reading the dissertation, providing feedback, and for participating in the defence ceremony. Professor Beller, thank you for hosting me in Rostock all these years ago to work on—back then very new—Mn^I reduction catalysis. Those weeks have had a big impact, and I think you can still see some of the things that I've learned from you, Kathrin, and Marcel in this dissertation. Professors Doyle, Hollmann, and Urakawa, and dr. Eelkema, thank you, thank you, thank you. I look forward to our discussions!

Finally, dr. Lefort, Laurent, thank you for being part of the committee. We also go back a long time, and I've always appreciated your vision, wisdom, and communication style (as well as our playtime with the A96). I remember when Evgeny and I visited you in early 2017 and the two of you made the case that I should do the Ph.D. that Evgeny had just offered me. I really hadn't decided at the time and wasn't convinced it was right for me. Our conversations helped me make up my mind, and it therefore only seems right that you're also involved at the end of this journey. Thanks for everything that you've done, Laurent, I appreciate it.

This dissertation couldn't have been without the contribution of several students whom I've had the pleasure to (co-)supervise: Christophe Besnard (affectionately known as *Monsieur Baguette*), Vincent de Munck (who figured out how to cleanly synthesise Mn^I-NHC complexes), Joeri Benschop (the master of hand-measured kinetics), Nathan Jiscoat, and Majid Mohamedhosein (the latter two constituting the *database and analytics* team). Guys, you've all been fantastic students. Thank you for working on these projects with all your enthusiasm, independence, and initiative—I've learnt a lot from you. All the best in your future careers!

Many others have been involved in some way. Evgeny Jr, solnyshko, I'm so glad you joined us in Delft. We work well together, and I'm very proud of the work that we've done. Let's see where we can take it next. Thank you for your guidance during our trip to Novosibirsk (also with the unexpected excursion to Барнаул), and for teaching me some Russian. I believe that I've at least managed to fool one Yandex driver who drove Wenjun and myself to the ITC. Annika, I'm also very glad that you came to Delft to continue your Dutchification. We started on the same day and have steadily built a friendship since then. Even though we oftentimes disagreed about the desirable temperature in the office, I genuinely appreciate our working together and enjoy our regular coffee chats and walks outside. Let's make sure we keep having these wherever we both end up!

Members of the ISE group: thank you for making the Ph.D. and time at work so much more fun. Robert, thanks for all the enjoyable discussions and for being such a well-behaved roommate. Good luck in the Heimat at BASF. Chong, thanks for the nice collaboration that we've had since our time in Eindhoven. Guanna, Ági, Annika, thanks for the legendary trip to Moscow. I'm glad we all left the metro in one piece. Georgy, dear BSc-thesis supervisor, thanks for sharing your experience and for helping out whenever difficult chemistry appeared. Evidently your hands are significantly better developed than mine. Elena, fellow Eindhoven-age 'Evgeny-veteran', good luck with the last phase of the Ph.D.! Christophe, friendly giant, keep eating that lasagne to make you grow tall and strong. Divya, thanks for the nice conversations in the hallway and great company during our trip to Germany.

Wenjun, your creativity never ceases to amaze me—keep that up! Apologies for my profanity when we were sleighing down the hill in Siberia. Chuncheng, thanks for educating me about proper Chinese culture and cuisine in such a fun way. I hope you won't get into trouble for being an Illuminati. Ali, dear Prince, thank you for creating so many chemical structures, several of which ultimately led to some parts of this book. Please get ready to memorise the lyrics to *Prince Ali*. Dapeng, thanks for teaching me the basics of how to work with Cartesius and how to submit DFT calculations. Jittima, all the best on this final leg of your Ph.D. journey. Vivek, thanks for helping Nathan when he was working on EPiC-DNA. And finally, a big thanks to the countless students and guests that we've had over the years—your contributions and excitement made the group what it is today.

During my years at TU Delft/TNW-Zuid I've had the pleasure to interact with many people from other groups: Ina Vollmer, Jaco Geuchies, Adrián Gonzalez-Nelson, Giorgio Colombi, Davide Ripipi, Davide Rega, Dmitrii Osadchii, Thomas Eldridge, Sorin Bunea, Donato Pinto, Robin Möller-Gulland, Stefano Canox, Maryam Alimoradi Jazi, Sólrún Guðjónsdóttir, Magnús Borgar, Ryan Crisp, Tom Burdyny, Dominik Benz, Lorenz Baumgartner, and plenty others: thank you for all the nice chats, occasional drinks, and ChemE runs. I really appreciate the camaraderie and collegial atmosphere. All the best in your professional careers and personal lives.

My time in the United States was enhanced in a similar way by a group of fantastic people, either at MIT or in Cambridge, MA: Margo Haverty, Alina Haverty, Lorenz Baumgartner (again), Victor Schultz, Natalie Eyke, Thomas Struble, Travis Hart, Justin Lumiss, Connor Coley, Anirudh Nambiar, Yiming Mo, Agnieszka Ladosz, Alexander Pomberger, Christina Kuhnle, and Ioannis Lignos: you all took me in like a family member. Thanks for making this such a welcoming place. Bente, it was great to have some actual family there at the same time—I've had a blast. How about we go for some hot pot to reincarnate the tradition?

Several people have helped with some of the work, have done measurements, or have made this work possible in some critical way, shape, or form. Pouyan, thanks for the nice chats—every time I walked away with something new to think about. Manuela Weber and prof. dr. Christian Müller, thanks for measuring our crystals at FU Berlin. The same goes for dr. Martin Lutz at Utrecht University—thanks! Roel, I'm glad we reconnected after all these years. Thanks for your help in setting up the fitting, and let's keep having these highly periodic coffees. Leon, thanks for fabricating our parts and for teaching us how to manufacture them in the real world. Tonny, thanks for being a voice of reason in the sometimes polarised debate about what is safe and what is safe enough. Emergency response team, thanks for all the good times when we could work and train together. It was fun to learn how to use the external breathing equipment and to run around in the fire-fighter suit.

ITC-people: Matvey, Daniil, Artem, большое спасибо! It was a true pleasure to visit Siberia in winter. (Admittedly it was the warmest winter on record, but still pretty cold.) Your experience, knowledge, and handiness are impressive. You guys are scientist in the truest and best sense of the word. Gents, thanks for the incredibly welcoming environment, for the fascinating science, and for teaching us about баня, водка, and the (unexpected) merits of ice hole swimming in February.

TU Delft valorisation centre, Justin, Ronald: thanks for everything that you've done. You guys were instrumental in applying for the patent and getting the NWO Take-off grant. Founding a company would have been so much more difficult without your help, advice, and experience. Ard and Ruben of EDP patent attorneys: thank you for the silky-smooth process and for giving us a crash course in legalese—I've been fascinated with it ever since.

Technicians and management assistants: you deserve your own paragraph, because you are really the ones who keep the show on the road. Liliana, thank you so much for your efforts to limit the mess in the lab. I know how much of an ungrateful task this is, but I think you did very well. Thanks for accidentally ordering approximately a million of those yellow tubs. I think by now they've all found a home. Bart, Willy, Harrie, Ben, Bart, Marcel, Ruben, Duco, Lars, Christiaan, Erwin: thank you for the excellent help whenever something was broken or I didn't have the tools to fix it—somehow one of you guys always did. Karin (and sometimes Astrid), thank you for your help and occasional administrative witchcraft. Navigating the TU's bureaucratic maze can be challenging at times, but with your help we've always made it through. Thanks also for organising several of the group trips, they were awesome—good memories all the way.

Finally, I'd like to say thanks to my close friends and family. Mom and dad, thanks for the endless support. Who knew we'd end up here after all these years of education. I think you'll be incredibly proud to finally have the book in your hands and see your boy defend it in the white tie. Bas, I'm so glad we still hang out after our time in Eindhoven together: Ah Mooi. I look forward to reading your book! Frey, thank you for your unconditional support while I was writing. Lynn, thank you for all your patience and support these years. I'm glad and thankful that you were there during the highs and lows. Thanks for seeing through that when I wasn't in the best of moods, and sorry for being a workaholic at times. I can't thank you enough for being by my side during this venture. I'm excited about what the future holds for us and can't wait to find out where we'll end up.

To all of you, and to those whom I have forgotten: thank you—this book is for you.

List of publications

Journal articles

R. van Putten, E.A. Uslamin, D.M. Polykhov, A.S. Poryvaev, J. Benschop, R.P.W.M. Tielen, D. Ripepi, F.D. Tichelaar, M.V. Fedin, E.A. Pidko, *In preparation*;

R. van Putten, N.S. Eyke, L.M. Baumgartner, V.L. Schultz, G.A. Filonenko, K.F. Jensen, E.A. Pidko, *In preparation*;

R. van Putten^{*,†}, E.A. Uslamin^{*,†}, E.A. Pidko, *Automated high-resolution sampling and multi-mode operando spectroscopy of (bio-)chemical reactions for kinetic analysis, reaction characterization, and quality control*, Submitted;

R. van Putten, G.A. Filonenko, A.M. Krieger, M. Lutz, E.A. Pidko, *Manganese-mediated C-C bond formation: alkoxycarbonylation of organoboranes*, *Organometallics* **2021**, *40*, 674–681;

R. van Putten, G.A. Filonenko, A. Gonzalez-de-Castro, C. Liu, M. Weber, C. Müller, L. Lefort, E.A. Pidko, *Mechanistic complexity of asymmetric transfer hydrogenation with simple Mn-diamine catalysts*, *Organometallics* **2019**, *38*, 3187–3196;

R. van Putten, J. Benschop, V.J. de Munck, M. Weber, C. Müller, G.A. Filonenko, E.A. Pidko, *Efficient and practical transfer hydrogenation of ketones catalyzed by a simple bidentate Mn-NHC complex*, *ChemCatChem* **2019**, *11*, 5232–5235;

R. van Putten[†], T. Wissink[†], T. Swinkels, E.A. Pidko, *Fuelling the hydrogen economy: scale-up of an integrated formic acid-to-power system*, *International Journal of Hydrogen Energy* **2019**, *44*, 28533–28541;

C. Liu, R. van Putten, P.O. Kulyaev, G.A. Filonenko, E.A. Pidko, *Computational insights into the catalytic role of the base promoters in ester hydrogenation with homogeneous non-pincer-based Mn-P,N catalysts*, *Journal of Catalysis* **2018**, *363*, 136–143;

G.A. Filonenko, R. van Putten, E.J.M. Hensen, E.A. Pidko, *Catalytic (de)hydrogenation promoted by non-precious metals – Co, Fe and Mn: recent advances in an emerging field*, *Chemical Society Reviews* **2018**, *47*, 1459–1483;

R. van Putten, E.A. Uslamin, M. Garbe, C. Liu, A. Gonzalez-de-Castro, M. Lutz, K. Junge, E.J.M. Hensen, M. Beller, L. Lefort, E.A. Pidko, *Non-pincer-type manganese complexes as efficient catalysts for the hydrogenation of esters*, *Angewandte Chemie International Edition* **2017**, 56, 7531–7534;

K. Liu, J. Pritchard, L. Lu, R. van Putten, M.W.G.M. Verhoeven, M. Schmitkamp, X. Huang, L. Lefort, C.J. Kiely, E.J.M. Hensen, E.A. Pidko, *Supported nickel-rhenium catalysts for selective hydrogenation of methyl esters to alcohols*, *Chemical Communications* **2017**, 53, 9761–9764;

G.A. Filonenko, M.B. Aguila, E.N. Schulpen, R. van Putten, J. Wiecko, C. Müller, L. Lefort, E.J.M. Hensen, E.A. Pidko, *Bis-N-Heterocyclic carbene ligands enable high activity in Ru-catalyzed ester hydrogenation*, *Journal of the American Chemical Society* **2015**, 137, 7620–7323;

J. Pritchard, G.A. Filonenko, R. van Putten, E.J.M. Hensen, E.A. Pidko, *Heterogeneous and homogeneous catalysis for the hydrogenation of carboxylic acid derivatives: history, advances and future directions*, *Chemical Society Reviews* **2015**, 44, 3808–3833;

G.A. Filonenko, R. van Putten, E.N. Schulpen, E.J.M. Hensen, E.A. Pidko, *Highly efficient reversible hydrogenation of carbon dioxide to formates using Ru PNP-pincer catalyst*, *ChemCatChem* **2014**, 6, 1526–1530.

Patents

R. van Putten[‡], E.A. Uslamin[‡], E.A. Pidko, *Sampling arrangement*, NL2024908 (PCT/NL2021/050091), filed 14 February 2020.

Oral contributions

R. van Putten, N.S. Eyke, K.F. Jensen, E.A. Pidko, *Automation-guided reaction development in homogeneous catalysis: enabling rapid scale-up of Ru catalysed asymmetric hydrogenations*, Netherlands' Catalysis and Chemistry Conference (NCCC XXI), 2–4 March 2020, Noordwijkerhout, the Netherlands;

R. van Putten, G.A. Filonenko, L. Lefort, E.A. Pidko, *Homogeneous Mn catalysts for the efficient hydrogenation of esters*, XXVIII International Conference on Organometallic Chemistry, 15–20 July 2018, Florence, Italy;

R. van Putten, G.A. Filonenko, E.A. Pidko, *Homogeneous manganese catalysts for the efficient hydrogenation of esters*, 5th International School-Conference on Catalysis for Young Scientists: “*Catalyst Design: From Molecular to Industrial Level*”, 21–24 May 2018, Moscow, Russian Federation;

R. van Putten, E.A. Uslamin, C. Liu, L. Lefort, E.J.M. Hensen, E.A. Pidko, *Catalytic hydrogenation of esters by well-defined MnPN complexes*, Netherlands' Catalysis and Chemistry Conference (NCCC XIX), 5–7 March 2018, Noordwijkerhout, the Netherlands. This contribution was awarded the NIOK Lecture award.

Poster contributions

R. van Putten, A.M. Krieger, C. Liu, G.A. Filonenko, E.A. Pidko, *Structure-activity relations in carbonyl reduction catalysis with Mn-X,N-systems (X = C, P, N)*, 136th BASF International Summer Course, 11–17 August 2019, Ludwigshafen, Germany;

R. van Putten, A.M. Krieger, C. Liu, G.A. Filonenko, E.A. Pidko, *Structure-activity relations in carbonyl reduction catalysis with Mn-X,N-systems (X = C, P, N)*, Netherlands' Catalysis and Chemistry Conference (NCCC XX), 4–6 March 2019, Noordwijkerhout, the Netherlands. This contribution was awarded the VIRAN Poster award;

R. van Putten, E.A. Uslamin, A. Gonzalez-de-Castro, L. Lefort, E.J.M. Hensen, E.A. Pidko, *Non-pincer-type manganese complexes as efficient catalysts for the hydrogenation of esters*, Netherlands' Catalysis and Chemistry Conference (NCCC XVIII), 7–9 March 2016, Noordwijkerhout, the Netherlands;

R. van Putten, G.A. Filonenko, L. Lefort, E.J.M. Hensen, E.A. Pidko, *Versatile bis-N-heterocyclic carbene ruthenium pincer catalyst platform: metal-ligand cooperative behavior and catalytic activity towards ester hydrogenation*, 20th International Symposium on Homogeneous Catalysis (ISHC XX), 10–15 July 2016, Kyoto, Japan.

Grant applications

R. van Putten[‡], E.A. Uslamin[‡], E.A. Pidko, *Autonomous high-resolution sampling of (bio-)chemical reactions for kinetic analysis and quality control*, NWO Take-Off phase I, budget: €40.000, *Granted*;

R. van Putten, F. Meirer, E.A. Pidko, *Computer-aided catalyst design: development of an automated microfluidic platform for next-generation data-driven catalysis R&D (AUTOKAT)*, NWO ENW-M-2, budget: €700.000, *Submitted*.

Curriculum Vitae

Robbert van Putten was born on the 8th of September 1992 in Zevenbergen, the Netherlands. He completed his secondary school education (VWO, Atheneum) in 2011 at the Norbertuscollege in Roosendaal, and started his BSc studies in chemical engineering and chemistry at Eindhoven University of Technology that same year. During this time he studied abroad at Queen's University Belfast and was awarded the Sixma Organic Chemistry prize. He finalised his BSc degree in early 2015 with the distinction *cum laude*.



That same year Robbert started his MSc studies in chemical engineering at the same university, during which he specialised in process engineering and catalysis, and was awarded an ASML Technology Scholarship. His graduation research focused on homogeneous ester hydrogenations and was supervised by prof. dr. Emiel Hensen and dr. Evgeny Pidko. Part of this work was performed at the Leibniz-Institut für Katalyse e.V. (Rostock, Germany) under the supervision of prof. dr. Matthias Beller and dr. Kathrin Junge. His MSc thesis was selected as the best thesis of the TU/e Department of Chemical Engineering and Chemistry in 2017. He then finalised his MSc studies with double internships at Shell Global Solutions International in Amsterdam and at ASML, where he worked on up-scaling of hydrodesulphurisation catalysts and improving intercontinental communication between ASML offices. Robbert received his MSc degree with the distinction *cum laude* in late 2017.

In January 2018, he joined the group of prof. dr. Evgeny Pidko at Delft University of Technology to start his Ph.D. research. The most important results of this work are described in this dissertation. During this time, he has given several lectures at inter(national) conferences and was a visiting scientist at MIT under the supervision of prof. dr. Klavs F. Jensen. He participated in the first EFCATS Young Scientist challenge, the 136th BASF International Summer Course, MIT's LeaderShape programme, and won the NIOK lecture award and VIRAN poster prize in sequential years of the annual NCCC conference. Robbert is a co-founder of CyberHydra B.V., a tech start-up that aims to bring advanced spectroscopic and kinetic chemical R&D tools to market. This start-up was awarded €40.000 by the Dutch Research Council (NWO) in December 2020 and won several prizes in 2021Q1/2's edition of the YES!Delft/Roland Berger *Ready to Start-up!* course.

“When an old and distinguished person speaks to you, listen to him carefully and with respect—but do not believe him. Never put your trust into anything but your own intellect.”

Linus Pauling


CATALYSIS, CHEMISTRY, AND AUTOMATION

Catalysis is a critical enabling technology that directly contributes to higher standards of living. This is a remarkable feat for a technology that most consumers have no direct contact with and perhaps only vaguely know from their car's catalytic converter. Even many technical users regard catalysts as ideal substances that promote a target transformation without being consumed in the reaction. Reality, however, is much more complex because catalysts can also produce undesirable side-products or stop working before the target reaction is complete. This dissertation explores such complexity.

The aim of this work was to study real catalytic systems under relevant reaction conditions. This challenge was approached from two different directions, and the dissertation is therefore divided into two parts. Part I describes our study of non-noble Mn complexes as catalysts for a variety of reduction chemistries. Particular attention was given to the study of deactivation phenomena to understand why some catalysts stop operating early in their lifetime. This work led to catalytic methods that enable improved operation at significantly lower catalyst loading. The second part of this dissertation focuses on the development and application of automation and data-rich experimentation methods for catalysis R&D. An automated reaction analysis platform was developed that simultaneously produces kinetic data and several representative data streams of *operando* spectroscopy. These tools were used to study and optimise the performance of a variety of chemistries, and are expected to provide the required dense data for contemporary data-driven methods.



ABOUT THE Author



Robbert van Putten (1992) received his MSc in chemical Engineering from Eindhoven University of Technology in 2017. After completing industrial internships with Shell and ASML, he moved to Delft University of Technology to start his doctoral research under the supervision of prof. Evgeny A. Pidko. His research was focused on developing and understanding complex homogeneous catalytic systems for the production of pharmaceuticals and fine-chemicals. The most important results of this work are described in this dissertation.

